Drops, vesicles and red blood cells: Deformability and behavior under flow

Magalie Faivre

UNIVERSITÉ JOSEPH FOURIER — GRENOBLE I
LABORATOIRE DE SPECTROMÉTRIE PHYSIQUE

pour obtenir le titre de

DOCTEUR DE L'UNIVERSITÉ JOSEPH FOURIER

Discipline : Physique

Présenté par

Magalie Faivre

—

Drops, vesicles and red blood cells: Deformability and behavior under flow

Gouttes, vésicules et globules rouges : Déformabilité et comportement sous écoulement

—

Octobre 2004 - Décembre 2006

Soutenue publiquement devant le jury composé de

Mme.	**Elisabeth CHARLAIX**	**Présidente du jury**
M.	**Bertrand FOURCADE**	
Mme.	**Brigitte PEPIN-DONAT**	**Directrice de thèse**
M.	**Frédéric RISSO**	**Rapporteur**
M.	**Howard A. STONE**	**Directeur de thèse**
M.	**Patrick TABELING**	**Rapporteur**
Mme.	**Annie VIALLAT**	**Directrice de thèse**

Remerciements

Je souhaiterais tout d'abord remercier Elisabeth Charlaix qui m'a fait l'honneur de présider le jury de cette thèse. Merci à Frédéric Risso et Patrick Tabeling qui ont eu la gentillesse d'accepter, malgré leur charge de travail, de juger ce travail de thèse et d'avoir la pénible tâche de rédiger les rapports sur mon manuscrit. Merci également à Bertrand Fourcade qui m'a fait l'honneur de sa présence dans le jury.

Cette thèse n'aurait pas été possible sans les efforts conjugués de mes trois directeurs de thèse. Je les remercie de leur ténacité sans laquelle cette thèse en co-direction n'aurait pas pu se réaliser.

Je voudrais remercier Annie Viallat de m'avoir ouvert les portes de son équipe de recherche d'abord au Laboratoire de Spectrométrie Physique de Grenoble, puis plus tard, à l'U600 de Marseille. Je lui suis reconnaissante d'avoir su me consacrer de son temps tout en me laissant de l'autonomie. Depuis notre première rencontre lors de mon stage de maîtrise, à travers son enthousiasme communicatif et ses conseils avisés, Annie a su me "refiler" le virus de la recherche. Je voudrais lui dire merci d'avoir fait son maximum afin que je puisse faire ma thèse malgré l'absence initiale de financement.

Je suis extrêment reconnaissante à Brigitte Pépin-Donat pour son soutien, sa confiance, sa sagesse et son aide. Elle a su se rendre disponible quand j'en avais besoin et me redonner confiance en moi durant les nombreux moments de doutes. Ses conseils avisés m'ont été très précieux notamment durant les difficiles journées de rédaction. Elle m'a transmis sa passion de la recherche et son honnêteté scientifique. Plus encore qu'une directrice de thèse, elle est devenue au cours de ces trois années, un modèle et j'espère un jour, devenir une scientifique de son niveau.

Enfin et surtout, je voudrais exprimer ma reconnaissance infinie à Howard A. Stone sans qui cette thèse n'aurait jamais été possible. Je le remercie de m'avoir accueillie dans son groupe à Harvard. Je voudrais lui dire à quel point sa confiance en moi, son soutien, sa disponibilité (en dépit d'un emploi du temps de ministre) et ses encouragements ont fait de la petite étudiante naïve qui a débarquée aux USA en janvier 2004, la jeune expérimentaliste plus sûre d'elle que je suis devenue maintenant. Merci de m'avoir permis d'évoluer dans un environnement scientifique aussi riche. Comment lui dire tout ce qu'il m'a appris... Que sous sa direction, j'ai développé un esprit critique et que j'ai appris à me poser les bonnes questions... Que je le considère comme mon "père scientifique" dont l'enthousiasme permanent a contribué à rendre l'atmosphère du "Stone group" si vivante et si chaleureuse...

Je tiens à remercier chaleureusement Manouk Abkarian pour tout ce qu'il a fait pour moi. Je le remercie pour son soutien quotidien, sa confiance et la patience dont il a fait preuve au cours de ces deux années passées ensemble. Il a su devenir plus qu'un encadrant pour moi, un véritable ami. Merci de m'avoir poussée au delà de mes limites et de m'avoir soutenue à travers les changements de cultures et les coups durs. Merci d'être resté disponible et de m'avoir communiqué son enthousiasme et sa passion de la physique. Merci aussi de m'avoir accompagnée tout au long des (pénibles) calculs théoriques. Et merci de m'avoir ramené ma valise ;)

De plus, je tiens à remercier tous les étudiants qui ont soufferts “sous mes ordres”. Merci à Brian qui n’a pas tourné de l’oeil une seule fois pendant les manips de globules rouges. Bonne chance à Kimberly et Renita pour leur thèse, l’une dans la chaleur des labos de Miami, l’autre dans le froid sidéral de la salle de manip d’Harvard... Je souhaite également le meilleur à Jewel, cette jeune lycéenne qui m’a époustouflée par son incroyable intuition des phénomènes physiques et qui s ést appliquée de manière acharnée pendant la fabrication des canaux microfluidiques. Merci à Thierry qui m’a partiellement guérie de ma phobie des araignées grâce au traitement de choc ordonné par le docteur François...

Un énorme merci à tous les membres du “Stone group”. Thomas merci de m’avoir appris tout ce que je sais sur la production de gouttelettes. Je remercie Laurent pour ses conseils avisés et pour ces heures que nous avons partagées dans la salle blanche ; Anand pour avoir su garder le sourire malgré la musique fran¸caise dans le bureau tous les jours. Bill, pour ton amitié qui m’a été très précieuse, je voudrais que tu saches à quel point je me suis sentie chaleureusement entourée par toute la famille Ristenpart, merci. Merci à Jiandi pour sa bonne humeur quotidienne, ses encouragements et son amitié. Je remercie Emilie pour avoir été une vraie amie et pour son rire qui a réchauffé les longues et froides journées d’hiver à Boston. Merci à Catherine avec qui j’ai adoré travailler et qui m’a tellement appris sur les globules rouges d’un point de vue médical et biologique.

Je remercie Jacy, Marcus, Marc, Matt et Ernst sans qui les pauses café et les “group meeting” n’auraient pas été aussi agréables. Marcus, Ernst et Bill, merci pour le temps précieux que vous avez passé à m’aider sur Matlab. Je voudrais remercier Armand Ajdari pour ses conseils avisés et sa disponibilité ; son sens de l’humour a animé les pauses et déjeuners du groupe. Merci à Kristian dont la patience a été mise à rude épreuve, il aura été un exemple pour nous tous (surtout en ce qui concerne les Happy hours !!!). Enfin, comment exprimer à Kate toute la gratitude que je ressens ? Je veux la remercier pour sa gentillesse et son aide. Elle a su rendre les nombreux allers-retours entre France et USA beaucoup plus tranquilles, simplifier les démarches administratives et rendre cette expérience à l’étranger encore plus agréable ; sa bonne humeur, sa joie de vivre et son efficacité font d’elle un élément indispensable du “Stone group”. Merci à

tous les visiteurs de passage pour nos conversations.

Merci aussi à tous les autres membres de la communauté “Harvard” pour les discussions passionnantes ; merci à Andy, Elise et Daren pour leur aide et leurs petits tuyaux qui m'ont permis de résoudre bien des problèmes de microcanal ; merci aussi pour les fous rires et les bières descendues au John Harvard Pub. Un grand merci à Martha Mooney, sa perpétuelle bonne humeur, son aide permanente et sa gentillesse ont élevé les corvées administratives au rang de broutilles. Merci pour tout, sans elle, je serais encore en train de remplir des formulaires... Je voudrais remercier infiniment Charles, pour avoir été auprès de moi lorsque la distance avec ma famille se faisait trop sentir ; merci pour son soutien, bonne chance en Californie.

Je voudrais ensuite remercier tous les membres de l'équipe du Labo de Spectro avec qui j'ai travaillé (peu importe oú vous êtes maintenant, vous resterez toujours le coeur du CERMO pour moi) pour l'ambiance incomparable qui a rythmé mes passages en France. Merci à Cyrille pour son aide en ce qui concerne LateX, lui qui a toujours répondu présent (“Cyrille !!!! au secours !!!”) pour lutter avec moi contre les rébellions de l'informatique. Merci pour son soutien, sa bonne humeur, ses conseils et nos rigolades. Tiens le coup, c'est bientôt la fin. Un grand merci á Clément et à Zen Hong d'avoir partagé leur bureau avec moi et d'avoir patiemment supporté la musique que j'écoutais. Je leur souhaite bonne chance pour la fin de leurs thèses.

Merci à Pauline pour nos discussions, merci d'avoir toujours eu l'air d'être encore plus paumée que moi ;) merci et bonne chance pour la suite. Merci à Yoann qui m'a encourag ée à sa fa¸con ; félicitation pour la thèse et bonne chance chez ST. Je voudrais aussi remercier Jacques Derouard et Antoine Delon qui ont su rendre mes passages au Labo de Spectro agréables, en m'accueillant chaleureusement dans le groupe. Merci à eux d'avoir toujours trouvé le temps de discuter avec moi. Merci spécialement à Jacques qui a fait que cette situation particulière de co-direction entre Grenoble, Marseille et Harvard se passe au mieux. Merci à Jessie pour nos conversations ; merci pour m'avoir écouté me plaindre en permanence, pour son aide, pour son amitié, pour sa bonne humeur et sa joie de vivre ; merci pour avoir rendu mes passages au Labo de Spectro aussi chaleureux.

Comment remercier les membres du CERMO sans remercier Philippe ? Ton inventivité et tes qualités d'ingénieur font de toi le pillier de ce laboratoire. Merci de m'avoir aidée à “capoter” le microscope pour garder les vésicules au chaud. Tu es celui qui est devenu au fil des temps un ami très cher. Merci pour tous nos restos, merci pour nos nombreux cafés, thés ou chocolats qui ont, à eux seuls, assuré la rentabilité de la machine à café. Au fait, tu me dois toujours une bière à EVE je crois ? ;)

Merci aux membres de l'U600 pour m'avoir accueillie au sein de leur labo et pour avoir iv fait de mon séjour à Marseille un moment agréable.

Merci aussi à l'équipe de thésards du CEA Grenoble qui a su rendre si agréable et chaleureuse chacune de mes visites au CEA. Myriam, Julia et Sandrine, bonne chance pour la thèse et la suite. Merci à AirFrance et la SNCF qui ont été présents tout au long de cette thèse, m'aidant (parfois malgré eux) à relier Boston et Grenoble ou encore Marseille et Grenoble... mais aprés tout, tous les chemins ne mènent-ils pas à Grenoble ? Comment ne pas remercier ceux qui ont été là depuis le début ? Yoanna, Fab et Sandra, la bande des quatre terribles. Merci d'être

présents même quand on ne s'y attend pas. Fab et Sandra, merci de m'avoir ouvert votre porte chaque fois que j'avais besoin de renouveler mon visa... Paris sera toujours synonyme de délires sur les Champs Elysés (avec photos à l'appui). Merci à Yoanna qui au cours des années m'a tirée vers le haut toujours plus haut jusqu'à la thèse. Merci de m'avoir maintenue la tête hors de l'eau, merci pour les soirées, les journées, les nuits, de Grenoble à Boston, en passant par Paris. Bref, merci d'être ma poulette...

Merci aux membres de ma famille.
Ceux de toujours. Ma Granny, toi qui as toujours su croire en moi. Toi qui me regardes encore avec des larmes plein les yeux. Merci aussi à Grappy, qui m'a toujours encouragé à sa fa¸con: je sais que tu étais avec moi en ce lundi 4 décembre. Maman, merci de m'avoir soutenue et d'avoir été présente en dépit de la distance (merci de m'avoir "supportée" dans tous les sens du terme !!!!) ; d'avoir su garder le contact entre le vieux continent et celui outre atlantique; d'avoir parlé des heures au téléphone quand cela n'allait pas ; d'avoir été là en toutes circonstances, bref d'être ma maman. Merci à Cendrine qui m'a soutenue et encouragée, elle qui m'a dit de ne pas lâcher durant les derniers jours de rédaction ; merci pour les relectures, les répétitions... Merci d'être la meilleure frangine du monde ; c'est aussi un peu pour être (encore plus) comme toi que j'ai décidé de faire de la recherche. Merci à Andrei pour avoir partagé sa vision personnelle des Physiciens avec moi. Maxime et Ethan, c'est en vous voyant vous émerveiller de tout, que vous m'avez donné la force de me dépasser pendant la rédaction. Merci aussi à Bruno, Peggy, et Papa.
Et aux nouveaux. Michelle et Hérvé, qui ont été présents à tout moment ; merci, vous êtes géniaux, et pas d'inquiétude pour la prochaine thèse à venir... Merci à Gérard et Annick pour la délicieuse semaine "gastronomique" qui ont rendu les dernières semaines de rédaction de ce manuscrit beaucoup plus douces et plus agréables. Enfin merci à toi Francois, pour avoir supporté tous mes coups de tête, mes coups de speed, mes coups de gueule, mes coups de blues, d'être resté pendant les crises de fous rires mais aussi les crises de larmes ; merci pour ¸ca et tellement d'autres choses... Et merci à tous ceux que je n'ai pas cité ici, mais qui ont été là tout au long du parcours, ils se reconnaîtront.

A Grenoble, le 7 décembre 2006

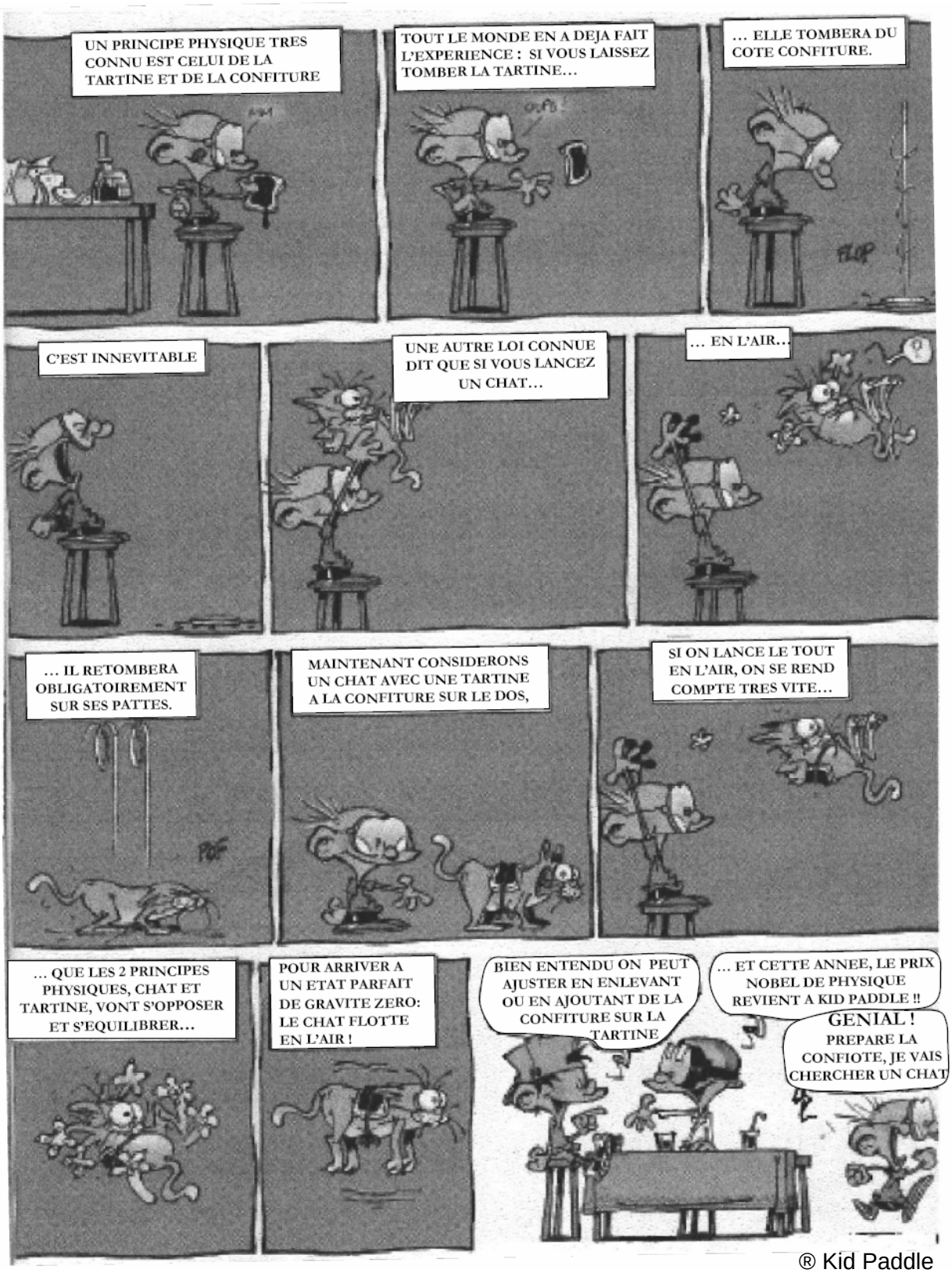
UN PRINCIPE PHYSIQUE TRES CONNU EST CELUI DE LA TARTINE ET DE LA CONFITURE
TOUT LE MONDE EN A DEJA FAIT L'EXPERIENCE : SI VOUS LAISSEZ TOMBER LA TARTINE…
… ELLE TOMBERA DU COTE CONFITURE.
FLOP
C'EST INNEVITABLE
UNE AUTRE LOI CONNUE DIT QUE SI VOUS LANCEZ UN CHAT…
… EN L'AIR…
… IL RETOMBERA OBLIGATOIREMENT SUR SES PATTES.
POF
MAINTENANT CONSIDERONS UN CHAT AVEC UNE TARTINE A LA CONFITURE SUR LE DOS,
SI ON LANCE LE TOUT EN L'AIR, ON SE REND COMPTE TRES VITE…
… QUE LES 2 PRINCIPES PHYSIQUES, CHAT ET TARTINE, VONT S'OPPOSER ET S'EQUILIBRER…
POUR ARRIVER A UN ETAT PARFAIT DE GRAVITE ZERO: LE CHAT FLOTTE EN L'AIR !
BIEN ENTENDU ON PEUT AJUSTER EN ENLEVANT OU EN AJOUTANT DE LA CONFITURE SUR LA TARTINE
… ET CETTE ANNEE, LE PRIX NOBEL DE PHYSIQUE REVIENT A KID PADDLE !!
GENIAL ! PREPARE LA CONFIOTE, JE VAIS CHERCHER UN CHAT

Contents

Chapter 1

Introduction

Les objets mous et déformables ont été étudiés intensivement durant ces 50 dernières années. L'industrie et la recherche médicale sont très intéressées par l'utilisation d'objets déformables (gouttes, vésicules, capsules, billes solides ou même cellules) sous champs externes, de type écoulement ou dégonflement osmotique, mais aussi par la compr éhension de la physique de ces phénomènes. Ces objets attirent l'attention des industries alimentaire, cosmétologique et pharmaceutique ainsi que de la recherche médicale.

Parmi d'autres applications possibles, les gouttes sont utilisées comme micro-réacteurs ou micro-réservoirs dans le cadre très à la mode des "laboratoires sur puce" ("lab on chip technology"). Les enveloppes lipidiques (liposomes et vésicules) sont utilisées pour l'encapsulation et comme objets modèles de cellules vivantes. Les globules rouge dont la déformabilité et la dynamique sont des paramètres clés dans leur mouvement au travers des réseaux complexes de la microcirculation est toujours sous étude intensive. Notamment leur comportement, tel que leur déformation, leur dynamique, ne sont pas totalement compris parce que les phénomènes physiques mise en jeu sont complexes. Par exemple l'écoulement éxerce un stress sur l'objet déformable et, en retour, celui-ci perturbe l'écoulement en adaptant sa forme aux contraintes externes. Pour expliquer la physique de tous les objets, nous avons choisi une interprétation commune qui est l'hydrodynamique à bas nombre de Reynolds.

Nous avons choisi détudier, au cours de ce travail de thèse, des objets appartenant à la classe des particules molles et déformables, organisées (ou structurées) et de taille micronique (de 1 à 100 microns de diamètre). Les propriétés physiques de ce type d'objets viennent de trois participations : une viscosité de membrane bidimensionnelle ou une modification de la tension de surface, une viscosité 3D et/ou une élasticité induite par le milieu interne et par l'interaction entre la membrane et le milieu interne. Bien évidement, c'est une combinaison subtile et complexe des trois contributions qui donne sa réponse mécanique à la particule. A l'échelle du micron, l'interface est très importante (ou dominante) et les phénomènes de surface (échanges, forces, rugosité...) ne peuvent être négligés.

Parmi les objets regroupés dans la classe précédente, nous nous sommes concentrés sur trois exemples : les gouttes, les vésicules et les globules rouges. Nous avons progressivement augmenté la complexité de nos objets, depuis une simple goutte à une vésicule pour finalement atteindre notre objectif : la compréhension de la dynamique des cellules sanguines dans la microcirculation. Ces particules déformables peuvent avoir des comportements similaires et spécifiques qui

sont la signature de leurs propriétés mécaniques particulières.

Gouttes et vésicules sont de très simples objets modèles de cellules vivantes. La tension de surface est le paramètre qui gouverne la minimisation de l'énergie de la goutte. La membrane lipidique d'une vésicule est caractérisée par la courbure (ou énergie de courbure). En ce qui concerne le globule rouge, l'élasticité de sa membrane est la clé de sa déformabilité. Sachant que les caractéristiques physiques sont différentes, pouvons-nous extraire la participation de chaque paramètre mécanique de la réponse des objets sous écoulement confiné ?

Nous avons choisi de nous intéresser à la réponse de nos systèmes sous écoulement confiné ou semi-confiné. De récentes avancées de la technologie microfluidique permettent de larges applications comme l'analyse environnementale (*in situ* analyse de contaminations environnementales), les applications biomédicales sont nombreuses (systèmes pour "drug delivery", diagnostiques, analyses...), les synthèses organiques à petite échelle ou les applications technologiques (imprimantes jet d'encre...). L'utilisation de systèmes microfluidiques présente de nombreux avantages, tel que la diminution du coût de production, la diminution du temps d'analyse, ou la réduction de la quantité de réactants consomm és. De plus, les canaux microfluidiques peuvent mimer la taille des capillaires et les conditions d'écoulement présentes in vivo dans la microcirculation. L'utilisation d'outils diagnostiques, de taille et de déformabilité similaires à celles trouvées en biologie, pourrait mener à une meilleure compréhension des comportements physiologiques et pathologiques.

Ce manuscrit est composé de six chapitres distincts. Le Chapitre 2 introduit sommairement la physique des trois systèmes étudiés. Dans le Chapitre 3, nous proposons une présentation détaillée mais non-exhaustive de l'état de l'art du comportement d'une grande variété d'objets sous deux types découlement. A travers de nombreux travaux théoriques et expérimentaux, nous avons voulu donner les résultats majeurs permettant une meilleure compréhension des chapitres suivants (5, 6 et 7). Nous nous sommes concentrés sur deux types d'écoulement: le cisaillement - sans conditions limites ou en présence d'une paroi - et l'écoulement de Poiseuille.

Dans le troisième Chapitre, nous exposons de manière brève les méthodes générales utilis ées au cours de nos expériences. Les techniques de microscopie et l'utilisation d'une caméra rapide sont expliquées dans une première partie ; dans une seconde partie c'est le dispositif expérimental associé avec la vue de côté et les différentes étapes de la fabrication des systèmes microfluidiques ; de même, sont décrits les écoulements oú le débit ou la pression sont imposés.

Dans le Chapitre 5 nous développons les résultats experimentaux que nous avons obtenus sur l'effet de la production de tensioactif in situ à l'interface, sur le comportement d'une goutte s'écoulant dans un canal. Il a été reconnu que les gouttes de petite taille peuvent être utilisées comme réacteurs chimique isolés , dont la composition et autre variables environnementales peuvent être précisemment controlées et mesurées. La technologie microfluidique permet l'étude de phénomènes rapides. C'est pourquoi, associer de l'utilisation de systèmes microfluidiques et de gouttes en tant que réacteurs chimiques est un moyen adéquat d'étude en vue d'expliquer le phénomène d'émulsification spontanée due à une réaction chimique. Dans ce chapitre nous présentons l'exemple d'une réaction chimique ayant lieu à l'interface d'une goutte s'écoulant dans un capillaire de même dimension. Nous détaillons les conséquences de la production de tensioactif à la surface d'une goutte sur le changement de forme de l'objet.

Le but du travail exposé dans le Chapitre 6, est d'abord la préparation de vésicules dont les propriétés visco- élastiques sont controlables, ce qui leur confère une grande résistance aux contraintes. De tels objets nous permettent de répondre à des questions physiques consernant le comportement de coques molles et déformables soumises à des contraintes externes (écoulement, pression...). Le second objectif est l'étude de systèmes (ici des vésicules DMPC) stimulables par un paramètre externe, dans notre cas la température ; nous avons notamment étudié l'effet de la modification de leur propriétés mécaniques sur leur comportement sous écoulement de cisaillement.

Une large partie de notre travail a été consacrée à l'étude de la dynamique de globules rouges sous écoulement ; elle est développée dans le Chapitre 7. Les résultats concernant les globules rouges sont divisés en trois parties : dans un premier temps nous présentons les protocoles de préparation des différentes solutions utilisées au cours de nos expériences afin de modifier les propriétés mécaniques des cellules sanguines (leur volume, leur déformabilité, la viscosité de la solution tampon...) ; puis dans une seconde partie nous avons étudié le comportement de globules rouges individuels soumis à un écoulement de cisaillement près d'une paroi ; finalement, dans la dernière sous-partie, nous nous sommes intéressés à l'étude de cas de nature plus physiologique et pathologique en géométrie fortement confinée.

Bien que les deux mouvements reconnus du globule rouge sous écoulement soient le mouvement de rotation solide (ou culbute "tumbling" en anglais) et, à plus fort taux de cisaillement, le mouvement de type goutte dit de chenille de char ("tanktreading" en anglais) durant lequel la cellule maintient une orientation stable pendant que la membrane tourne autour du fluide interne, nous avons aussi exploré le mouvement de globules rouges à faible taux de cisaillement proche de la transition culbute/chenille de char.

L'adaptation au stress externe de la forme de globules rouges, s'écoulant dans un capillaire de taille similaire, est étudiée en faisant varier de nombreux paramètres physiques (vitesse des cellules, viscosité externe, taille du capillaire). Nous nous intéressons aux paramètres responsables de la transition d'une forme à une autre.

Dans le cas du fort confinement offert par les canaux microfluidiques, nous rapportons la mesure de la variation de la chute de pression dynamique le long d'un canal de taille micronique, et le potentiel de cette technique est illustré par la présentation de mesures de la chute de pression produite à l'echelle d'une cellule individuelle.

Finalement nous avons étudié la séparation du plasma des cellules sanguines par l'utilisation de la tendance naturelle des particules déformables sous cisaillement à décoller loin des parois sous l'effet de la force de portance.

Soft and deformable objects have been intensively studied for the past 50 years. Industrial and medical research are very interested in the use of soft objects (drops, vesicles, capsules, solid beads or even cells) under external stresses, such as flow or osmotic deflation and in the understanding of the physics of the phenomenon. Those objects captured the attention of the food, pharmaceutical and cosmetic industries as well as the medical research. Among other

applications, drops are used as micro-reactors or micro-reservoirs for the trendy "lab-on-chip" technology. Lipid bags (liposomes and vesicles) are used in the encapsulation and are mimetic particles for living cells. The red blood cell which deformability and dynamics are key in their motion through the complex network of the micro-circulation is still under intensive study. Although, their behavior such as deformation or dynamics is not totally understood because, the physics brought into play is complex. For example, the flow exerts a stress on the deformable particle, the object adapts its shape to the external constrains and in return the new shape impacts and perturbs the flow. The approach of interpretation chosen to explain the physics is the same for all the objects: the hydrodynamics at low Reynolds number.

Soft and deformable, structured (or organized), micron-size particles (from 1 to 100 microns in diameter) are the objects of the class, we chose to study. The physical properties of such objects come from three participations: a 2D viscosity in the membrane or a modification of the surface tension, a 3D viscosity and/or elasticity induced by the internal media and the interaction between the membrane and the internal media. Of course, it is a genius and tricky combination of the 3 contributions that gives to the particle, its mechanical response. At the micron scale, the interface is very important (or dominant) and the surface phenomena (exchanges, forces, roughness,...) cannot be neglected.

Among all the objects regrouped in the previous class, we focused on three examples: drops, vesicles and red blood cells. We progressively increase the complexity of our objects, from a simple drop to vesicles to finally reach our objective: the understanding of the dynamics of blood cells in the microcirculation. Those soft particles can have generic as well as specific behavior which are a signature of their particular mechanical properties. Droplets and vesicles are very simple common mimetic objects of living cells. The parameter governing the minimization of the energy of a drop is the surface tension. The vesicle's lipid membrane is characterized by the curvature (or bending energy). For the red blood cell, the elasticity of the membrane is the key of its deformability. Knowing that their physical characteristics are different, can we extract the participation of each mechanical parameter from the response of the object under confined flow ?

We chose to look at the response of our system when flowing in confined or semi-confined environment. Recent advances in the microfluidic technology, allow wide applications like environmental testing (in situ analysis of environmental contamination), biomedical applications (device for drug delivery, diagnostic, analysis...), small scale organic synthesis or technological application (print-jet...). The use of microfluidic systems leads to many benefits among which decreasing coast in manufacture, decreasing analysis time, or reducing the consumption of reagents. In addition, microfluidic channels can mimic the size of capillaries and flow conditions found *in vivo* in the microcirculation. The use of diagnostic devices of the same size and with similar deformability as found in biology could lead to greater understanding of physiologic and pathologic behaviors.

This manuscript is composed of six distinct chapters. The Chapter 2 introduces the physics of the systems under study. In the Chapter 3, we propose a detailed but non-exhaustive presentation of the state of the art of the behavior of a large variety of objects under two types of flow. Through various theoretical and experimental work, we want to give the important results allowing a better understanding of the three following chapters (5, 6 and 7). We focus on two types of flow: the shear flow, without boundaries or with the presence of a wall and the Poiseuille

flow.

In the third chapter, we reveal briefly the general material and methods used during our experiments. The technics of microscopy, the use of high speed cameras are explained in a first part; in a second one, the experimental set-up associated with the side view and the different fabrication steps of the microfluidic systems, as well as the flow rate and pressure-driven flows are described.

In the Chapter 5 we develop the experimental results we got on the effect of the interfacial production of surfactant on the behavior of a drop flowing in a channel. It has been recognized that small droplets can act as isolated chemical containers, whose composition and other environmental variables can be carefully controlled and monitored. The microfluidic technology allows the study of fast phenomena. Therefore, the association of the use of microfluidic systems and droplets as chemical reactors is suitable to study and find an explanation of the spontaneous emulsification phenomena due to chemical reactions. In this chapter we present the example of an interfacial chemical reaction taking place on a droplet flowing in a close fitting channel. We will detailed the consequences of surfactant production at the surface of the drop on the change in the shape of the object.

The goal of the study exposed in the chapter 6, is to prepare viscoelastic vesicles with controlled mechanical properties, which confer to them an enhanced resistance to external stresses, thus allowing to address open physical questions relative to the behavior of deformable soft shells submitted to external stresses (flow, pressure...). A second objective is to study responsive systems - here DMPC vesicles - triggered by an external parameter, in our case the temperature. We study the effect of the modification of their mechanical properties with temperature, on their behavior under flow.

A large part of our work was dedicated to the study of the dynamics of red blood cells under flow are developed in the Chapter 7. The results on the red blood cells (RBCs) are divided into three major parts: in a first part, we present the different preparations used during our experiments in order to modify the RBCs properties (volume, deformability, external viscosity...), in a second part, individual red blood cells are submitted to shear flow near a plane; finally, we focus on more physiologic and pathologic flows in high confinement.

Although the two admitted RBC movements are the unsteady tumbling solid-like motion, and the drop-like "tanktreading" motion for higher shear stresses (where the cell maintains a steady orientation while the membrane rotates about the internal fluid), we explore the RBC motion at smaller shear rate and close to the tumbling-tanktreading transition.

The adaptation of the shape of RBCs flowing in close-fitting capillaries to the external stresses is investigate varying several physical parameters (speed of the cells, external viscosity, capillary size). We look at the parameters responsible of the transition from one shape to another.

For the case of strong confinement offered by microchannels, measurements of dynamical pressure-drop variations along a micrometer-sized channel and illustrate the potential of the technique by presenting measurements of the additional pressure drop produced at the scale of individual flowing cells are reported.

Finally we investigate the separation of plasma and blood cells and use the natural tendency of sheared deformable cells to move away from boundaries, i.e. drift via hydrodynamic lift.

Chapter 2

Physics of the systems

Dans ce chapitre nous proposons une présentation sommaire des trois objets que nous avons étudié durant ce travail de thèse. Dans un premier temps nous exposons les paramètres déterminant la physique d'une goutte. Puis nous détaillons les différentes quantités physiques responsables de la forme et de la dynamique d'une vésicule lipidique géante. Enfin nous établissons l'importance de l'élasticité du globule rouge dans sa déformabilité.

We propose in this chapter, a brief presentation of the three objects studied during this PhD work. In a first time, we will present the parameters determinant of the physics of a drop. Then we will detail the physical quantities responsible for the dynamics of a giant lipid vesicle. Finally, we will establish the importance of the elasticity of the red blood cell in its deformability.

2.1 Drops

Drops are small amount of liquid immersed in another immiscible fluid (could be gas or liquid). They have a compressible interface (non-fixed surface area), and the equilibrium shapes are set by surface tension rules (see Fig. 2.1).

Figure 2.1: *A drop of water on a super-hydrophobic (which doesn't like water) substrate adopts a spherical shape [1].*

2.1.1 Surface tension

The interfacial tension or surface tension is a material property of a fluid-fluid interface whose origins lie in the different attractive intermolecular forces that act in the two fluid phases. Its action is confined to the free surface. The result is an interfacial energy per area that acts to resist the creation of new interface and consequently favoring the sphere (smaller surface area for a given volume) as an equilibrium shape. Surface tension γ has the units of force/length or equivalently energy/area, and is defined by:

$$\gamma = \partial F / \partial A, \tag{2.1}$$

F being the free energy of the drop and A its surface area. Several methods are used to characterize the interfacial tension. Among them, the pendant drop method [55] consists in the adjustment of the shape of a pendant drop to an equilibrium shape and to extract γ from the shape equation.

2.1.2 Surfactant

Surfactants are usually organic compounds that are amphiphilic, meaning they contain both hydrophobic groups (their "tails" which are preferentially attracted by non polar solvent) and hydrophilic groups (their "heads" which are attracted by water). Therefore, they are typically sparingly soluble in both organic solvents and water. The addition of surfactant in the drop results in the decrease of the surface tension of the droplet.

2.1.3 Viscosity

The viscosity is a measurement of the resistance to the deformation. It is the coefficient that link linearly the shear stress to the strain rate. The viscosity of the drop can be modified by adding some polymer to the dispersed phase if aqueous or, if not, by the appropriate choice of organic solvent or by the addition of organo-soluble polymer. Surfactants can also, if covering abundantly a surface, induce a surface viscosity to the drop.

2.2 Vesicles

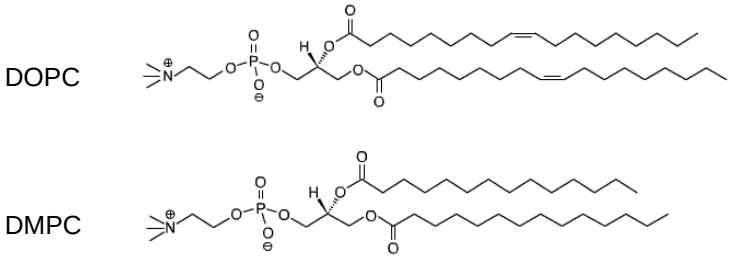

Figure 2.2: *Chemical formulas of two commonly used lipids: DOPC and DMPC [2].*

Giant unilamellar vesicles (GUV) are an approximate, accessible and reproducible imitation of certain aspects of biomembranes, (such as the typical size, the structure, possibility of insertion of proteins in the membrane, lipid composition of the membrane...). Therefore, they became an important tool in the understanding of some phenomena applied to membranes of biological objects, such as exchange with the external medium and deformation.

2.2.1 Structure of a vesicle

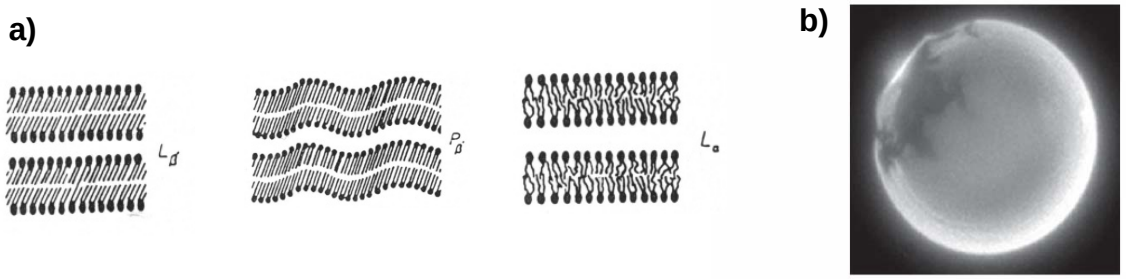

Figure 2.3: *a) Three different phase transitions experienced by the lipid bilayer[135]. b) Image of a vesicle composed of two phases: a gel phase (dark phase) and a fluid phase (fluorescent one). We can note that the composition of the vesicle is 50% w/w of Sphingomyeline and 50% w/w of DOPC. [119]*

The phospholipids are amphiphilic molecules composed of a polar head group, which is hydrophilic (it likes water), and one or several long carbon chains, which are hydrophobic (it prefers non polar solvent). We present in Figure 2.2a), the chemical formulas of two lipids commonly used to produce vesicles: the 1,2dioleolyl-sn-glycero-3-phosphocholine or DOPC and the 1,2-dimyristoyl-sn-glycero-3-phosphocholine or DMPC. Those lipids are commonly found in the composition of cells membrane. When hydrated, the lipids spontaneously assemble into two leafs associated face to face and form a membrane roughly 6 nm thick.

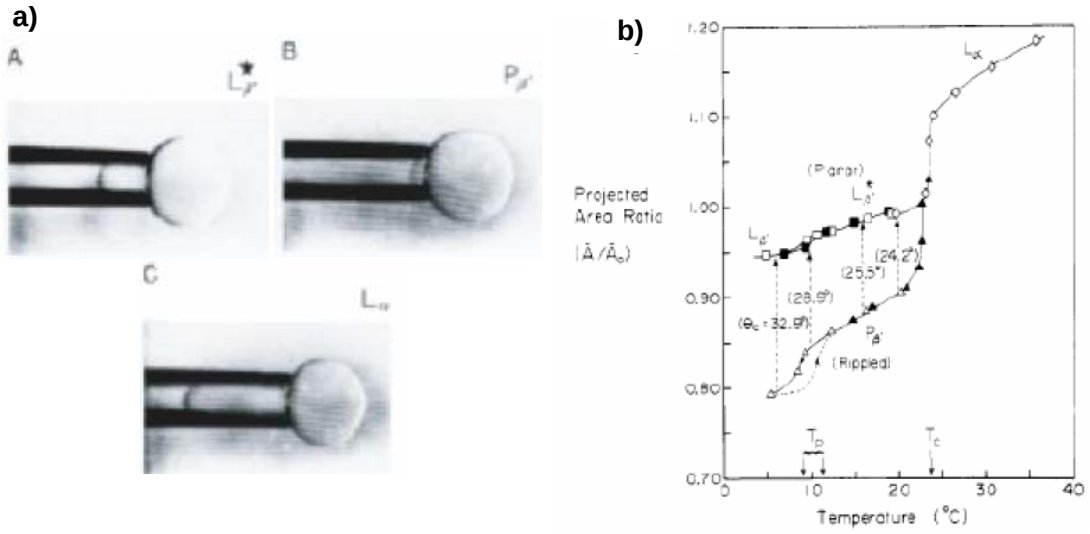

Figure 2.4: *a) Pictures of a DMPC bilayer vesicle in three structural phases. The membrane is placed under tension and as the temperature is increased, the vesicle experiences phase transitions leading to a change of the length inside the pipette. Note: length in pipet represents projected area of bilayer structure [50]. b) The change in surface area ΔA normalized by the initial surface area A_0 of the vesicle, due to a modification in lipid arrangement associated with a temperature change is represented for the three different phases [50].*

However the organization of the lipid bilayer can evolve with temperature. The lipids, which are highly packed in the layers, tend to assemble in a liquid crystal type of conformation. They have an orientational order fixed by the temperature. By increasing the temperature, we can evolve from a phase $L_{\beta'}$ where the lipids are inclined compared to the bilayer plane to a rippled

phase $P_{\beta'}$ (Fig. 2.3a)). If one increases further the temperature above the critical temperature T_c, we can even go from the so-called "gel state" of the membrane to a phase L_α where the lipids are in a fluid state. Such a transition is reported in Figure 2.3b).

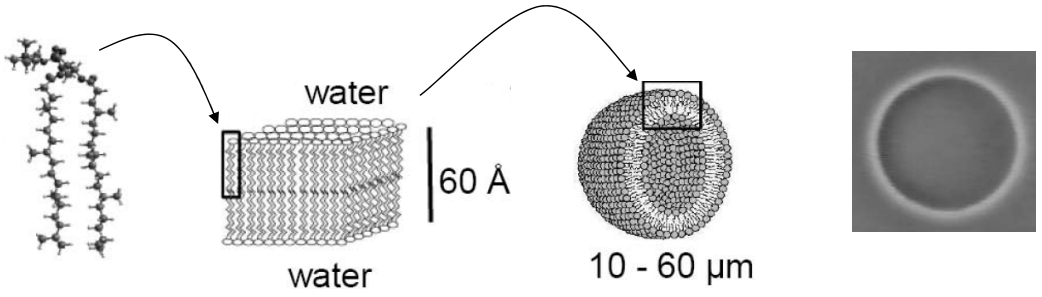

Figure 2.5: *Structure of a giant lipid vesicle. On the right, we can see a phase contrast observation of a vesicle.*

The transition from one phase to another has been studied by Evans and Needham [50] with micropipette aspiration experiments as shown in Figure 2.4a) and b). The study reveals a decrease in surface area of the objects when going from the L_α phase to the $L_{\beta'}$ gel state. If the system is under stress when going through the transition, the surface area tends to decrease even more dramatically while the lipids end-up in the $P_{\beta'}$ phase. The appropriate choice of lipid or mixture of lipids allows the subtle control of the membrane properties, such as thermal stability, rigidity, electrical charge, permeability.

These membranes tend to close to form vesicles where the internal media is isolated from an identical or different external fluid. Such assembly is presented in Figure 2.5. Although different methods to obtain vesicles exist, we will only cite here the well known electroformation method [16].

A word about the gel phase of the membrane

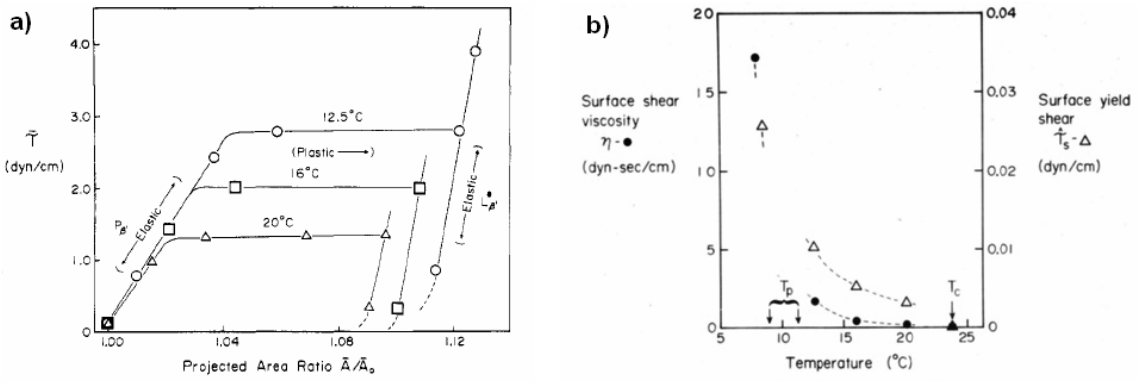

Figure 2.6: *a) Ripple phase elasticity, yield, and plastic deformation followed by planar phase elasticity for a single vesicle at three different temperatures [112]. b) Measurements of • surface shear viscosity and △ surface shear rigidity versus the temperature, realized on "frozen" DMPC vesicles under the phase transition temperature T_c [50]. Note: for an equivalence between the different units, report to the table in Annexe D.*

Membranes in the gel phase ($L_{\beta'}$ or $P_{\beta'}$ phases) have a plastic behavior, which means that the deformation persists after the annihilation of the stress. They are characterized by two main features:

1. A critical tension to overcome in order to plastically deform (See Figure 2.6a). Indeed, if a tension is applied, an elastic behavior, essentially reversible, is observed but above a threshold level of 2.8x10^{-3} N.m^{-1} at 12^{o}C, the vesicle behaves purely viscously.

2. A high viscosity of the membrane (see Fig. 2.6b)). At 8^{o}C, from the Fig. 2.6b) and an estimated thickness of the membrane of 4.45 nm [94], we can estimate a 3D membrane viscosity to be around 40x10^{-3} Pa.s.

2.2.2 Physical properties of vesicles

A lipid bilayer is characterized by a series of physical parameters: bending modulus, extension modulus, viscosity, tension, and permeability. Although the values of these quantities may vary from one lipid to another, these parameters are a signature of the structure of the vesicle.

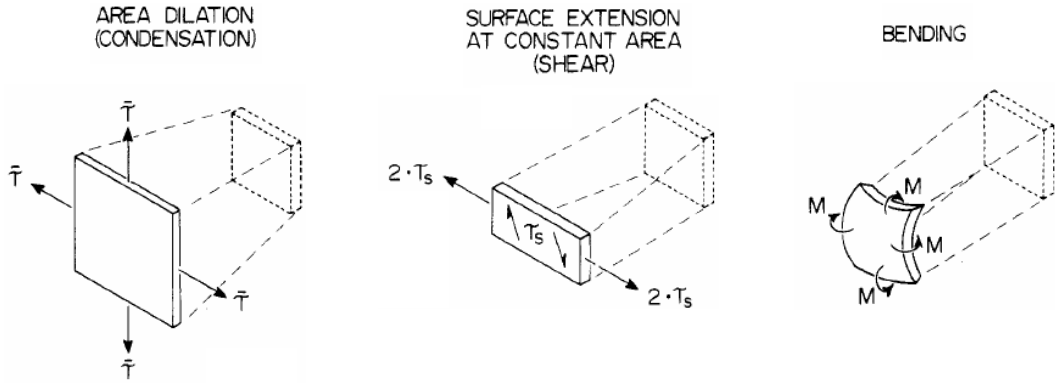

Figure 2.7: *Independent modes of deformation and force momentum resultants for an element of a thin-surface material [50].*

The bilayer can be deformed in three different ways presented Figure 2.7: it can be stretched or compressed (by changing its thickness), it can be sheared and it can be bent (by compressing the "inner" leaflet and by extending the "outer" leaflet). In fact, any constraint applied to the membrane can be decomposed as a combination of these three elementary deformation modes. For a fluid membrane, the shear energy of the system can be neglected as the molecules can move freely and relax any stress due to pure shear. In the case of DMPC vesicles in the gel phase, the shear contribution to the energy can not be neglected anymore. Typical values for the bending, extension and shear moduli are presented in Table 2.2.2.

Bending modulus

For a fluid membrane, the Hamiltonian H is essentially given by the integral - over the whole surface - of the local energy of curvature $E_{bending}$ given by unit of surface:

$$E_{bending} = \frac{1}{2}k_c(C_1 + C_2 - C_0)^2 + \frac{1}{2}k_{c'}(C_1C_2) \tag{2.2}$$

where C_0 is the spontaneous curvature of the membrane, C_1 and C_2 are the principal curvatures defined by $C_1 = 1/R_1$ and $C_2 = 1/R_2$ where R_1 and R_2 are two local radii of curvature, k_c its

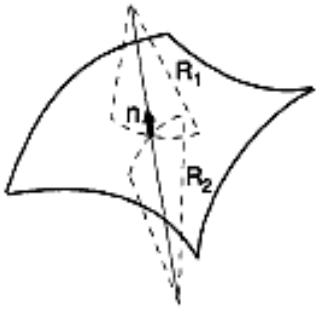

Figure 2.8: *Curvature on a 2D surface. The length scales R_1 and R_2 denote the radii of curvature. The vector n denotes the normal [135].*

bending modulus and $k_{c'}$ its gaussian bending modulus. The totale energy of the membrane is the integral of $E_{bending}$ over the whole surface area of the object. The theorem of Gauss-Bonnet shows that the gaussian curvature (C_1C_2) integrated over the total surface of the vesicle is a topological invariant, so then when the vesicle keeps the same topology (no formation of "handle"), which is our case, the gaussian component of the energy can be neglected. In the fluid phase, it is the energy of curvature that governs the equilibrium shapes of the vesicles. The typical values for the bending modulus k_c are reported in the Table 2.2.2 for the different cases encountered later in this manuscript.

Lipid	DOPC	DMPC	DMPC
Phase	L_α	L_α	$L_{\beta'}$
Bending modulus k_c	10 $k_BT \approx$ 4x10^{-20} J [43, 95]	10^{-20} J	10^{-19} J
Extension modulus χ	10^{-1} J [51, 116, 129]	0.145 J [50]	0.855 J [50]
Shear modulus $\mu_m(2D)$	/	/ [50]	10^{-3} N.m^{-1} [40]
Lysis tension σ	3 mN.m^{-1} [116]	2-3 mN.m^{-1} [50]	15 mN.m^{-1} [50]
Permeability	$\sim$ 3x10^{-3} cm.s^{-1} [116]	$\sim$ 7x10^{-3} cm.s^{-1} [158]	$\sim$ 27x10^{-3} cm.s^{-1} [158]

Table 2.1: *Values of the bending modulus, the extension modulus, the shear modulus, the lysis tension and the permeability for two different lipids and different phases.*

Extension modulus

The extension modulus is a measure of the energy necessary to change a unit area of the membrane and characterizes the cohesion between the lipids of the membrane. The extension modulus is given by the expression of the extension/compression energy $E_{extension}$:

$$E_{extension} = \frac{1}{2}\chi(\frac{\Delta A}{A_0}) \tag{2.3}$$

where χ is the extension modulus, $\Delta A/A_0$ is the surface area variation of the membrane relative to its initial value A_0 during the deformation. The typical values of χ are reported in the Table **??**. It costs a lot of energy ($10^{20} k_b T$) to move the lipids away from each other.

Viscosity

A vesicle can have two viscous components: a 3D viscosity coming from the fluid encapsulated in the vesicle and a membrane viscosity. The viscosity of the membrane in the fluid phase is found in the literature [152, 40, 39] to be of the order of 10^{-3} - 10^{-2} Pa.s.

Tension

The tension is define by the Laplace law:

$$\Delta P = \sigma(\frac{1}{R_1} + \frac{1}{R_2}) \tag{2.4}$$

where ΔP is the pressure difference between the inside and the outside of the vesicle, σ is the tension applied to the membrane and R_1 and R_2, the two local radii of curvature. Although the tension of the membrane of a giant vesicle at rest is a delicate parameter to evaluate theoretically and to measure experimentally, the lysis tension, i.e. the critical tension at which the membrane ruptures, is easier to estimate. Micropipette aspiration experiments [51], allow an evaluation of the lysis tension $\sigma_{rupture} \approx 3$ mN.m^{-1}, which corresponds to a maximum extension of the surface area between 3 and 5% (equivalent to the unfolding of the thermal fluctuations) before the rupture of the envelop.

We can note that the tension of a vesicle is coming from its free energy F which is changing with the augmentation of projected surface area ΔA of the object. We therefore retrieve the classical definition of the surface tension 2.1 seen earlier.

Thermal fluctuations

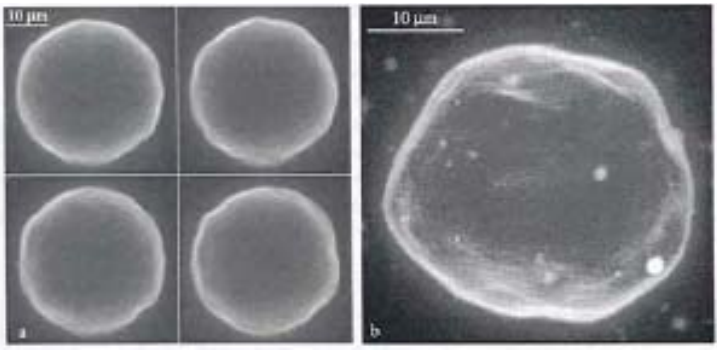

Figure 2.9: *Thermal undulations of a giant vesicle, observed in fluorescence microscopy: a) at various instants in the same focal plan, and b) by projection of several focal plans [131].*

In the fluid phase, the bending modulus k_c is very small (of the order of a couple of $k_b T$), therefore the curvature of the membrane of a vesicle can be changed easily, leading to the apparition of thermal fluctuations. We can see in Figure 2.9, we can see the thermal fluctuations of a giant

lipid vesicle, observed in fluorescence microscopy. The fluctuations act like a hidden reservoir of surface area for the lipid membrane. As a part of the thermal fluctuations constituent ΔA is too small in amplitude to be observed, the experiments always measure an augmentation of projected surface area A_p, relative to the value under zero tension A_p^0. It is equal to the absolute value of the unwrapped surface area, if we consider the total surface of lipid A constant during the whole experiment:

$$A_p + \Delta A = A_p^0 + \Delta A^0 = A$$

The estimation of the diminution of the excess of surface area, compare to the state with zero tension is:

$$\frac{\Delta A - \Delta A^0}{A_p^0} = -\frac{k_b T}{8\pi k_c} ln(1 + \frac{A_p^0}{\pi^2 k_c}\gamma) \tag{2.5}$$

Permeability

Vesicles are also characterized by their permeability. Indeed, lipid membranes allow hydrophobic molecules (O_2, CO_2, N_2, benzene...) and very small, polar, uncharged molecules (H_2O, urea, glycerol among others) to travel from the inside to the outside of the vesicle. On the contrary, it is impermeable to larger polar, uncharged molecules (such as glucose and saccharose) and to ions (H^+, Cl^-, Ca^{2+}, Mg^{2+}...).

Osmotic pressure

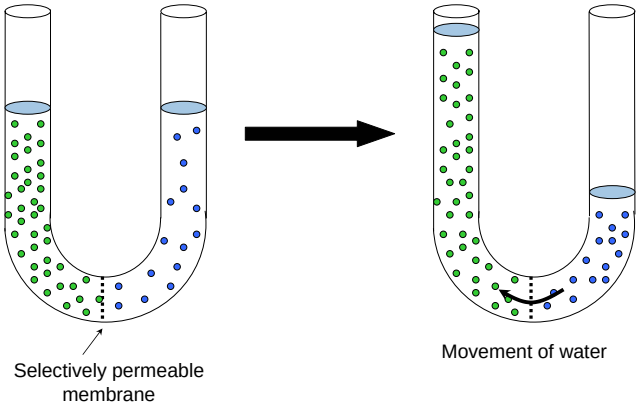

Figure 2.10: *Notion of osmotic pressure: water tends to diffuse across the membrane in order to equilibrate the two concentrations.*

The selective permeability of lipid membranes leads to the concept of osmotic pressure for vesicles. The concentration difference between the interior and the exterior of a vesicle creates an osmotic pressure π on the membrane:

$$\pi = \mathsf{R}Tln(\frac{N_{in}}{N_{out}})$$

where N_{in} and N_{out} are the number of solute molecules - $\frac{N_{in}}{N_{out}}$ is equivalent to $\frac{C_{in}}{C_{out}}$, where C_{in} and C_{out} are the inner and outer solute concentrations, respectively - in the internal and external media respectively, R is the universal gas constant and T is the absolute temperature. Water tends to diffuse across the membrane in order to assure the equilibrium of the chemical potentials

in both internal and external media. Thus, the permeability allows the tunability of the vesicle's volume at a constant total surface area, allowing us to deflate it and to obtain various shapes and more deformable objects.

2.2.3 Deflated shapes

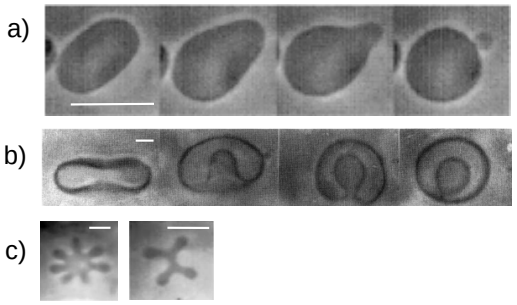

Figure 2.11: *Several deflated shapes: a) Budding process on a initially prolate vesicle [42]. b) Transition from a oblate shape to a stomatocyte triggered by an increase of the temperature [135] and c) Starfish-like shape vesicles [159]. The white bars represents 5 μm.*

Experiments have shown that these vesicles display a rich variety of shapes (see Figure 2.11) as osmotic pressure is changed. Numerous study have been dedicated to the inventory of vesicles equilibrium shapes and to their mechanical properties [101]. The study of equilibrium shapes of vesicles under external stresses use interconnection of theoretical, numerical and experimental efforts [135]. Experimental work validate the theory and in return the models developed are used to interpret the experiments on vesicles in order to measure physical parameters of the membrane (energy of curvature, tension, coupling with a gel, adsorption of proteins, etc).

Area Difference Elasticity (ADE) model

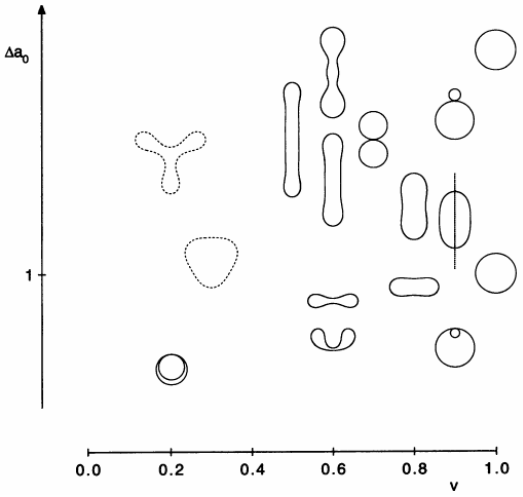

Figure 2.12: *Phase diagram of vesicle with the ADE model [110]. The difference of surface area ΔA_0 between the two leaflets of the bilayer is represented versus the reduced volume ν.*

The present understanding of the diversity of vesicle shapes and of the transformations occurring between distinct shapes has largely been based on a simple model. The model takes into account that the areas of the individual monolayers are not fixed but can independently expand elastically under stress. Each monolayer has a preferred or relaxed area (A_0^{in} or A_0^{out}), based on the number of lipid molecules it contains, but can have an actual area (A^{in} or A^{out}) which may be larger or smaller, provided that an appropriate cost in elastic energy is paid. The energy of the vesicle is a sum of the bending energy and the energy rising from the global curvature due to the difference in the number of lipids between the two leaflets [107].

$$H \equiv \frac{1}{2}k_c \oint dA[C_1 + C_2 - C_0]^2 + \frac{1}{2}\overline{k_c}\frac{\pi}{Ae^2}(\Delta A - \Delta A_0)^2 \tag{2.6}$$

where e is the bilayer thickness, $\Delta A_0 \equiv A_0^{out} - A_0^{in}$ is the difference of the unstressed monolayer areas, and k_c and $\overline{k_c}$ are the local and the non-local bending moduli of the membrane, respectively. To predict the deflated shapes, the energy discribed by the equation 2.6 is minimized. The important parameter is the volume to area ratio, also called the reduced volume, and defined as:

$$\nu = \frac{V}{(4\pi/3)R_A^3} \tag{2.7}$$

where $R_A = (A/4\pi)^{1/2}$ is the radius of the sphere with the same surface area as the vesicle of volume V.

2.3 Red blood cell

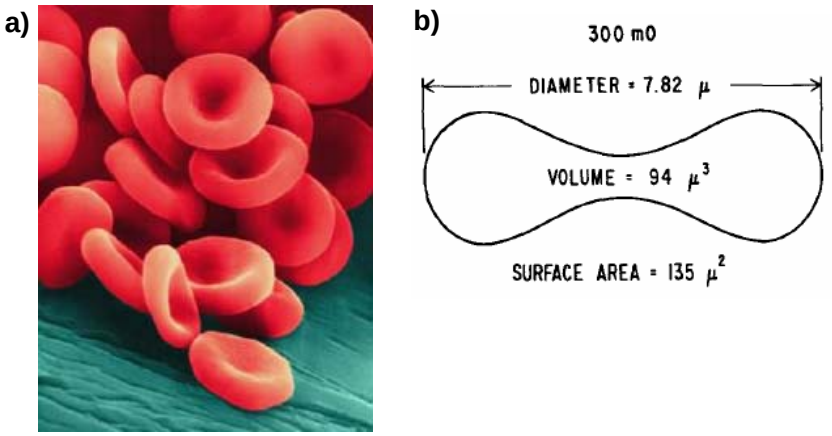

Figure 2.13: *a) Healthy RBCs with its usual discocyte shape [3]. b) Typical dimensions of a healthy RBC [47].*

2.3.1 Structure and composition of a RBC

The human RBC is the most numerous cell in blood (4 to 5 million cells per μL) and performs the most important blood duty: delivering oxygen. Its life span is approximately 120 days during which it recirculates around 170,000 times. Under physiological conditions, RBCs have the shape of biconcave disks of 8 μm in diameter, 2 μm in thickness at the periphery and 1 μm at

the center as shown in Figure 2.13. Their volume and surface area are roughly 94 μm^3 and 135 μm^2 respectively [47]. This correspond to a reduced volume of 0.7 (from equation 2.7).

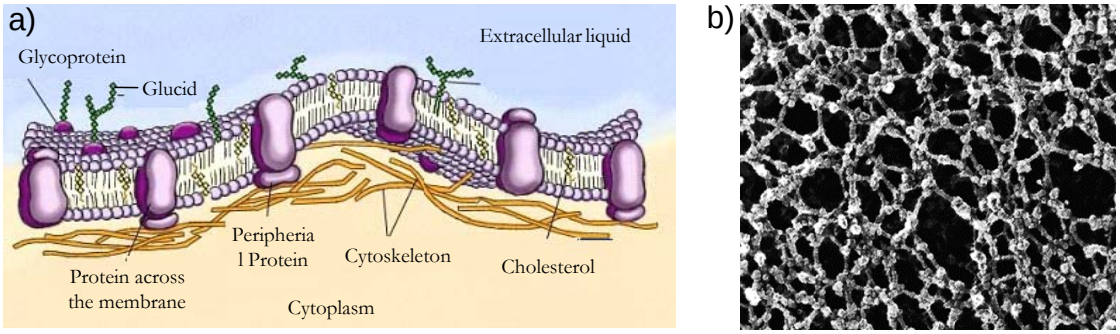

Figure 2.14: *a) Composition of the membrane of a RBC [15]. b) Image of the spectrin cytoskeleton [76].*

It is the simplest cell since it has no nucleus and can be crudely seen as a bag used for the transport of hemoglobin. As shown in Figure 2.14a), the red cell is composed of a lipid membrane with an underlying two-dimensional (10 nm in thickness) elastic network of spectrin [108]. The cytoskeleton is anchored to the lipid bilayer through proteins crossing the membrane. The triangular structure of the spectrin network is presented in the Figure 2.14b). This particular geometry, as well as the intrinsic elastic properties of the spectrin, give remarkable deformability to the RBC. The red cell membrane encloses a solution of a Newtonian fluid: the hemoglobin. The viscosity of the cytoplasm is 10 mPa.s^{-1} at 25^{o}C. With aging the RBC expels water, thus its internal viscosity increases. In a single drop of blood, all the cells are at different aging states, therefore they might have different internal viscosities.

2.3.2 Mechanical properties of the RBC

The membrane of the RBC is recognized to possess remarkable mechanical properties (deformability, elasticity, shear resistance, etc). Together with the cytoplasmic fluid, the membrane controls the overall deformability of the cell and, thus, its ability to go through the small capillaries of the microcirculation. Under normal conditions, the membrane deforms at constant area and exhibits both elastic and viscous behaviors. The extension of the membrane is governed by the lipid bilayer which tends to resist an area expansion. Evans et al. [48] suspected that the shear resistance of the membrane was mainly due to the cytoskeleton, an hypothesis backed up by Waught et al. [157] who showed that the shear resistance is directly linked to the density of spectrin and, thus, to the cytoskeleton. The RBC's membrane is usually characterized by two material properties: the elastic modulus μ_m and the extension modulus K of the membrane.

The elasticity of the membrane has been frequently investigated by the mean of several techniques, such as: deformation by a flow [83], aspiration by a micropipette [48, 84] and optical tweezers [80, 99]. The typical value for μ_m depends on the deformation regime. Therefore in the micropipette aspiration experiments, the RBC undergoes large deformations leading to a measurement of μ_m between 4 and 10 μN.m^{-1}. On the contrary, for the optical tweezers, measurements are realized in a region where deformation is small and yield a value $\mu_m \approx 2.5$ μN.m^{-1} [98]. The micropipette techniques allow also the measurement of the extension modulus K be-

tween 300 and 500 mN.m^{-1} and gives an estimate of the bending modulus B ($B \sim$ several k_BT). The optical tweezer experiments give an estimate of the extension modulus of 5 μN.m^{-1} for the cytoskeleton alone, i.e. after dissolution of the lipid bilayer; so it seems like the lipid membrane itself is basically responsible for the resistance to extension.

Question of the "shape memory"

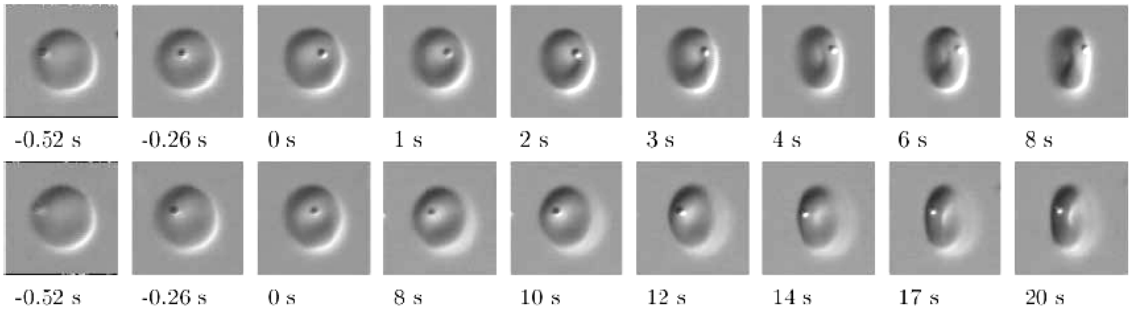

Figure 2.15: *Two go-and-stop experiments performed on the same red cell. The numbers indicate relative times. In the first two columns, the red cell is shown tank treading in shear flow (flow direction horizontal, shear rate $\approx 10s^{-1}$). Shearing was done by motor drive of the cone-plate chamber. The third column shows the red cell after stopping the flow. In the following columns, the subsequent transient is shown. The difference between the two experiments, (two different rows) is the direction of motion of the latex sphere during the transient [57].*

The actual state of deformation of the elastic skeleton (whether or not there is some elastic energy stored in the membrane) either in the flowing or in the resting RBC is still a subject of conjecture. The human red cell can be deformed by external forces but returns to the biconcave resting shape after removal of the forces. If after such shape excursions the rim is always formed by the same part of the membrane, the cell is said to have a memory of its biconcave shape. If the rim can form anywhere on the membrane, the cell would have no shape memory. The shape memory was probed by Fischer [57] with an experiment called go-and-stop. Locations on the membrane were marked by spontaneously adhering latex spheres. Shape excursions, during tank-treading mode, were induced by shear flow (go) applied using a rheoscope (two first columns in Fig. 2.15). The rotation was stopped (third columns noted t=0)(stop) when the position of the latex bead indicated that the membrane parts forming the dimples at rest were at the rim of the tank-treading cell as shown in Figure 2.15; the transient leading to the rest state occurred either by a tank-tread motion of the membrane (following columns). After the flow was stopped and during the return of the latex sphere to its original location, the red cell shape was biconcave.

Chapter 3

Dynamics of objects under flow

Dans ce chapitre, nous faisons une revue non-exhaustive de l'état de l'art des différents comportements de toute une série d'objets : une sphère rigide, un ellipsoïde rigide, une goutte, un globule rouge, un ellipsoïde fluid ou encore une capsule, sous champs externes. A travers des travaux variés aussi bien théoriques qu'expérimentaux, nous avons voulu mettre en lumière les résultats importants pour une meilleure compréhension des résultats dévelloppés dans les chapitres suivants (5, 6 and 7). Entre autre, nous abordons les ecoulements de cisaillement en présence ou non d'une paroi, ainsi que l'écoulement de Poiseuille. Nous soulignons aussi le mouvement solide de rotation d'un ellipsoïde rigide sous cisaillement, le mouvement de chenille de char d'un ellipsoïde fluide ou d'une vésicule (mouvements que l'on retrouve également pour un globule rouge sous écoulement de cisaillement), la force de portance exercée sur une vésicule sous cisaillement près d'une paroi, ainsi que la forme spécifique dite de parachute, du globule rouge s'écoulant dans un capillaire.

This chapter is a non-exhaustive review of the state of the art of the behavior of different types of objects (solid sphere and ellipsoid, vesicle, capsule, droplet and red blood cell) under flow. Through various theoretical and experimental work, we want to highlight the important results allowing a better understanding of the chapters dealing with the results (5, 6 and 7). We focus on two types of flow : the shear flow, without boundaries or with the presence of a wall and the Poiseuille flow.

3.1 Shear flow

3.1.1 Without boundaries

The frame of interpretation of the behavior of colloidal objects such as solid beads, drops, capsules, vesicles and cells is the hydrodynamics at low Reynolds number $\Re_e$ (10^{-5} - 10^{-2}) defined as $\Re_e = \frac{\rho L v}{\eta}$, where ρ and η are the density and the viscosity of the fluid in motion, respectively; L is the characteristic length of the system and v the speed of the object. The two main types of motion have been reported for objects submitted to low Reynolds number shear flow : the solid-like tumbling motion, and the tank-treading movement. Here, we provide, a short review of the different motions of different type of particles in shear flow.

Rigid sphere

The motion of a rigid sphere in shear flow is induced by a viscous force F, defined as:

$$F = 6\pi\eta_{out}Rv, \tag{3.1}$$

where R is the sphere radius, and v its velocity.

Rigid ellipsoid

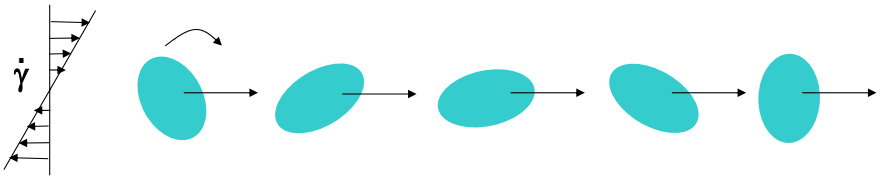

Figure 3.1: *Schematic of the solid-like tumbling motion of an ellipsoid particle in a shear flow.*

Jeffery [85] calculated the motion of a rigid ellipsoidal particle in a viscous fluid. He found that the ellipsoid was periodically flipping around one of the axis perpendicular to the flow direction (see schematic Figure 7.2). This motion is often called the solid-like rotation.

Drop

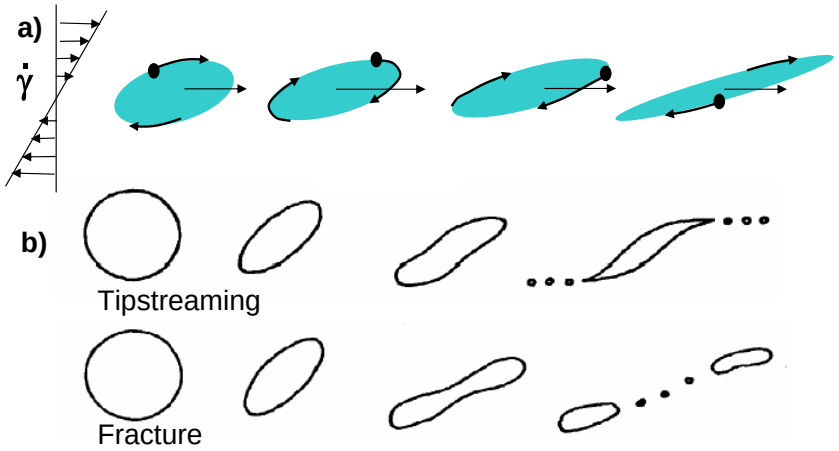

Figure 3.2: *a) Schematic of a drop in a shear field. The drop gets elongated with a movement of tank-treading (internal circulation), highlighted by a particle at the interface. b) Modes of drop break-up observed in simple shear flows [37].*

Lets consider a drop of fluid, with an internal viscosity η_{in}, a surface tension σ and a characteristic radius R, suspended in a solvent with a viscosity η_{out}, in a purely shear flow with shear rate $\dot{\gamma}$. The shear flow exerts a viscous stress $\eta_{out}\dot{\gamma}$, that stretches the drop. This stress is counteracted by the drop's surface tension σ which tends to make the drop spherical. The equilibrium shape is ellipsoidal, as shown in Figure 3.2. If the viscous stress on the drop exceeds its capillary pressure (defined as σ/R), i.e. if $\eta_{out}\dot{\gamma} > \sigma/R$, the drop will rupture. Each rupture reduces the size of

the drop, which drives up the capillary pressure. This rupturing process will halt when the drop reaches the radius limit $R_\star$ obtained approximately by:

$$R_\star = \sigma/\eta_{out}\dot{\gamma} \tag{3.2}$$

The tip-streaming effect

We can note that if we add some surfactant molecules, the drop will give the exterior flow something to grab onto and causes the drop to lose small droplets off their pointed ends; this phenomenon is called "tip-streaming". The tip-streaming in simple shear flows is a mode of droplet break-up in which the droplet develops a sigmoidal shape and a stream of tiny droplets is ruptured off the tips of the drop. De Bruijn suggested some causes to the tip-streaming phenomenon [37]. It was found that tip-streaming can occur if interfacial tension gradients can develop, resulting in low interfacial tension at the tips and a higher tension elsewhere.

Red blood cell

The RBC specific response to a viscous shear flow, featured by various types of cell motion and strong cell deformation, enabling its migration through narrow capillaries, has a great influence on flow and mass transport in the microcirculation in both health and disease [32]. The full understanding of this response requires i) a direct comprehensive observation of cell motion and deformation, and ii) a theoretical analysis that provides a complete model for deducing the cell intrinsic properties from its behavior in shear flow. With the development of the rheoscope [58], several investigators have studied individual RBCs submitted to a uniform shear field [133, 71, 58, 59]). It was found that the human RBC under such flow exhibits one of two types of overall motion: an unsteady motion in which the shape of the cell remains essentially unchanged from its resting shape while the cell undergoes a flipping motion (tumbling), or a steady motion at a stationary orientation with the membrane circulating about the cell interior similar to the motion of a tank tread (tank-treading) (see Figure 3.3).

Figure 3.3: *Top view of the tank-treading motion of a RBC highlighted by the movement of a bead attached to the membrane of the cell [58].*

In order to understand and extract values of the mechanical properties from the observed behavior, one needs a model for the motion of a human RBC in a shear field. Keller and Skalak [91] considered the motion of a fluid ellipsoid with a fixed shape in order to have a better understanding of these two motions.

Fluid ellipsoid with a fixed surface area

Keller and Skalak [91] looked at the motion of a fluid ellipsoid with a fixed surface area. They considered the motion of an ellipsoidal membrane encapsulating an incompressible Newtonian liquid immersed in a plane Couette flow of another incompressible Newtonian fluid as a model

system for RBC motion. The motion of the object is determined by equilibrium and energy considerations. The particle is assumed to be neutrally buoyant, and because the Reynolds numbers characteristic of red-cell motions are much less than unity, inertial effects are neglected.

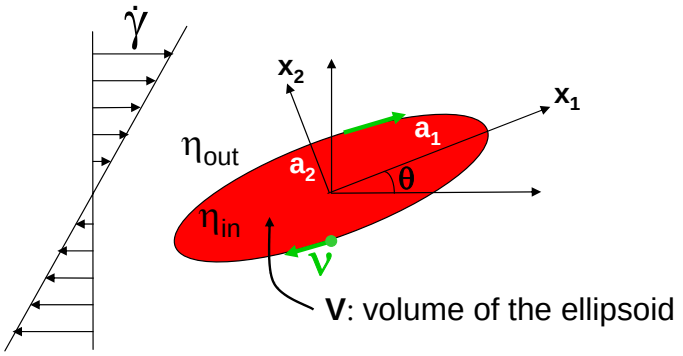

Figure 3.4: *Schematic of the system and definition of the parameters.*

The elements of the membrane are prescribed to move in a plane (x_3=constant) on ellipsoidal trajectories with a kinematical law given by:

$$\left\{ \begin{array}{lcl} x_1(\vec{x^0},t) & = & x_1^0 cos(\omega) - \frac{a_1}{a_2} sin(\omega) \\ x_2(\vec{x^0},t) & = & x_2^0 cos(\omega) + \frac{a_2}{a_1} sin(\omega) \\ x_3(\vec{x^0},t) & = & x_3^0 \end{array} \right. \tag{3.3}$$

where $\omega = \int_0^t \nu(t')dt'$ and ν is the frequency of tank-treading, and x_i^0 is the position of a material point on the membrane at the time $t = 0$. This implies that if ν is constant, the membrane moves completely around the cell interior with a period T_{tt}:

$$T_{tt} = 2\pi/|\nu| \tag{3.4}$$

Hence the velocity of a material point attached to the membrane relative to the reference frame fixed to the ellipsoid, is given by:

$$\left\{ \begin{array}{lcl} v_1 & = & \dot{\omega}(-\frac{a_1}{a_2})x_2 \\ v_2 & = & \dot{\omega}(\frac{a_2}{a_1})x_1 \\ v_3 & = & 0 \end{array} \right. \tag{3.5}$$

The system must fulfill two conditions:

1. Equilibrium of moments: the total moment of the system fluid + ellipsoid is equal to zero,
2. Energy conservation: the rate of work done by the external fluid is equal to the rate at which the energy is dissipated in the internal fluid. The membrane contribution to the dissipation is taken into account by substituting η_{in} by η_{app} explicitly written below.

The first condition leads to the establishment of an equation for the tumbling velocity:

$$\dot{\theta} = \widetilde{A} + \widetilde{B}\cos(2\theta), \text{ where } \left\{ \begin{array}{l} \widetilde{A} = -(\frac{1}{2}\dot{\gamma} + \frac{2a_1a_2}{a_1^2+a_2^2}\dot{\omega}) \\ \widetilde{B} = \frac{1}{2}\dot{\gamma}\frac{a_1^2-a_2^2}{a_1^2+a_2^2} \end{array} \right. \tag{3.6}$$

The conservation of energy can be expressed by:

$$W_p = D' \tag{3.7}$$

where W_p is the total rate at which external flow work is done on the particle, and D' is the rate of dissipation of the energy in the internal fluid. W_p is expressed as:

$$W_p = V\eta_{out}(f_2\dot{\omega}^2 + f_3\dot{\gamma}\dot{\omega}\cos(2\theta)), \tag{3.8}$$

$$\text{where } \begin{cases} f_2 = 4z_1^2(1-2/z_2), & f_3 = -4z_1/z_2 \\ z_1 = \frac{1}{2}(r_2^{-1} - r_2), & z_2 = g_3'(\alpha_1^2+\alpha_2^2) \end{cases}$$

The terms f_2 and f_3 are functions of the axis ratios r_2 and r_3, defined as $r_2 = a_2/a_1$ and $r_3 = a_3/a_1$, and of the parameters α_1, α_2 and g_3' which are also geometrical parameters defined by:

$$\alpha_i = \frac{a_i}{(a_1a_2a_2)^{1/3}} \text{ and } g_3' = \int_0^\infty \frac{ds}{(\alpha_1^2+s)(\alpha_2^2+s)\sqrt{(\alpha_1^2+s)(\alpha_2^2+s)(\alpha_3^2+s)}}$$

The rate of dissipation of the energy is expressed as:

$$D' = V\eta_{in}f_1\dot{\omega}^2, \text{ with } f_1 = (\frac{a_2}{a_1} - \frac{a_1}{a_2})^2 \tag{3.9}$$

Energy is also dissipated within the red-cell membrane. Although the membrane volume is two orders of magnitude smaller than the haemoglobin solution volume, because of its high shear viscosity [49, 34] the energy dissipated in the membrane may exceed that in the haemoglobin solution. Keller and Skalak decided to account for the energy dissipated in the membrane by replacing η_{in} in equation 3.9 with an apparent viscosity η_{app} defined by:

$$\eta_{app} = (1+d)\eta_{in} \tag{3.10}$$

where d is the ratio of the rate of energy dissipation in the membrane to that in the inner liquid. The quantity D' would then represent the rate at which energy is dissipated in the inner liquid and in the membrane.

The conservation of energy requires that the rate at which work is done on the particle be equal to the rate at which energy is being dissipated inside the particle. Indeed, injecting 3.8 and 3.9 into 3.7, the equation of the tank-treading particle becomes:

$$\dot{\theta} = A + B\cos(2\theta), \text{ where } \begin{cases} A = -\frac{1}{2}\dot{\gamma} \\ B = \dot{\gamma}(\frac{1}{2} + 2(\frac{a_1a_2}{a_1^2-a_2^2})f_3[f_2 - (\eta_{in}/\eta_{out})f_1]^{-1}(\frac{a_1^2-a_2^2}{a_1^2+a_2^2}) \end{cases} \tag{3.11}$$

There are two types of solutions to 3.11:

1. If $0 < -A/B < 1$, the angle $\theta(t)$ asymptotically approaches a constant value

$$\theta^* = \frac{1}{2}\arccos(-A/B)$$

2. If $-A/B > 1$, the solution for $\theta(t)$ is periodic, corresponding to a flipping motion of the ellipsoid, described by:

$$\theta(t) = (\arctan\frac{A+B}{(A^2-B^2)^{1/2}})\tan[(t-t_0)\pi/T]$$

where t_0 is such as $\theta(t_0) = 0$, and T is the period of flipping through an angle π.
The transition between a flipping motion and a stationary orientation occurs when $B = -A$ and only depends on geometrical parameters: $r_2 = a_2/a_1$ and $r_3 = a_3/a_1$ and on the ratio of the viscosities $\frac{\eta_{in}}{\eta_{out}}$.

Capsule

Several studies tried to introduce the notion of deformability by looking at the dynamics of capsules. Barthés-Biesel and coworkers [23, 20, 21, 96] have numerically considered elastic or viscoelastic liquid-filled membranes, which were initially spherical, in a Couette flow. Pozrikidis [121] and Ramanjuan [128]studied numerically the behavior of an initially biconcave capsule submitted to shear flow.

3.1.2 Presence of a wall

Rigid sphere

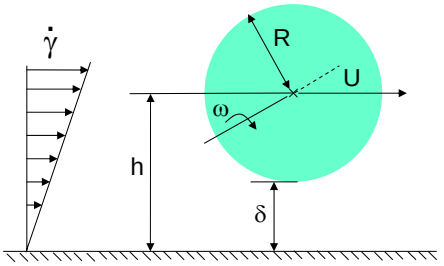

Figure 3.5: *Definition of the parameters of the system. The sphere of radius R, submitted to a shear flow at a distance δ from a plane, is traveling at a velocity U, and rotates with a speed ω.*

Goldman et al. [67] devoted several papers to the study of the motion of a rigid sphere adjacent to a wall, in shear flow. The parameters of the problem are defined in Figure 3.5 The results of their calculation lead to the establishment of the law of variation of the translational speed U as well as the rotational speed ω:

$$\frac{U}{h\dot{\gamma}} = \frac{0.7431}{0.6376 - 0.2\ln(\delta/R)}, \tag{3.12}$$

where h is defined as $h_G = \delta + R$, δ being the distance between the sphere and the wall and R its radius,

$$\frac{\omega}{0.5\dot{\gamma}} = \frac{0.8436}{0.6376 - 0.2\ln(\delta/R)} \tag{3.13}$$

Fluid ellipsoid

The presence of a plane bounding a shear flow has been shown to induce a lift force on non-spherical objects which results in the drift of the particles away from the wall. Olla [117, 118]

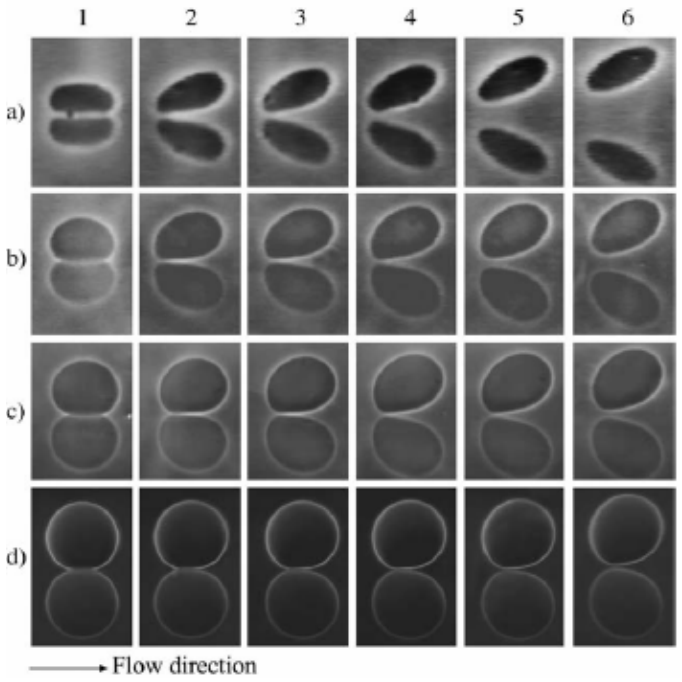

Figure 3.6: *The lift force pushes the vesicles away from the wall [14]. Each row of pictures represents the deformation of one vesicle for a different flow rate. We can note that we distinguish the vesicle and its reflection on the substrate.*

calculated the the drift undergone by a fluid deformable ellipsoid and obtained an expression for the drift velocity v_d given by:

$$v_d = \kappa \frac{\dot{\gamma} R^3}{h^2}, \tag{3.14}$$

where $\dot{\gamma}$ is the applied shear rate, R is the radius of the sphere of the same volume as the ellipsoid, h the distance between the wall and the particle, and κ is a dimensionless parameter dependent on the orientation of the tank-treading cell and its shape, which in turns also depends on the viscosity ratio η_{in}/η_{out} between the cell and the suspending medium.

Among other studies, the effects of the lift force were indeed experimentally observed on buoyant vesicles [13, 14] (Figure 3.6) which have the capacity to unbind from the wall at high wall shear rates. By balancing this lift force with vesicle buoyancy, Abkarian et al. [14] were able to establish the following expression for the lift force:

$$F_l = \eta_{out} \dot{\gamma} \frac{R^3}{h} f(\nu), \tag{3.15}$$

where ν is the reduced volume of the object which allows its shape to self-adjust to the external strains.

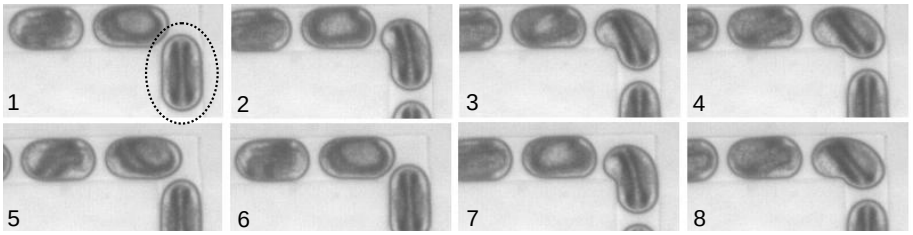

Figure 3.7: *A water drop filled with flow tracers (1 μm size polystyrene beads) flows through a 90º corner. Before the corner, the particles are aligned with the circulation inside the droplet and get mixed as the drop experience mixing in the corner [4].*

3.2 Poiseuille flow

3.2.1 Drops

One of the easiest ways for achieving mixing is by making a drop flow through a corner. In fact, corners add an additional shear to the uniform flow and enhance the mixing. In the Figure 3.7, Cristobal shows how a droplet undergoes mixing when flowing through a 90º corner [4]. Flow tracers, 1 μm size polystyrene beads, are suspended inside the drop. Before the corner (1), the tracers are aligned in the circulation inside the droplet. The drop gets mixed as it flows through the 90º corner (2),(3), (4). The drop need to flow for a long time in a straight part of the channel, to establish a new stable circulation inside the droplet (5), (6), (7), (8). Further in the channel, colloids segregate again.

3.2.2 Vesicle

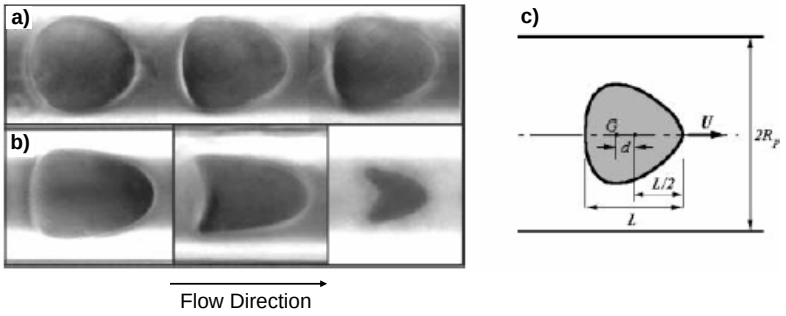

Figure 3.8: *Vesicles flowing in capillaries from left to right. a) Montage showing the deformation of one vesicle (R_0=20.2 μm, ν= 0.983, λ=0.71) at increasing velocities (U = 36, 292, 491 $\mu m.s^{-1}$). b) Other types of shapes observed in the experiment (the corresponding parameters are R_0=20.9, 18.8 and 8.7 μm; ν=0.947, 0.827 and 0.802; λ=0.80, 0.67 and 0.40; U=219, 541 and 505 $\mu m.s^{-1}$ and a = 0.15, 0.29 and 0.50). Scale: the picture height is about 50 μm. c) Definition of geometrical parameters. G is the vesicle's center of mass. The parameters are: the nominal radius R_0 of the vesicle $R_0 = \sqrt{S/4\pi}$ where S is the surface area of the vesicle; the reduced volume $\nu = V/(\frac{4\pi}{3}R_0^3)$, where V is the vesicle's volume; the flow confinement is defined as $\lambda = R_0/R_p$; a is defined as an eccentricity $a = 2d/L$.*

The flow of giant vesicles through cylindrical capillaries and the characterization of their deformation and mobility have been experimentally investigated by Vitkova et al. [154]. In their study, deflated vesicles (with reduced volumes between 0.8 and 1, corresponding to prolate spheroidal equilibrium shapes) are aspirated into a capillary tube with a diameter close to the vesicle

size and a constant flow rate is imposed, as presented in Figure 3.8. Significant deformation of the membrane occurs and increases when the velocity, confinement or deflation of the vesicle are increased.

3.2.3 RBCs

Flow of single cells

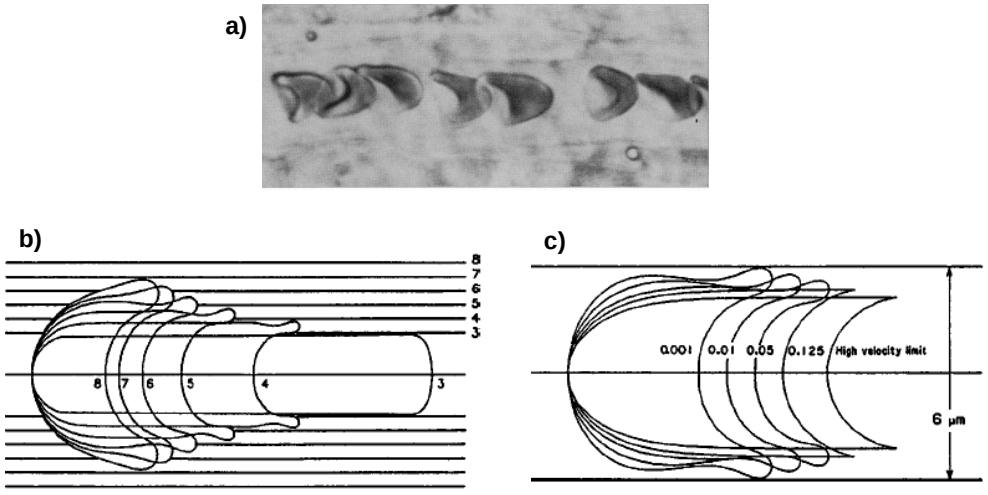

Figure 3.9: *a) Shapes of RBCs in vivo in a capillary about 7 µm in diameter. Most of the cells show the parachute-like shape; the cell on the left shows the slipper-like appearance [139]. Computational shapes of RBCs [134], b) varying the tube diameter (numerical values displayed in µm) for a cell speed of $U = 0.01$ $cm.s^{-1}$ and c) varying the velocity of the blood cell (displayed in $cm.s^{-1}$) in a vessel diameter of 6 µm.*

As they flow through the microcirculation, red blood cells deform to fit the smallest capillaries dimensions as shown in Figure 3.9a). The picture represents RBCs in vivo flowing through a capillary; most of the cells have a parachute-like shape, except the leftmost red cell exhibits a slipper-like shape. Several studies investigated the different shapes experienced by the cells with various conditions. Among them, Secomb [134] studied the evolution of the RBCs shape as the velocity of the object or the capillary size is varied. The results are presented in Figure 3.9b) and c). For a given speed of 0.01 $cm.s^{-1}$, the capillary diameter is increased (Fig. 3.9b)), consequently the cell is less elongated. In a second experiment, the diameter of the capillary is fixed at 6 μm and the RBC's velocity is increased (Figure 3.9c)). As the speed rises, the cell elongates and the rear of the object becomes stiffer.

In order to understand the mechanism of this deformation, the dynamics of red blood cells in cylindrical capillary flow was studied numerically by Noguchi et al. using a three-dimensional approach [115]. As the flow velocity increases, the model RBC transits into a parachute shape. The RBC often forms a non-axisymmetric slipper-like shape around the transition velocity, as shown in Figure 3.10b). The new shape is stable because it obstructs solvent flows less than a discocyte in coaxial orientation. RBCs with similar slipper-like shapes have been observed experimentally in microvessels [139, 145]. When the flow velocity is reduced, the parachute shape returns to a discocyte. The results imply that in the investigated regime of elastic parameters, the flow forces required to induce a shape transformation are linearly related to the elastic

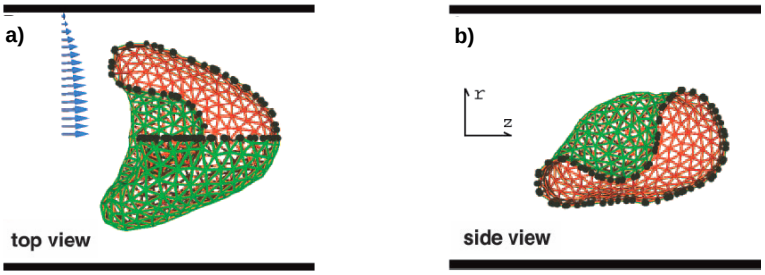

Figure 3.10: *Snapshots of RBC model in capillary flow. a) RBC with parachute-like shape. With increasing velocity, the cell deforms into b) slipper-like shape. The blue arrows represent the velocity field of the solvent; the outside and inside of the cell are depicted in green and red, respectively.[115]*

bending and stretching forces. This result is consistent with the experimental results of [145] and is in the range of microcirculation in the human body. The dependence of the cell shapes on the elastic moduli, was also investigated. As the elastic modulus μ increases, the deformations of the blood cell are reduced: they are less elongated in the flow direction, and their front ends become more smoothly rounded.

Concentrated suspension of red blood cells

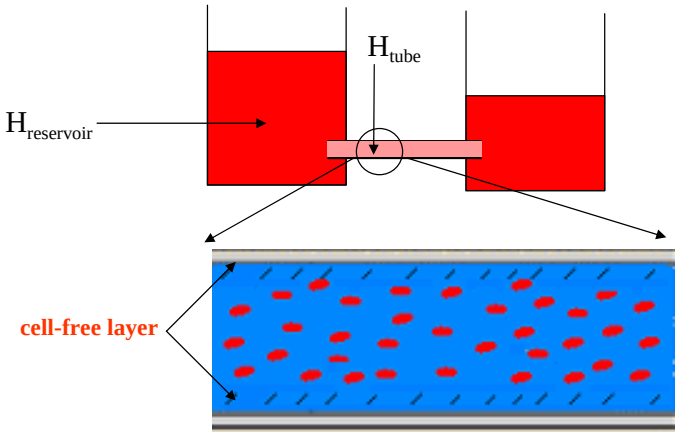

Figure 3.11: *Illustration of the Fähraeus effect: blood flowing from a reservoir into a tube decreases in percentage hematocrit. Magnification of the tube allows us to highlight the presence of a cell-free layers adjacent to both the top and bottom walls of the tube.*

First Poiseuille in 1840 [120] and then Fähraeus in 1931 [52] have reported that when blood flows from a large diameter tube through a capillary tube, with a diameter inferior to 300 μm, the average hematocrit - relative volume of all the cells with the total volume of whole blood solution - of the capillary blood is less than that of the blood in the larger tube [61]. Thus, for a given volume of plasma, the percentage hematocrit is less in the tube than in the reservoir. Their explanation for this phenomenon is that a cell-free layer exists which lines the top and bottom walls of the microchannels [60] due to a lateral migration of the particles away from the vessel wall [70]. Figure 3.11 helps to show this reservoir-tube relationship and the existence of the cell-free layer. Barbee et al. [19], Pries et al. [123] and Goldsmith et al. [70] studied what is designed as the Fähraeus effect and the subsequent effects, the Fähraeus-Lindqvist effect and

the Fähraeus network or plasma skimming effect.

The Fähraeus-Lindqvist effect states that in tubes <300 μm in diameter, the relative viscosity of blood - and so the resistance to blood flow - decreases with decreasing tube diameter ; it is due to the difference in the mean velocity of cells and plasma in the smaller vessel associated with a non-uniform distribution of the particles. The extension of the classical Fähraeus effect to microcirculatory network (also named Fähraeus network effect) is described as a combination of the repeated phase separation of red cells and plasma at capillary bifurcations and the single-vessel Fähraeus effect; red blood cells will preferably flow in daughter capillaries with the higher flow velocities, leading to a lack of red cells in the daughter channel fed by the side of the main vessel.

3.2.4 Capsule

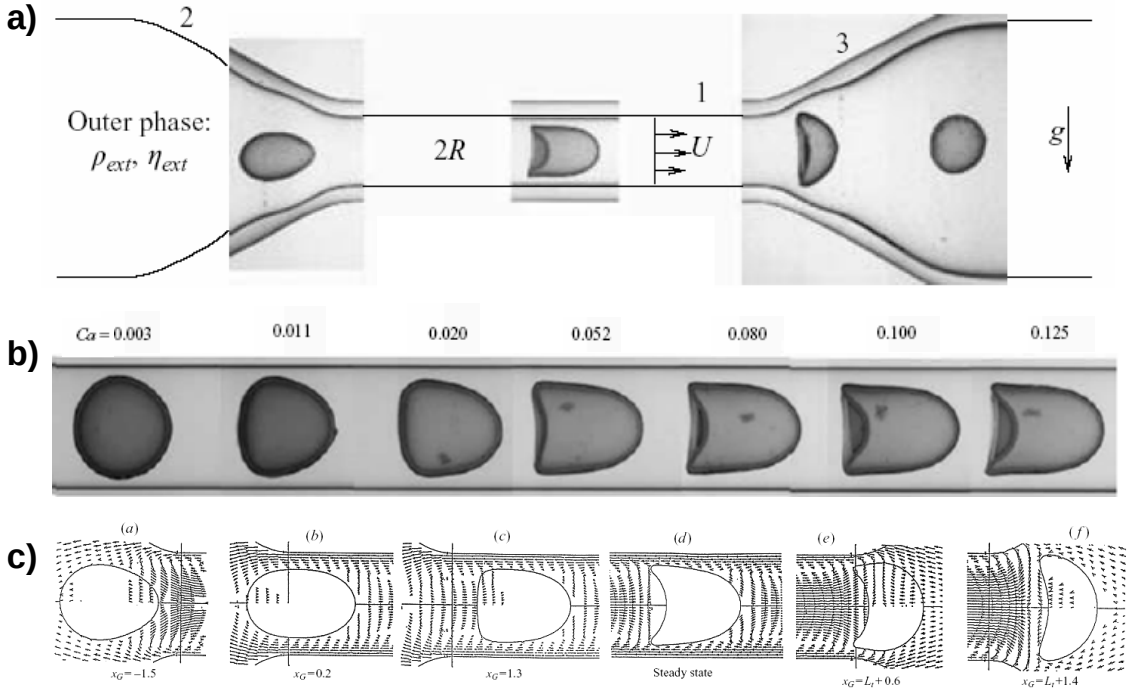

Figure 3.12: *a) Schematic of the experimental setup : 1. test section, 2. converging section, 3. Diverging section. [130]. b) Stationnary shapes for a/R=0.81 - a/R being the size of the capsule, normalized by the size of the tube - and for different capillary numbers : ε=0.003, 0.011, 0.020, 0.052, 0.08,0.01 and 0.125 from [130]. c) Flow field and sequence of deformation of a capsule with R = 0.8 and the capillary number associated with it is ε=0.005 [126].*

The sequence of deformation of a capsule entering, going through and exiting a close fitting channel has been studied experimentally by Risso [130] and theoretically by Barthés-Biesel and co-workers [126]. The experimental results are shownFigure 3.12a). Stationary shapes of capsules for different capillary number ε et ratio a/R (a being the initial radius of the capsule and R the radius of the cylindrical pore) are presented. We report here the results for one value of the ratio a/R=0.81. We can note that for a capillary number ε=0.052, the capsule adopts a stationary parachute-like shape. In their paper, Barthés-Biesel and co-workers [126] report the

evolution of the capsule's shape when flowing through a cylindrical pore and the associated flow field, a/R=0.8 and ε=0.04. The velocity distribution shows the coupling between the internal and external flows. At steady state, the capsule experiences a parachute-like shape and behaves as an underformable particle, as the internal velocity vanishes.

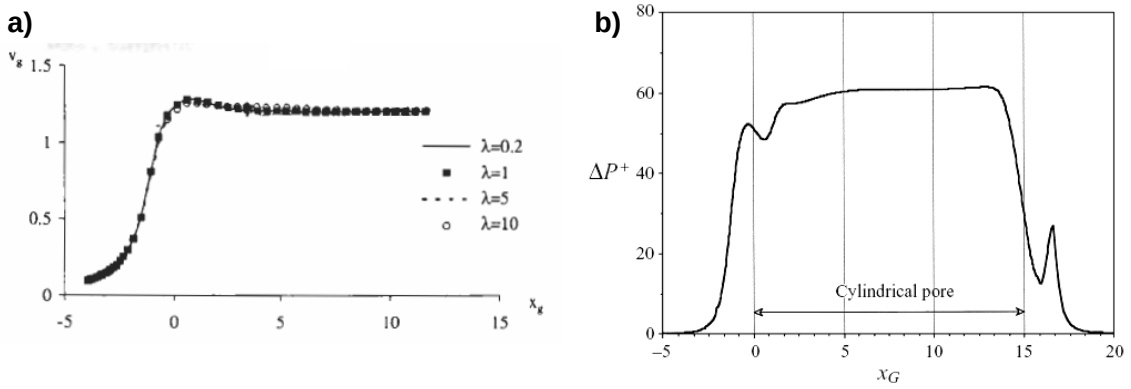

Figure 3.13: *a) Pressure drop associated with the flow of an elastic capsule through a geometrical constriction. The capsule size is R=1.2 and capillary number ε = 0.005 [126]. b) Steady pressure drop ΔP^{+SS} due to a spherical elastic capsule, for R = 1.4; 1.2; 1.0; 0.9; 0.8; and 0.5. Burst occurs when ε exceeds a critical value that depends on size [126].*

Barthés-Biesel and co-workers also calculated the excess of pressure associated with the entrance of a capsule in a cylindrical pore [38, 126]. Such pressure drop has never been measured previously due to the lack of system, sensitive enough to measure the change in pressure at the scale of a single object. The model computes the additional pressure drop, the position and the velocity of the capsule center of mass as a function of time or position along the tube axis. We report in Figure 3.13a), the evolution of the velocity of the particle center of mass v_G, versus its displacement x_G in the tube. As the capsule enters the pore, its velocity increases with a slight overshoot before reaching an unvarying speed. The computation is stopped when the particle reaches a steady state. In the Figure 3.13b), ΔP^+ - the excess of pressure non-dimensionalized by $\mu_{out} v_0 / R_{tube}$, where η_{out} is the outer viscosity, Q is the applied flow rate and v_0 is the fluid mean velocity, defined by $v_0 = Q/\pi R_{tube}^2$ - is represented versus x_G, the capsule's axial displacement relative to the pore radius R_{tube}. At the entrance of the pore, the pressure drop increases until reaching a steady pressure drop ΔP^{+SS}, and then decreases back to zero when the capsule exits the channel. We can note that during the entrance phase, the capsule almost plugs the pore which results in an entry peak before the establishment of the steady pressure drop ΔP^{+SS}. The computation also predicts the bursting of the object when ε - defined as $\varepsilon = \eta_{out} v_0 / E_s$, where E_s is the elastic tension - is increased above a critical value that depends on the ratio between the size of the object and the size of the pore.

Chapter 4

General materials and methods

Ce chapitre est consacré au développement des techniques générales utilisées au cours de l'étude de nos objets. Dans un premier temps nous présentons les méthodes de microscopie (champ clair, contraste de phase et fluorescence) et d'enregistrement vidéo (caméra CCD ou camera rapide). Puis dans une seconde partie nous passons en revue les différents types d'écoulements confinés étudiés dans ce manuscrit: écoulement de cisaillement en présence ou non d'une paroi (nous détaillons le montage de la chambre d'écoulement ainsi que sa calibration) et un écoulement de type Poiseuille. Nous exposons notaMment le mode de fabrication des systémes microfluidiques ainsi que les deux modes de mise en mouvement des fluides : débit contre pression.

In this section, we will develop the general techniques used on the objects studied. In section 4.1, we will focus on the methods of observation and recording used during all of our experiments. Then, in section 4.2, we will look at the different types of flows under confinement: near a plane and in microfluidic flows.

4.1 Video-microscopy

4.1.1 Microscopy

Since the objects that we are studying are micron-size (from 5 to 200 μm in diameter), the observations during our experiments require the use of a microscope. We used an inverted microscope (Leica DM IRB, Wetzlar, Germany). Several techniques have been used preferentially to fit to the observation needs. In fact, the drops and red blood cells are easy to observe in classic transmission microscopy but the study of vesicle requires the use of phase-contrast microscopy. Fluorescence microscopy allows us to emphasize the presence of certain molecules at the surface, or in the internal media of our objects. Bright-field, phase-contrast and fluorescence microscopy are briefly developed in this section.

The bright-field microscopy

With a conventional bright-field microscope, light from an incandescent source is aimed toward the condenser, through the specimen, through an objective lens, and to the eye through the binocular. We see objects in the light path because natural pigmentation or stains absorb light

differentially, or because they are thick enough to absorb a significant amount of light despite being colorless.

The phase contrast microscopy

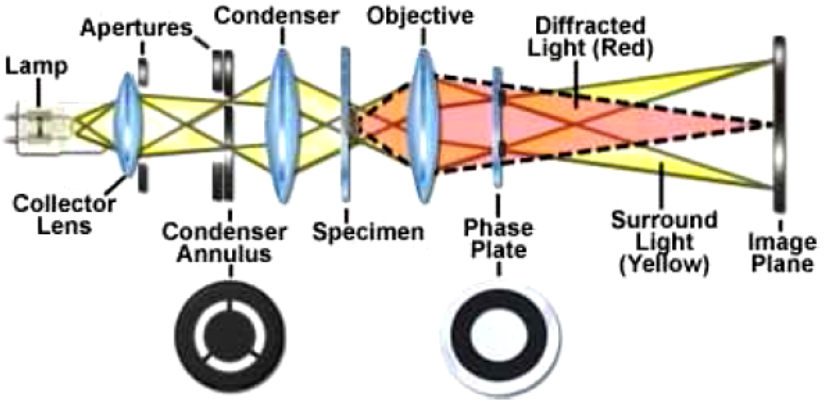

Figure 4.1: *Principle of the phase contrast microscopy [5].*

The principle of the phase contrast microscopy is shown in Figure 4.1. Phase-contrast is a widely used technique that shows differences in refractive index in a specimen as difference in contrast. The system consists of a circular annulus in the condenser which produces a cone of light. This cone is superimposed on a similar sized ring within the objective. The ring in the objective has special optical properties: first of all, it reduces the direct light in intensity, but more importantly, it creates an artificial phase difference of about 1/4 wavelength. As the physical properties of this direct light have changed, interference with the diffracted light occurs, resulting in the phase contrasted image.

The fluorescence microscopy

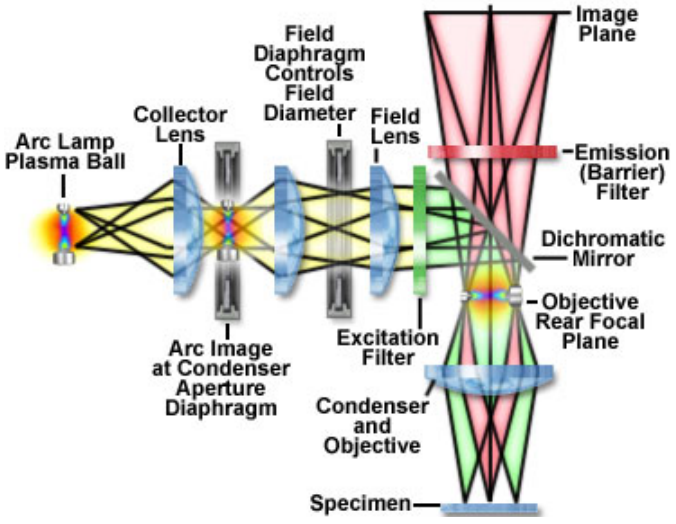

Figure 4.2: *Principle of the fluorescence microscopy. The dichroic mirror transmits the light emitted by the specimen but blocks the excitation light [6].*

In Figure 4.2, we can follow the trajectory of the light through the different elements of a fluorescent microscope [6]. The light emitted by a mercury lamp is first collected by a lens and then focused homogeneously on the specimen through an aperture diaphragm, lenses and a field diaphragm. A specific wavelength is selected by the excitation filter to specifically interact with the fluorescent molecules present in the sample. The fluorescent light emitted by the sample differs in wavelength (color) from the excitation light. The dichroic mirror is transparent to the emitted light but blocks the excitation light reflected by the sample.

4.1.2 Video and Analysis

In order to make quantitative measurements, all the experiments are recorded with a camera. Two types of cameras, a CCD camera and a high-speed camera, have been used depending on the speed of the phenomenon. Once recorded and digitized all the images are analyzed using different analysis softwares. We will describe here the most commonly used.

CCD camera

For relatively "slow" motion (deflation of vesicles, sedimentation, shear near a plane...), a simple CCD camera (Cohu 4910) allows us to obtain a real-time image on a standard television. Long sequence of several seconds (sometimes minutes), are first recorded thanks to a VCR linked to the camera. Then sequences of interest are digitized on a computer with an acquisition PC card Scion LG-3. We also used a Digital Videocassette Recorder (Sony DVCam SDR-25) directly connected to the camera. Once recorded, the moves had to be transferred to a computer for analysis.

High-speed camera

When using microfluidic devices, the objects flow at typical velocities of the order of magnitude of a centimeter per second. The observation of such fast motion requires the use of a high-speed camera (PCO, photron and phantom cameras) capable of recording with frame rates up to 10000 $fr.s^{-1}$.

Image Analysis

Most of the experiments we performed require image analysis. To do so we used two different softwares: National Institutes of Health (NIH) Image J 1.32j - freely available on the web [7] - and Matlab 7.0.4. Both programs were used to determine several parameters such as the speed of the particles, their volume, the typical dimensions (radius for spheres and major and minor axis for ellipsoids), the orientation of cells, as illustrated in the Figure 4.3a) or the deflation of an interface as detailed in Fig. 4.3b) (this specific analyze will be developed further in this manuscript).

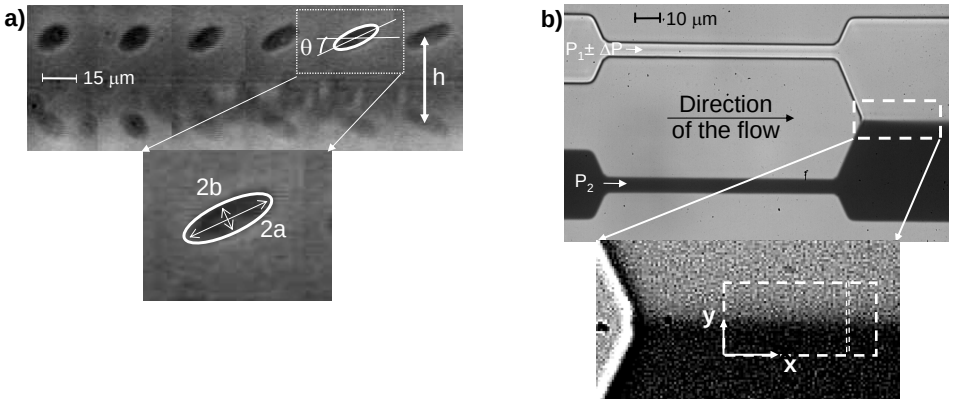

Figure 4.3: *a) Image J allows to measure distances, angles of orientation, and by fitting the object with an ellipse, we can extract the lengths of both the major and minor axis. b) Matlab can be programmed to detect the motion of an interface as a function of time.*

4.2 Flows

4.2.1 Near a plane

The side view chamber

In order to study the flow by microscopy, we used a parallelepiped-plate flow chamber - spectrophotometric circulation chamber from Hellma (Müllheim, Germany), height d = 1 mm, width a = 10 mm, length = 55 mm - with four optical faces made of quartz. The observation is made through the smaller dimension of the chamber (see schematic figure 4.4a)). The chamber is open at the two further ends to allow the circulation of fluid inside. As shown in the figure 4.4b), a system of tubing allows the circulation of fluid as well as the injection of the colloidal suspension. We carefully "bath" the chamber with a solution of sulfochromic acid for several hours after each experiment and after an abundant washing with distilled water, then we dry it with a flux of argon to avoid traces and wrap it in optical paper before storage.

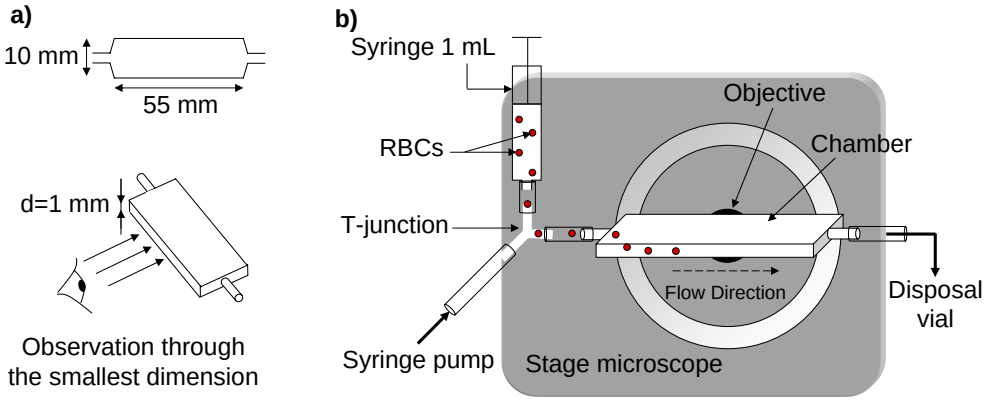

Figure 4.4: *a) Dimensions of the flow chamber. b) Schematic of the injection set-up.*

The tilted microscope

What we call a "side view" is in reality an observation of the objects in a vertical plane, perpendicular to gravity and parallel to the plane of shear. To do that, we lay down the microscope and work at a low angle of incidence. A picture of the tilted microscope and a close-up of the chamber mounted on a homemade stainless steel holder keeping the chamber horizontal is shown in Figure 4.5. This configuration allows us to observe a well defined side view of the objects and their reflection on the substrate.

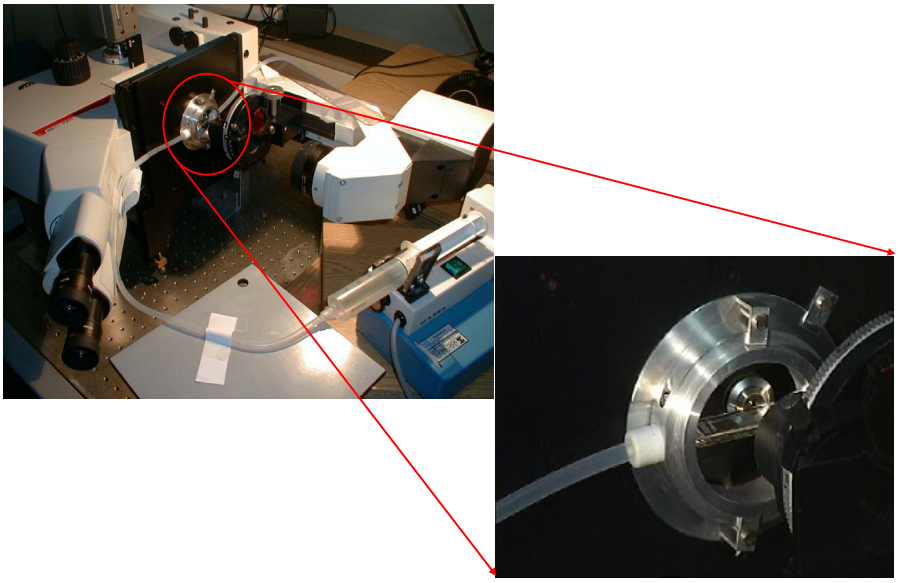

Figure 4.5: *The tilted microscope allows an observation perpendicular to gravity.*

The linear shear flow

The flow is applied using a standard syringe pump as show in figure 4.5. The syringe pump gives the flow rate applied q in arbitrary units, so we need to proceed to the measurement of the shear rate $\dot{\gamma}$ in the chamber. Parallel to the substrate, the velocity field is a parabolic Poiseuille-type profile, at least far from the vertical side walls of the chamber (for height $\ll$ width) as shown in the schematic in Fig. 4.6. At the scale of the objects studied, the profile of velocity field is linear and the shear rate $\dot{\gamma}$ is proportional to the flow rate.

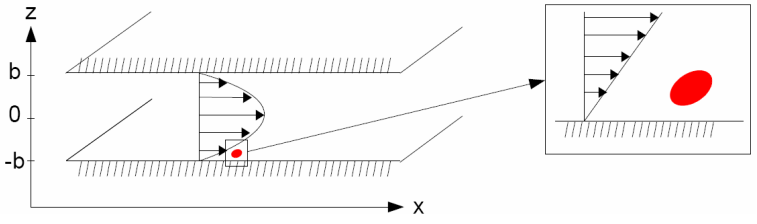

Figure 4.6: *The velocity profile is parabolic in the chamber, however at the scale of the cells, the velocity field is considered linear.*

The laminar wall shear rate $\dot{\gamma}$ was calibrated using suspensions of 2 μm diameter latex beads. The bead velocities were measured at specified arbitrary flow rates as a function of their distance

to the substrate. The velocities were found to vary linearly with the distance to the substrate (up to a distance of 150 μm from the wall where the parabolic character of the flow appears) and the slopes of the obtained linear curves yielded the wall shear rates. A typical calibration curve is shown in figure 4.7. The effect of the lateral walls have been previously studied [10] and the results show that the lateral plane disturbs the Poiseuille flow on a distance in the order of magnitude of the height of the chamber (around 1 mm). Therefore if we make our measurements sufficiently far from the lateral walls (at least 1.5 mm far from it), the flow is not changed.

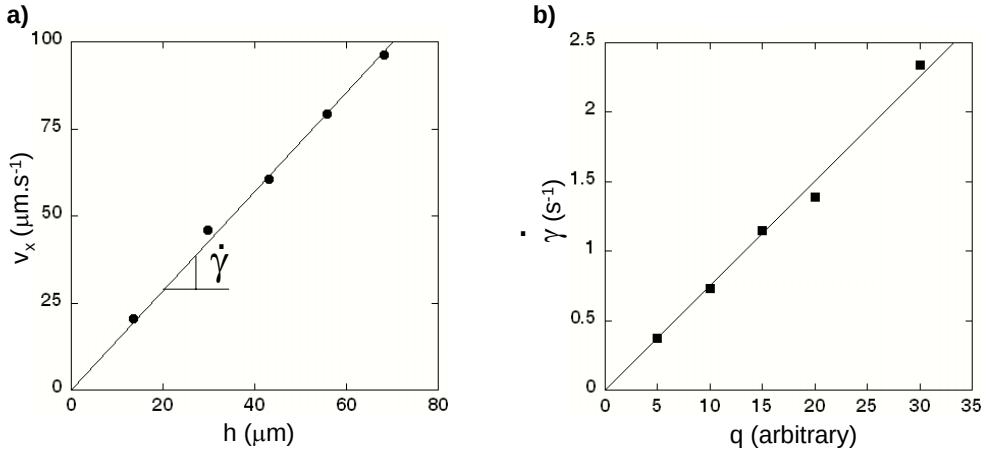

Figure 4.7: *a) The velocities of beads vary linearly with the distance to the wall. b) Calibration of the shear rate $\dot{\gamma}$ as a function of the arbitrary flow rate.*

4.2.2 Microfluidic flow

Fabrication

Several techniques to produce microfluidic devices exist (photolithography, etching in silicon and glass...). We chose to use devices made of PDMS because it is optically transparent and malleable, it can seal easily and irreversibly (if exposed to plasma treatment) to itself or to glass. The fabrication of microfluidic devices in Poly(Dimethylsiloxane) (PDMS) is based on the techniques of soft lithography, and replica molding [103].

We first create the desired design with a computer-aided design software (Clewin). The desired design is then printed on a transparency (for "large" features between 10 and 200 μm) or engraved in a chrome mask (for small features below 10 μm) by a high-resolution commercial image setter. This transparency (or chrome mask) serves as the photomask in contact photolithography.

The soft lithography step consists in producing a positive relief of photoresist (SU-8) on a silicon wafer. The speed of the spin-coater sets the thickness of this layer of photoresist, controlling the height of the channels. Then, we pre-bake the wafer for several minutes at 65^{o}C and 95^{o}C (the exact time depends on the brand of the photoresist and the desired thickness) in order to initiate the polymerization of the SU-8. A UV source is used to expose the silicon wafer which is covered with the photomask. Another baking step finishes to cure the photoresist. Dissolving away the unilluminated - and so unpolymerized - photoresist leaves a positive relief that serves as a master.

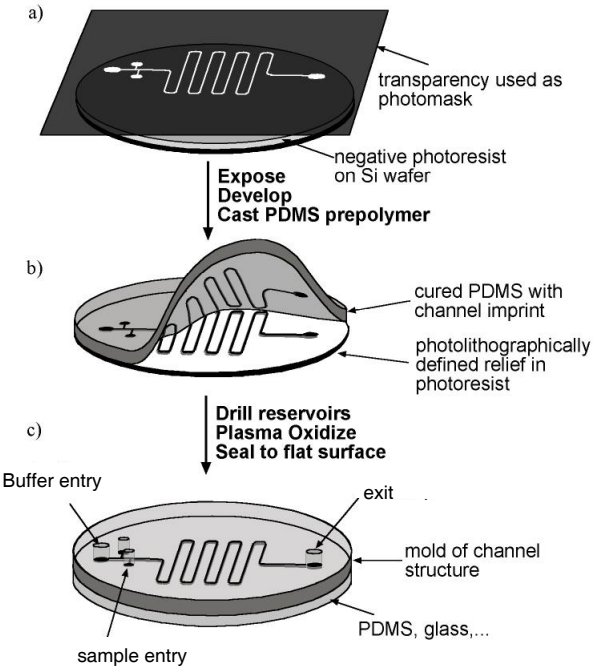

Figure 4.8: *Fabrication steps of a PDMS microfluidic device [8].*

The PDMS channels are formed by replica molding (ridges on the master appear as valleys in the replica). We mix a solution of silicone elastomer with a curating agent (Sylgard 184 kit silicone elastomer, Dow Corning) in a ratio 9/1 and homogenize the mixture. After pouring the solution into a petri dish over the master, we degas under a vacuum in order to get ride of any bubbles. The whole preparation is cured in an oven at 65^{o}C for 1 hour. The replica is then peeled from the master and access holes for the channels are punched out of the cured layer by using a truncated needle.

Note: In the case of a PDMS/PDMS device, the preparation of the PDMS is made with an excess of the curating agent (ratio 5/1) to allow the crosslinking to take place between the two blocks of PDMS.

The PDMS device can be sealed to a cover glass or to another blank piece of PDMS. To do so, the surfaces of the two units (PDMS and PDMS/glass) are activated by a plasma treatment during 90 seconds in a plasma cleaner (Plasma cleaner PDC-32G, Harrick plasma). Immediately after the treatment, the two pieces are put in contact to let them stick together. The device is then stored at 65^{o}C over night to allow the strengthening of bonding between the two blocks.

Flow-rate-driven flow versus pressure-driven flow

Several methods exist to move fluids through the device: by electrokinetic, thermal effects or phase transition effects... In our experiments, the fluids are driven by static pressure or by the use of a syringe pump. Although in a single-phase flow these two types of experiment would be equivalent, the same is not true in a multiphase flow since the shape of the fluid-fluid interface, which is determined by the flow itself, complicates the relationship between the pressure drop

and the flow rate.

These methods are distinct since the use of specified pressures sets up corresponding flow rates of the two phases while a syringe pump maintains a specified volume flow rate by appropriate adjustment of the force applied to the syringe, which changes the pressure in the fluid. The case of multiphase flow will be addressed further later, so we focus here on the case of a single-phase flow. The two different set-ups are presented here and we discuss briefly the benefits and drawbacks of the two methods.

Flow rate-driven flow

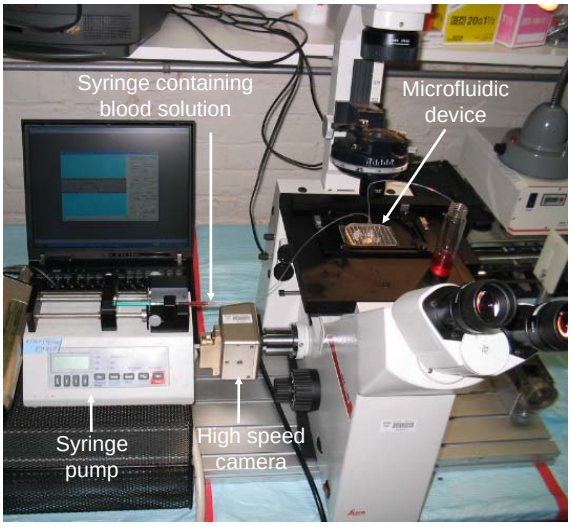

Figure 4.9: *Experimental set-up for a microfluidic experiment. The fluid is moved by a motor syringe pump.*

As presented in the Figure 4.9, the syringe approach for fluid delivery requires the use of a standard motor-driven pump to achieve a given flow rate. The typical flow rate used during our experiments range from 0 to 5000 μL.s^{-1}. The syringe pump used for the microfluidic experiments displayed the applied flow rate such that no calibration was needed. The pump pushes on the syringe linked to the microfluidic device by a tubing (I.D.=0.38 mm; O.D.=1.09 mm).

Pressure-driven flow

In the Figure 4.10, the experimental set-up of a microfluidic system activated by the pressure is shown. In the static pressure pumping approach the fluids are placed in syringe tubes and the air pressure above the fluid is regulated. The pressure is controlled by precision regulators (Bellofram Type 10) with a sensitivity of 5 mPsi. The pressure is measured using test gauges (Wika) with a resolution of 150 mPsi.

Qualitative comparison

The main unquestionable benefit coming from the use of pressure to move fluids is the fast response of the liquids. When using a syringe pump, we need to wait the full establishment of the flow and its stabilization for inertia to be overcome. With the two methods different ranges of velocity are reached for the flow of objects. For example, red blood cells flowing in glass capillary (of diameter less than 10 μm) travel at a speed of several centimeters per second for

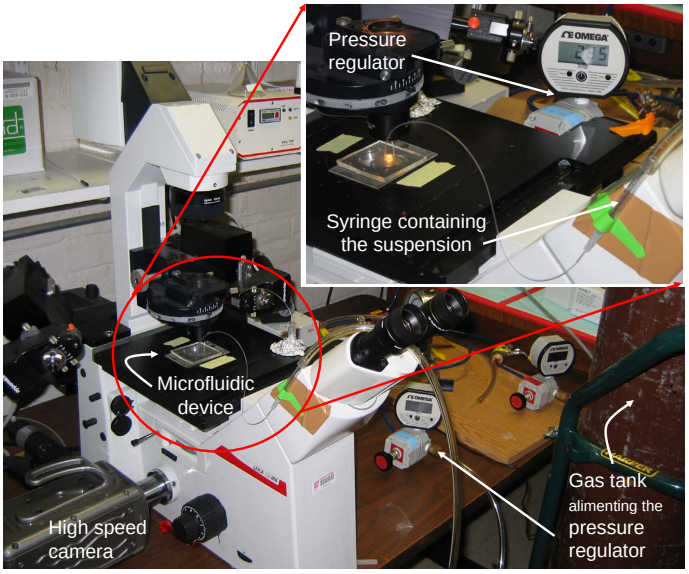

Figure 4.10: *The pressure-driven set-up shows a gas bottle providing the gas to a manometer in order to push the fluid in the syringe.*

flow-rate-driven flows (from 0 to 120 μL.s^{-1}) versus several millimeters per second for pressure driven flows (from 200 to 1400 Psi).

Chapter 5

Interfacial production of surfactant

Nous présentons, dans ce chapitre, l'étude menée sur le comportement d'une goutte s'écoulant dans un canal de dimension comparable, et dont les propriétés mécaniques sont modifiées par la production de tensioactif à sa surface. La production de tensio-actif, in situ à l'interface est le résultat d'une réaction chimique (acide/base). Nous développons l'effet de la concentration en tensioactif, ainsi que celui de la géometrie du canal microfluidique, sur la forme et la dynamique des gouttes.

It has been recognized that small droplets can act as isolated chemical containers, whose composition and other environmental variables can be carefully controlled and monitored. Thus, for example, biological species may be grown in a precision controlled environment to control population density and specimen yield [26, 28]. The microfluidic technology allows the study of fast phenomena. Therefore, the association of the use of microfluidic systems and droplets as chemical reactors is suitable to study and find an explanation of the spontaneous emulsification phenomena [102, 114, 136] due to chemical reactions. In this section we present the example of an interfacial chemical reaction taking place on a droplet flowing in a close fitting channel. We will detailed the consequences of surfactant production at the surface of the drop. We will investigate the effect of the reagents concentration as well as the influence of the channel's size on the behavior of the droplet.

5.1 Experimental set-up

5.1.1 Device geometry

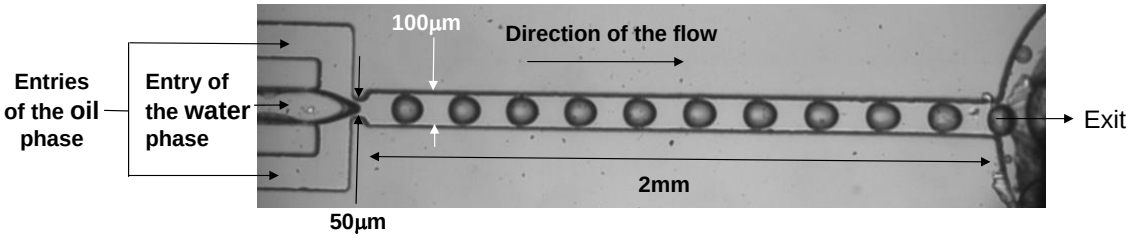

Figure 5.1: *The geometry used is a flow focusing: two streams of oil focus the stream of water and break it into a series of monodisperse droplets.*

The microfluidic device was manufactured using the principles presented earlier in section 4.2.2 and the fluids were pushed with the pressure-driven flow approach introduced in the section 4.2.2. The dimensions of the channel are: 100 μm in width, except for the zone where the breaking occurs where the width decreases to 50 μm, 2 mm in length, and 75 or 50 μm in depth depending on the device. In order to produce the drops, we used the flow focusing geometry [17] as presented in Figure 5.1. The principle of the flow focusing device lies on the focusing by the two streams of oil (upper and lower channels on the left) of the water stream (middle channel) and break it into a series of monodisperse droplets (with the same physical properties: size, composition, speed...). Because of the fast motion of the objects, with a typical speed of the order of 1 cm.s^{-1}, the movies were taken with a high-speed camera using a frame rate of 1000 frames.s^{-1}.

5.1.2 Solutions

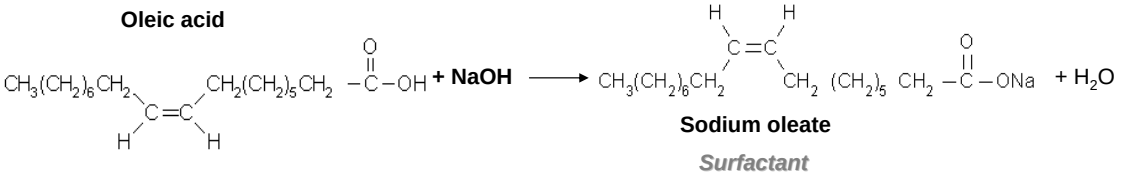

Figure 5.2: *The chemical reaction produces surfactant in situ at the interface of the droplets.*

The system used during our experiment is an acid/base chemical reaction. Oleic acid, a fatty acid soluble in oil, reacts with the sodium hydroxide, diluted in the aqueous phase, and produces sodium oleate, a non-ionic surfactant, as well as some water. The oleic acid, the sodium hydroxide and the mineral oil were purchase from Sigma and used as received. The sodium oleate has been obtained by total chemical reaction of oleic acid and sodium hydroxide following the reaction presented in Figure 5.2. The mineral oil viscosity was measured to be 0.123 Pa.s at 25^{o}C, its density is 0.88 g.mL^{-1}.

Experiment designation	Composition of the dispersed phase	Composition of the continuous phase	Type of the experiment
A	water	mineral oil	control experiments
B	water	10 mM oleic acid	
C	10 mM NaOH	mineral oil	
D	5 mM NaOH	5 mM oleic acid	interfacial chemical reaction experiments
E	7.5 mM NaOH	7.5 mM oleic acid	
F	10 mM NaOH	10 mM oleic acid	
G	20 mM NaOH	20 mM oleic acid	
H	5 mM sodium oleate	mineral oil	oleate experiments
I	7.5 mM sodium oleate	mineral oil	
J	10 mM sodium oleate	mineral oil	

Table 5.1: *Table of composition of the dispersed and continuous phases used for the droplet production.*

The solutions used as the dispersed phase in the droplet production are several concentrations of sodium hydroxide (0 mM, 5 mM, 7.5 mM, 10 mM, 15 mM and 20 mM) in the interfacial

chemical reaction experiments and several concentrations of sodium oleate (0 mM, 5 mM, 7.5 mM, 10 mM, 15 mM and 20 mM) for the oleate experiments. The continuous phase is composed of several concentrations of oleic acid in oil (0 mM, 5 mM, 7.5 mM, 10 mM, 15 mM and 20 mM) in the interfacial chemical reaction experiments. The list of the experiments are gathered in the Table 5.1.

Surface tension measurement: the pendant drop method

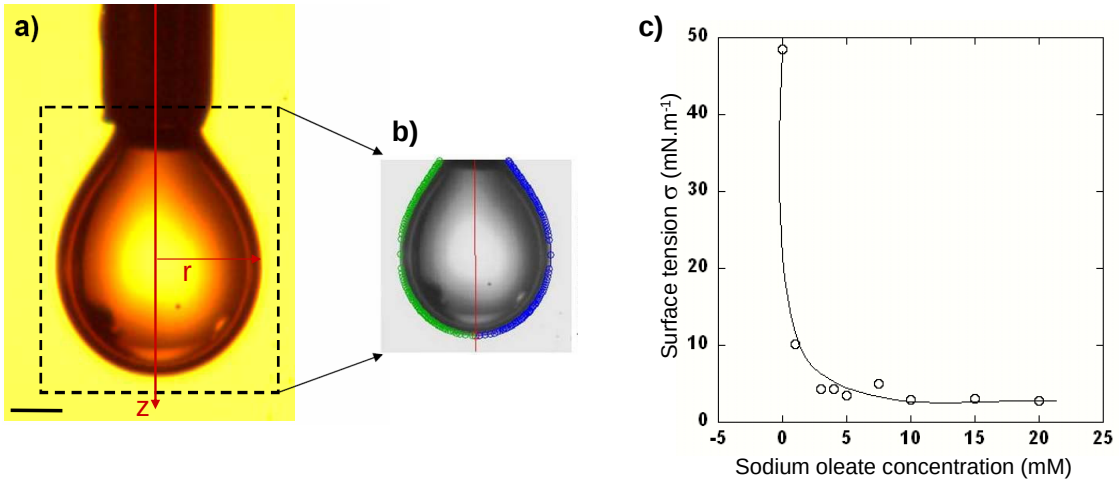

Figure 5.3: *The pendant drop method is used to measure the surface tension of our solutions. a) A drop of 1mM sodium oleate in a mineral oil solution. The black line in the left lower corner corresponds to 0.70 mm. b) Matlab treatment of the preceding picture. The surface tension parameter is extracted from the adjustment of the curvature of the droplet. c) The evolution of the surface tension with increasing concentration of surfactant.The solid line is just a guide for the eyes.*

The pendant drop measurement was used to determine the surface tension of the different sodium oleate concentrations dispersed in oil. The principle of this measurement, briefly introduced in section 2.1.1, is explained in more detail here. The pendant drop is immersed in a container full of the continuous phase as shown in the Figure 5.3a); a picture is taken right before the drop detached from the needle. By determining the curvature C of the drop (see fit Fig. 5.3b) and using the measured values in the equation that governs the shape of the droplet, we can extract the surface tension γ between the liquid inside the drop and the oil solution:

$$\gamma C = \rho g z, \tag{5.1}$$

where ρ is the density of the dispersed phase, and z the vertical distance from the needle. The results of the surface tension measurements are presented in the graph Figure 5.3c). We can see that the surface tension drops very quickly with the addition of surfactant. The Critical Micellar Concentration (CMC) is defined as the critical concentration of surfactant above which the molecules form micelles in a solution. It corresponds to the critical surfactant concentration above which the surface tension doesn't evolve anymore. Above this critical value, the surface of the drop is saturated with surfactant molecules and the rise of surfactant concentration increases the number of micelles formed without change dramatically the surface tension. The CMC can be estimated from the graph in Figure 5.3c) to be between 1 and 5 mM in sodium oleate.

5.1.3 Droplet production

The specific geometry of the device associated with the appropriate system to propel the fluids has an important impact on the droplet production as developed in Appendix A. In this experiment, we choose the pressure-driven flow approach detailed in section 4.2.2. We now investigate how the presence of surfactant modifies the droplet production.

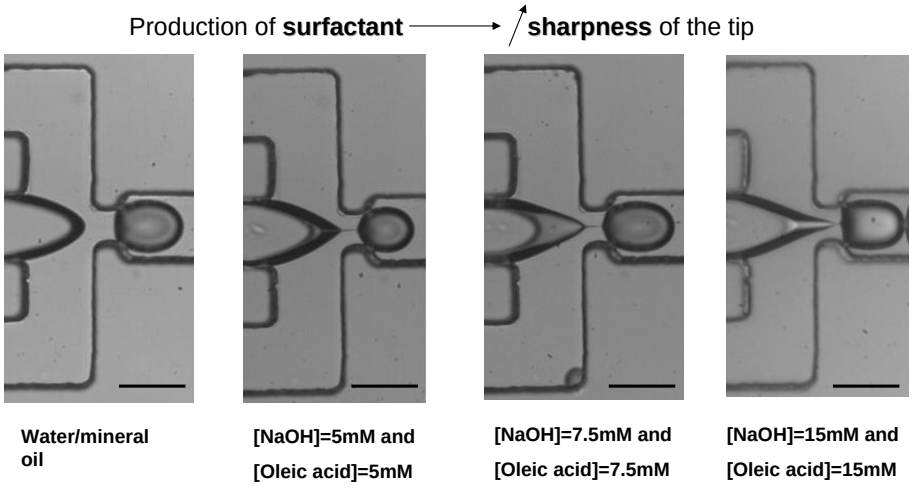

Figure 5.4: *Pictures are taken right after the aqueous thread breaks into a drop. As the surfactant production is increased, the tip becomes sharper, changing the physical properties of the emulsion produced. The black lines in the lower right corner of each image represent 100 μm*

The chemical reaction between the two phases begins as soon as the two fluids enter in contact: just before the formation of the drops. The production of surfactant impacts the "breaking" process of as illustrated in the Figure 5.4. The pictures are taken right after the dispersed phase breaks into drops; we can note that as the surfactant concentration is increased, the tip of the aqueous phase gets sharper leading to a slightly different breaking process. Therefore, the droplets produced will have different physical characteristics: different size, different velocity, different frequency of production, and different spacing between two following droplets. This will complicate the comparison of experiments using two different concentrations. In order to solve this issue, it would be necessary to improve the design of the device and to trigger the chemical reaction a posteriori of the droplet production. Thus all the droplets would be identical from experiment to experiment and after the drops production, we would bring into contact the two reagents and trigger the interfacial chemical reaction independently from the breaking process.

5.2 Effect of surfactant at the drop interface

The experiment consists in producing droplets using a flow focusing device and studying their behavior when flowing in a straight channel with a rectangular cross section (either 75 or 50 μm). In the experiment A (water/mineral oil) reported in Figure 5.5a), the water thread breaks into drops which adopt immediately a steady shape until they exit the main channel. The Figure 5.5b) shows that in the experience E, once the droplets of sodium hydroxide surrounded by oleic acid are produced, the drops experiment a deformation that can be separated in three regimes. In the first regime, the drops get elongated in the flow direction. Then the length stabilizes and

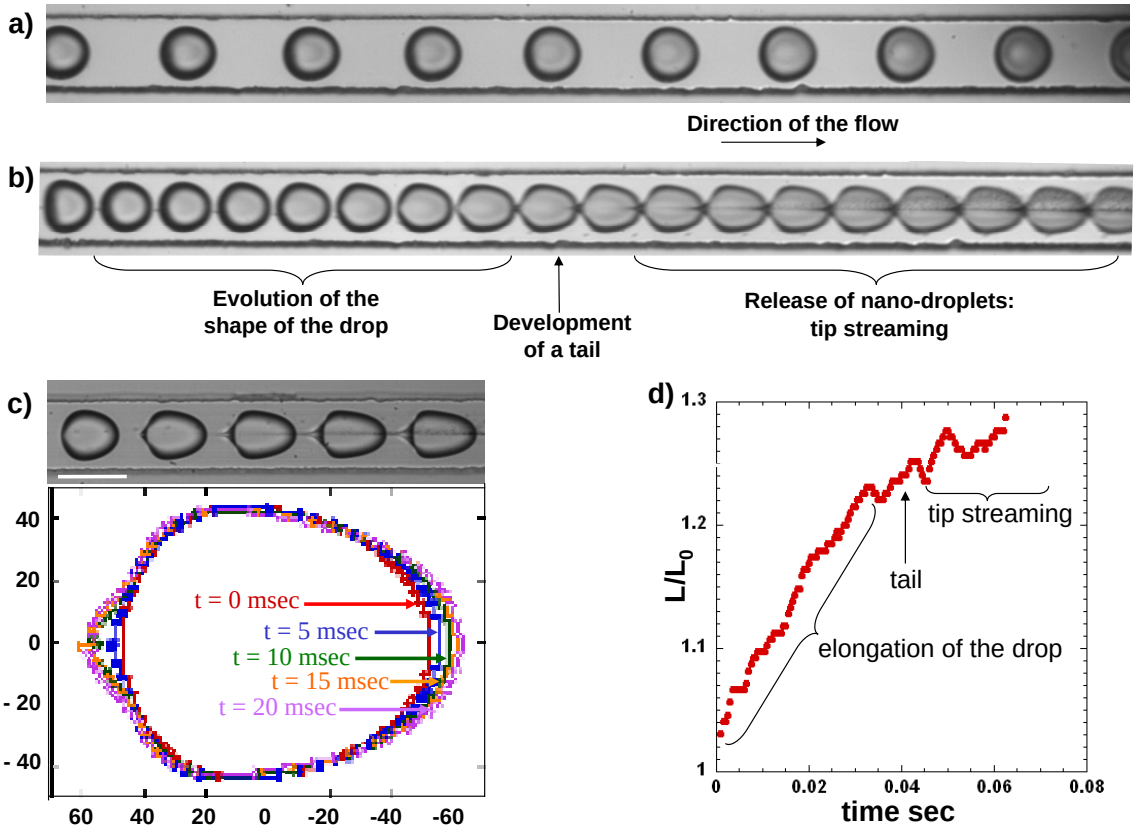

Figure 5.5: *a) Series of water droplet, dispersed in mineral oil, flowing in a channel with 100×75 μm^2 in cross section. The oil solution and the water are pushed at 10 and 5 Psi, respectively. b) A series of drops of 7.5 mM of sodium hydroxide dispersed in 7.5 mM of oleic acid. P_o=10 Psi and P_w=10 Psi. c) Evolution of the drop length L (in the flow direction) normalized by the initial length L_0 as a function of time. d) Drops of 5 mM NaOH dispersed in 5 mM oleic acid flowing in a device with a cross section of 100×50 μm^2. Shape evolution of one drop every 5 msec.*

the droplets develop a "tail-like" structure; finally the third regime consists in the ejection of tiny droplets (sort of black cloud in the figure) from the rear of the main drops. This phenomenon is called tip-streaming.

Two control experiments are realized in order to verify that the deformation undergone by the drops are not due simply to the presence of oleic acid or sodium hydroxide molecules. In the experiment B (water/10 mM oleic acid), the droplets behave exactly like water drops in pure mineral oil: no deformation and no tip-streaming are observed. This result rules out the possibility that only the presence of oleic acid can trigger the behavior observed with the production of surfactant. In the same way, the droplets of the experiment C (10 mM sodium hydroxide/mineral oil) adopt a steady shape right after their production. These results confirm that the deformation observed in Figure 5.5b) is due to the presence of surfactant at the interface of the drop combined with the specific flow in this geometry.

In Figure 5.5c), we reconstruct the evolution of the drop shape as a function of time for a system of 5 mM NaOH/5 mM Oleic acid. We note that the drop gets elongated in the flow direction

without changing its width. We can also remark that the back of the drop get more and more "pointed" which is the development of the precursor of the tail. In order to characterize the deformation undergone by the drop, we study the evolution of its length L in the flow direction normalized by the initial size L_0, after its detachment from the aqueous thread, as a function of time. The results are presented in Figure 5.5d); we retrieve the three regimes observed: first the linear increase of the quantity L/L_0 corresponds to the stretching of the droplet. Then the drop length stabilizes around 0.045 sec. This change in the slope corresponds roughly to the appearance of the tail (around 0.04 sec). The plateau indicates the establishment of a steady shape which correspond to the tip-streaming regime. We can define a typical time τ necessary for the drop to establish a steady shape.

5.2.1 Interpretation

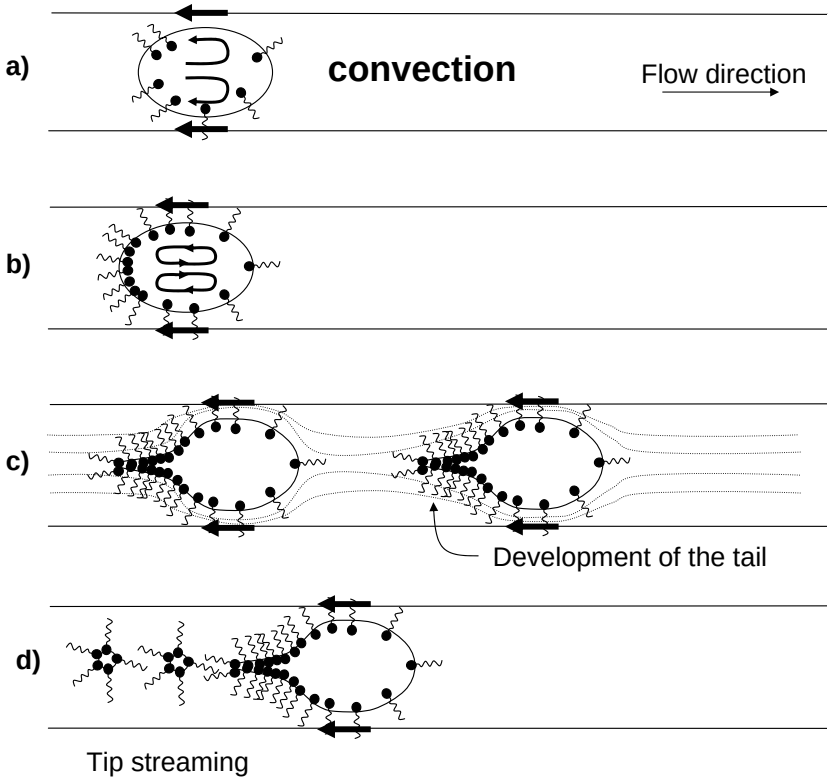

Figure 5.6: *a) In the reference frame of the drop's center of mass, the walls are moving from the front to the back of the object inducing some convection inside the drop. b) The surfactant molecules are driven from the front to the back, leading to a gradient of surface tension on the interface. c) The very low surface tension at the back of the drop, associated with the flow between two following droplets, induces the formation of a tail. The dashed lines represent the flow lines. d) The accumulation of surfactant molecules at the tail, decreases the surface tension enough to allow the detachment of sub-micron droplets. This phenomenon is called tip-streaming.*

We explain this behavior as a direct effect of the presence of surfactant molecules at the interface. The resulting decrease of the surface tension of the droplet induces a deformation of the drop (Fig. 5.6a)). The elongation of the droplet slows down and stops when the equilibrium with the external stress is reached. Because the drop is flowing in the channel, a circulation

establishes inside the object and drives the surfactant from the front to the back, at the interface of the droplet. A gradient of surfactant concentration along the interface results from the convection (Fig. 5.6b)). When the concentration of surfactant, which build up at the back of the drop, reaches a critical value, the sufficiently low surface tension, associated with the circulation between two following drops, allows the stretching of a thin film of liquid from the back of the drop similar to a "tail" (Fig. 5.6c)). More surfactant is brought to the tip of the tail, leading to another decrease of the surface tension; the droplet releases the excess of surfactant by detaching very small droplets of aqueous solution which we assume are covered with sodium oleate molecules: this is the tip-streaming phenomenon (Fig. 5.6d)).

We now study the effect of the different parameters of the problem on the typical time necessary for the drop to adopt a steady shape, and their influence on the equilibrium shape. Among them, we will develop the effect of the surfactant concentration, the drop size and the device geometry.

5.3 Effect of surfactant concentration

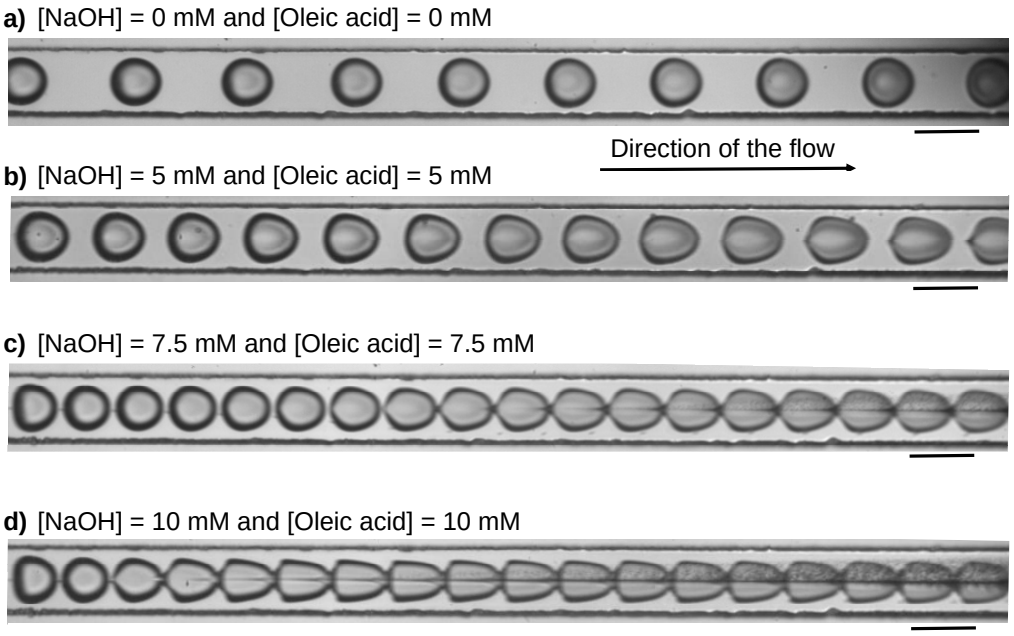

Figure 5.7: *Effect of surfactant concentration on the time to establish a steady shape. Four series of droplets with different reagent concentrations. The channel dimensions are w=100 μm and h=75μm. The black lines represent 100 μm.*

We now investigate the effect of the surfactant concentration on the time necessary for the object to establish a steady shape. In Figure 5.7, we show four series of droplets with increasing concentration of reagent, i.e. with increasing surfactant concentration produced as a function of time. We clearly see in the pictures that, as the concentration of the reagents is increased, the tail appearance happens faster. In Figure 5.7a) corresponding to the experiment A, no tails are developed because there is no surfactant production. In the experiment D (Fig. 5.7b)) the tail starts to develop shortly before the exit of the main channel. By increasing the concentration

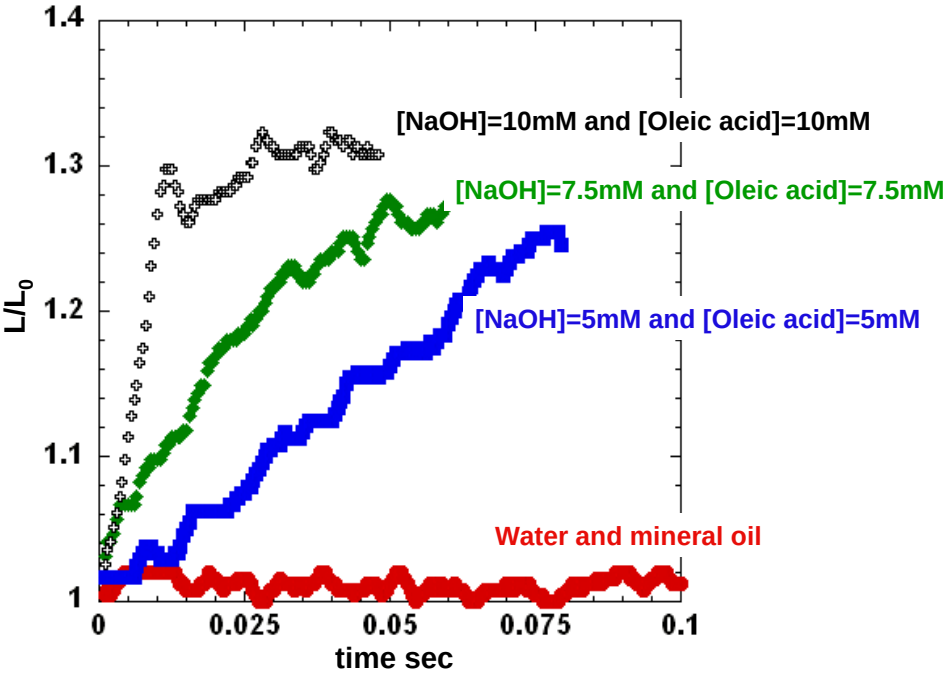

Figure 5.8: *Evolution of the dimension L of the drop, normalized by the initial length L_0, as a function of time for four different surfactant concentration. P_o=10 Psi and P_w=5 Psi.*

to 7.5 mM (experiment E), we see that the tail is fully developed around half the distance from the exit, while the high concentration droplets from experiment F forms a tail at the rear right after the droplet production.

This acceleration of the deformation can be quantified by measuring the evolution of the drop length L/L_0 as the surfactant concentration is increased as shown in Figure 5.8. The plateau, indicator of the establishment of a steady shape of the drop, is reached around 150 msec for the system of experiment F, at 400 msec for experiment E, and at a time superior than 750 msec in the case of experiment D. As the surfactant is produced, the drops become more deformable and adapt their shape to the external stresses faster.

Remark

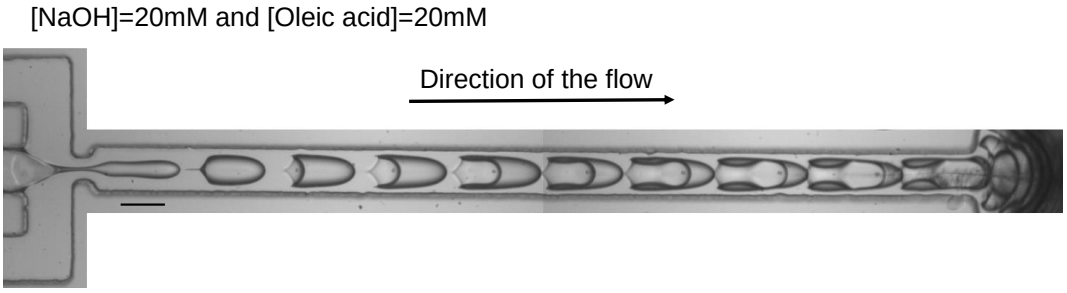

Figure 5.9: *Drops deformation for high surfactant concentration. P_o=5 Psi and P_w=2 Psi. The black line represents 100 µm. The height of the channel is 30 µm and the width if the main channel is 100 µm.*

If the reagent concentration is too high (i.e. experiment G), the large presence of ions modify the wetting properties of the PDMS channel's walls. The resultant effect is shown in Figure 5.9. We also see that the droplets deforms much more than with the low concentrations. It seems that the oil phase is "digging" in the aqueous drop which starts to develop the bullet-like shape specific to the RBCs. Further in the channel, the droplet's shape deforms into a "horseshoe".

5.3.1 Effect of drop size compared to channel size

The equilibrium shape assumed by the drops depends on the relative size of the drop compared to the channel size, which have a rectangular cross-section in our experiments. Indeed, we present in Figure 5.10 different final shapes of droplets from experiment D, in a channel with a width w=100 μm and a depth h=50 μm.

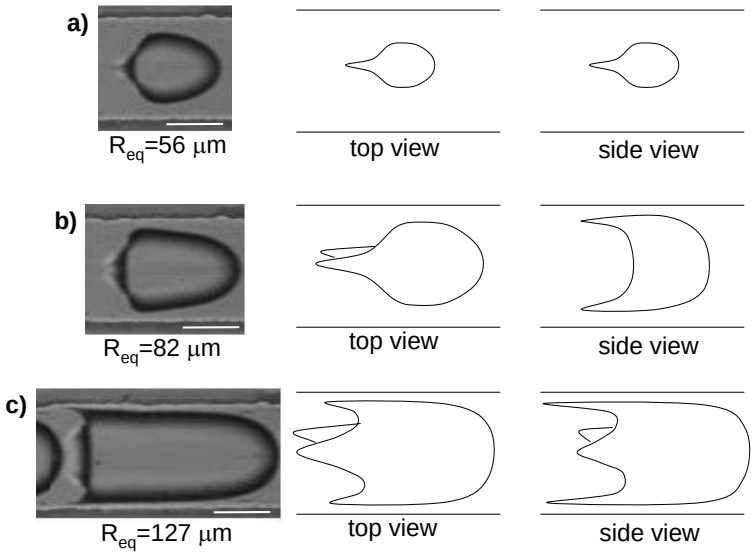

Figure 5.10: *Experimental pictures and schematic interpretation in top and side views of the number of "tails". [Oleic acid]=5 mM [NaOH]=5 mM, a) P_o=7.5 Psi and P_w=3 Psi, b) P_o=7.5 Psi and P_w=3.5 Psi and c) P_o=7.5 Psi and P_w=4.5 Psi. The white lines represent 50 μm.*

When the equivalent radius $R_{eq} = 56\mu$m, defined as the radius of the sphere of same volume as the axisymmetric drop, is smaller than w and h ($R_{eq} \ll w$ and h), the drop develops a tail at the rear and assumes a axisymmetric tear-like shape as represented in Figure 5.10a). For a bigger drop, where $R_{eq} = 80 \approx h$ but $R_{eq} \ll w$, two tails are preferentially developed at the closest wall, in our case the upper and lower walls (see Figure 5.10b)). We note that the shape of the droplet with two tails is similar with the bullet-like shape of RBC's flowing in a capillary (see Chapter 7) The Figure 5.10c) shows a droplet with a R_{eq}=127 μm (i.e. $R_{eq} \approx w$ and h) with four tails. The two tails closer from the upper and lower walls are bigger than the two other ones. This results suggest that the stress due to the presence of the walls plays an key role in the development of the tail. Therefore, the tails at the closest wall are longer than the two other ones.

5.4 Reaction time versus convection time

In order to discriminate the contribution of the reaction time (kinetics of the reaction) and the convection time (the diffusion time being too long to dominate the time scale of the phenomenon) from the typical time τ necessary to assume a steady shape, we compare two experiments: in the first case, experiment F, the sodium hydroxide molecules react with the oleic acid and produce in situ at the interface, some surfactant; in the experiment J, the surfactant is first produced, in a vial and introduced inside the droplet in pure mineral oil. Such experiments are presented in Figure 5.11.

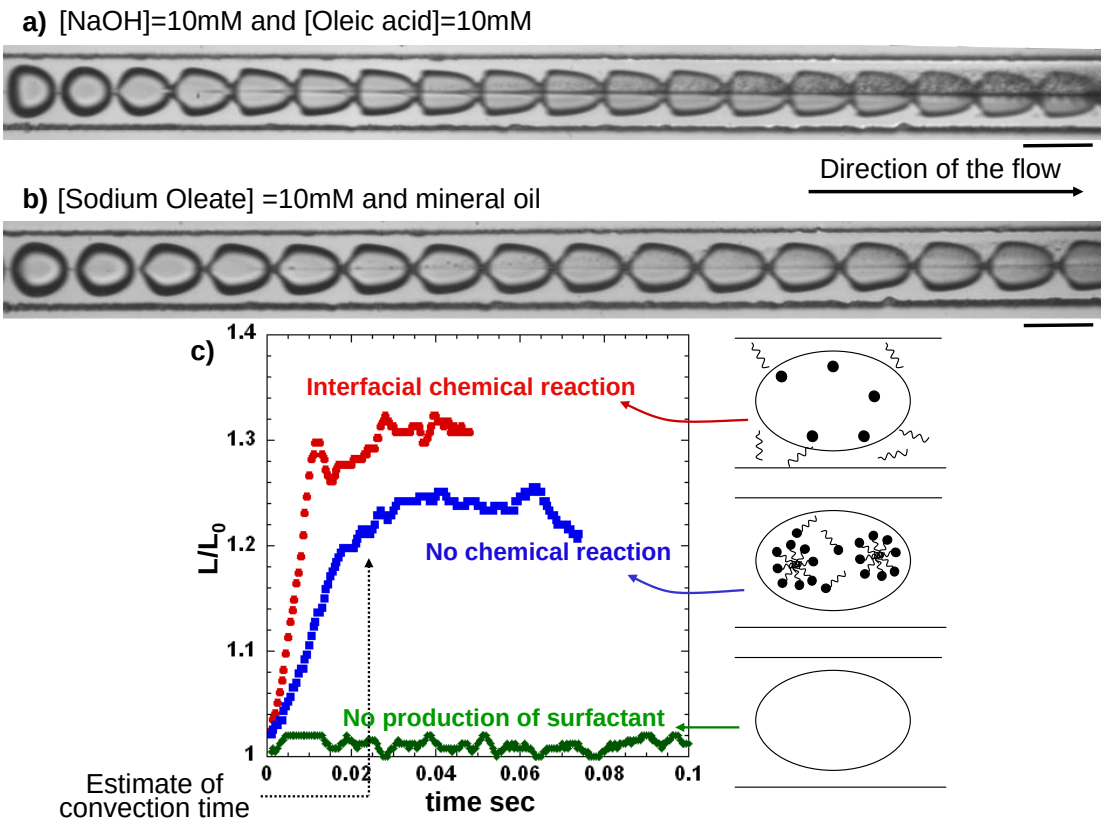

Figure 5.11: *Comparison between a) oleic acid/sodium hydroxide and b) mineral oil/sodium oleate experiments. The parameters are the same: [Oleic acid]=5 mM [NaOH]=5 mM, [Sodium oleate]=5 mM, P_o=10 Psi and P_w=5 Psi. The black lines represent 100 µm. c) Evolution of the non-dimensionalized length of the drop L/L_0 versus time for 3 different systems: oleic acid/sodium hydroxide, mineral oil/sodium oleate and mineral oil/water.*

Figure 5.11a) show the deformation of a series of droplets during the production of surfactant. We retrieve the three regimes described earlier: elongation, development of the tail, and tip-streaming. The same behavior is observed in the case of a drop containing the surfactant in pure mineral oil (see Fig. 5.11b)). The two experiments are quantitatively compared by the study of the parameter L/L_0 as a function of time. The graph in Figure 5.11c) shows that the typical time necessary to reach a steady shape for the 10 mM sodium oleate droplet is approximately 0.025 sec. We estimate the convection time t_{conv}, from the typical size of the droplet R_{eq} and its speed v, to be $t_{conv} = R_{eq}/v$=0.022 sec. We conclude that in the oleate experiment (oleate

in the drop in oil), the motion of the molecules at the interface is governed by the convection time. We measure the time τ to reach the equilibrium shape for the chemical reaction at the interface to be 0.012 sec. It appears that the steady shape occurs much faster with the chemical reaction than in the case with the convection. One explanation to this result, could be that the surfactant is forming micelles, in the sodium oleate droplet, because we are above the CMC. We would need to evaluate the typical time scale necessary for the micelles to dissociate and take this into account in our estimations.

5.5 Effect of the geometry

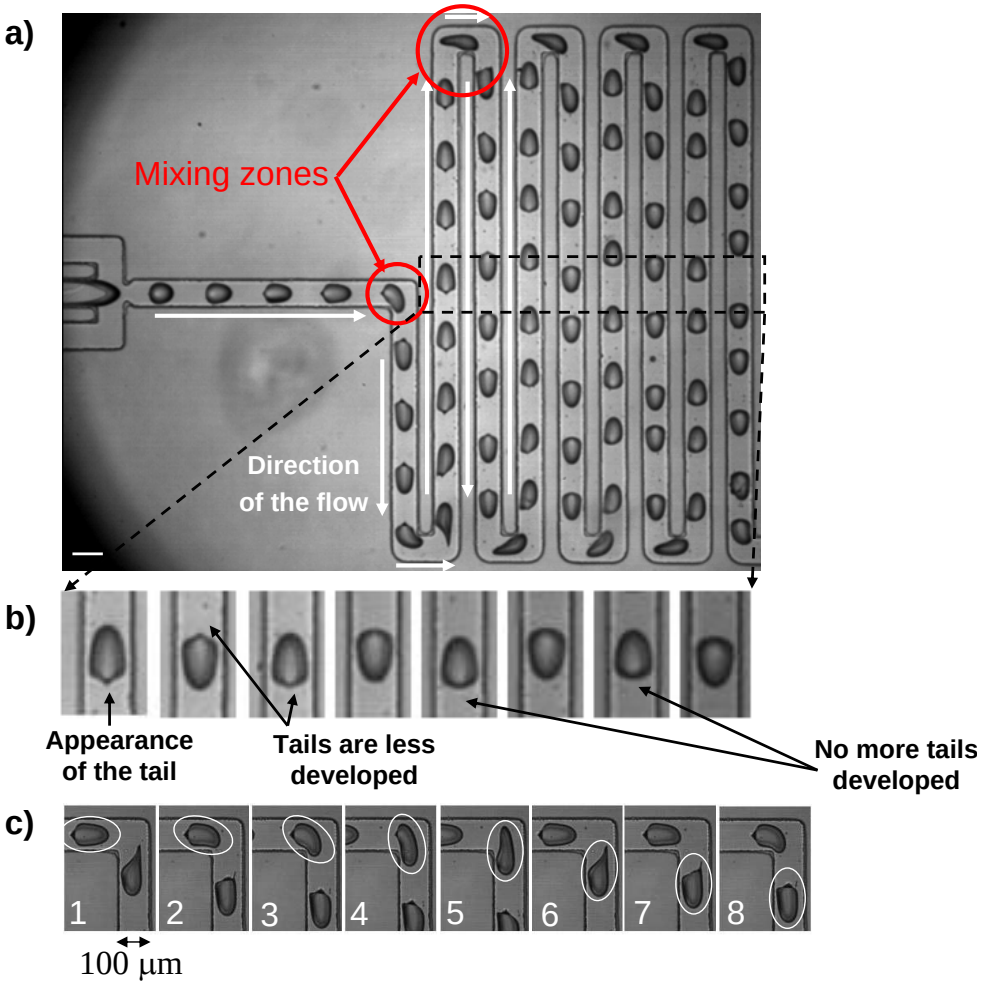

Figure 5.12: *Effect of the specific geometry on the tail appearance and desappearance. The system studied is 5 mM Oleic acid/5 mM NaOH. a) A series of droplets is going through a succession of 180° corners. b) Shapes of a drop flowing in the successive linear parts of the channel. As the drop is flowing further, the tail disappears progressively. The width of the channel is 100 µm. c) Deformation and mixing of a drop flowing through a 90° corner.*

We now investigate the effect of the geometry on the establishment of a steady shape by introducing a snake-like geometry after the flow focusing. The succession of 180° corners affects the

circulation flow as well as the total residence time of the drops in the device. The new geometry is shown in Figure 5.12, and the behavior of drops of 5 mM sodium hydroxide in 5 mM oleic acid is studied. We first see in Figure 5.12a) two of the three regimes previously described: elongation and development of a tail; the tip-streaming phenomenon is not detectable because of the low magnification chosen for the experiment. If we compare the shape of the drop in each linear section of the device, reported in Fig. 5.12b), we note that as we go further in the device, the tails gets less and less developed at the rear of the drops.

We interpret this behavior in terms of the total chemical reaction. Indeed, new surfactant molecules are produced due to the chemical reaction, and supply continuously the rear of the object despite of the ejection of the excess of surfactant by the tip-streaming phenomenon. Once the chemical reaction is complete - meaning that all the oleic acid has reacted with the available sodium hydroxide in the dispersed phase - no more surfactant molecules are produced and driven to the back of the drop by the circulation leading to a decrease of the surfactant concentration at the tail. As this sodium oleate concentration drops below the critical values, the surface tension becomes too large to allow the deformation at the rear of the object.

A closer look at the behavior of a drop at one of the corners is presented in Figure 5.12c). A drop of 5 mM NaOH suspended in 5 mM oleic acid is flowing through a 90^o corner. In (1) and (2), the circulation inside the droplet is from left to right, bringing all the produced surfactant at the rear of the droplet. As described in section 3.2.1, the corner adds an additional shear to the uniform flow and the mixing of the droplet occurs, (3), (4) and (5). It results from this shear, the re-initialization of the gradient of concentration of sodium oleate at the drop interface. The surface tension of the drop tends to become uniform on the whole surface of the drop, making the tail disappear. Further in the channel, (6), (7) and (8), the drop adopts a new internal circulation from bottom to top. It will be necessary to wait for the drop to flow through a longer straight part of the channel in order to re-construct the gradient of surfactant concentration, and consequently to develop a new tail.

5.6 Conclusion

In these experiments, we describe an specific behavior in a droplet in the presence of a chemical reaction which produces an insoluble surfactant in situ at the interface. We observe three distinct regimes: the elongation of the drop, the development of a tail at the rear of the object and the tip-streaming process. The production of surfactant, due to the interfacial chemical reaction, increases the deformability of the droplets and induces a deformation specific to the geometry and the corresponding flow. A typical time scale τ for the evolution of the drops shape can be defined. We showed that τ decreases with increasing reagents concentration. The results also show that the equilibrium shape is strongly dependent on the relative size of the drop compared to the size of the channel. The establishment of the steady shape happens faster when the chemical reaction occurs than when the surfactant is dispersed in the volume of the drop. Finally, the mixing induced by the flow through multiple corners accelerates the total reaction.

Chapter 6

Responsive visco-elastic vesicles

La fabrication et l'étude sous contraintes externes de vésicules, aux propriétées visco-élastiques - dites "complexes" - modulables par une modification de la température, sont détaillées dans ce chapitre. Dans un premier temps, nous indiquons le processus de fabrication de vésicules lipidiques géantes encapsulant une solution de polymère ou un gel covalent de PolyNIPAm; nous développons l'effet de l'action de la température sur ces vésicules renforcées. Dans un second temps, nous étudions le comportement de vésicules DMPC, en phase fluide et en phase gel, sous écoulement de cisaillement près d'une paroi.

The lipid bilayer membrane of vesicles exhibits basic properties of biological membranes [106, 101]. However, their poor mechanical properties due to the absence of cytoplasm and cytoskeleton, limit their relevance as minimal models for living cells. Therefore, the increase of the complexity of the mechanical properties of liposomes is a unavoidable step. Therefore, composite objects with functionalized surfaces and mechanical properties responsive to external parameters are the new challenges the scientists are working on. Our objective was to prepare viscoelastic giant lipid vesicles with controlled and responsive mechanical properties triggered by an external parameter (pH, electrochemical potential, temperature...). Such systems could for instance release material or move by themselves in successive contraction/extension stages. We chose two different systems to study: the first one, a polymer solution or a covalent gel of PolyNIPAm enclosed in the vesicle ensures 3D viscoelastic properties to the lipid envelope. In the second system, giant vesicles made of DMPC express either a fluid, either a gel behavior of the membrane whether the temperature is above or below the transition temperature.

6.1 Responsive vesicles enclosing PolyNIPAm solution or covalent gels [54]

Apart studies concerning gel beads coated with lipids [63, 87, 92, 161, 75, 36, 90], lipid vesicles were mainly combined with physical gels, used as external coating (rigid actin filaments [78]) or internalized in the vesicle volume (rigid actin networks [74, 100], agarose gels [153], solutions of aggregated Poly(N-isopropylacrylamide) (PolyNipam) [86]). A recent work dealt with controlled covalent PolyNipam gels but concerned submicronic liposomes [143, 142]. Previous works in the laboratory report the difficulty to enclose long chains of polymer such as Dextran [104] in the vesicles. The strategy we chose to adopt is the encapsulation of the reagents in the

vesicle during its formation and then to initiate the polymerization inside. We present here the preparation of such vesicles, the first characterization and their responsive behavior when exposed to temperature.

6.1.1 Volume phase transition of PolyNIPAm

The well known phase transition of PolyNIPAm gels occurs around 33°C and as been abundantly studied during the last 20 years [81, 147, 148, 82, 132, 160, 146, 105]. When external condition such as temperature, solvent composition or osmotic pressure are changed, the gel reversibly swells or shrinks but does so discontinuously as presented in Figure 6.1 [81]. The volume change at the transition depends on both the degree of ionization and the elasticity of constituent polymer chains, and can be as large as 1000 times [149]. Several theoretical and experimental studies have been performed on the kinetics of the volume phase transition of a gel.

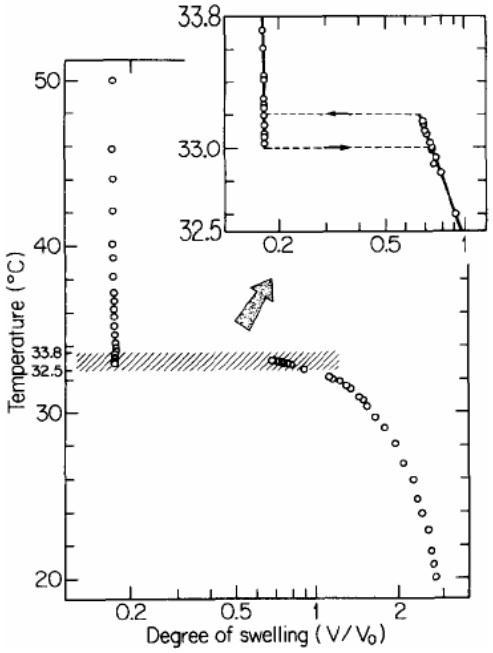

Figure 6.1: *The degree of swelling of a NIPAm gel in pure water is plotted versus temperature. The curve on the right is an expanded graph in which the hysteresis of the discontinuous volume transition can be observed [81].*

In 1979, Tanaka and Fillmore [148] presented a theory of the kinetics of the swelling of a gel. The characteristic time of swelling τ is found to be proportional to the square of the size d of the gel and is also proportional to the diffusion coefficient of the gel network D:

$$\tau = \frac{d^2}{D}, \tag{6.1}$$

where $D = \frac{K+4\mu/3}{f}$, K and μ, being the shear modulus of the bulk and the polymer network alone respectively and f the friction coefficient between the network and the fluid medium. Such theoretical model was applied to describe the swelling of spherical 5% Polyacrilamide gels, and a good agreement [148] was found between the diffusion coefficient D experimental measured and the one calculated by Tanaka and Fillmore.

6.1.2 Solutions and preparation

Pregel solutions

The giant vesicles were made of DOPC purchased from Sigma. The monomer, N-isopropylacrylamide (NIPAm), intended to constitute the polymer/gel and the photoinitiator, 2,2-diethoxyacetophenone (DEAP), were purchased from Acros Organics. The crosslinker, necessary to the formation of the covalent gel, N,N'-methylen-bis-acrylamide (MBA), was purchased from Sigma. The chemical formulas of the different products are shown Figure 6.2. The vesicles were prepared by the standard method of electroformation [16] for 6 hours. The solution to be encapsulated by the vesicles, which we refer to as pregel solution, is composed of 100 mM sucrose, 300 mM NIPAm, 0mM, 3 mM or 9 mM MBA (according to whether we want the polymer solution or a elastic gel) and 1 μL.mL^{-1} DEAP.

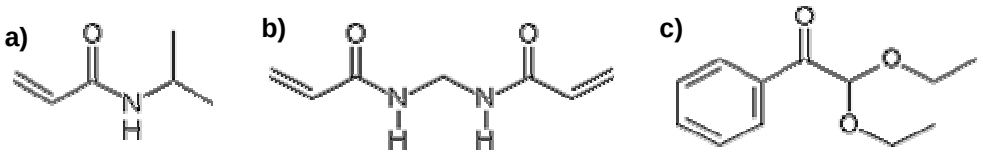

Figure 6.2: *Chemical formulas of the different reagents: a) NIPAm, b) MBA, c) DEAP.*

Photopolymerization

After the electroformation, a concentrated suspension of vesicles enclosing (and suspended in) the pregel medium was obtained. The photopolymerization of the polymer-filled vesicles didn't require any special procedures regarding the external media. At this time of the experiment, the challenge was to be able to form the PolyNIPAm gel inside without trapping the vesicles in the external media. Indeed, the photoirradiation of this raw suspension would lead to the formation of a bulk macroscopic gel entrapping gel-filled vesicles. It was therefore necessary to change the external solution to avoid its gelation. The simplest idea was to dilute the suspension of vesicles in a large excess of water to lower the crosslink concentration below the critical gelation concentration. However, NIPAm, MBA and DEAP are able to diffuse through the membrane and, consequently, external dilution would result in emptying the vesicles from reagents due to osmotic forces. Moreover, we observed that when a strong gradient (roughly 0.1 M) of NIPAm concentration was applied between the inner and the outer part of a vesicle, its membrane often became unstable and broke. Therefore, we ensured the same initial NIPAm concentration inside and outside the vesicles and we used two different protocols to prevent gelation outside the vesicles.

The first protocol consisted in limiting external polymerization by adding Cu^{2+} copper ions in the outer solution, which has the effect to chelate NIPAm monomers and crosslinks. We injected a small volume of the concentrated suspension of vesicles (containing 100 mM sucrose, 300 mM NIPAm, 3 mM MBA and 1 μL.mL^{-1}) DEAP and a drop of aqueous solution of $CuNO_3$ in a small plexiglass tank beforehand filled with a solution of 100 mM glucose, 300 mM NIPAm, 3 mM MBA and 1 μL.mL^{-1} DEAP. The resulting concentration in Cu^{2+} was equal to 10 mM. Chelation of NIPAm monomers in the outer solution partially inhibited polymerization [138].

In the second set-up, no crosslinker was introduced in the external medium in order to avoid gelation outside of the vesicles. It was expected that the diffusion of crosslinking molecules outside of the vesicles, through the membrane, was slow enough to allow internal gelation. We electroformed vesicles using different solutions: a solution containing 100 mM sucrose, 300 mM NIPAm, either 3 mM or 9 mM MBA and 1 μL.mL^{-1} DEAP. Then, we injected a small volume of each concentrated suspension of vesicles in small plexiglass tanks filled with a solution of 100 mM glucose, 300 mM NIPAm, 1 μL.mL^{-1} DEAP and which did not contain the crosslink (MBA).

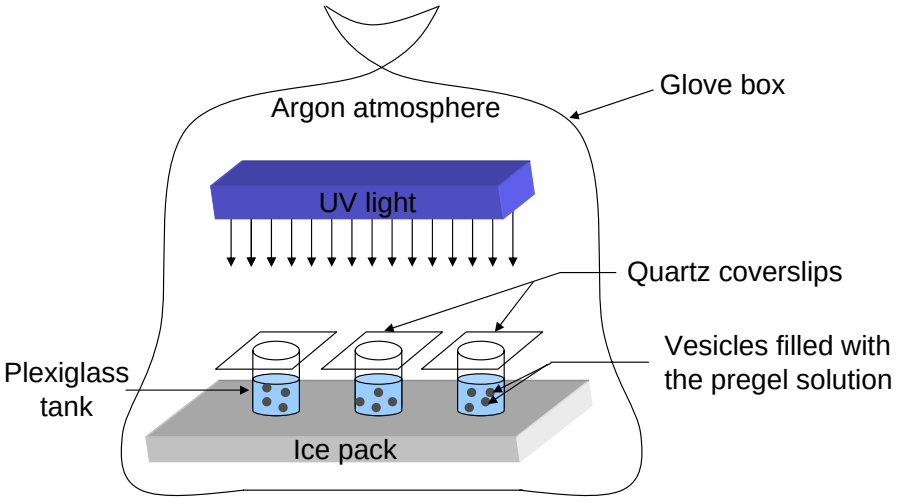

Figure 6.3: *Schematic of the polymerization set-up.*

Finally, as shown in Figure 6.3, the Plexiglass tanks were covered by quartz coverslips and were placed over an ice pack (Medicool coolpack MC-15) in order to maintain a temperature lower than the temperature of transition of PolyNIPAm to ensure an homogeneous reaction (the reaction being exothermic). UV irradiation was performed for one hour using a UV lamp (UV-B Mid-range 300nm Sunlight-Erythemal AH 68-1091 F6T5E, Harvard Apparatus,). All solutions were first deoxygenated by bubbling with dry argon for 30 minutes and all manipulations were performed in a glove bag under argon atmosphere (oxygen is a strong poison for polymerization). Once transformed into PolyNIPAm polymer or gel, the vesicle can be manipulated without particular precautions in regard with the oxygen. After illumination the tanks were stored at 5^{o}C. Small amounts of the resulting medium were then withdrawn from the tanks, were diluted into observation chambers filled with a 0.1 M glucose solution, and were observed using the phase-contrast microscope.

The protocol selected for the rest of the experiment is the second one, without crosslinker in the outer solution. It is much simpler than the other and has been verified to be reproducible and is now very well developed.

6.1.3 Characterization of vesicles enclosing a polymer solution

The polymeric nature of the inner vesicle volume was characterized after breakage of the membrane upon injection of a detergent (commercial name Decon90, Prolabo, France) close to the vesicle. The behavior of a polymer sol filled-vesicle is illustrated in Figure 6.4a, b, c. Upon Decon

injection, the membrane of the vesicle (initial state, Fig. 6.4a) breaks and the inner polymer solution progressively vanishes, since it is fully soluble (Figure 6.4b-6.4c).

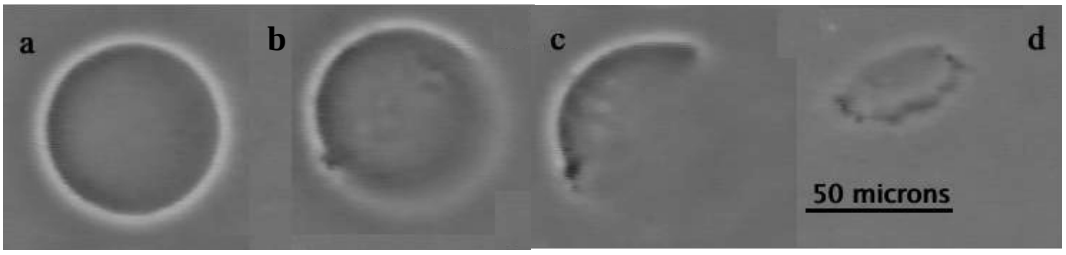

Figure 6.4: *Dissolution of the polymer solution after destruction of the lipid membrane.*

PolyNIPAm solutions are known to exhibit a reversible microphase separation which is triggered by the temperature upon crossing the lower critical solution temperature (T=32^{o}C in water and lower in the presence of sucrose). Indeed, micro-phase separation upon heating with formation of large aggregates in the inner volume of linear PolyNIPAm-filled vesicles is observed, as shown and recently reported by Jesorka et al [86]. When heated at 40^{o}C, the internal volume of the vesicles becomes heterogeneous, as shown in Figure 6.5a and 6.5b, which indicates a micro-phase separation attributed to the collapse of polyNIPAm chains. After accidental rupture of the membrane of the vesicle which is displayed in Fig. 6.5, we observe the leakage and the dispersion of collapsed polymer chains in the observation chamber (Fig. 6.5c).

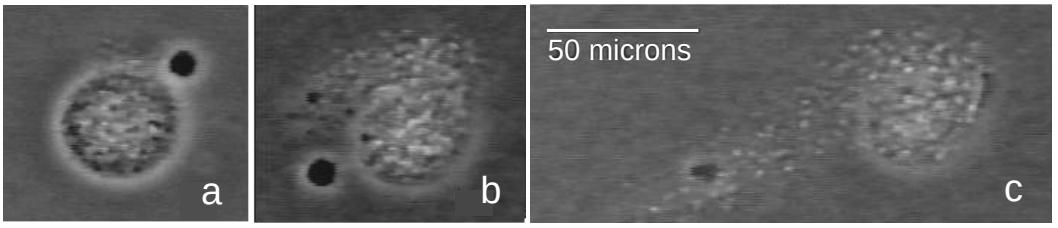

Figure 6.5: *Microphase separation of the PolyNIPAm solution above 32^{o}C.*

6.1.4 Characterization of vesicles enclosing a covalent gel

The detergent experiment performed on gel-filled vesicles is illustrated in Figure 6.6. The initial vesicle is shown in Figure 6.6a. The progressive destabilization and breakage of the lipid membrane is clearly observed upon Decon injection (Fig 6.6b, c, d). Contrary to the previous observations with the polymer-filled vesicle, the inner volume of the vesicle does not vanish; it retains its initial quasi-spherical shape and dramatically shrinks (Fig. 6.6b), thus revealing the presence of a 3D network. Shrinkage occurs after the breakage of the membrane, when the polyNIPAm gel comes into contact with Decon, which is a poor solvent for PolyNIPAm. The Decon was then diluted at the vicinity of the observed vesicle by addition of 100 mM glucose solution. During this fast dilution, the gel re-swells and maintains its initial quasi-spherical shape with a small irregularity on the right side (fig. 6.6c). Its final size is much greater than the initial vesicle size (the gel volume has increased by a factor roughly 3.5), i.e. its swelling ratio has increased. The large increase of the surface area of the gel during its final overswelling

stage confirms that the vesicle membrane has broken upon Decon addition, since lipid vesicles have a constant surface area.

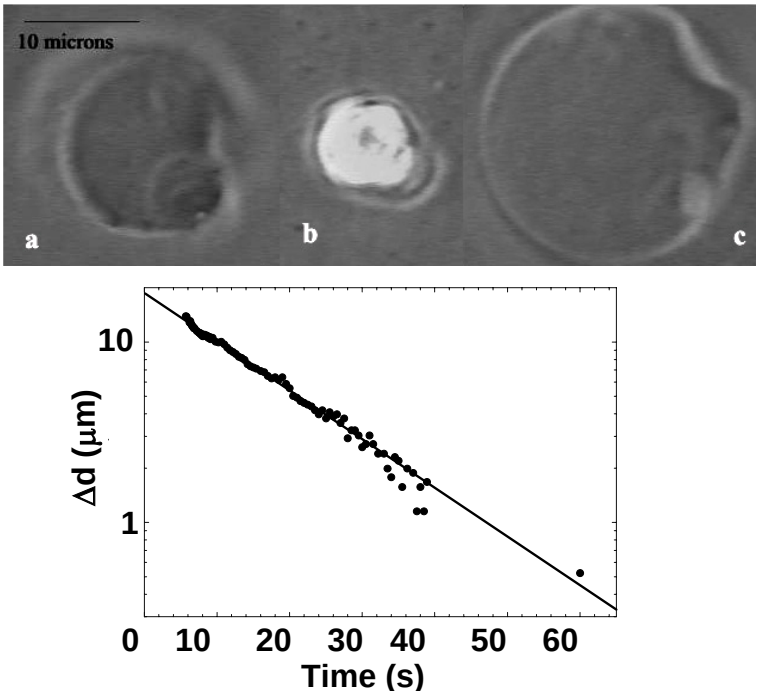

Figure 6.6: *a) After the destruction of the lipid membrane, the gel overswells. b) Kinetics of gel swelling from (b) to (c): variation of the gel diameter versus time.*

We propose a first characterization of the gel which fills the vesicle presented in Fig. 6.6a by studying its kinetics of re-swelling, starting from its shrunken state in presence of Decon until its final swollen state after dilution of Decon in glucose solution. We consider that Decon dilution in the vicinity of the gel is fast so that the kinetics of gel swelling is limited by water diffusion within the gel. In Fig. 6.6b, we plot the measured difference between the final diameter d_f of the gel sphere, and the diameter d at time t: $\Delta d = d_f - d(t)$, as a function of time in a semi-log scale. The time just before dilution of Decon (shrunken state) is taken to be zero. The semilog results exhibit a linear decrease which is in good agreement with Tanaka's model for gel swelling, which predicts a single exponential behavior after decay of higher order terms of the Fourier series solution of the diffusion equation for swelling [148]. Following Tanaka, it is possible to estimate the order of magnitude of the collective diffusion coefficient of the gel network, D, from the value of the decay time, τ: $\tau = \frac{d_f^2}{4D}$. We find τ=16 s, which yields $D \approx 10^{-7}$ cm^2.s^{-1}. This value is in agreement with that recently reported for similar gels ($4.3\text{x}10^{-7}$ cm^2.s^{-1}) by Laszlo et al [97]. Complementary experiment with a fluorescent probe introduce in the membrane have been performed [54] in order to demonstrated the presence or the absence of the lipid by-layer.

6.1.5 Temperature-induced phase transition

More interesting than the polymer-filler vesicles is the behavior of gel-filled vesicles. Figure 6.7 depicts selected time frames from movies that show the typical size changes induced by a cycle of temperature (25^{o}C-40^{o}C-25^{o}C) of three gel-filled vesicles. Above the transition temperature,

vesicles contract rapidly (Fig. 6.7a and b) while retaining their spherical shape. They reach a stationary size when the temperature is maintained at 40^{o}C (fig. 6.7c). Finally, when the temperature is lowered back to 25^{o}C, vesicles re-swell and retrieve their initial size (Fig. 6.7d).

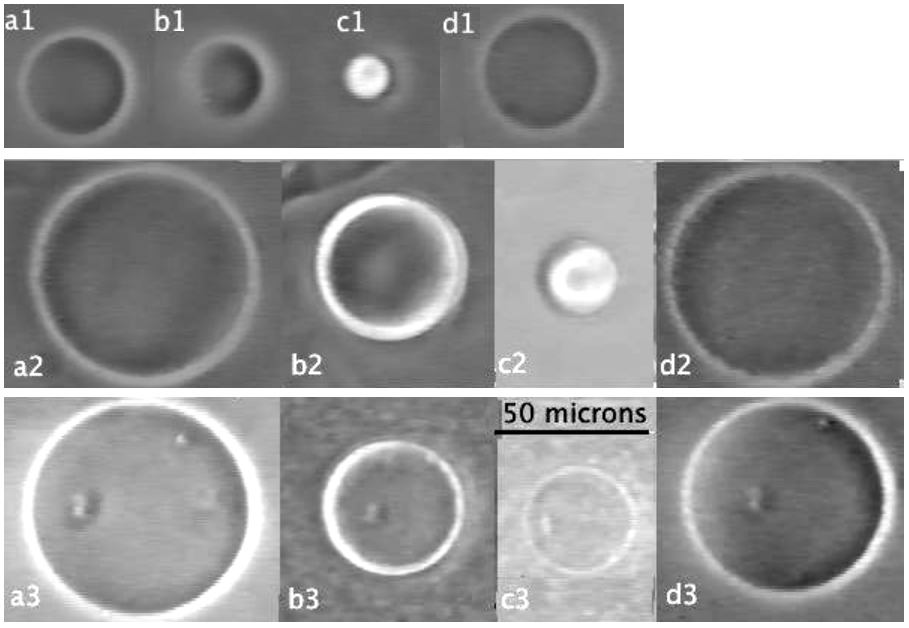

Figure 6.7: *Phase transition of gel-filled vesicles induced by temperature changes.*

The same experiment has been repeated on fluorescent vesicles containing rhodamine [29]. It is clearly seen that the membrane is not destroyed during both gel contraction and expansion stages. It also indicates that the membrane is coupled to the gel during the volume transition and is believed to crumple onto the surface. The mechanisms of crumpling and the origin of PolyNipam-lipid interactions have still to be studied.

6.1.6 To conclude

The fabrication of giant lipid vesicles with specific mechanical properties responsive to an external stimulation, the temperature, was our first goal. We proved here that we managed to produce giant vesicles with a solution of polymer or a covalent gel enclosed. In the future, we need to study the mechanical properties of such objects and to look at their behavior under flow. This aspect is currently under investigation in our laboratory. Indeed, one of the purposes of the PhD of Clément Campillo [29] is to measure by micropipette aspiration mechanical properties of these objects and to study the coupling of the membrane with the Poly-NIPAm.

6.2 Effect of temperature on the dynamics of DMPC vesicles

The DMPC is known to undergo a phase transition at 23,4^{o}C and to exhibit distinctive mechanical properties while in the gel state [40, 50, 112, 113]. But the influence of theses specific mechanical properties on the response of DMPC gel vesicles under stress is still to be investigated. Here we propose the study of DMPC vesicles under osmotic pressure and under flow under and at the transition temperature.

6.2.1 Vesicle preparation

It is important to electroform the DMPC (purchased from Avanti Polar Lipids) vesicles when the lipid is in the fluid phase. Indeed, the electroformation lasted for two hours at a controlled temperature of 30^{o}C, which is above the phase transition in 100 mM sucrose. After their formation, the vesicles are withdrawn from the electroformation chamber and the temperature is decreased below the critical temperature. Once the lipid membrane is in gel phase, the vesicles are stored in the fridge at 4^{o}C.

6.2.2 Deflation of vesicles in the gel phase

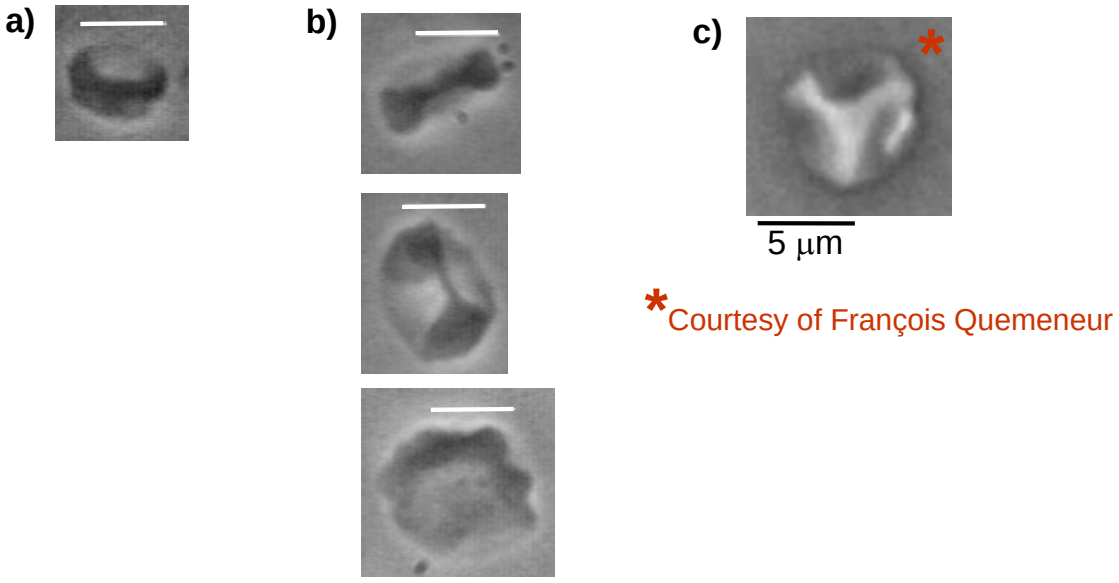

Figure 6.8: *Shapes of DMPC vesicles obtained by osmotic shocks with an external solution of: a) 200 mM glucose and b) 250 mM glucose. The white lines represent 10 µm. c)Deflated vesicle enclosing a solution of 150 mM sucrose suspended in a solution of 430 mM glucose, which correspond to a reduced volume ν of 0.35.*

We first investigate the effect of the high viscosity of the membrane on the deflation of vesicles in the gel phase, by osmotic pressure. To apply an osmotic shock, the vesicles are injected in two different solutions of glucose: 200 mM and 250 mM - equivalent to a reduced volume (volume of the object/volume of the sphere with the same surface area as the object) of 0.5 and 0.4 respectively - while the temperature is maintained at 10^{o}C. The typical shapes observed for these deflation rates are shown in Figure 6.8a), b) and c).

Tentative of interpretation

In the gel phase, the DMPC vesicles are polycrystalline membrane and can be considered as elastic shells with a constant surface. When deflated, the loss of volume induces buckling of the objects. The deflated shapes obtained are different from the shapes predicted by the ADE model developed in section 2.2.3 because the phenomenon is not governed by the curvature. We believe the resultant shapes are an expression of the specific mechanical properties of the membrane in the gel state (the DMPC vesicles are characterized by a high viscosity of the membrane and an

elastic modulus) and reflect the plastic behavior characteristic of this state [50, 40]. The deflation mechanism, as well as the inventory of the large variety of shapes obtained are currently under investigation in our laboratory. Indeed, one aspect of the PhD of François Quemeneur [127] consists in the establishment of a phase diagram of DMPC vesicles, at a temperature under the transition temperature and for various reduced volume.

6.2.3 Dynamics of DMPC vesicles under shear flow

The aim of this study was to analyze the influence of the membrane properties (elastic in the gel phase or viscous in the fluid phase) on the dynamics of the vesicles under shear flow. We observe the behavior of DMPC vesicles near a plane using the side view set-up described in 4.2.1. In order to discriminate the different motions of the vesicles (tumbling or tank-treading) we deflate slightly the objects so they loose their sphericity. Experimentally we deflate the vesicles in a solution of 175 mM glucose (equivalent to a reduced volume ν of 0.57) at a temperature of 6^{o}C. Typical results obtained are presented below.

Membrane in the gel phase

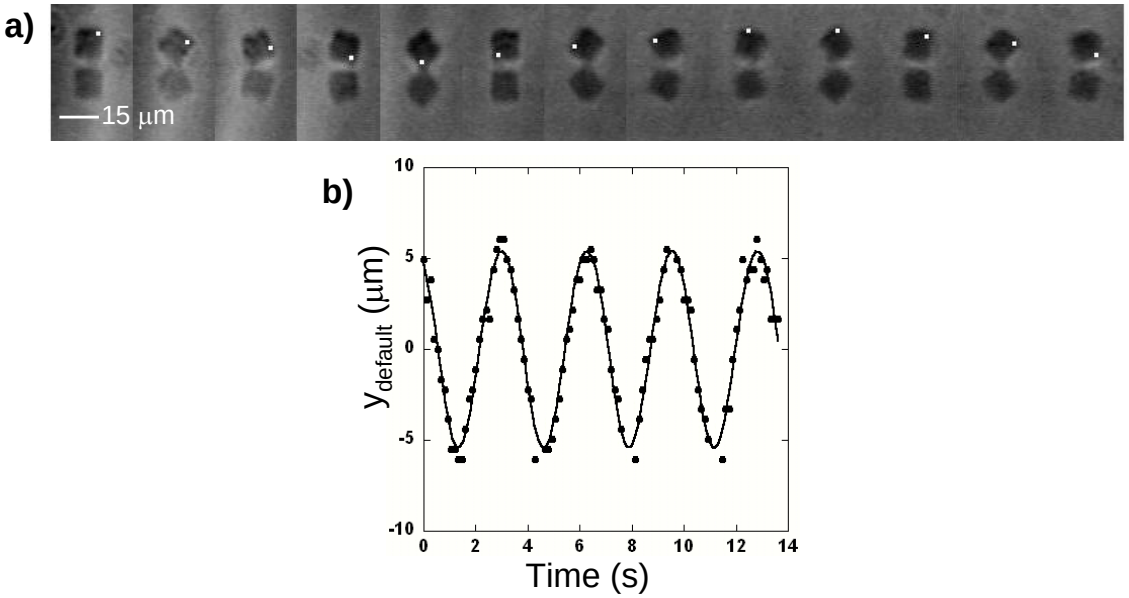

Figure 6.9: *The membrane of the "cubic" vesicle is in the gel phase at 22.5^{o}C. a) The tumbling motion is identified with a white marker at the upper-right corner of the vesicle (Time step between 2 pictures is 0.33 s). b) Relative position of the marked corner compered to the center of mass of the vesicle.*

First we note that the vesicle presented in the figure 6.9c) is "cubic" (similar to the shape presented in Fig. 6.8c)) in a solution of 175 mM glucose. At a temperature of 22.5^{o}C and at a shear rate of 2.7 s^{-1}, the vesicle tumbles as it can be seen on the Figure 6.9a) where we marked one corner of the cubic object with a white dot.

Although the analytic calculation [91] and experimental work [153] predict and observe a motion of tank-treading for a vesicle near the substrate with a contrast of viscosity η_{in}/η_{out}=1, the DMPC "cubic" vesicle is tumbling. A simple calculation of the coefficient $\frac{\omega R}{v}$ allows us to estimation the rolling over sliding participation in the motion of the object, where ω is the rotational

speed of the object, R its typical size and v its translational speed. The speed v of the vesicle is measured to be roughly 29 μm.s^{-1}, the typical size R of the object, chosen as the distance from the center of mass to the marked corner of the vesicle, is found equal at 7 μm and the rotational velocity is given by the Figure 6.9b). We present on Figure 6.9b), the coordinates of the marked corner in the referential of the center of mass of the particle as a function of time. ω is defined as $\omega=\frac{2\pi}{f}$ where f is the frequency of rotation and is found equal at 1.9 s^{-1}. We deduce that $\frac{\omega R}{v}$=0.46; i.e. the vesicle is sliding more that rolling. Although it is not spherical, the motion of the "cubic" vesicle can be described with the theory of Goldman [67] for the motion of a rigid sphere in a shear flow close to a wall.

After disconnecting the flow, the vesicle stops and the temperature is increased above T$_c$. It deforms at rest and becomes ellipsoid. As we let the temperature decrease back below T$_c$, the vesicle changes into a sphere (6.10a).

Membrane in the fluid phase

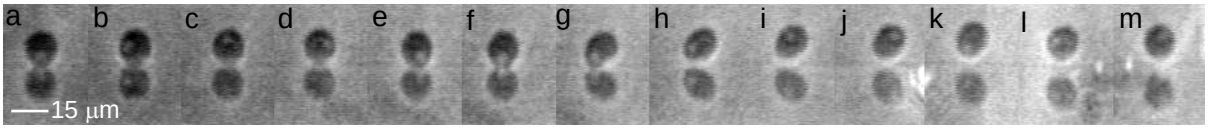

Figure 6.10: *Sequence of deformation and motion of a deflated vesicle at $\dot{\gamma}$=4.5 s^{-1} as the temperature is raised above T_c and then cooled down.*

A flow is then applied (shear rate $\dot{\gamma}$ = 4.5 s^{-1}) and a small "defect" on the membrane allows us to see the vesicle rolling on the substrate (6.10 a-e). As the temperature increases and reaches the critical temperature of transition, the vesicle deforms into an ellipsoid (6.10 f and g) and lifts off the substrate (6.10 h and i) to finally reach a mean height (6.10 j and k) of 10 μm. Once the vesicle acquires an ellipsoidal shape, its motion changes into a tank-treading motion (detectable using a defect) with a steady orientation. The temperature is then decreased back under T$_c$=23.4^{o}C, and the vesicle recovers its initial spherical shape (6.10 l and m).

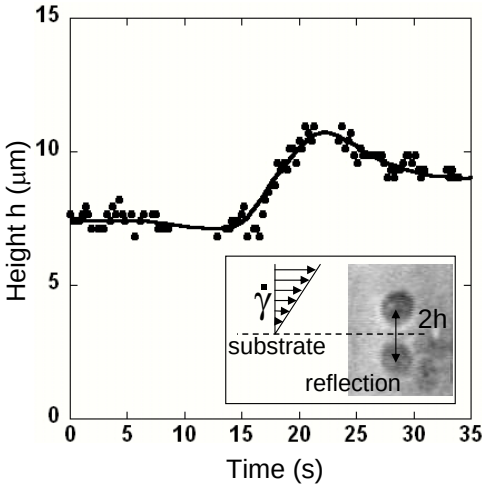

Figure 6.11: *Distance of the vesicle from the substrate as a function of time.*

Note: To be sure that the behavior of the vesicle undergoing temperature changes is not an artefact of our set-up, complementary experiments on the shape evolution of deflated vesicles in the gel state subjected to an increase of the temperature above T_c followed by a decrease below Tc temperature are being performed.

We define the height of the vesicle as the half of the distance between the center of mass of the vesicle and the center of mass of the reflection on the substrate (See insert in Figure 6.11). The measurement of the height of the object as a function of time is represented in Figure 6.11. The first plateau corresponds to the rolling of the vesicle on the substrate. When the temperature reaches T_c, the new ellipsoidal shape of the vesicle makes it sensitive to the lift force. Indeed, the vesicle takes off. In the mean time, we decrease the temperature below T_c and before reaching another plateau, the vesicle returns to a spherical shape. As it loses its ellipticity, the vesicle undergoes a decreasing drift, until the force is not big enough to compensate the weight of the object and then it starts to sediment; that is why the height of the vesicle after 22 seconds decreases slightly.

Figure 6.12: *Sequence of deformation of a DMPC vesicle at $\dot{\gamma}$=2.7 s^{-1}. The object tends to align with the flow direction as the ellipticity increases during the phase transition of the lipids. T between 18 and 27° C.*

We can also see in the Figure 6.12 that, as the reduced volume of the vesicle decreases, the ellipsoid tends to align itself with the flow. Indeed, we looked at the evolution of the orientation of the major axis of the vesicle as the reduced volume ν of the liposome gets smaller with the temperature. We measure the length of the major and minor axis of the vesicle, respectively 2a and 2b, and basing our estimation on the hypothesis that the volume of the vesicle is constant along the experiment, we deduce the third axis of the ellipsoid, the parameter c by the relationship:

$$c = 3V_{ves}/4\pi ab, \tag{6.2}$$

V_{ves} being the volume of the vesicle (determined when the object was spherical). Then by estimating the surface area of the ellipsoid S_{ves} by the equation:

$$S_{ves} = 2\pi a^2[1 + (\frac{b}{a})^2 \frac{\tanh^{-1}(ecc)}{ecc}], \tag{6.3}$$

where $ecc = \sqrt{1 - (\frac{b}{a})^2}$ is the eccentricity of the ellipsoid. We can calculate the radius of the sphere R_{sph} with the same surface area as the ellipsoid, according to:

$$R_{sph} = \sqrt{\frac{S_{ves}}{4\pi}} \tag{6.4}$$

Finally, we can estimate the reduced volume as being:

$$\nu = V_{ves}/\frac{4\pi}{3}R_{sph}^3 \tag{6.5}$$

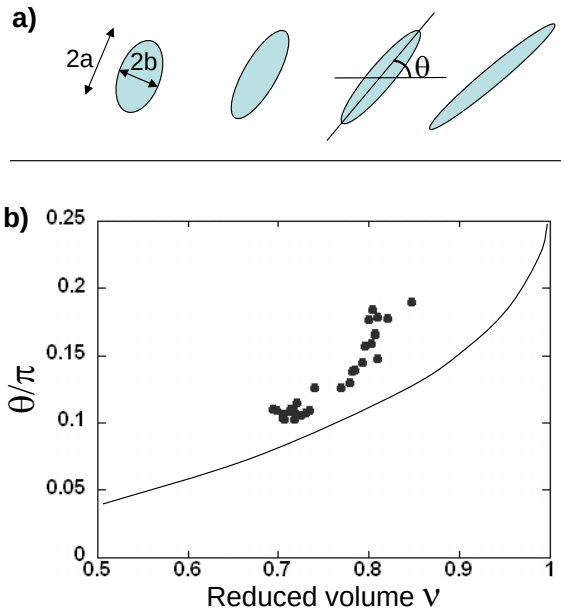

Figure 6.13: *a) Schematic representing the evolution of the orientation of the object as the reduced volume is modified. b) The non-dimensionalized orientation θ/π of the major axis versus the reduced volume ν. The dots are the experimental data and the solid line correspond to the theory from Kraus et al. [93].*

The angle formed by the major axis of the ellipsoid and the direction of the flow, as describe in Figure 6.13a), is also extract from the movie. The Figure 6.13b) represents the evolution of the angle of inclination θ of the object versus ν.

Interpretation

The orientation θ of the vesicle is known to depend only on the are-to-volume ratio of the vesicle [93]. As the temperature increases, the lipids are freed from the reservoir attached to the membrane which leads to the increase of the surface area of the object. The orientation of the vesicle changes in response to the diminution of ν. The experimental data are similar with the numerical results from Kraus et al. However the quantitative difference could be explain by the fact that the volume of the vesicle does not stay constant during the experiment, probably due to the opening of a pore in the membrane.

Conclusion

Their very high membrane viscosity and their elastic modulus in the gel state makes of DMPC vesicles, very interesting objects for the buckling phenomenon induced by reduction of the volume. The unusual deflated shapes obtained after osmotic shocks under the transition temperature are similar with some virus shapes. The study of these shapes as well as the behavior under flow of such objects could be use as mimetic objects in the study of the mechanical properties of virus.

Chapter 7

Dynamics of red blood cells under flows

Ce chapitre, concernant l'étude du comportement de globules rouges sous écoulement, se compose de deux études principales. Dans une première partie nous développons la dynamique d'un globule rouge isolé sous cisaillement ; nous révélons notamment un régime dit d'oscillations - caractéristiques des capsules élastiques - superposé à celui de chenille de char. Nous présentons un modèle qui prévoit à la fois le mouvement d'oscillation et la dépendance de la transition du mouvement de rotation solide vers le mouvement de chenille de char par rapport à la contrainte appliquée. Ce modèle démontre l'existence d'une mémoire de la déformation élastique de la membrane et, permet de déterminer d'une part la viscosité de la membrane et d'autre part, le module élastique du globule rouge grâce à une comparaison avec les résultats expérimentaux.

Dans une seconde partie nous nous focalisons sur des écoulements plus pertinents du point de vue physiologique, puisqu'il s'agit d'étudier le comportement des cellules sanguines en milieu confiné. Nous avons établi un diagramme de formes de globules rouges s'écoulant dans des capillaires en verre de diamètre variable. Nous étudions l'importance de la vitesse de déplacement des cellules, de la viscosité de la solution tampon et de la taille du capillaire. Nous présentons également une technique permettant la mesure de la chute de pression associée à la présence d'un objet déformable dans un canal de dimension similaire. Nous rapportons l'effet du volume, de la déformabilité, de la vitesse des cellules, ainsi que de la géométrie du canal sur la mesure de la chute de pression associée avec le passage de la cellule. Enfin nous étudions la formation d'une zone vide de toute cellule, à proximité des parois du canal, due à l'écoulement d'une suspension plus concentrée de globules rouges à travers une constriction. Nous détaillons l'effet des différents paramètres du problème (débit, géométrie, viscosité de la solution tampon, concentration des cellules, volume et déformabilité) sur la zone vide de toute cellule près des parois du canal.

There are three key points in the study of RBCs under flow: their behavior as individual objects in a semi-infinite geometry, the deformation and the motion of a single red blood cell when flowing in a close-fitting capillary, and of course the interaction between the cells, i.e. the collective effects. We propose in this section to investigate the effect of the presence of a wall on the motion of single cells in a shear flow. Then we will focus on the behavior of red cells in high confinement and exposed to different stresses through different geometries. We will try to

introduce the notion of collective effects by looking at the effect of cell concentration.

7.1 Preparation of RBCs solutions

The blood used in all of the experiments was collected from a single healthy donor. We explain in this section the protocol used to obtain and prepare the RBCs solutions used in the rest of this chapter. We will present the different alterations processed on the cells in order to change their mechanical properties or the preparation of the different buffers used.

7.1.1 Solutions of RBCs

In order to prevent their aggregation over long times and their adhesion on the non-treated surfaces, we remove the plasma from the whole blood solution by washing the cells twice in an aqueous solution of Phosphate Buffer Saline (PBS), purchased from Sigma. The buffer solution was verified to maintain the RBCs in physiologic conditions; its pH and osmolarity were measured, respectively, to be 7.4 and 300 $\pm$ 10 mOsmol.kg^{-1}. During the experiments, the shape of the RBCs was continuously monitored to check any evolution from the healthy biconcave form. After gentle centrifugation, this model cellular solution was dispersed into the suspending media chosen for the experiment.

7.1.2 Outer viscosity effect

In order to test the effect of the viscosity of the surrounding fluid, several suspending media were prepared by dissolving dextran at a molecular weight equal to 2×10^6 (purchased from Sigma) in the PBS buffer. The viscosities of the solutions were measured and varied with respect to the concentration of dextran added. Although dextran is known to facilitate aggregation of blood cells, no aggregates were observed during the time of our experiments.

7.1.3 Rigidified RBCs

The rigidity of the red blood cells was modified using a standard method [44]. First, the cells were treated with a solution of glutaraldehyde 1% v/v for 5 minutes at room temperature. Then, the cells were washed again in PBS (as explained previously) and dispersed in a solution of dextran with the chosen viscosity.

7.1.4 Hypotonic RBCs

We also modified the volume of the cells by changing the osmotic pressure of the surrounding fluid through the dilution of the PBS buffer previously prepared. The new osmotic pressure was measured to be 200 ± 10 mOsm/kg. The modified buffer was used to wash the red blood cells and the cellular solution was dispersed in a solution of dextran with the chosen viscosity made with the hypotonic buffer. Such hypotonic conditions swell the cells [47].

7.1.5 Motion of the cell's membrane

To discriminate the eventual rotation of the membrane of the cell, we need to look at the displacement of beads stuck on the membrane. To do so, we add to the solution of RBCs + PBS, a drop of a suspension of carboxyled beads of 1 μm in diameter. Then, we let the beads

adsorb under constant agitation at 10°C. The solution is then gently centrifugated in order to get ride of the excess of unattached beads. The supernatant is eliminated and the cells are dispersed into the suspending media chosen for the experiment.

A- Red Blood Cells under shear flow

7.2 Dynamics of RBCs under shear flow near a plane [12]

The dynamics of red cells under shear flow has received a considerable attention for more than 40 years. It is generally admitted that the two possible RBC movements are the unsteady tumbling solid-like motion partially described by analogy with the flipping of a coin [71], and the drop-like "tanktreading" motion where the cell maintains a steady orientation with an increasing deformation for higher shear stress, while the membrane rotates about the internal fluid, as reported respectively for RBCs suspended in plasma or in high-viscosity media and submitted to high shear stresses [71, 58, 59, 150, 151]. However, the understanding of RBC movement at smaller shear rate and close to the tumbling-tanktreading transition, has not been fully addressed. Moreover, the actual state of deformation of the elastic skeleton either in the flowing or in the resting RBC is still conjectural ("shape memory" problem) [57].

Most models [150, 151, 144] derive from the analytical framework of Keller and Skalak [91], which treats the RBC as a fluid membrane of fixed ellipsoidal shape enclosing a viscous liquid. Although this model qualitatively retrieves the two observed modes of motion, it does not capture the shear-rate dependency of the tumbling/tanktreading transition. In particular, the model does not account for the possible elastic energy storage induced by the local deformations of the cytoskeleton during tanktreading [140]. Approaches including membrane elasticity are either restricted to spherical resting shapes [22] because of analytical complexities, or propose encouraging but still limited numerical analysis on tanktreading elastic biconcave capsules [128]. Therefore, although the exploitation in clinical hemorheology assays of observations of flowing RBC coupled to mathematical analysis attests a certain success [41, 109, 18], it remains within its potentiality.

Here, we reveal a new regime of motion for RBCs under small shear flow, characterized by an elastic capsule-like oscillation of the cell inclination superimposed to tank-treading that we name swinging. We develop a model, which predicts both swinging and the shear-stress dependence of the tumbling-tanktreading transition. It demonstrates the existence of the elastic shape memory in the membrane and, from the interplay with the tanktreading movement, allows to determine both membrane viscosity and elastic shear modulus.

7.2.1 Preparation and experimental set-up

The blood used in all of the experiments was collected and prepared according to the protocol reported previously in section 7.1. In order to investigate the effect of the external viscosity, we incorporate some dextran in the PBS solution at different concentrations: 40, 60, 75 and 90 $g.L^{-1}$. The viscosity of the different solutions have been measured and are reported in Table 7.1. To discriminate the motion of the cell, we need to highlight the eventual rotation of the membrane. To do so we stuck some beads on the cell's membrane according to the protocol of Lenormand [98] reported earlier.

Concentration % dextran ($g.L^{-1}$)	Viscosity ($mPa.s^{-1}$)	η_{in}/η_{out}
40	11	1
60	20	0.5
75	31	0.33
90	47	0.21

Table 7.1: *Table of viscosity measured for the different buffer solutions prepared.*

We use the side-view experimental set-up as described in section 4.2.1. We show in Figure 7.1 a typical image that we observe during our experiments; and we define some of the different parameters measured, such as the velocity v of the center of mass of the object, its distance h from the substrate, the orientation θ of the major axis of the RBC with the flow direction, the length of the major and minor axis, $2a$ and $2b$ respectively, etc...

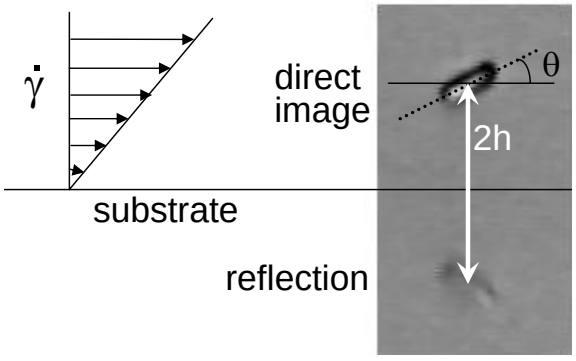

Figure 7.1: *Typical image observed and definition of the physical parameters measured to characterize the motion of the cell.*

7.2.2 A solid-like motion: the tumbling

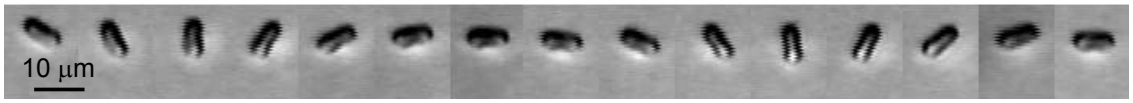

Figure 7.2: *Sequence of solid-body like rotation of a RBC, 54 μm far from the wall ($\dot{\gamma}$=0.8 s^{-1} and η_{out}=47 $mPa.s^{-1}$).*

In this section, we focus on red blood cells far from the wall ($h > 20\mu$m). At low shear rates $\dot{\gamma}$, i.e. at low shear stress, the solid-body like motion of tumbling is observed (Fig. 7.2). It is associated with a significant deformation of the RBC (Figure 7.3) which depends on its orientation. Indeed, the length of major axis is maximum when the cell's orientation is aligned with the elongational component of the flow, i.e. around $\pi/4$; and minimum when perpendicular to this component of the flow as noted on the insets Fig. 7.3. The length 2a of the major axis of the cell varies more than 2 μm in amplitude.

The dependence of the orientation θ of RBC's major axis on the viscosity ratio η_{in}/η_{out} is predicted by the calculation of Keller and Skalak. Indeed, we show in the Figure 7.4a), that the more

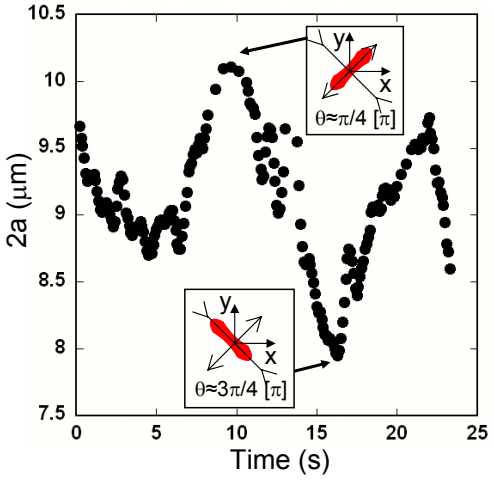

Figure 7.3: *Evolution of the cell's major axis ($\dot{\gamma}$=0.8 s^{-1} and η_{out}=47 $mPa.s^{-1}$).*

viscous is the outer media, the faster the cell rotates. The rotational motion is also compared to equation 3.11. We can see in the Figure 7.4b) that the agreement between the theoretical curve and the experimental data is pretty good in this figure. A is the mean value of $\dot{\theta}$ versus θ and B the amplitude.

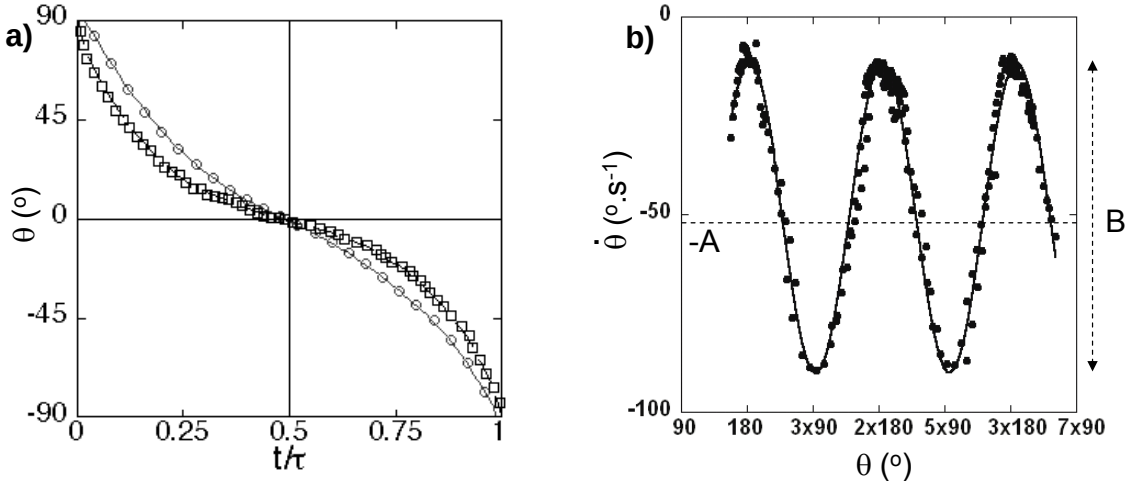

Figure 7.4: *a) Orientation θ of the major axis of the cell versus time for different outer viscosity at $\dot{\gamma}$=0.13 s^{-1}. (□) η_{out}=47 $mPa.s^{-1}$, (○) η_{out}=31 $mPa.s^{-1}$. b) Rotational speed $\dot{\theta}$ of the cell inclination versus its orientation θ for η_{out}=47 $mPa.s^{-1}$, $\dot{\gamma}$=1.86 s^{-1}. The solid line is the theoretical calculation 3.11.*

The parameter A is extracted from the curve 7.4b) and reported versus the applied shear rate on Figure 7.5. We see that the data align on a single curve, as $-A$ is independent of η_{in}/η_{out}. However, while Keller and Skalak predict $-A = 0.5\dot{\gamma}$, we find $-A \approx 0.39\dot{\gamma}$, indicating that the RBC rotates slower than a rigid body. This effect is ascribed to a loss of energy associated with the rotation, which is dissipated to deform the cell. Moreover Keller and Skalak also predict that the factor B/A, which determines whether the ellipsoid tanktreads or tumbles, is independent of $\dot{\gamma}$ and depends only on the object geometry and on the viscosity ratio η_{in}/η_{out}

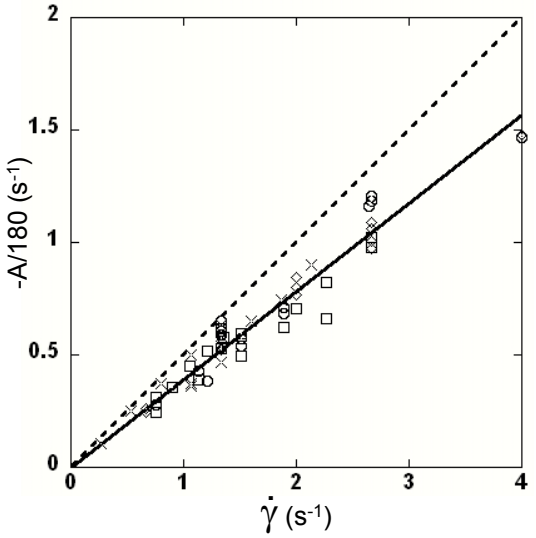

Figure 7.5: *Variation of the parameter -A/180 versus the applied shear rate $\dot{\gamma}$ for (○) η_{out}=10 mPa.s^{-1}, (□) η_{out}=22 mPa.s^{-1}, (◊) η_{out}=31 mPa.s^{-1}, (×) η_{out}=47 mPa.s^{-1}. Slope of the dashed line=0.5 from Keller and Skalak [91] and slope of the linear fit of the data=0.39.*

[91]. Although this model applies to viscous objects [115, 88, 104], it fails for RBCs where the transition of movement from tumbling to tank-treading (respectively tanktreading to tumbling) can be induced by tuning up (respectively down) the applied shear rate.

7.2.3 The swinging motion: oscillation of the cell

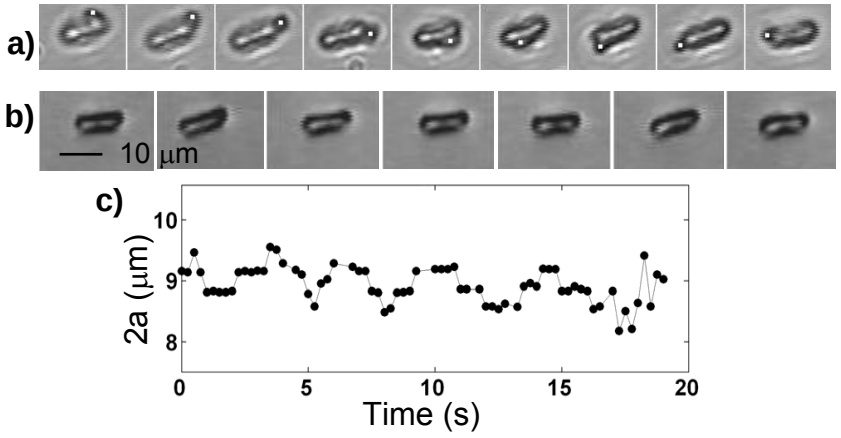

Figure 7.6: *a) Rotation of a bead stuck on the membrane of a RBC with $\dot{\gamma}$=6 s^{-1}, and η_{out}=47 mPa.s^{-1}. Time between 2 pictures=2 s. b) Time sequence of a RBC swinging at $\dot{\gamma}$=0.8 s^{-1} and η_{out}=47 mPa.s^{-1}. Time between 2 pictures=4 s. c) Length of the major axis 2a versus time for $\dot{\gamma}$=1.3 s^{-1} and η_{out}=47 mPa.s^{-1}.*

For the highest value of the external shear stress $\eta_{out}\dot{\gamma}$, tank-treading is observed. It is characterized by i) the rotation of the membrane, revealed from the motion of small carboxyled beads stuck on the membrane as shown on Figure 7.6a), ii) an oscillation of the cell inclination about a mean value (Figures 7.6b) and 7.7) and iii) the cell shape, which is very close to the rest shape

and considered as quasi stationary. Indeed, we note on Figure 7.6c) that the amplitude of the shape oscillation is less than 1 μm.

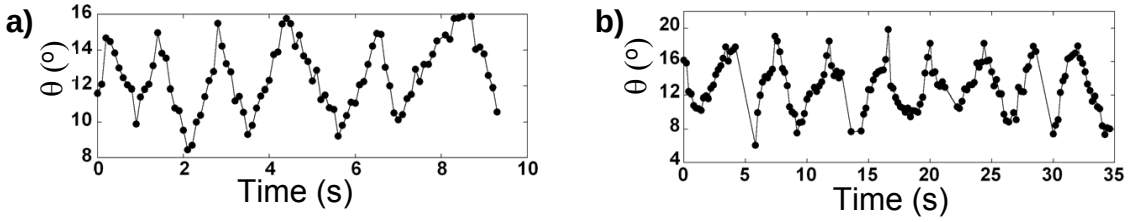

Figure 7.7: *Orientation θ versus time for two cells. a) $\dot{\gamma}$=1.8 s^{-1} and η_{out}=22 $mPa.s^{-1}$, b) $\dot{\gamma}$=6.6 s^{-1} and η_{out}=47 $mPa.s^{-1}$.*

Such oscillations are not seen on purely viscous lipid objects such as giant vesicles [14] nor they are predicted by Keller and Skalak. They are however, observed for non-perfectly spherical elastic millimeter-scale capsules [31, 155] or protein-coated drops [?], and in numerical simulations on biconcave elastic shells [128].

We now propose a simple model based on a fluid ellipsoid that accounts for membrane elasticity and cell shape memory. This model predicts all observed regimes of movement, including swing characteristics (magnitude and period of cell inclination) and the critical shear stress of the transition towards the solid-like tumbling motion. We show that this swing movement allows assessment of membrane shear modulus and viscosity.

7.2.4 A simple model

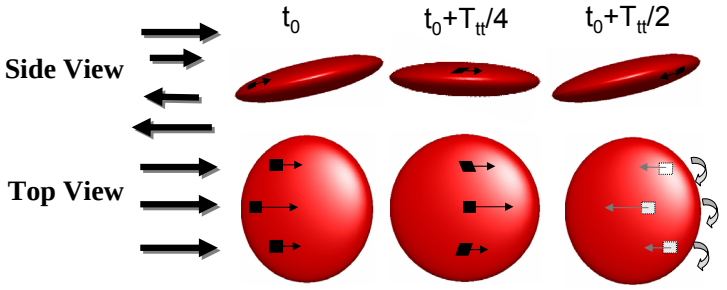

Figure 7.8: *Schematic of periodic deformation of membrane elements on a swinging cell.*

We explain the oscillatory phenomenon by assuming shape memory of the RBC. We state that the local elements of the composite membrane (cytoskeleton and lipid bilayer), including the elements which for the rim and the dimples are not equivalent and are not deformed in the biconcave resting shape. Consequently, they do not store elastic energy. Thus, during tank-treading, the elements which form the rim at rest rotates about the stationary cell shape to reach the dimples after $\pi/2$ rotation and reciprocally, the dimples change into rims. These elements are then locally strained and store elastic energy (Figure 7.8). Both local deformation and energy storage are periodic: each time the membrane make a π-rotation, the elementary

elements retrieve their initial shape and are no more deformed.

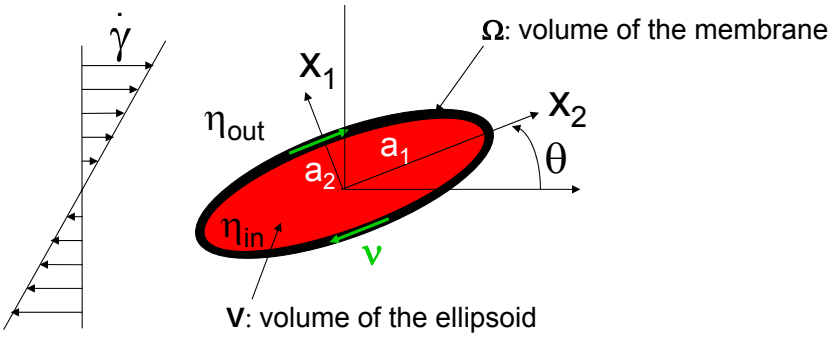

Figure 7.9: *Schematic of the system and definition of the parameters.*

We model this phenomenon based on the approach of Keller and Skalak [91]. In their calculation, the shape memory of the membrane is not taken into consideration. In deed, the rim or the dimple of the RBC are not equivalent during tanktreading. Hence, for each π rotation, the cytoskeleton in rotation, stocks and releases shear strain elastic energy. We propose to take into account this periodic exchange of energy by modifying the assumption 2 of the model of Keller and Skalak. The new assumption we propose is:

3. Energy conservation: the rate of work done by the external fluid is equal to the sum of the internal dissipation rate and the energy stored in the periodic elastic shear strain of the cytoskeleton.

The estimation of the shear strain elastic power is simply given by:

$$P_{el} = \int_{\Omega} Tr(\underline{\underline{\sigma}}.\underline{\underline{D}})d\Omega \tag{7.1}$$

where $\underline{\underline{\sigma}}$ is the shear stress tensor in the membrane and $\underline{\underline{D}}$ the deformation rate tensor. By definition, $\underline{\underline{D}}$ is simply given by:

$$\underline{\underline{D}} = \frac{1}{2}(\underline{\underline{\nabla\, v}} + \underline{\underline{{}^t\nabla v}}) = \frac{1}{2}\nu(\frac{a_2}{a_1} - \frac{a_1}{a_2}) \begin{bmatrix} 0 & 1 & 0 \\ 1 & 0 & 0 \\ 0 & 0 & 0 \end{bmatrix} \tag{7.2}$$

We note that the trace $Tr(\underline{\underline{D}})$=0, the movement of the membrane is then producing a pure shear deformation of its constitutive elements.

In the case of $\underline{\underline{\sigma}}$, we need to give ourselves a constitutive law of the material forming the membrane. We propose as a first approximation a Kelvin-Voigt model of the membrane. The shear stress is then the sum of a viscous part and an elastic part. The viscous part comes indeed from the fluid nature of the lipid bilayer while the elastic strain resistance comes from the underlying cytoskeleton capable of bearing shear stresses:

$$\underline{\underline{\sigma}} = \underline{\underline{\sigma_{vis}}} + \underline{\underline{\sigma_{el}}} \tag{7.3}$$

If we consider the membrane as being an isotropic, incompressible, homogeneous, linear and elastic material then we can express its constitutive law simply by the Piola-Kirchhoff stress

tensor:

$$\underline{\underline{\sigma_{el}}} = \pi^0 \underline{\underline{I}} + 2\mu_m \underline{\underline{e}} = 2\mu_m \underline{\underline{e}} \tag{7.4}$$

where π^0 is the initial stress of the membrane that we will consider equal to zero, μ_m is the shear modulus of the membrane, $\underline{\underline{I}}$ represents the identity matrix in three dimensions and $\underline{\underline{e}}$ the strain tensor in the lagrangian representation. By definition, $\underline{\underline{e}}$ is given by:

$$\underline{\underline{e}} = \frac{1}{2}(\underline{\underline{\nabla\xi}} + \underline{\underline{{}^t\nabla\xi}} + \underline{\underline{{}^t\nabla\xi}}.\underline{\underline{\nabla\xi}}), \tag{7.5}$$

where $\xi_i = x_i - x_i^0$.
Therefore, the elastic stress tensor is given by:

$$\underline{\underline{e}} = \frac{1}{2}\begin{bmatrix} [(\frac{a_2}{a_1})^2 - 1]sin^2(\omega) & (\frac{a_2}{a_1} - \frac{a_1}{a_2})sin(\omega)cos(\omega) & 0 \\ (\frac{a_2}{a_1} - \frac{a_1}{a_2})sin(\omega)cos(\omega) & [(\frac{a_1}{a_2})^2 - 1]sin^2(\omega) & 0 \\ 0 & 0 & 0 \end{bmatrix} \tag{7.6}$$

Because Tr($\underline{\underline{D}}$)=0, the viscous stress tensor is simply given by:

$$\underline{\underline{\sigma_{vis}}} = p\underline{\underline{I}} + 2\eta_m \underline{\underline{D}}, \tag{7.7}$$

where p is the pressure in the membrane. Finally, from 7.4 and 7.7, the total stress tensor is expressed as:

$$\underline{\underline{\sigma}} = -p\underline{\underline{I}} + 2\eta_m \underline{\underline{D}} + 2\mu_m \underline{\underline{e}} \tag{7.8}$$

We conclude that the viscoelastic power produced in the membrane per unit time and volume is expressed by:

$$\begin{aligned} Tr(\underline{\underline{\sigma}}.\underline{\underline{D}}) &= Tr((-p\underline{\underline{I}} + 2\eta_m \underline{\underline{D}} + 2\mu_m \underline{\underline{e}}).\underline{\underline{D}}) \\ &= -p\underbrace{Tr(\underline{\underline{I}}.\underline{\underline{D}})}_{0} + 2\eta_m \underbrace{Tr(\underline{\underline{D}}.\underline{\underline{D}})}_{\frac{1}{2}\dot\omega^2(\frac{a_2}{a_1} - \frac{a_1}{a_2})^2} + 2\mu_m \underbrace{Tr(\underline{\underline{e}}.\underline{\underline{D}})}_{\frac{1}{2}\dot\omega(\frac{a_2}{a_1} - \frac{a_1}{a_2})^2 sin(\omega)cos(\omega)} \end{aligned}$$

$$Tr(\underline{\underline{\sigma}}.\underline{\underline{D}}) = \frac{1}{2}\dot\omega(\frac{a_2}{a_1} - \frac{a_1}{a_2})^2[2\eta_m\dot\omega + \mu_m sin(2\omega)] \tag{7.9}$$

The total viscoelastic power exchanged within the whole membrane is:

$$P_{el} = \int_\Omega Tr(\underline{\underline{\sigma}}.\underline{\underline{D}})d\Omega = \frac{1}{2}\dot\omega(\frac{a_2}{a_1} - \frac{a_1}{a_2})^2[2\eta_m\dot\omega + \mu_m sin(2\omega)]\Omega \tag{7.10}$$

where Ω is the volume of the membrane.

The equation of conservation of energy 3.7 becomes:

$$W_p = D' + P_{el} \tag{7.11}$$

Adding 7.10, the balance of energy becomes:

$$V\eta_{out}(f_2\dot\omega^2 + f_3\dot\gamma\dot\omega\cos(2\theta)) = V\eta_{in}f_1\dot\omega^2 + \frac{1}{2}\dot\omega f_1(2\eta_m\dot\omega + \nu_m sin(2\omega))\Omega$$

which gives

$$\dot{\omega} = -\frac{\eta_{out} f_3 \dot{\gamma}}{\eta_{out}(f_2 - \eta_{in} f_1(1 + \eta_m/\eta_{in}\Omega/V)} \cos(2\theta) + \frac{\frac{1}{2} f_1 \mu_m \Omega/V}{\eta_{out}(f_2 - \eta_{in}(1 + \eta_m/\eta_{in}\Omega/V)} sin(2\omega) \quad (7.12)$$

Hence, from 3.6 and 7.12 the differential system that we obtain is:

$$\begin{cases} \dot{\theta} = -(\frac{1}{2}\dot{\gamma} + \frac{2a_1a_2}{a_1^2+a_2^2}\dot{\omega}) + \frac{1}{2}\dot{\gamma}\frac{a_1^2-a_2^2}{a_1^2+a_2^2} cos(2\theta) \\ \dot{\omega} = -\frac{\eta_{out} f_3 \dot{\gamma}}{\eta_{out}(f_2 - \eta_{in} f_1(1+\eta_m/\eta_{in}\Omega/V)} \cos(2\theta) + \frac{\frac{1}{2} f_1 \mu_m \Omega/V}{\eta_{out}(f_2 - \eta_{in} f_1(1+\eta_m/\eta_{in}\Omega/V)} sin(2\omega) \end{cases} \quad (7.13)$$

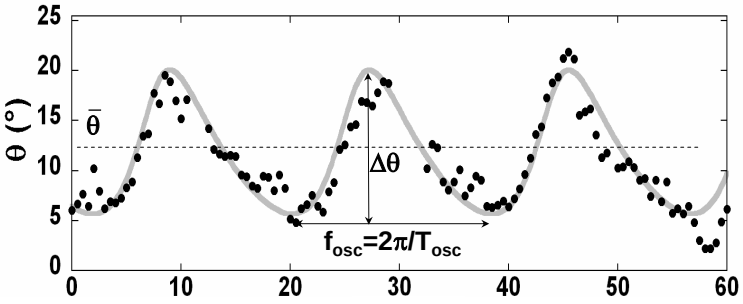

Figure 7.10: *Orientation θ versus time for a RBC with ($\dot{\gamma}$=0.8 s^{-1}, η_{out}=47 $mPa.s^{-1}$). The solid line is the theoretical fit (equations 7.13) with (η_{in}=10 $mPa.s^{-1}$, η_m=200 $mPa.s^{-1}$, μ_m=0.5 Pa).*

We numerically solve the equations using the following set of parameters: a_1=a_3=4 μm , a_2=1.5 μm, Ω=Σ.e, where Σ is the oblate ellipsoid area (see Annexe B) and e=50 nm is the membrane thickness [77]. We obtain θ(t), $\dot{\theta}$(t), ω(t) and $\dot{\omega}$(t). The limiting case μ_m=η_m=0 corresponds to Keller and Skalak. Suitable couples of μ_m and η_m values were found for which the cell oscillates in a movement similar to the one observed experimentally as seen in Figure 7.10. Experimental and numerical swinging curves are analyzed from two parameters: the magnitude $\Delta\theta = \theta_{max} - \theta_{min}$ and the frequency f_{osc} of oscillation as defined in Figure 7.10.

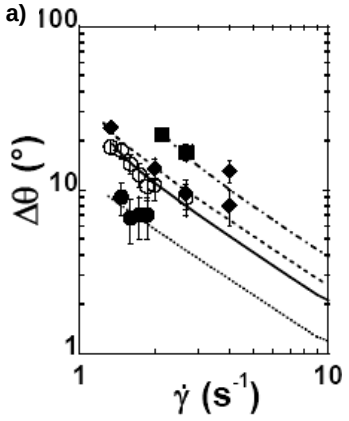

Figure 7.11: *Units: $[\eta_m]$=$[\eta_{in}]$=$[\eta_{out}]$=$mPa.s^{-1}$ and $[\mu_m]$=Pa. Experimental data of $\Delta\theta$ versus $\dot{\gamma}$: (•) η_{out} = 22; (♦) η_{out} = 47; (■) η_{out} = 31; (○) Single RBC, η_{out} = 22. Corresponding fits of μ_m with η_m = 700 fixed: (···) μ_m = 0.21, (—) μ_m = 0.38, (- - -) μ_m = 1.05, (-·-) μ_m = 1.05.*

Experimental and numerical variations of $\Delta\theta$ are inversely proportional to $\dot{\gamma}$, with a sharper raise $\dot{\gamma}$ upon decreasing down to a critical value $\dot{\gamma}_c^-$ below which the cell tumbles at least once

as shown on Figure 7.11. By adjusting the value of the membrane shear modulus μ_m, entered in the model, for given external viscosity and shear rate, we can obtain a pretty good agreement between the model predictions and the experimental data, as shown on Figure 7.11, with the variation of the amplitude of oscillation $\Delta\theta$ represented versus the applied shear rate $\dot{\gamma}$. Thus the model may provide a new method to accurately determine μ_m.

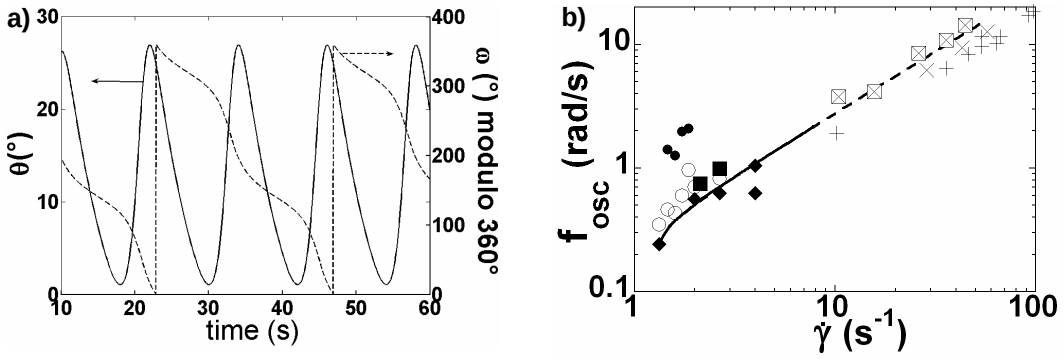

Figure 7.12: *a) Theoretical variations of (—) $\theta(t)$ and (- - -) $\omega(t)$ modulo 360°, with η_{out}=22 mPa.s^{-1}, η_{in}=10 mPa.s^{-1}, μ_m=0.8 Pa, η_m=200 mPa.s^{-1}, and $\dot{\gamma}$=1 s^{-1}. b). Solid line : fit for (♦) (η_{out}=47 mPa.s^{-1}, η_{in}=10 mPa.s^{-1}) with μ_m=2.4 Pa and η_m=1500 mPa.s^{-1}. (×) Tanktreading frequency $\dot{\omega}$ taken from [150]) with η_{out}=35 mPa.s^{-1}, (+) from [59] with η_{out}=18, 31 and 59 mPa.s^{-1}, (⊠) from [58] with η_{out}=70 mPa.s^{-1}.*

The relation between oscillation and tanktreading frequencies, f_{osc}=2$\dot{\omega}$, is indeed inherent to the model as presented in Figure 7.12a) and is coherent with previous numerical simulations of elastic capsules and experimental observations. Actually, during the time necessary for a material point of the membrane to make an entire rotation and come back to its initial position, the cell had the time to oscillate twice. This relationship allows to plot $\dot{\gamma}$-variations of $f_{osc}/2$, determined from our experimental data, and $\dot{\omega}$, reported in the literature [150, 59], on a unique curve covering an extended $\dot{\gamma}$-range presented on Figure 7.12b). The shape of the curves is well-fitted by the model. The non linear part observed at low shear rate, close to $\dot{\gamma}_c^-$, is due to the membrane elastic contribution. The linear domain observed at high shear rate is essentially governed by viscous contributions and was used by Tran-Son-Tay et al. to determine the membrane viscosity [150]. In this respect, it might be easier to use f_{osc} rather than $\dot{\omega}$ to determine the $\dot{\gamma}$ versus frequency curve, since the measurement of the frequency f_{osc} does not require the bead-labeling of the membrane.

The model also predicts the transition between the two movements, swinging to tumbling and reciprocally tumbling to swinging, which characteristics are developed hereafter.

7.2.5 Transition between the two movements

This transition is illustrated in Figure 7.13. As shown in Fig. 7.13a), the transition from swinging to tumbling, is associated with a local deformation moving with the membrane during the tanktreading of the cell, then the cell starts tumbling and the local deformation resorbs slowly. The second transition mode, i.e. from tumbling to swinging, is associated with strong deformation as presented in Fig. 7.13b).

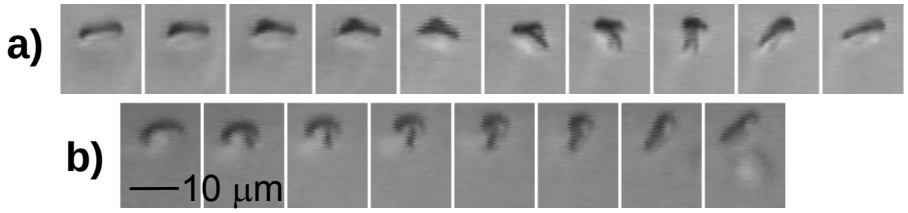

Figure 7.13: *The transition modes a) from swinging to tumbling, b) from tumbling to swinging.*

The more striking feature of the transition is the existence of a $\dot{\gamma}$-domain, where the cell at a given $\dot{\gamma}$ presents successively periods of tumbling and swinging as experimentally and numerically shown in Figures 7.14. For example, Fig. 7.14a) presents the evolution of the orientation of the major axis of a cell at $\dot{\gamma}$=1.53 s^{-1} and η_{out}=22 mPa.s^{-1}. A rotation of the cell during the tumbling is followed by a couple of oscillations associated with the swinging motion. The solid curve shows that this behavior is predicted by the model. Moreover, if we consider the curve in Figure 7.14b) at a given shear stress $\eta_{out}\dot{\gamma}_c$=0.06 Pa, we see that a cell drifting away from the wall, will have successively a motion of tumbling near the surface, and then a swinging movement between 20 and 60 μm from the substrate and finally again a motion of tumbling further from the wall.

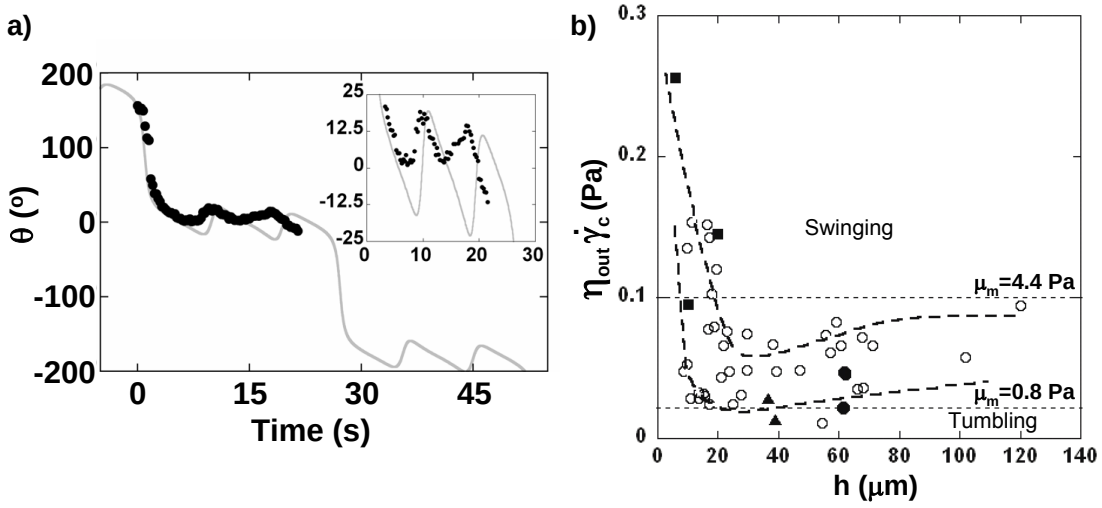

Figure 7.14: *a) (•) Experimental data representing successive swinging and tumbling at η_{out}=22 mPa.s^{-1}, $\dot{\gamma}$=1.53 s^{-1}; (-) Numerical calculus with η_{out}=22 mPa.s^{-1}, η_{in}=10 mPa.s^{-1}, $\dot{\gamma}$=1.53 s^{-1}, η_m=200 mPa.s^{-1}, μ_m=1.4 Pa. b) (○) Experimental critical shear stress of transition versus h. Hysteresis shown for two RBCs at η_{out}=31 mPa.s^{-1}: (▲) transition tumbling-swinging at $\dot{\gamma}_c^+$=1 s^{-1}; swinging-tumbling $\dot{\gamma}_c^-$=0.47 s^{-1}; (•) transition tumbling-swinging at $\dot{\gamma}_c^+$=1.73 s^{-1}; swinging-tumbling $\dot{\gamma}_c^-$=0.8 s^{-1}. The dashed curves are guides for the eye. (■) Data extracted from [58].*

Moreover, the transition exhibits an hysteresis: it occurs at different $\dot{\gamma}_c$, whether one increases $\dot{\gamma}$ from tumbling up to the observation of a first swinging ($\dot{\gamma}_c^+$) or one decreases $\dot{\gamma}$ from tank-treading down to solid rotation ($\dot{\gamma}_c^-$). This hysteresis is represented Figure 7.14b) by the solid triangles (▲) and the solid circle (•). The first cell (▲) goes from tumbling to swinging at $\dot{\gamma}_c^+$=1 s^{-1}, and from swinging to tumbling at $\dot{\gamma}_c^-$=0.47 s^{-1}. The second one (•) passes the transition tumbling-swinging at $\dot{\gamma}_c^+$=1.73 s^{-1} and the swinging-tumbling one at $\dot{\gamma}_c^-$=0.8 s^{-1}. The observed

typical difference in the critical shear rates of transition ranges from 0.1 to 1 s^{-1} depending on the cell and the external viscosity.

Finally, experimental values of $\eta_{out}\dot{\gamma}_c^+$ and $\eta_{out}\dot{\gamma}_c^-$ measured on a large RBCs sampling are shown Figure 7.14b) versus the distance h from the wall. The observed dispersion characterizes the natural variability of the RBC elastic modulus and the hysteresis effect. Fits indicates that μ_m ranges from in the interval 0.8-4.4 Pa. Such values are in good agreement with that reported for 2D elastic shear modulus, $\mu_{m,S}$ [98] by setting $\mu_{m,S}$=μ_m.e we obtain values ranging from 4 to 22.10^{-8} N.m^{-1} (e=50 nm). It also illustrates how the proximity of the substrate, which locally modifies the external hydrodynamic stresses, acts on the RBC's movement.

7.2.6 To conclude

The swinging movement and the shear stress triggered transition of motion of RBCs demonstrate the existence of their shape memory and is a signature of their membrane elasticity. Measurements of the magnitude of swinging, the oscillation frequency and the shear stress of transition allow one to determine the shear modulus and the viscosity of the membrane at small deformation. Despite its simplicity, our model provides correct fits of μ_m and further refinements that include more realistic constitutive law and velocity field should allow an easy and accurate determination of individual RBC mechanical properties. Finally, such experimental approach coupled to the proposed model should also apply to a wide variety of soft shells [31, 155, 45] and holds promises for applications in surface rheology measurements.

B- Red Blood Cells under confinement

In this section, we are interested in more physiological flows such as the one occurring in the microcirculation. We looked at the deformation of single cells in capillaries. Then we will study the behavior of cells in a pathologic case: the microthrombus, where we will try to introduce the notion of collective effects by changing the concentration. Finally, we will focus on a microrheometer we developed to measure the pressure drop at the scale of a single cell.

7.3 Flow of single RBCs in capillaries

The study of red blood cells under flow involves necessarily the study of their behavior when flowing through small capillaries mimicking the flow through the microcirculation. The deformation of red cells when entering and exiting small capillaries as a function of time and along the capillary is a important step towards the mechanical characterization of the cells membrane. In this section, we present the establishment of a diagram presenting shapes of red blood cells flowing in small capillaries. The different parameters varied during our experiments are the stress - through the speed of the objects or the viscosity of the outer medium - and the ratio between cell's size and the capillary radius.

7.3.1 Experimental procedure

Blood Preparation

The RBCs used during the experiment are extracted from a droplet of blood obtained pricking the finger of a healthy donor. The blood sample is diluted and washed twice with a solution of phosphate buffer saline (PBS) at a physiological osmolarity of 300 mOsmol. All the solutions are verified to be at pH 7.4 and are made with dextran of molecular weight of 2×10^6 at different concentrations : 4, 6 and 9% w/w, which correspond to a viscosity of 11 cp, 20 cp and 47 cp, respectively (see section 7.1).

Experimental setup

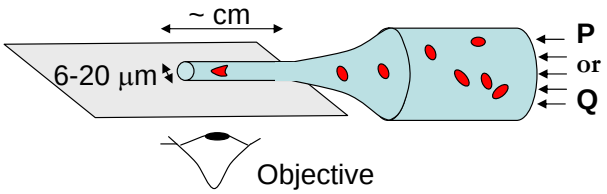

Figure 7.15: *Schematic of the experimental set-up: the red blood cells are injected in the glass capillary by pressure or flow rate-driven flow. The radius of the capillaries have been varied from 6 to 20 µm.*

We pulled circular glass capillaries with different final diameters using a basic micropipette puller. The capillary is then connected to a syringe via the appropriate choice of tubing. The fluid is set into motion by the two methods: with a given flow rate (syringe pump approach) or with a given applied pressure (pressure driven flow) developed earlier in section 4.2.2.

7.3.2 Non axisymetric slipper-like shape

Effect of cell velocity

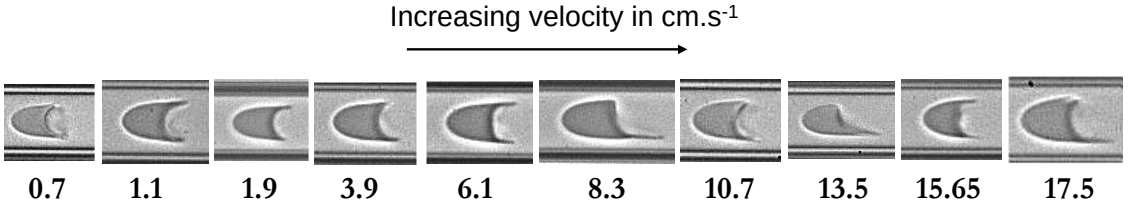

Figure 7.16: *From axisymmetric toward slipper-like shapes: Shape evolution of red blood cells with increasing velocities.*

We first look at the evolution of cells shape with increasing velocity, in a capillary of roughly 8.5 μm in diameter. Pictures describing such shape evolution are presented in Figure 7.16. We note that with increasing speed v, the cells are more and more deformed and lose their axisymmetry: the red cells develop a "tail" and consequently adopt a slipper-like shape. With increasing speed, the "tail" of the slipper-like shape becomes thinner and sharper. The experimental results are in good visual agreement with the predicted cells shapes obtained by Secomb [122] and presented in section 3.10: the cell gets elongated in the flow direction and the extremities at the rear of the object become more pointed.

Effect of external viscosity

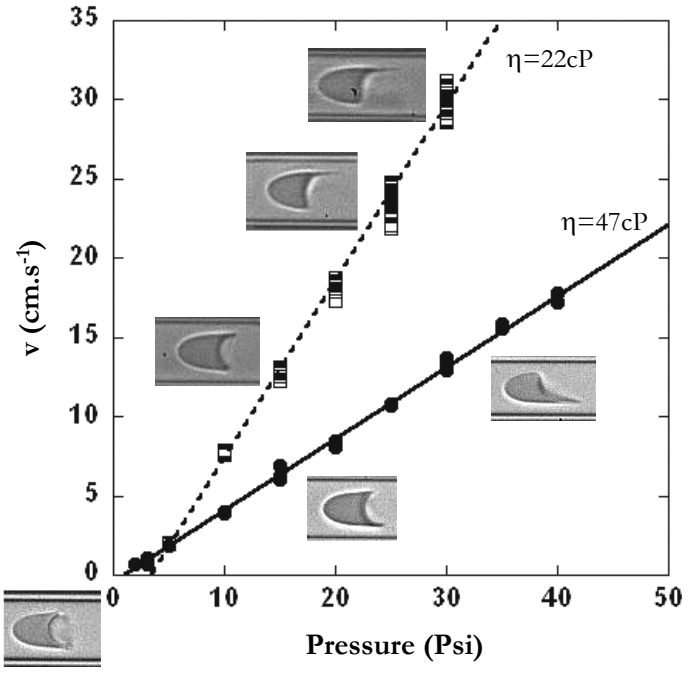

Figure 7.17: *Effect of the outer viscosity on the shape evolution. For a given velocity of 13-14 cm.s^{-1}, the cell go from a parachute-like shape to a non-axysymetric slipper-like shape as the outer viscosity is increased from 22 to 47 cP.*

We then investigate the effect of the outer viscosity on the shape of the red blood cells, for capillaries with the same diameter (8.9 μm). The results are presented in the Figure 7.17 for two different buffer viscosities η_{out}: 22 and 47 mPa.s^{-1}. First, we can note that there is a minimum pressure to apply to the suspension of cells in order to get a motion of the fluid (the curves do not go through the origin). The pictures of the cells associated with the typical speeds, show that for a higher buffer viscosity, but for the same displacement speed, the non-axisymmetry of the cell's shape is enhanced. The transition from the axisymmetric parachute-like shape to the non-axisymmetric slipper-like shape depends also on the outer viscosity. This result suggests that an important parameter in the transition is the capillary number associated to the cells, defined by:

$$Ca = \eta_{out} v / \mu_m, \tag{7.14}$$

where E_s is the surface shear modulus of the red blood cell.

Effect of capillary diameter

Finally, we vary the radius of the capillaries from 6 to 20 μm, and look at the effect on the resultant shape of the red cells. In Figure 7.18a, we present the shapes of three RBCs flowing in capillaries with increasing diameter. The first cell (on the left) is flowing in a capillary of 9.47 μm in diameter, we can see that the shape of the cell is axisymmetric and that the cell is centered with the axis of the capillary. The second cell experiences the same shape with the same flow conditions (same speed and approximately same capillary size). Finally in the third case, a cell flowing in a capillary of 17.15 μm in diameter adopts a non-axisymmetric shape, developing a

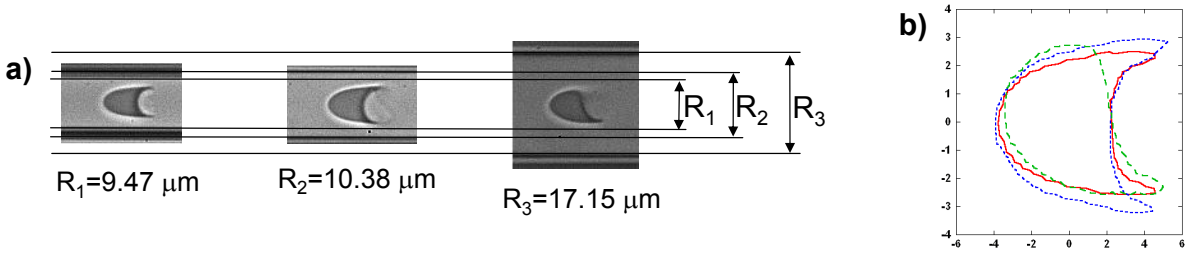

Figure 7.18: *a) Shapes of three RBCs flowing, in capillaries with different diameter R, at the same velocity (around 1.9 cm.s^{-1}; η_{in}=22 cP). b) Reconstruction of the shape of the three precedent RBCs. - (R_1=9.47 µm), — (R_2=10.38 µm), ... (R_3=17.15 µm). The center of mass of the cells are aligned.*

"tail" preferentially on one side. The details of the shape evolution is presented in Figure 7.18b). We reconstruct the shape of the three cells. We clearly see the effect of a important increase of the capillary diameter on the axisymmetry of the shape.

7.3.3 Establishment of a phase diagram of the shape of RBCs flowing in small capillaries

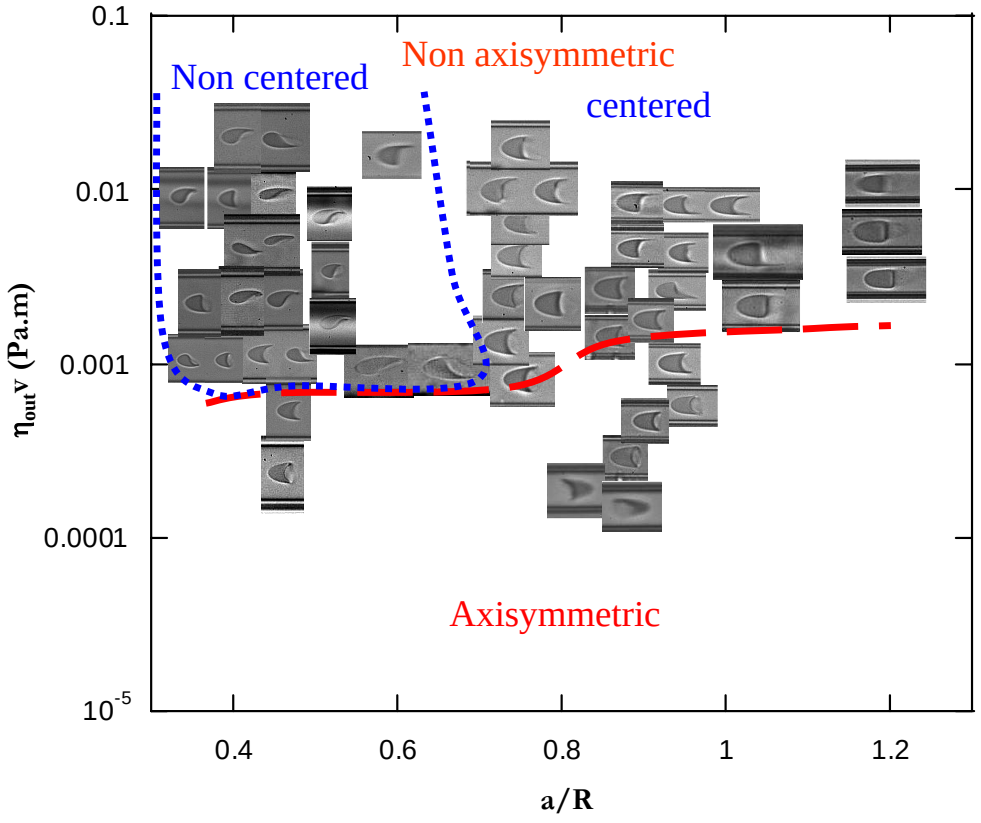

Figure 7.19: *Phase diagram of RBCs shape as a function of the non-dimensionnalized particle size a/R and the external stress $\eta_{out}v$.*

Varying two parameters: $\eta_{out}v$, and the ratio a/R, between the cell's typical size a and the

capillary's radius R, we built the phase diagram in Figure 7.19, representing the shape of RBCs flowing through circular glass capillaries. We can define two regions out of the diagram: a region where the shape of the cells is axisymmetric, parachute-like shape, and a second region regrouping the cell's with non-axisymmetric slipper-like shape. The axisymmetric region can be divided itself into two zones: in the first one, all of the cells are centered with the axis of the capillary, while in the second one the center of mass of the red blood cells is slightly off-set compared to the axis of the capillary. The data suggests a transition from the parachute-like shape to the non-axisymmetric slipper-like shape around $\eta_{out} v \approx 0.001$, which is equivalent to a capillary number $C_a = 2\text{x}10^{-4}$ for a typical shear modulus μ_m of 5 μN.m^{-1}. The transition from a centered to a non-centered position relative to the axis of symmetry of the capillary tube happens for $a/R \approx 0.7$.

7.3.4 To conclude

We built here the first phase diagram of RBCs shape flowing in cylindrical capillaries. We document the existence of a critical capillary number above which the shape evolves from a parachute-like shape to a slipper-like shape. We report here the first observation of a slipper-like shape of red blood cell non-centered inside the capillary tube. By increasing the applied stress or by decreasing the diameter of the glass capillary, the "tail" becomes more and more pointed and sharper. Could the non-axisymmetric slipper-like shape of the cells be a intermediate state of deformation towards hemolysis ?

7.4 Pressure drop associated with the flow of a single RBC [11]

The flow and shape of blood cells is controlled by a competition between the object properties, the fluid pressure and the viscous stresses acting on the boundaries that resist the motion. The hydrodynamic resistance resulting from this fluid-structure interaction is reflected in a dynamical variation of the pressure drop along the channel during the flow and hence represents a crucial parameter to be measured. There is a long history of the study of cells at the micrometer scale for assessing mechanical properties [46] and cell shape [62] and for applying these ideas for understanding microcirculatory diseases [33, 111]. Nevertheless, rapid variations of pressure are very difficult to measure at the micron scale and below. For instance, when a single red blood cell (RBC) enters a channel of 5 μm $\times$ 5 μm, the volume variation produced by a flow at physiological speeds of few mm.s^{-1} is about 100 fL in a few milliseconds, which represents a typical pressure drop variation of tens to hundreds of Pa. Such rapid pressure measurements at the cellular scale, crucial to future device and microcirculatory advances, are not available at this time. Here we report a technique overcoming these limitations and demonstrate the ability to measure rapid variations of pressure drop between two points in a microfluidic device.

7.4.1 Experimental procedure

Blood Preparation

The RBCs used during the experiment are extracted from a droplet of blood obtained by pricking a finger of a healthy donor. The blood sample is diluted and washed twice with a solution of phosphate buffer saline (PBS) at an osmolarity of 300 mOsmol (physiological value). All the solutions are verified to be at pH 7.4 and are made with dextran of molecular weight of 2×10^6 at a concentration of 9 %w/w, which correspond to a viscosity of 47 cp. In the process of blood

separation a few white blood cells are gathered with the RBCs allowing the study of their motion in the microchannels as well.

In order to obtain rigidified RBCs, which allows characterization of the changes in pressure drop due to mechanical changes in the cell membrane, an extra step is added in the process of dilution. The RBCs are maintained in PBS solution containing a given concentration of glutaraldehyde (0.001 %v/v to 0.01 %v/v) at 25°C for four minutes. The rigidified cells are then dispersed in the PBS solution with the same osmolarity, pH and viscosity as described previously.

Remarks

We used two sets of RBCs to do this experiment: normal cells, prepared as described above, and RBCs treated with a Fatty Acid Ethyl Esther (FAEE). The second type of solution was used at the occasion of a study on the effect of FAEE on RBCs mechanical properties [24]. We were unable to measure any significant change in mechanical properties of the cell treated with FAEE with the pressure drop measurement device. Indeed, we concluded that whatever effect is induced by the treatment of healthy RBCs with FAEE, it is below the resolution of our device. Therefore, we used the FAEE treated cells without distinction from healthy cells. The preparation of FAEE treated cells can be consulted in Annexe C. Given the dosage and the duration of exposure, we may not anticipate big changes in the RBC's mechanical properties. However given a more chronic exposure the effect might more dramatic and detectible by our set-up.

Device geometry

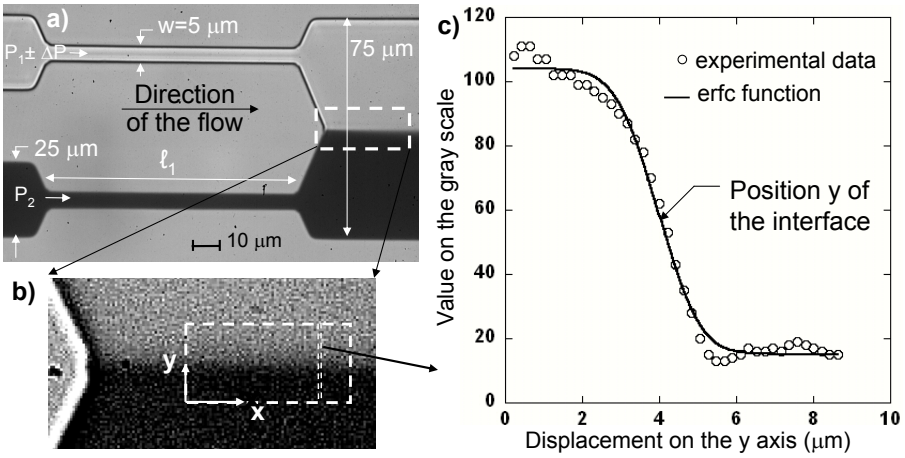

Figure 7.20: *a) The specific geometry of the device allows the measurement of the pressure drop induced by the flow of a close-fitting cell in the upper channel. The length x of the small channel has been varied between 60 and 100 µm b) Close-up on the interface. c) Image analysis determines the variation ΔY of the position of the co-flowing line that marks the interface.*

The microfluidic device was manufactured using the principles presented earlier in section 4.2.2 and the fluids pushed with the pressure driven flow approach introduced in the section 4.2.2. In order to measure simultaneously the dynamical deformation of the cells and the variation of the pressure drop produced by their motion in the channel, we developed a device with twin channels:

a test channel (upper channel in Fig. 7.20a)) and an identical control, or "comparator" channel (lower channel Fig. 7.20a)), both producing downstream two parallel and adjacent streams of fluid. In order to maintain a stable interface, the two fluids are miscible and the liquid flowing through the control channel is dyed in order to visualize the interface downstream. The typical dimensions of the device are shown in Figure 7.20a). The cross section of the close-fitting channel was chosen to be 5 μm by 5 μm in order to deform the cells significantly.

7.4.2 Principle of the measurement

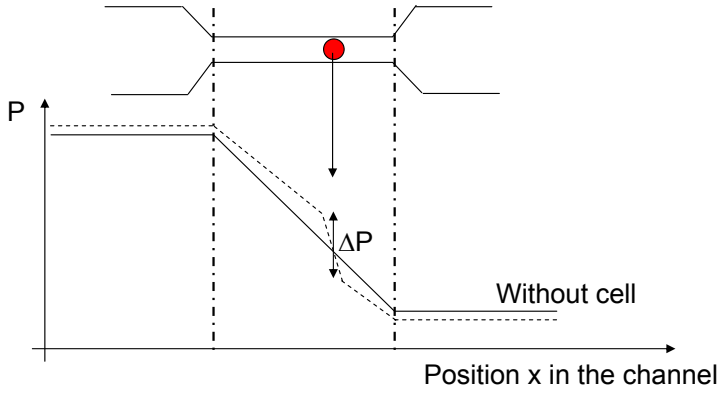

Figure 7.21: *Sketch of the principle of the device.*

The principle of the measurement lies in the use of the second control channel to detect any variation of pressure in the test channel when a cell is flowing through it. This principle is reported on the sketch Fig. 7.21. The pressure profile of the upper channel, in the absence of any object, is shown by the solid line. The pressure on the left is the applied pressure P_1 and the pressure on the right is the outer pressure P_{out}=atmospheric pressure. We consider that the change in the pressure due to the hydrodynamic resistance is mainly happening in the narrower section of the device.

When an object enters the constriction, the pressure profile changes slightly as shown with the dashed line on Fig. 7.21. Indeed, for a given applied pressure difference across the device, the placement of an object in the channel decreases the flow rate and consequently increases the pressure drop that occurs in the narrow test section. A change in the pressure drop along the channel alters the position of the interface downstream. The measurement of this deflection allows the pressure to be determined following a basic calibration procedure (see next paragraph), and consequently we are able to monitor the time-dependent dynamical changes in the pressure drop in the test channel. In the particular case of steady channel flow, Groisman et al. [73] used a similar approach of comparator channels for static measurements of pressure drop in a microfluidic "diode" (i.e., a device in which the pressure varies nonlinearly with flow rate and the direction of flow). We note that by directly imaging the two channel system, it is possible to get simultaneously the sequence of deformation of suspended cells and the dynamical variations of the pressure drop.

A high-speed camera is used to follow the motion and the deformation of the cells through the capillaries; typically we use an imaging rate of a few thousands frame per second. The field of

view of the camera allows simultaneous observation of the cells and the deflection of the interface.

7.4.3 Calibration

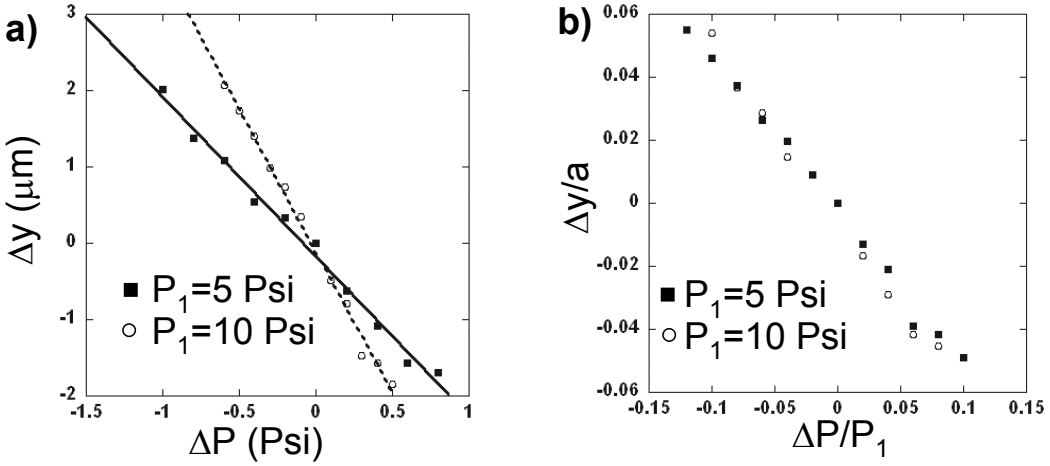

Figure 7.22: *Variation of Δy as a function of the change in pressure ΔP in the upper channel for two different upstream pressures P_1: (•) at 5 psi and (■) at 10 psi.*

It is first necessary to calibrate the deflection of the interface as a function of the pressure drop. The flow is produced by pressurizing the fluids in the syringes connected to the two inlets of the microfluidic device. With no RBCs in the solution, the pressure P_1 applied in the test channel and the pressure P_2 in the control channel are fixed so that the fluid-fluid interface downstream is centered in the main exit channel (Fig. 7.20)a). We change the pressure P_1 in small increments ΔP without changing the pressure P_2 in the control channel and follow the displacement of the interface in the Y direction by performing image analysis with Matlab software (Figure 7.20)b)).

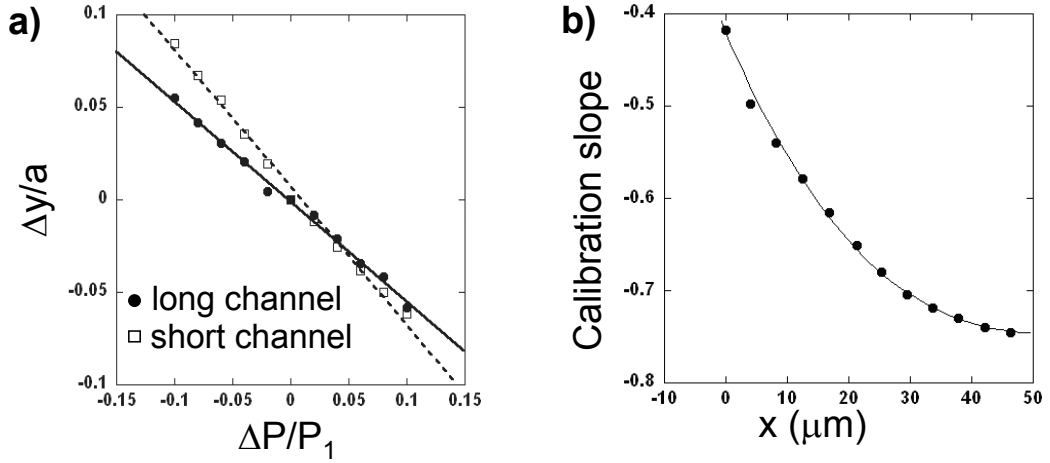

Figure 7.23: *a) Variation of Δy as a function of the change in pressure ΔP in the upper channel for $P_1 = 10$ Psi, for two different length of the channel: • ℓ_1=60 μm, □ ℓ_1=100 μm. b) Calibration of the device is reported at several locations along the interface.*

The variation Δy is linear in ΔP for the two initial working pressures applied, $P_1 = 5$ psi and $P_1 = 10$ psi as presented in Figure 7.22. Also, the slope of $\Delta Y(\Delta P)$ - which we refer to as calibration slope at $P_1 = 5$ psi is twice as large (in absolute value) as the slope at $P_1 = 10$ psi ; both responses are expected for small variations of this viscously driven flow. We then realized the calibration for two channels of difference lengths: 60 and 100 μm. The calibration curves are shown in Figure 7.23a). We note that the slopes of the curves are slightly different, we explain this discrepancy by the small variability in the height of the channels due to technical issues during the fabrication process of the device.

The image analysis of the calibration curve has been repeated at several positions x along the interface and the results are reported Figure 7.23b). We are limited in our field of view so that the analysis of the motion of the interphase has to take place close to the merging between the two channels. It shows that the co-flow is not entirely established within our field of view. A pseudo-analytical model has been proposed by Kristian Smistrup [141], in order to explain the calibration process (See Fig. 7.24). Figure 7.24a) shows the results of a Comsol Multiphysics, the black fluid represents the ink solution. We note that the interface exhibits a curvature near the the merging of the two small channels. It appear that the steady co-flow is reached 50 μm into the main channel which is close to the results obtained from Figure 7.23b). Δy is measured as an imposed ΔP is applied. Figure 7.24b) shows the results of several such calculations for different values of $\beta = \eta_{in}/\eta_{out}$. It is seen that the shape of the function $\Delta y(\frac{\Delta P}{P_1})$ is the same for the two values of β. At small scale around the origin, the curve behaves linearly, which is in good agreement with the experimental calibration. Therefore, there are some small quantitative differences about the calibration factors which can be explained by the curvature of the interface.

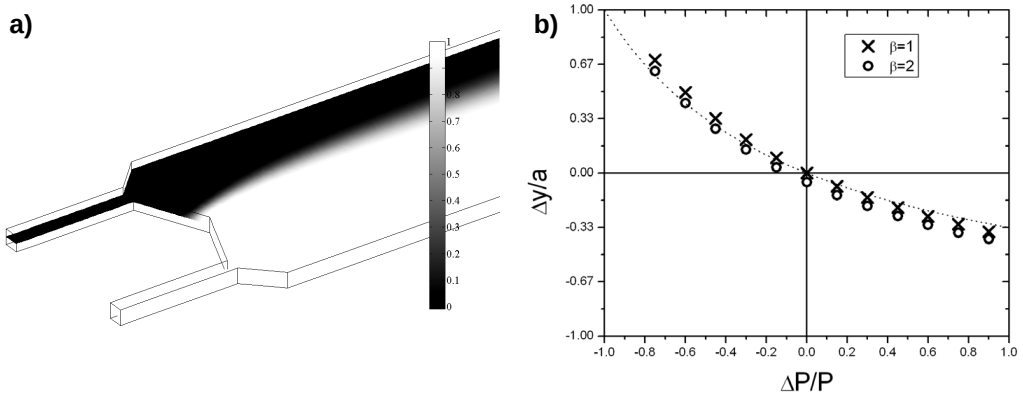

Figure 7.24: *a) The graphic shows the concentration field for $\beta = \eta_{in}/\eta_{out}$=2 and $\frac{\Delta P}{P_1}$=-0.6. A steady co-flow is reached 50 μm into the channel. The gradient of color traduces the diffusion between the ink and the other solution. b) Non-dimensional deflection delta versus pressure difference $\frac{\Delta P}{P_1}$ plotted for different values of the ratio between the viscosities $\beta = \eta_{ink}/\eta_{cells}$. The points are Comsol Multiphysics calculations (crosses and circles), along with the pseudo-analytical results (dotted and dashed lines).*

7.4.4 Pressure drop measurements induced by the flow of a red blood cell followed by a white blood cell

After calibration of the interface deflection as a function of the change in pressure drop, the dilute suspension of RBCs is introduced in the device. Each time a cell enters the test channel, we record a movie of the whole field of view, which allows us to follow the position of the interface

and the deformation of the cell. Each event is analyzed with Matlab software to measure the dynamical variations of the interface position (i.e. the pressure drop) as a function of time and of the deformation of the cell. We decide to consider all the measurements of ΔP as positive numbers.

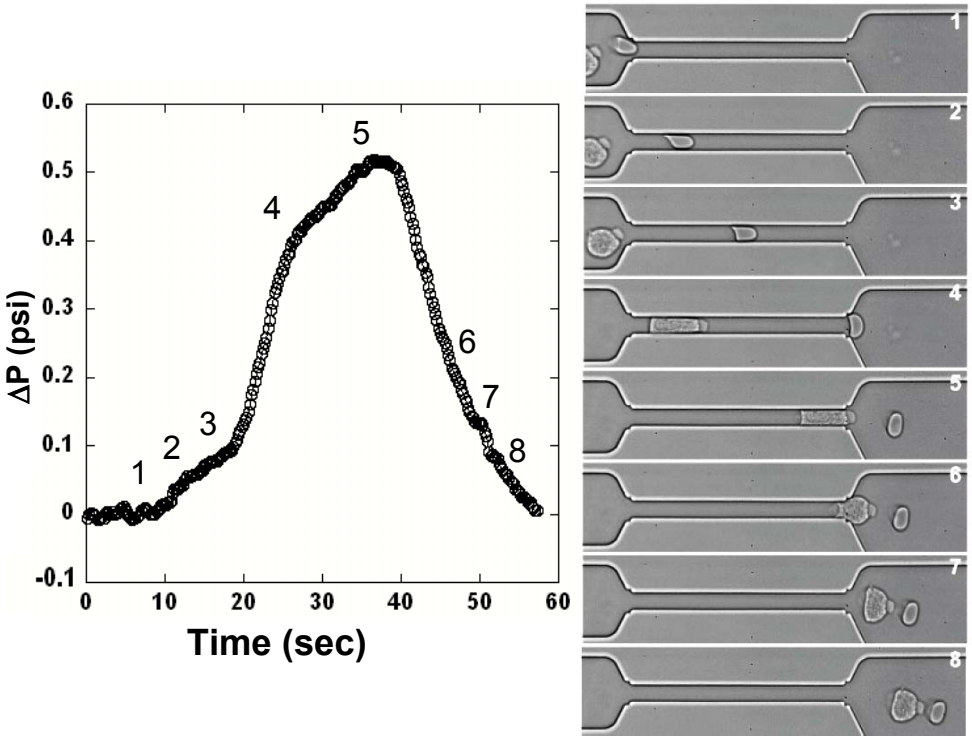

Figure 7.25: *Sequence of deformation of a white blood cell followed by a red blood cell flowing in a close fitting 80 μm long channel and the measurement of the pressure drop associated.*

An example, in order to illustrate our technique, consists in the measurement of the complete sequence of the deformation and the time evolution of the excess pressure drop when the cells flow in the channel as shown in Figure 7.25. A red cell enters the channel followed shortly thereafter by a larger (and stiffer) white blood cell (WBC). The time trace of the pressure drop variations can be compared with the images of the sequence of deformations represented in the Figure 7.25. The time evolution of the pressure drop while the same cell is in the channel, and away from either the entrance or exit, is a consequence of the deformation of the cell. This example illustrate the ability to monitor dynamically pressure drop and mechanical processes comparable to in vivo conditions occurring in the microcirculation.An example of the measured pressure-drop variations following the entry of a cell into a channel and continuing until after the cell has exited the channel is shown in Fig. 1D. The second bump in Fig. 1D corresponds to the exit of the cell near the co-flow line which directly disturbs the position of the interface, but does not have any physical significance in terms of the global pressure-drop variations.

Remarks

Two comments about details of the measurement approach are in order. First, PDMS channels are known to be deformable under pressure-driven flow. It is thus necessary to estimate the

maximum deformation produced by the passage of a cell which causes a pressure drop ΔP. The additional strain in the walls of the PDMS channel is estimated by the ratio of ΔP (order of 700 Pa) to the Young modulus Y of PDMS (approximately 5×10^5Pa), which is less than 10^{-3}. Hence, any such deformation is negligible.

Second of all, the time response of our system is related to the pressure-driven flow characteristics. The two relevant time scales are (i) propagation of sound waves (speed c) along the channel (length ℓ_1 and height h), which controls the axial development of the velocity profile, is estimated to be $\sim \ell_1/c \sim 10^{-6} - 10^{-7}$ s, and (ii) the diffusion of vorticity across the channel which controls the evolution of the nearly parabolic velocity profile, is estimated to be $\sim \mathrm{h}^2/\nu \sim 10^{-6}$ s. Both time scales are much shorter than the millisecond response we visually observe linking the motion (and instantaneous position) of the cell to the deformation of the interface.

7.4.5 Effect of cell deformability

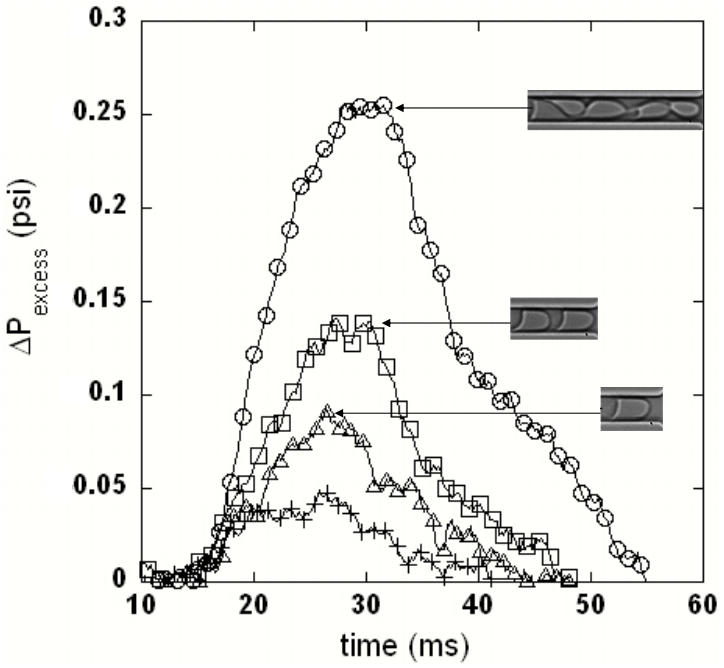

Figure 7.26: *Pressure drop versus time for different conditions characterizing the state of the RBCs; the driving pressure is 5 psi. + healthy RBC; open symbols: RBCs treated with 0.001% glutaraldehyde; △ one RBC; □ a train of two RBCs; ○ a train of five RBCs.*

We next consider the change in the hydrodynamic resistance that occurs when the mechanical properties of the cells are modified. In Fig. 7.26, we compare a single healthy cell with a glutaraldehyde treated cell, which is known to be stiffer [56]: the pressure drop is enhanced following treatment with glutaraldehyde and the stationary shape of the cell is obtained at later times. Thus, we conclude that our approach allows differentiation of cells with different mechanical properties or geometrical features, which may provide a simple biomedical tool for clinical hemorheology and pharmaceutical testing.

7.4.6 Effect of number of cells

The interactions of cells, and their number density, in the microcirculation impact the overall pressure drop in a tissue and is still not well understood [79]. Next, we report in Figure 7.26 results suggesting a way to study these hydrodynamical interactions of cells through the measurement of the pressure drop in the channel, for the flow of 1, 2 and 5 cells translating through a microchannel (cells are closely spaced similar to rouleaux). The pressure drop systematically increases as the number of cells increases but the results are not proportional to the number of cells. This qualitative response is typical of confined geometries with suspended particles spaced closer than the microchannel width.

7.4.7 Effect of the cell's volume

Measurement of the volume of the cell

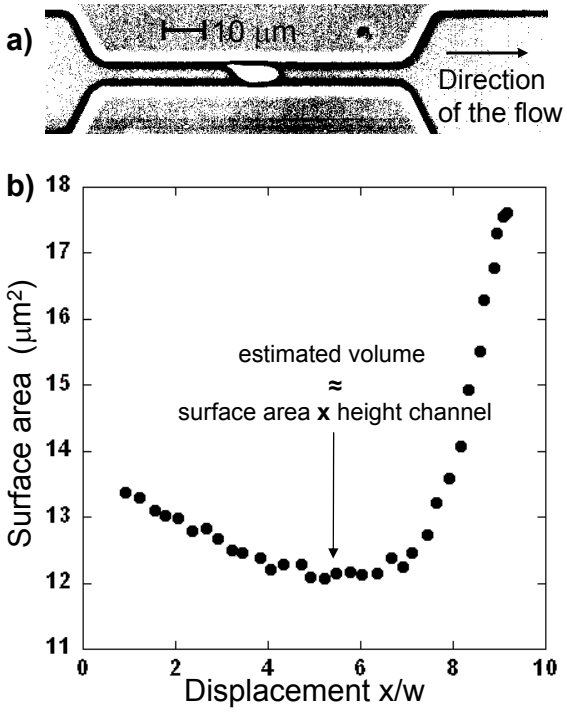

Figure 7.27: *a) Threshold picture of a cell flowing in the device. b) Measured surface area of the cell versus the non-dimensionalized displacement x/a, ℓ_1=60 µm. The estimated volume of the cell is determined as being the minimum surface area times the height of the channel.*

The pressure drop measurements are sensitive to how much the particle clogs the channel; inevitably, the pressure drop is linked to the volume of the object. Therefore, in order to quantify the effect of the volume of the cell on the induced pressure drop, we need to find a reliable way to estimate the object's volume. We are observing the cell from the top. Consequently, we only have access to the projected surface area of the cell inside the channel. We estimate as a first approximation that the volume of the cell is equal to the product of the projected steady state surface area of the object times the channel's height. After treating the movies to obtain thresholded images as shown in Figure 7.27a), we extract the projected surface area of the cell

as a function of its displacement x normalized by the channel width w.

A typical measurement is reported in Figure 7.27b). The minimum value of the projected surface area is chosen for the estimation of the cell's volume: the smaller is the projected surface area, the less stretched is the cell leading to a better filling of the channel's cross section. The estimated volume found with our approximation are consistent with typical values for the volume of RBCs found in the literature (Fung [60] reports a cell volume of 98 fL); a comparison between the two, reveals a slight underestimation of the volume with our method. Finally, we note that the minimum projected surface area is obtained roughly in the middle of the channel.

Velocity of the cell

Next, we examine the velocity of the cells in channels of different lengths: 60 μm and 100 μm. In particular, we track an individual cell along the device and report its speed as a function of the position of the cell's center of mass x normalized by the channel width w (Fig. A.3a)). The origin of time is chosen as when the cell enters the channel. We also show in the figure the sequence of deformation for a cell in the 100 μm long channel.

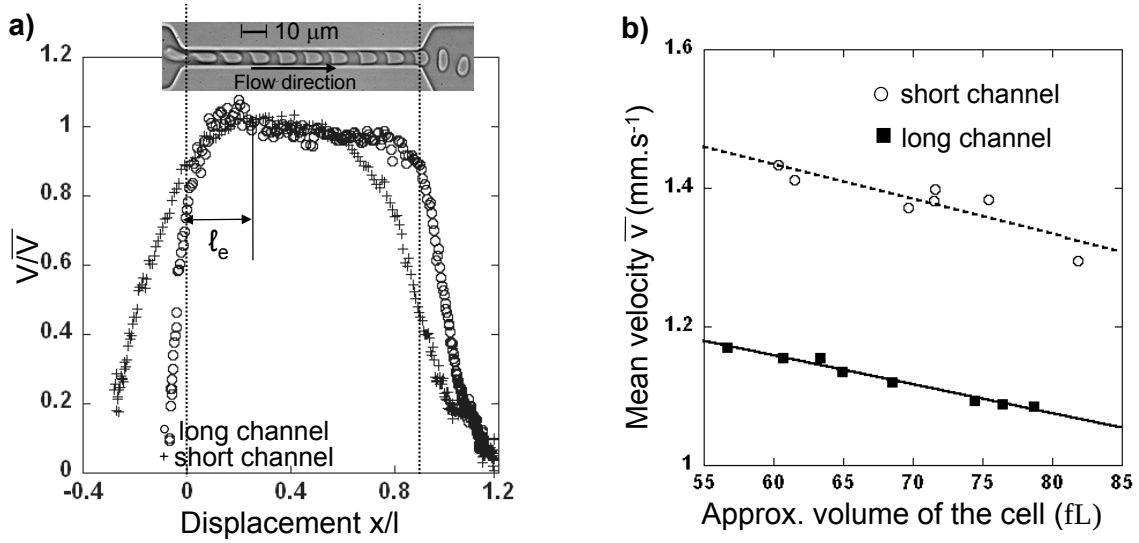

Figure 7.28: *a) Speed of 2 cells of same volume (≈ 65 fL), versus its non-dimensionalized displacement x/a. + ℓ_1=60 μm long channel, ∘ ℓ_1=100 μm long channel. $\overline{v}$ is the mean velocity of the cell. ℓ_e represents the length necessary to the cell to reach a steady speed. Insert represents a sequence of deformation of the cell flowing in the channel (ℓ=100 μm). b) Mean speed $\overline{v}$ of the cell versus its approximate volume. ∘ l_1=60 μm long channel, ■ ℓ_1=100 μm long channel.*

We observe that the speed of a RBC increases as it approaches the entry of the channel. Once inside the channel, the particle velocity continues to increase until it reaches a steady speed; we note that in both experimental trajectories there is a small overshoot in the speed. We note that it takes a certain "entrance" distance ℓ_e to establish a steady-state velocity $\overline{v}$. Our measurements, including others not reported in this paper, indicate that ℓ_e is approximately five times the width of the channel (or three times the typical size of a cell). The details of this adjustment depend on the way the cell enters the channel, e.g. whether it enters along or above the centerline. Finally, as they approach the exit, the cells slow down to adopt the new downstream flow profile. We

note that the curves for the entry and the exit velocity versus position have similar features. The results of the curve Fig. A.3a) is qualitatively similar as the results obtained by Diaz and Co-workers [38] about the entrance of an elastic capsule in a cylindrical pore presented earlier in this manuscript (Fig. 3.13).

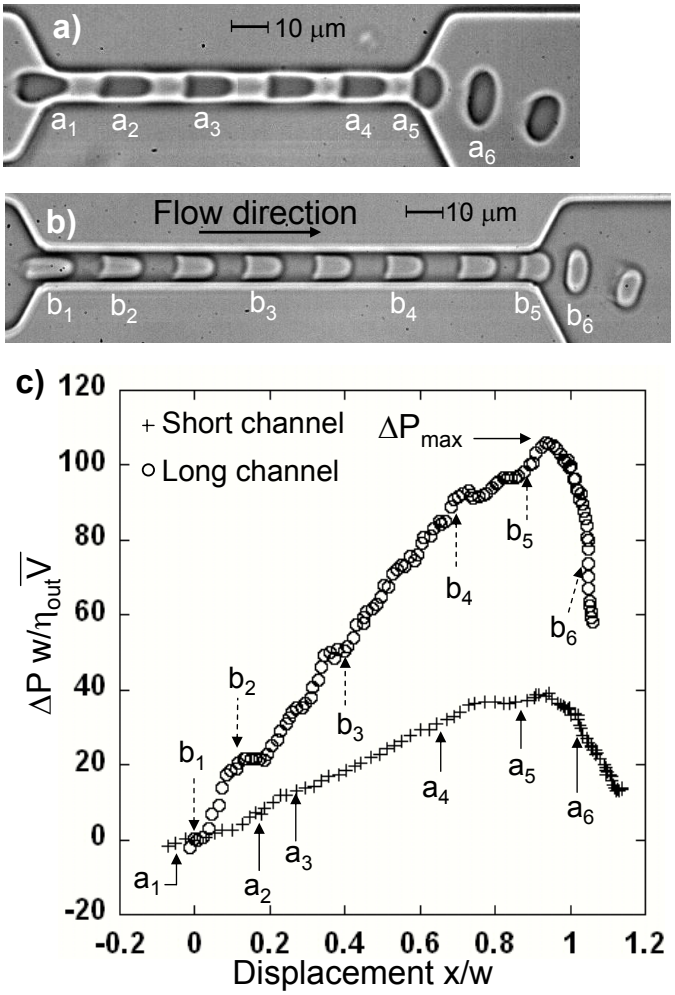

Figure 7.29: *a)Sequence of deformation of a cell entering the short channel, l_1=60 μm. b) Sequence of deformation of a cell entering the long channel, l_1=100 μm. c) Measured pressure drop versus the non-dimensionalized displacement of the cell x/a. + l_1=100 μm long channel, ○ l_1=60 μm long channel. ΔP_{max} is the maximum drop of pressure.*

We next compare two cells of about the same volume in channels of different lengths. First, as shown in Figure A.3a), the two cells increase their speed at about the same rate as they enter the channel. The speed of the cell flowing in the 100 μm long channel reaches a plateau $\overline{v} \approx 1.15$ mm/sec. The cell flowing the short channel is just able to establish a steady speed $\overline{v} \approx 1.35$ mm/sec, before being influenced by the exit. This difference can be explained by the different hydraulic resistances in the test channels due to small variabilities in fabrication. The hydrodynamic resistance of the channels are $\propto \ell/w^3$, and thus the ratio of resistances is $(60/4.7^3)/(100/5^3)) \approx 0.7$, which is approximately the ratio of the speeds in the two channels $(1.15/1.35 \approx 0.85)$. It may also be the case that even though the two cells have approximately

the same volume, thy do not block the channels the same way, which may also influence the speed. A careful examination of the picture in Figure A.3a) indicates that cell continues to deform even after having reached a steady speed.

We made many measurements of the mean cell speed $\overline{v}$ as function of the the approximated cell volume. The results are shown in Figure A.3b), which indicate that the speed of the cell is decreasing linearly with their volume.

Pressure drop measurements

The sequence of deformation of a cell with an estimated volume of 65 fL flowing in a 60 μm long channel, is reported on the Figure 7.29a). Another cell of the same estimated volume, flowing in a 100 μm long channel is presented on the Figure 7.29b). The cells deform as they enter the channels(respectively a_1 and b_1). While flowing along the channels (a_2, a_3 and b_2, b_3), the shape of the RBCs evolves to reach a steady shape (a_4 and b_4). At the exit of the channels, the cells get stretched (a_5, a_6 and b_5, b_6) and elongate perpendicular to the flow, then relax to the final relaxation shapes.

The excess pressure induced by the presence of a cell in the channel is represented in Fig. 7.29c) as a function of displacement x/w. As the cell goes along the channel, the pressure drop increase to finally reach a maximum ΔP_{max} before decreasing with the exit of the RBC. We notice that as the cells deform to exit the channel ((a_5) et (b_5)), the drop of pressure increases slightly before returning back to normal. We first notice that both drop of pressure increases with the same slope. In the case of shorter channel, the RBC leaves the device before reaching a steady pressure drop. We report on the graph the different positions corresponding to the deformation states of the cells shown in Figure 7.29a) and b).

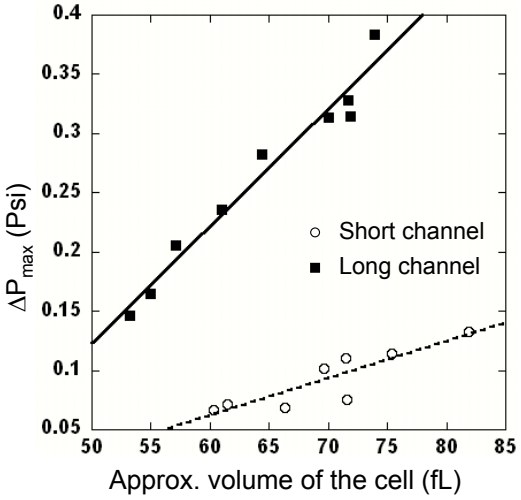

Figure 7.30: *Measurement of the maximum pressure drop ΔP_{max} versus the approximate volume of the cell. ○ ℓ_1=60 μm long channel, ■ ℓ_1=100 μm long channel.*

We report the pressure drop as a function of the approximate volume of the cells on Figure 7.30. The excess pressure seems to be linear with the volume of the cell. The drop of pressure in the

long channel is systematically higher than the pressure drop in the shorter channel for cells of same volume. This difference is due to the fact that the cells exit the shorter channel before reaching the plateau, i.e. the maximum steady pressure drop.

7.4.8 Lysis of a cell

As an other example illustrating the new insights that can be obtained with our microfluidic differential manometer in Figure 7.31a), we visualize an inflated cell approaching the entrance to a channel (A), deforms to flow through the channel - (B) and (C) - and the subsequent hemolysis event (the cell membrane ruptures) (D). The pressure drop associated with the lysis is presented in Figure 7.31b). When the blockage event begins, the pressure drop increases linearly and reaches a maximum value about 0.4 psi when hemolysis happens. We then see the ghost of the RBC - (E) and (F) - as well as the hemoglobin solution exiting the channel; we can note that the hemoglobin follows the parabolic velocity distribution. The critical value of stress necessary for hemolysis, measured to be 0.38 Psi is in good agreement with the approximate value 4000 Pa $\approx$ 0.6 psi found with static micropipette experiment on pre-swollen RBCs [108].

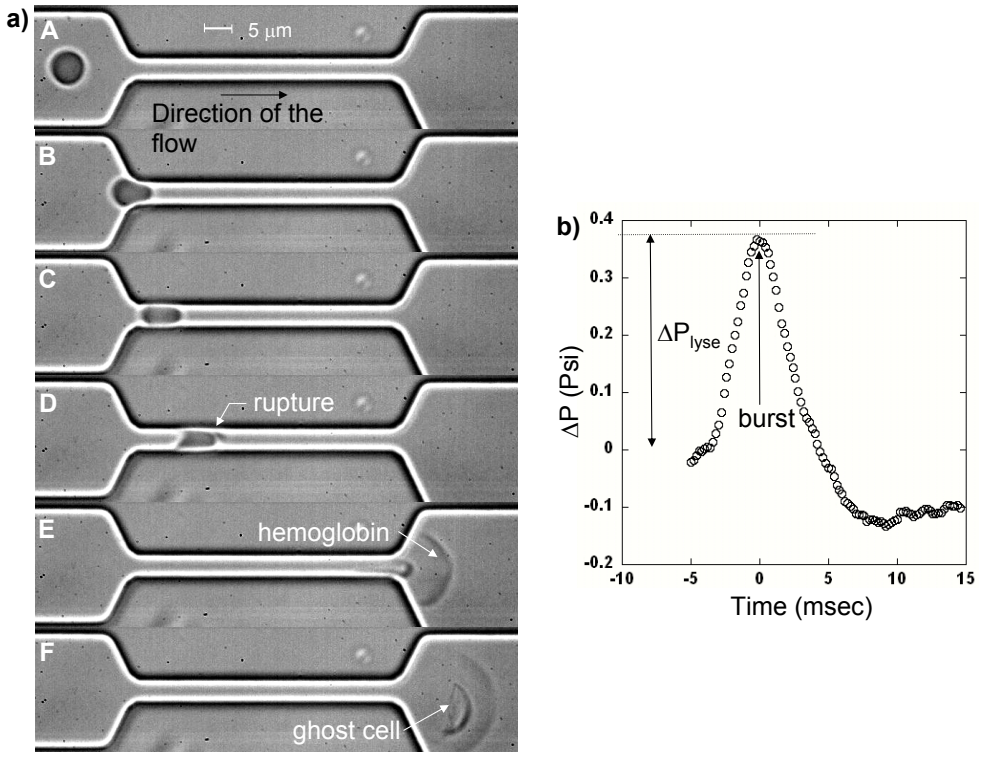

Figure 7.31: *a) Sequence of deformation and lyse of an inflated red cell in a 60 µm long channel. b) Pressure drop associated with the burst of the cell in the channel.*

Lets just note that it takes roughly three milliseconds to the interface to reach back the equilibrium position, while the overall crossing of the same channel by a regular cell takes around 100 msec. This tends to confirm that the motion of the interface corresponds to the instantaneous value of the excess of pressure induced by the flow of the cell in the close-fitting channel.

7.4.9 Conclusion

Recent advances in computational mechanics have treated cell entry and translation in cylindrical geometries with models for the mechanical response of the cell. In one study [126], the red blood cell is treated as a viscous droplet surrounded by a thin elastic membrane of 2D modulus μ_m. The dynamical response of these systems depends on the capillary number which is a dimensionless parameter $C_a = \eta_{out} v_0/\mu_m$, where η_{out} is the viscosity of the outer fluid and v_0 is the mean velocity of the fluid in the channel. For example, the maximum additional pressure drop ΔP_{add} during the flow is calculated to be $\Delta P_{\text{add}} = O(10-100)\mu_m/R_t$ for $10^{-3} < C_a < 0.05$, where R_t is the radius of the circular capillary (see Fig. 14 in [126]). Using the measurements in Figure 7.26, our results give $\Delta P_{\text{add}=9\mu_m}/R_t$, which is in good agreement with the order of magnitude from the computational model. Finally, we note that the computational models provide ΔP_{add} as a function of the position along the channel and our results are in qualitative agreement. A detailed comparison of simulation and experiment would require the same geometry and should in principle allow extraction of the mechanical properties.

7.5 Flow of RBCs through a constriction [53]

At the heart of our investigation lies the concept of hydrodynamic lift of deformable cells in shear flow and the cell-free layer produced adjacent to the boundaries. These ideas are commonly discussed in the hemodynamics literature. Indeed, one of the oldest and best known hemodynamic phenomenon of the microcirculation is the Fähraeus effect [70, 123], which refers to the decreased hematocrit concentration in small tubes relative to the larger reservoirs to which they are connected [19]. The Fähraeus effect is well understood as arising from hydrodynamic drift of the deformable cells away from the high shear rate (and high shear stress) regions adjacent to the walls of the vessel [59, 69, 71]. Thus, a cell-free layer, typically comparable to the size of a single cell, exists in large portions of the microcirculation. This cell-free layer is also responsible for the nonuniform distribution of cells in a vessel network such as a tissue. Briefly, the concentration of red blood cells in a network of daughter arterioles, capillaries or venules in the microcirculation can be lower than the concentration in the mother feeding vessel; this is usually referred to as the plasma skimming or the network Fähraeus effect [70, 123]. As we show below, we used the plasma skimming concept as a developmental strategy to design a microdevice for separation of cells from plasma.

It is well known that when a suspension of cells flows in small vessels (arterioles or venules), there exists a cell-free layer of few microns adjacent to the vascular walls [52, 19]. Using an *in vitro* model, we show experimentally that a geometrical constriction in the flow can artificially enhance the cell-free layer up to ten times its original value before the constriction, for a fixed flow rate. Hence, we show that rapid variation of the geometry coupled to the deformability of the cells can dramatically modify their spatial distribution in the channel. The effects of the constriction geometry, flow rate, suspending fluid viscosity, cell concentration, and cell deformability are studied and the results are interpreted in terms of a model of the hydrodynamic drift of an ellipsoidal cell in a shear flow. We propose a microfluidic application of this focusing effect for separation of the red blood cells from the suspending plasma.

7.5.1 Experimental procedures

The blood used in all of the experiments was collected and prepared according to the experimental procedures related at the beginning of this chapter in 7.1. For most of the experiments, two concentrations of red blood cells were studied: 0.1% v/v and 2.6% v/v hematocrit. In order to test the effect of the viscosity of the surrounding fluid, two suspending media were prepared by dissolving dextran in the PBS buffer. The viscosities of the solutions were measured to be 0.02 Pa.s and 0.047 Pa.s, respectively, at concentrations of 6% and 9% w/w dextran.

The rigidity of the red blood cells was modified by a standard method [44] as explained in the section 7.1 and dispersed in a solution of dextran with a viscosity of 0.02 Pa.s. We also changed the osmotic pressure of the cells with the protocol explained earlier and the cellular solution was dispersed in a solution of dextran with a viscosity of 0.02 Pa.s made with the hypotonic buffer. Such hypotonic conditions swell the cells [47].

As a control we also studied trajectories of polystyrene beads of 8.7 microns in diameter, dispersed in a solution of dextran at a viscosity of 0.02 Pa.s. This size particle was chosen since it is the same as the maximum diameter of the RBCs.

Experiments were performed in a microfluidic setup with the flow rate driven flow approach described in section 4.2.2. The geometry of the microfluidic channel is presented Figure 7.32. We varied the width w and the length L of the constriction as well as the applied flow rate from 10 to 1000 μL/hr, which corresponds to an average fluid speed of 0.1 to 10 cm.s^{-1}. Movies were taken with a high-speed camera using a frame rate between 2000 and 5000 frames.s^{-1}.

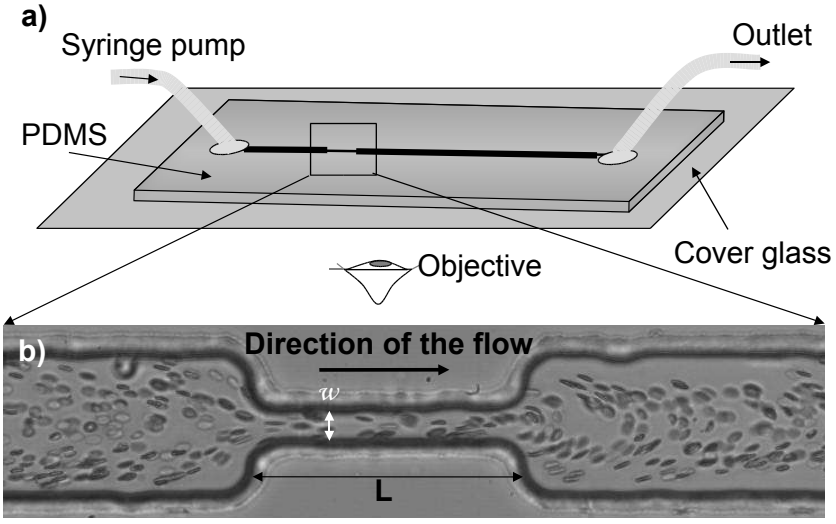

Figure 7.32: *Microfluidic setup for the flow of red blood cells through a constriction. The channel height is 75 μm and the dimensions of the constriction shown are L=200 μm and w=25 μm (a) Side view. (b) Top view.*

Procedures for image analysis were performed with the software "Image J" for the experiments with 2.6% hematocrit. We proceeded to the projection of an image along the axis perpendicular to the image plane of the movie of each experiment in order to detect the statistical distribution

of red blood cells at a given position along the channel. The projection of the average intensity is output such that each pixel stores the average intensity over all images in the movie stack at a corresponding pixel location [9]. Hence, a region where statistically a large number of red blood cells pass will appear darker than the background (see Figure 7.34a). In the case of the experiments conducted with a low concentration of cells (hematocrit of 0.1%), this approach is inefficient for localizing the cell-free layer (not enough cells are passing). Therefore, we also measured the cell-free layers on a given movie by visually locating the red blood cells closest to the walls and measuring their distance to the walls up- and downstream. We applied this second method to some movies obtained at 2.6% hematocrit in order to verify the good agreement of the results obtained by the two different procedures.

In the next section we present experimental observations of a narrow cell-free layer upstream of the constriction [72, 89, 30, 117] and we document how this cell-free layer is substantially enhanced downstream of the obstruction. We systematically investigate the enhancement of the width of the cell-free layers downstream of the constriction by varying the flow rate, the geometry, the concentration or hematocrit, the viscosity of the suspending fluid, and the mechanical properties of the cells. Finally, the experimental results are used to design a separator that takes advantage of this constriction-enhanced cell-free layer.

7.5.2 Behavior of rigid spheres

First, it is important to recognize the constraints associated with low-Reynolds-number flows [27] and to exhibit the flow profiles for rigid particles. In Figure 7.33 we show the trajectories of the centers of mass of rigid spherical particles, which have a size comparable to red blood cells, for typical flow conditions where the Reynolds number (based on the channel height) is about 0.01; the Reynolds number is calculated as $\rho_{out}Q/(\eta_{out}H)$, where ρ_{out} and η_{out} are, respectively, the density and viscosity of the suspending phase, Q is the flow rate, and H is the channel height. The trajectories are fore-aft symmetric about the center of the constriction, as expected since such particles follow the fluid and the streamlines of the flow are fore-aft symmetric when the Reynolds number is less than one. Consequently, for the asymmetric trajectories of red blood cells that we show below for the same magnitude of Reynolds numbers, we conclude that the asymmetries and the corresponding enhanced cell-free layer are due to some combination of the deformability and non-spherical shape of the cells.

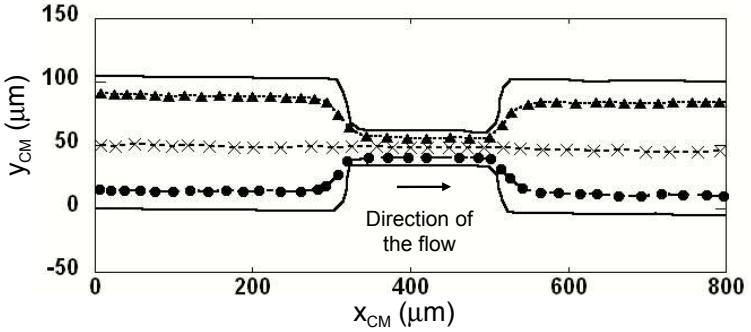

Figure 7.33: *Trajectories of three spherical polystyrene beads (8.7 microns in diameter) dispersed in a dextran solution with viscosity 0.02 Pa.s; Q=50 μL/hr, L=200 μm and w=25 μm.*

7.5.3 Cell-free layers up- and downstream of the constriction

We begin with a description of the typical experiments with red blood cells in constricted flows (Figure 7.34). In particular, there are regions of the flow that have essentially no cells, *i.e.* cell-free layers. We measure the locations and widths of the cell-free layers and we report also the widths of the distribution of cells before and after the constriction as shown in Figure 7.34a. The gray-level image in Figure 7.34a illustrates the existence of a cell-free layer, about 4 μm in width (which is half the size of a cell), before the constriction and clearly documents the substantial influence of the constriction on the downstream flow. A plot of the gray-scale values across the channel, both up- and downstream of the constriction, is shown in Figure 7.34b. For the conditions in Figure 7.34, the downstream cell-free layers have been enhanced to about 18 μm, which is roughly twice the size of the cell. We scanned more than 1 centimeter downstream of the constriction and, perhaps surprisingly, the enhanced cell-free layer remains largely unchanged.

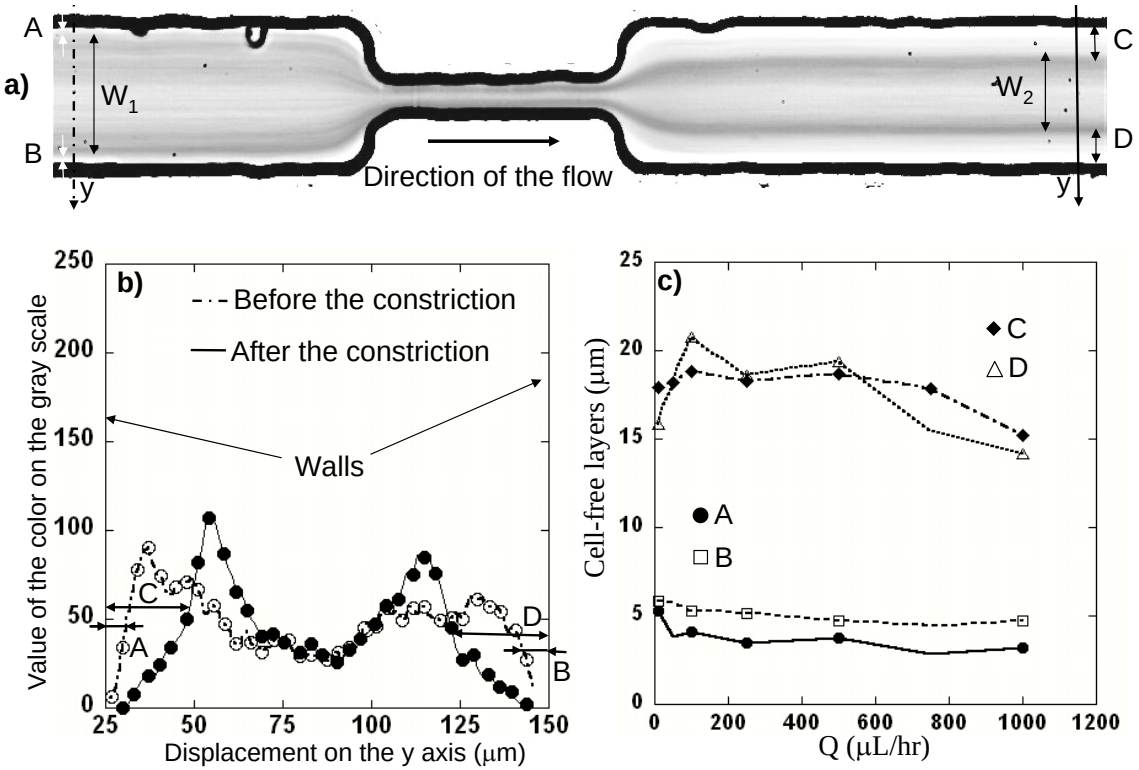

Figure 7.34: *(a) Image obtained after treatment of a typical movie by "Image J" software. A, B and C, D represent the cell-free layers, respectively, up- and downstream and W_1 and W_2 denote the widths of the distributions of the cells, respectively, before and after the constriction; L=200μm and w = 25 μm. (b) Value of the intensity of the gray scale versus the displacement y across the channel (○) before and (●) after the constriction. (c) Measured cell-free layers versus the flow rate Q with a Hematocrit at 2.6%. The red blood cells are suspended in a dextran solution with viscosity 0.02 Pa.s; L=300 μm and w=25 μm.*

The data also suggest one additional feature introduced by the constriction: assuming an approximate correspondence between the gray-scale level and the cell number density, we note in Figure 7.34b that there appears to be a maximum cell density off the centerline and somewhat close to the wall. We shall return to this point below.

7.5.4 Enhancement of the downstream cell-free layer as a function of the different parameters

Effect of the flow rate

We next investigate the effect of the flow rate. In Figure 7.34c, we report, as a function of the flow rate Q, the evolution of the cell-free layers at the top and bottom walls up- and downstream of the constriction, respectively labeled as A,B and C,D. We note in the Figure 7.34c that the effect of the constriction is symmetrical top to bottom, as the cell-free layers near the upper and lower walls are equivalent (A≈B and C≈D). Upstream of the constriction the cell-free layers A and B are equal in width (on the order of 4 microns) and slightly decrease with the flow rate Q. The cell-free layers C and D decrease only a little as we increase Q and tend to the same value (about 15 μm).

We then extract the widths of distribution of the red blood cells up- and downstream, respectively denoted W_1 and W_2. A plot of the ratio W_2/W_1 with Q is shown in Figure 7.35a for four different lengths of the constriction. Representative images of the different geometries are shown also. The results show very little variation of the cell-free regions with the flow rate, but the cell-free layer is enhanced significantly for larger lengths of the constriction. Because of the weak effect of Q on W_2/W_1, the results are presented for a fixed flow rate Q=50 μL/hr.

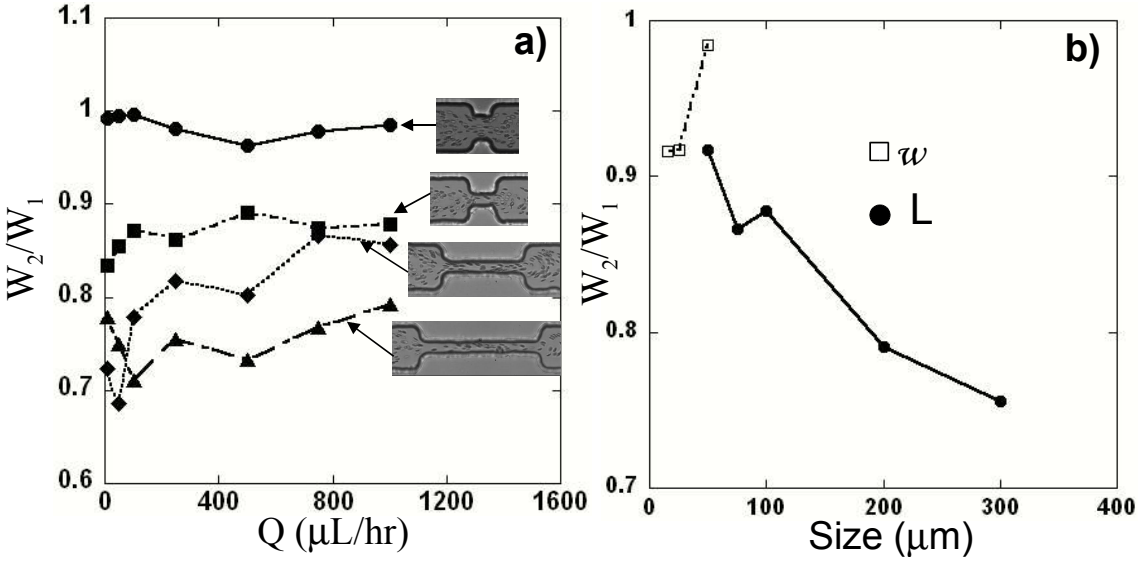

Figure 7.35: *(a) Ratio of the widths of distribution of the red blood cells W_2/W_1 versus the flow rate Q for different geometries of the constriction: • (L=50µm and w=50 µm), ■ (L=75 µm and w=25 µm), ♦ (L=200 µm and w=25 µm) and ▲ (L=300 µm and w=25 µm). (b) Ratio of the widths of distribution of the cells W_2/W_1 versus the length L or the width w of the constriction for a fixed flow rate of Q=50 µL/hr. For both (a) and (b) the dextran solution has viscosity 0.02 Pa.s and the hematocrit concentration is 2.6%. Typical images of the relative length of the constriction are shown on Figure 4a.*

Effect of the geometry

It is clear that the constriction is responsible for enhancement of the cell-free layer so we now document the effect of the geometry of the constriction for a fixed viscosity of the outer fluid of 0.02 Pa.s. The mean values of W_2/W_1 (Figure 7.35a) are extracted from the gray-level data and reported versus the length L of the constriction for a fixed width w or versus w for a fixed L. These results are shown in Figure 7.35b. Although we do not have extensive data on the influence of the constriction width, it is nevertheless clear that the cell-free layer after the constriction is enhanced as the constriction gets longer and narrower.

Effect of the cell concentration

There are several physical properties of the liquid and the cells that may impact the enhancement produced by the constriction so we next turn to these experiments. First, we modify the cell (hematocrit) concentration. In Figure 7.36, we report the ratio W_2/W_1 versus the length L of the constriction for two very different concentrations of 0.1% and 2.6% for a fixed outer fluid viscosity (0.02 Pa.s). The results illustrate that an increase in the cell concentration results in an enhancement of the width of the cell-free layer downstream.

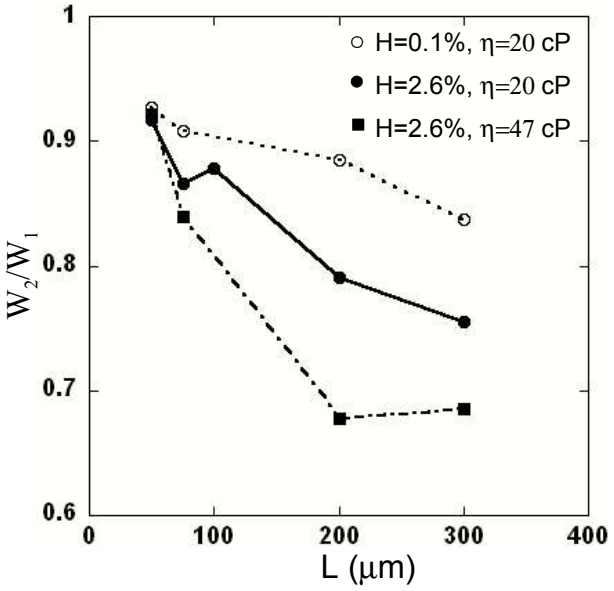

Figure 7.36: *Ratio of the widths of distribution of the cells W_2/W_1 versus the length L of the constriction (for w=25 μm) for different hematocrit concentrations and solution viscosities (Q=50 μL/hr).*

Effect of the buffer viscosity

We have modified the viscosity of the suspending fluid by changing the concentration of dextran. The results are presented in Figure 7.36 for two different viscosities of the suspending fluid. An increase of a factor two in the viscosity of the solution results in an enhancement in the thickness of the downstream cell-free layer.

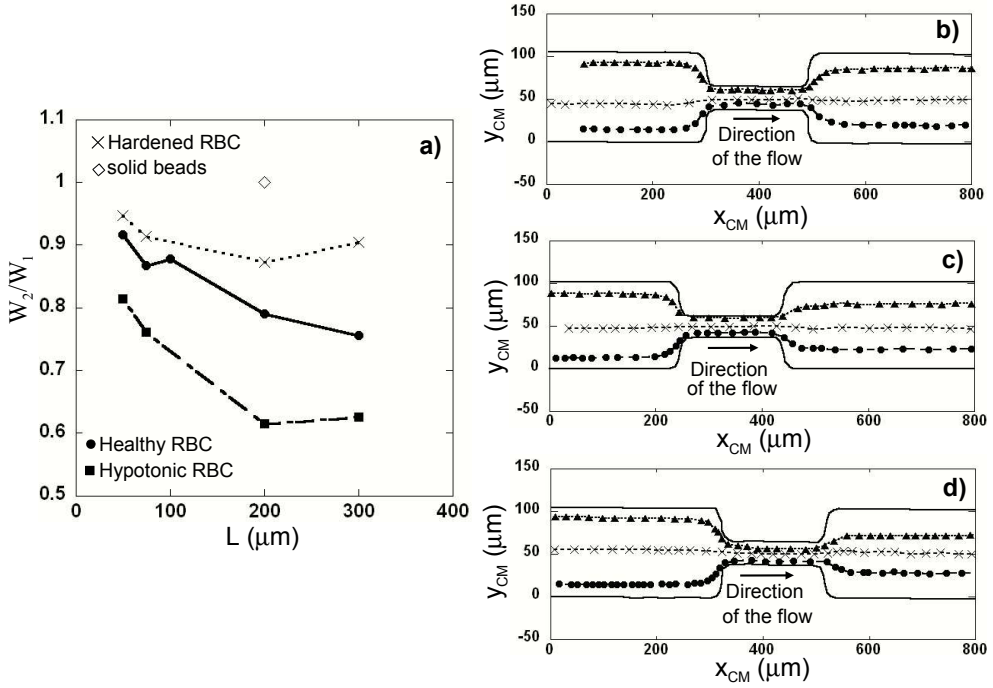

Figure 7.37: *(a) Ratio of the widths of distribution of the cells W_2/W_1 versus the length L of the constriction (for w=25 μm) for different kind of red blood cells. Typical trajectories of (b) Hardened RBCs, (c) Healthy RBCs and (d) Hypotonic RBCs. The flow rate and the outer fluid viscosity are fixed respectively at Q=50 $\mu L/hr$ and $\eta = 0.02$ Pa.s.*

Effect of the deformability and volume of the cells

We have already indicated that the deformability of the red blood cells is the key to understand the enhancement of the cell-free layer. Thus, we next report results for different degrees of deformability. Four types of particles are used to conduct the experiments: solid spherical beads, healthy cells, hardened red blood cells and hypotonic erythrocytes (*i.e.* cells that are swollen due to a lower osmotic pressure). For these experiments the viscosity of the suspending fluid is fixed at 0.02 Pa.s. The results are reported in Figure 7.37 in two ways: in Figure 7.37a we report W_2/W_1 as a function of the constriction length L for each of the different particles and in Figures 7.37b-d we report trajectories for each of the three different types of experiments with the red blood cells. We observe that the experiments conducted with rigidified red blood cells show an enhanced cell-free layer after the constriction compared to the cell-free layer upstream. However this effect is smaller than for healthy cells. The results in Figure 7.37a indicate that an increase in the volume of the cells (*i.e.* the hypotonic data) leads to an enhancement of the downstream cell free-layer; see also the trajectories in Figures 7.37c,d.

7.5.5 Summary of the effects

It is well known that flows in the microcirculation are characterized by a narrow cell-free layer adjacent to the walls of the capillaries. This cell-free layer is the origin of the Fähraeus effect [70, 125, 124], which we observe upstream of the constriction. Moreover, we have identified a new feature of this old phenomenon, at least with respect to the interpretation in terms of the number density distribution of cells, through the enhancement of this cell-free layer downstream

of a constriction. In order to understand the various results, we collect the major experimental observations in Table 7.5.5. In particular, the cell-free layer downstream is enhanced with increases in the length of the constriction, the concentration of cells, the viscosity of the suspending media, the cell deformability, and the volume of the cells. A decrease in the width of the constriction increases the cell-free layer. In addition, the flow rate does not affect in a significant way the measured downstream cell-free layer.

parameters	range of variation	downstream cell-free layer
Q ↗	10-1000 μL/hr	weak effect
L ↗	50-300 μm	increased
w ↘	50-15 μm	increased
hematocrit ↗	0.1%-2.6%	increased
η ↗	20-47 cP	increased
deformability and volume ↗	solid beads, hardened, healthy and hypotonic cells	increased

Table 7.2: *Summary of the effects of the different parameters on the cell-free layer downstream of the constriction.*

7.5.6 Non-uniform cell concentration

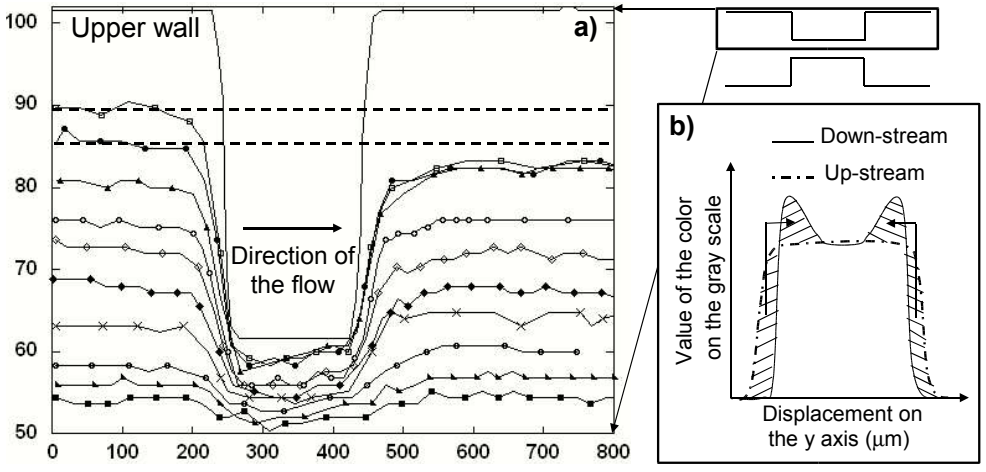

Figure 7.38: *(a) Trajectories of the center of mass of healthy cells dispersed in a suspending media with a viscosity of 0.02 Pa.s, Q=50 μL/hr. (b) Sketch of the value of the intensity of the gray scale (or number density of cells) versus the displacement y across the channel: dashed line before and solid line after the constriction.*

The radial dispersion of solid and deformable objects in low-Reynolds-number flows is documented in the literature [72, 68, 69], but to the best of our knowledge the effect of a constriction on this dispersion has not been investigated. We previously noted in Figure 7.34b that there was evidence pointing to the constriction giving rise to a local maximum in the cell number density at positions off the centerline. Therefore, we tracked individual cells in order to understand how the drift occurs at different positions across the channel; these results are shown in Figure 7.38a.

After the constriction, the three closest cells from the wall end up on about the same streamline. We also note that beyond a certain distance from the wall all of the cells have fore-aft symmetric trajectories.

These results provide a rational explanation for a local non-centered maximum in the number density of cells downstream of the constriction (see Figure 7.34b) and the idea is indicated in the sketch in Figure 7.38b: the concentration of cells gets modified by the migration across streamlines of the cells closest to the wall. Therefore, downstream of the constriction the maximum concentration is positioned just at the edge of the cell-free layer, while the cell concentration at the center of the channel remains unchanged.

7.5.7 Interpretation in terms of drift

We interpret these results quantitatively in terms of the cross-streamline drift undergone by the cells [72, 89, 30, 117], which occurs in the high shear rate region (*i.e.* the constriction). Although the detailed hydrodynamic description is complicated, some basic features are summarized in a model [117] of a tank-treading ellipsoidal cell in a shear flow adjacent to a planar boundary: the flow is assumed to be at low Reynolds numbers, and the object, assumed far from the wall, migrates away from the wall with a drift velocity v_d that depends approximately linearly on the shear rate $\dot{\gamma}$; the drift across streamlines results in enhancement of the cell-free layer. In our experiments, the cell experiences this drift primarily during the time τ it is in the constriction, since it is there that the shear rates are the highest. Although in our system we cannot expect quantitative agreement since the cells are never far from the wall, we use the functional form suggested by Olla [117] as representative since the basic physical ideas are similar. The drift d is predicted to be of the form:

$$d = v_d.\tau, \tag{7.15}$$

with the drift velocity v_d given by [117]:

$$v_d = \kappa \frac{\dot{\gamma} R^3}{h^2}, \tag{7.16}$$

where R is the radius of the sphere of same volume as the cell, h is the distance of the particle to the wall in the constriction as described in Figure **??**a, and κ is a dimensionless parameter dependent on the orientation of the tank-treading cell and its shape, which in turns also depends on the viscosity ratio η_{in}/η_{out} between the cell and the suspending medium (the same scaling for the drift velocity was obtained by Chaffey et al. for the drift away from a wall of a deformable drop in a shear flow [30]. The parameter κ is proportional to the capillary number of the drop). The known analytical result for flow in a narrow channel with $w < H$ gives:

$$Q = \dot{\gamma} H w^2/6 \tag{7.17}$$

Knowing the relationship between the shear rate and the flow rate Q for a rectangular channel of length L, width w and height H, given by 7.17, estimating the passage time in the constriction as $\tau \approx LwH/Q$, and combining equations (7.15) and (7.16) we obtain:

$$d \approx 6\kappa \frac{LR^3}{wh^2}. \tag{7.18}$$

Neglecting the impact of shear rate on the parameter κ, we note that according to equation (7.18) the drift is independent of the flow rate applied, which is in agreement with the results shown in Figures 7.34c and 7.35a. In order to test (7.18) we selected a value of h (measured at the middle of the constriction, see figure 7.39a), representative of typical cells at the outermost edge of the cell-free layer, and measured the cross-streamline drift downstream of the constriction for various values of both L and w; because of the expansion, the spacing of the streamlines changes downstream of the constriction by the geometric ratio w_c/w, where w_c is the width of the main channel, and so for this measurement we expect:

$$d \approx 6\kappa \frac{LR^3 w_c}{w^2 h^2}. \tag{7.19}$$

The experimental results are shown in Figure 7.39b, which indicates that the final value of the cell-free layer d varies linearly with a parameter characteristic of the geometry of the constriction Lw_c/w^2 as predicted here.

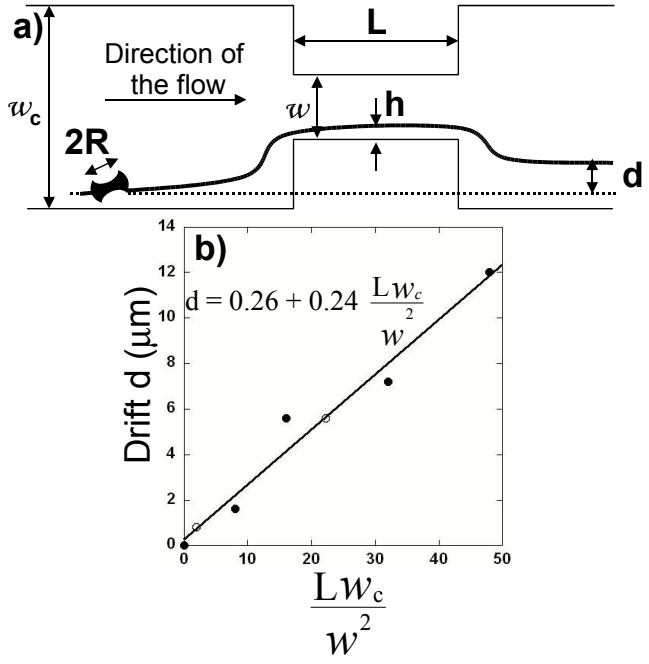

Figure 7.39: *((a) Definition of the parameters for the calculation of the drift d. (b) Drift measured (for h=2.4 μm) versus* $\frac{Lw_c}{w^2}$ *for • w=25 μm, L varying and for ∘ L=50 μm, w varying. The suspending media has a viscosity of 0.02 Pa.s, and Q=50 μL/hr.*

It is possible to estimate the prefactors from the idealized theory of Olla [117] and also compare with the experimental measurements. We used the experimental value of 1/2 for the ratio of the cell internal viscosity to the suspending fluid. We then used equation (7.19), to determine κ from the experimental data in Figure 7.39b. We find $\kappa \approx 0.01$. For a deformed cell with a prolate shape with aspect ratio 1/5 (consistent with the photographs) Olla's model calculation gives $\kappa \approx 0.45$. Thus, we conclude that qualitative and scaling features of the idealized theory are quite reasonable though quantitative agreement is clearly complicated owing to the complexity of the actual geometry and flow.

There are three further points to make. First, a decrease of the osmotic pressure of the suspending fluid from 300 mOsm/kg to 200 mOsm/kg results in a 23% increase of the volume of the cells [47]. In our experiments we find a significant enhancement of the cell-free layer when the cell volume is increased as documented on Figure 7.37a. This result is quantitatively consistent with the dependence of d on the volume of the cell ($\propto R^3$).

Second, we examine the variation of the drift distance d with the deformability of the cells. When the concentration of the cells is increased, the effective viscosity of the solution is also increased, [137] and, correspondingly, the parameter κ is known to decrease as the viscosity ratio between the cell and the suspending fluid decreases. This response is consistent with our experimental results relating the cell concentration, deformability and the suspending media.

Third, we note that from a technological perspective, small devices introduced into a blood vessel in order to monitor, detect, and sample a flow, or to assist in drug delivery, may also act as a local obstruction. Although, the hematocrit concentrations we used are ten times or more less than typical physiological values, and the buffer viscosities used during our experiments are higher than the *in vivo* conditions. Nevertheless, such perturbations may apply to physiological conditions and may modify the downstream distribution of the blood cells. Similar effects should occur in the flow of deformable particles, such as capsules or droplets, in viscous flows in constricted channels.

7.5.8 Technological application

Finally, we apply the principle of the enhanced cell-free layer to the implementation of a microfluidic component for the separation of blood from plasma. In the Figure 7.40, we show a device where downstream of the constriction there are three channels in parallel. Because of the enhanced cell-free layer, the liquid collected in the outermost channels is totally composed of plasma (a). When we increase the width of the outermost channels to extract more plasma some cells are also entrained (b). In such cases, decreasing the width or increasing the length of the constriction again leads to the extraction of essentially pure plasma as shown successively in (c) and (d).

In addition, the volume of plasma withdrawn from the initial solution of blood can be estimated. Knowing the initial concentration of the solution (16 %v/v), its total volume (1 mL), the flow rate of injection (200 μL/hr), and estimating the flow rate through the outermost channels (typical particle mean velocities are measured to be about 1.4 mm/s), we can estimate the ratio between the initial volume of blood and the volume of plasma extracted. We find for the conditions shown in figure 7.40a that 24% of the initial plasma is continuously withdrawn, and, equivalently, the cellular content in the middle channel is enriched by 24%.

7.5.9 To conclude

In this section, we reported experiments on the flow of red blood cells in model constrictions. We showed how a rapid variation of the cross-section coupled with the deformability of the cells can produce a dramatic enhancement of the cell-free layer. We studied the influence of all the physical parameters on this geometrically enhanced cell-free layer. We used this knowledge to design a separator of blood plasma and demonstrated our control on the flow by varying the geometrical parameters such as the length and width of the constriction. Finally, it should be

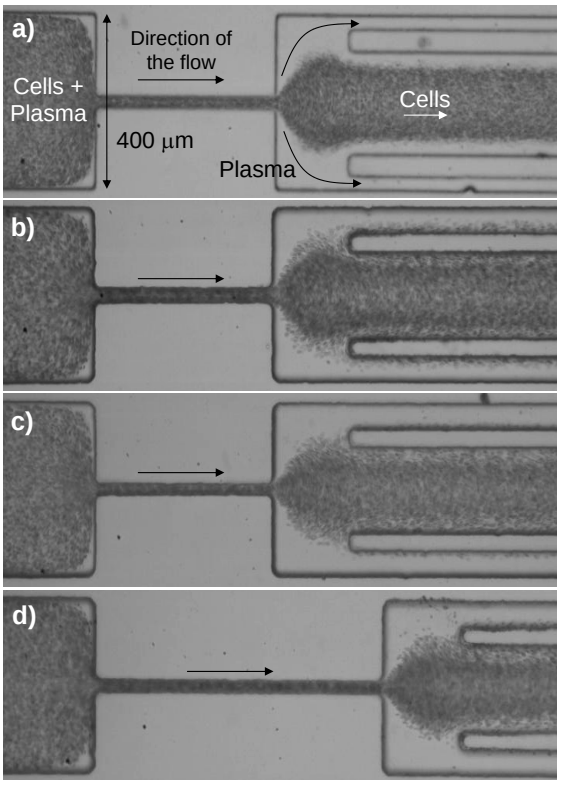

Figure 7.40: *A microfluidic design for separating plasma from blood. (a) $w = 25\mu m$, $L = 500\ \mu m$, $Q = 200\ \mu L/hr$, width of the outermost channel is 30 μm. (b) Increase of the width of the outermost channel to 50 μm, with $w = 25\ \mu m$, $L = 500\ \mu m$, $Q = 200\ \mu L/hr$. (c) Decrease of the constriction width to $w = 15\ \mu m$ with $L = 500\ \mu m$, $Q = 200\ \mu L/hr$ and the width of the outermost channel is 50 μm. (d) Increase the length of the construction to $L = 800\ \mu m$ with $w = 25\ \mu m$, $Q = 200\ \mu L/hr$, and the width of the outermost channel is 50 μm.*

noticed that such kind of constrictions could mimic natural geometric blockages associated with a thrombotic microangiopathy and other diseases of the arterioles and venules [**?**]. Our in-vitro experiment suggests that the cell-free layer present in the microcirculation could be affected by a natural or artificial constrictions, which we refer to a geometrically enhanced Fähraeus effect. Other variants of these physical ideas to effect separation of plasma from blood cells should be possible as we have demonstrated in Figure 7.40.

Chapter 8

Conclusion

Durant ce travail de thèse nous avons étudié la réponse mécanique de trois types d'objets différents - gouttes, vésicules et globules rouges - sous champs externes : principalement sous écoulement, mais aussi sous dégonflement osmotique et sous l'action de la température. Les propriétés mécaniques d'objets mous très différents: une goutte acqueuse avec un réservoir quasi infini de surfaceet dont la forme est gouvernée par les r'egles de tension de surface, une membrane lipidique à surface fixée, dont la forme est déterminée par le module de courbure, un globule rouge dont l'élasticité de la membrane est la clé de sa déformabilité, sont au centre de cette étude. Bien que les caractéristiques physiques de ces objets soient différentes, ils expriment des comportements similaires sous la même gamme de stress. Ainsi nous rapportons nos observations concernant le comportement de ces trois objets soumis à des contraintes variées ; et nous établissons les effets de la modification de leurs propriétés mécaniques, et des différents param'etres du probl'eme, sur leur comportement.

La production de tensioactif à l'interface de gouttes acqueuses change la tension de surface de l'objet induisant des déformations et des comportements spécifiques. Nous avons notamment mesuré l'effet de la concentration en réactifs, i.e. l'effet du taux de production du tensioactif, de même que l'influence de la géométrie sur le comportement des gouttes. Les formes adoptées par les gouttes s'écoulant dans des capillaires de dimensions similaires ne sont pas sans rappeler les formes axisymétriques rapportées dans le diagramme de forme des globules rouges.

En effet, nous avons établi un diagramme de formes de globules rouges s'écoulant dans des capillaires de dimension similaire. Nous avons notamment montré l'existence d'un nombre capillaire critique $Ca = \eta_{out} v/\mu_m$ au-dessus duquel on observe la transition de la forme de parachute à celle de pantoufle. Nous avons aussi observé la transition d'une position centrée du globule dans le capillaire vers une position décalée par rapport à l'axe de symétrie du tube ; cette transition a lieu pour une valeur critique de la taille du capillaire par rapport à la taille du globule.

Nous avons montré l'expression de l'élasticité de la membrane du globule rouge à travers sa réponse dynamique sous écoulement de cisaillement. Nous avons révélé, à faible taux de cisaillement, un nouveau régime caractérisé par des oscillations de l'angle d'inclinaison de la cellule (typique d'une capsule élastique), oscillations superposées au mouvement de chenille de char. Nous avons développé un modèle qui prédit à la fois les oscillations, et la dépendance de la transition entre les deux mouvements par rapport au taux de cisaillement appliqué. Le model démontre l'existence d'une mémoire de forme élastique de la membrane ; il permet la détermi-

nation de la viscosité de membrane et celle du module élastique.

La chute de pression additionnelle produite à l'échelle d'une cellule individuelle est une autre expression des propriétés mécaniques du globule rouge. Afin d'évaluer ce paramètre, nous avons mis au point un système microfluidique permettant la mesure dynamique de variations de chute de pression le long d'un canal de taille microm'etrique. L'influence de la modification des propriétés mécaniques de la membrane, due à des traitements chimiques, est montrée. Enfin nous avons observé simultanément une hémolyse sous écoulement de même que la pression de lyse associée.

L'étude de l'effet de la déformabilié sur le comportement d'une solution concentrée de globules rouges sous écoulement est une étape importante dans l'étude de la dynamique du sang. Nous avons montré expérimentalement que la déformabilité des cellules, couplée à une rapide variation de la géométrie, peut modifier de mani'ere dramatique leur distribution spatiale dans le canal. Les effets de la déformabilité, de la concentration en cellules, de la géométrie de la constriction, du débit et de la viscosité de la solution tampon ont été étudiés ; et les résultats sont interprétés par un modèle réalisé pour une particule ellipsoïdale soumise à un écoulement de cisaillement s'éloigant de la paroi. Nous proposons une application microfluidique de cet effet de concentration pour la séparation des globules rouges du plasma environnant. Les effets collectifs ont été étudiés en détail par une série d'expériences oú le nombre de cellules a été varié.

Nous avons également fabriqué des vésicules aux propriétés visco-élastiques. Nous avons montré que l'encapsulation d'un hydrogel de PolyNIPAm conf'ere des propriétés mécaniques spécifiques, en particulier une haute résistance des vésicules aux contraintes. Elles affichent une transition de volume déclenchée par la température. Les expériences en temp érature ont également suggéré l'existence d'une forte intéraction entre la membrane et le polymère encapsulé. La concentration et la nature des composés du contenu des vésicules peuvent être variées afin de moduler à la fois leurs propriétés mécaniques et la température de transition. Une caractérisation compl'ete des propriétés mécaniques d'une de ces vésicules "résistantes" est l'une des continuations logiques de ce travail.

Même si nos objets ont des propriétés mécaniques spécifiques - tension de surface pour les gouttes, module de courbure pour les vésicules, module élastique pour les globules rouges - nous avons observé des déformations similaires et des comportements identiques dans la gamme de stress explorée. Les propriétés mécaniques complètes des objets sont délicates à extraire de nos observations. Toutefois, l'interconnexion des efforts analytiques, numériques et expérimentaux permettent l'évaluation des caractéristiques mécaniques de ces objets (élasticité, tension de surface, ou grande viscosité de membrane).

Les perspectives ouvertes par un tel travail sont nombreuses. Premi'erement, la continuation logique de ce travail de th'ese est l'étude du comportement de tous les objets présentés dans ce maniscrit (gouttes avec ou sans tensioactif, vésicules viscoélastiques ou vésicules dans la phase gel, et globules rouges), sous écoulement dans la même géométrie ; de telles expériences sont actuellement en cours de réalisation. On pourrait aussi s'intéresser à l'utilisation de la flexibilité du design et à la facilité de fabrication de syst'emes microfluidiques en PDMS de mani'ere à mimer des écoulements pathologiques ou encore à étudier la dynamique de cellules sanguines et autres objets biomimétiques dans un réseau de canaux représentant toute une section de la

microcirculation. Finalement l'étude de la dynamique de cellules malades (malaria, anémie falciforme...) et de cellules traitées chimiquement, de même que des objets biomimétiques modifiés, peuvent mener à la caractérisation des effets de telles maladies ou traitement pharmaceutique sur le comportement de cellules sanguines sous écoulement.

During this PhD thesis, we studied the mechanical response of three different types of objects - drops, vesicles and red blood cells - submitted to different stresses: principally under flow, under osmotic pressure and with the action of the temperature. The modification of mechanical properties of soft objects as different as: an aqueous droplet with an quasi-infinite reservoir of surface area which shape is governed by surface tension's rules, a lipid bilayer membrane with a fixed surface area, which shape is determined by the bending modulus and a red blood cell which elasticity of the membrane is the key to its deformability. Although their physical characteristics are different, they express generic behavior under the same range of stresses. Thus, we report in this manuscript our observations of the behavior of the three objects submitted to various stresses and document the effect of the modifications of their mechanical properties and the different parameters of the problems on these behaviors.

The production of surfactant at the interface of the aqueous droplets changes the surface tension of the object inducing specific deformations and dynamics. We assessed the effect of the reagents concentration, i.e. the effect of surfactant production rate, as well as the influence of the geometry on the behavior of the droplet. The shapes adopted by the drops flowing in close-fitting channel are not without remembering the axisymmetric shapes reported in the phase diagram of RBCs shape.

Indeed, we established a phase diagram of shapes of RBCs flowing in close fitting channels. Indeed, we showed the existence of a critical capillary number $C_a = \eta_{out} v/\mu_m$ triggering the transition from the parachute-like shape to the non-axisymmetric slipper-like shape. We also observed a transition from a centered to a non-centered position relative to the axis of symmetry of the capillary tube happens for the relative size of the capillary to the typical RBC's size.

We showed that another signature of the elasticity of the cell's membrane is the dynamics of RBCs under shear flow near a plane. We revealed a new regime of motion for RBCs under small shear flow, characterized by an elastic capsule-like oscillation of the cell inclination superimposed to tanktreading that we name swinging. We developed a model, which predicts both swinging and the shear-stress dependency of the tumbling-tanktreading transition. It demonstrates the existence of the elastic shape memory in the membrane and, from the interplay with the tanktreading movement, allows to determine both membrane viscosity and elastic shear modulus.

The additional pressure drop produced at the scale of individual flowing cells is another expression of the mechanical properties of red cells. To measure this parameter, we designed a high-speed microfluidic device for measuring dynamical pressure-drop variations along a micrometer-sized channel. The influence of drug-modified mechanical properties of the RBC membrane is shown. Finally, single hemolysis events during flow are recorded simultaneously with the critical pressure drop for the rupture of the membrane.

The study of the effect of the cell deformability on the flow of a concentrated solution of blood

cells is an important step on the study of the blood dynamics. We showed experimentally that the deformability of the cells coupled to a rapid variation of the geometry can dramatically modify their spatial distribution in the channel. The effects of the cell deformability, cell concentration, constriction geometry, flow rate and suspending fluid viscosity were studied and the results were interpreted in terms of a model of the hydrodynamic drift of an ellipsoidal cell in a shear flow. We proposed a microfluidic application of this focusing effect for separation of the red blood cells from the suspending plasma. The collective effects could be studied in more details by a set of experiments where the number of cells flowing in the device would be increased gradually.

We also conferred visco-elastic characteristics to vesicles. We showed that the encapsulation of a hydrogel of PolyNIPAm confers specific mechanical properties, in particular a high resistance, to simple lipid vesicles. They exhibit a reversible volume transition triggered by temperature. Temperature experiments also strongly suggest that an interaction between the membrane and the inner polymer exists. The concentration and the nature of components in the inner volume of the vesicles can be varied to modulate both their mechanical properties and the volume transition temperature. A complete characterization of the mechanical properties of these "resistant" vesicles under stress is the next logical step to be accomplished.

Even though each of our objects has specific mechanical properties - surface tension for droplets, bending modulus for vesicles, elastic modulus for RBCs - we observed similar deformations and generic behavior in the range of stresses explored. The complete mechanical properties of the objects are tricky to extract from our observations. However, the interconnection of analytical, numerical and experimental efforts allow the extraction of mechanical characteristics (elasticity, surface tension, or high membrane viscosity).

The perspectives open by such a work are numerous. First, the logic continuation to this PhD is the study of the behavior of all the objects discussed in this manuscript (drops with or without surfactant, visco-elastic vesicles or vesicles in the gel phase, and red blood cells), under flow in the same geometry; such experiment is actually in progress. One could also be interested in using the flexibility of the design and fabrication of the PDMS microfluidic devices in order to mimic pathologic flows or to study the dynamics of blood cells and other biomimetic objects in a network of channels representing a whole branch of the microcirculation. Finally, the study of the dynamics of diseased (malaria, sickle cell anemia...) and chemically treated cells, as well as modified biomimetic objects, could lead to the characterization of the effect of such diseases or pharmaceutical molecules on the behavior of blood cells under flow.

Appendix A

Modes of production of droplet

Nous présentons dans cette section une comparaison entre deux modes de production de gouttelettes dans un système microfluidique: dans une première méthode les fluides sont propulsés par un pousse-seringue ; et dans la seconde, c'est la pression qui entraine les fluides à travers le dispositif.

The first step to any study involving droplets is the production of the objects. One significant advantage of microfluidic devices is the ability to control the formation of drops at the very scale at which drops are desired. Associated with the specific geometry, the appropriate choice of method to set the fluid into motion has an important impact on the droplets production, as well as on their characteristics. In a first part of this annex, we will detail the two ways of production of droplets commonly used with the microfluidic technique. Then we will present the case of droplet used as chemical containers and how the interfacial production of surfactant modify their behavior under flow.

A.1 Drops production: flow rate versus pressure-driven flows [156]

We experimentally study the production of micrometer sized droplets using microfluidic technology and a flow-focusing geometry. Two distinct methods of flow control are compared: (1) control of the flow rates of the two phases and (2) control of the inlet pressures of the two phases. The flows are at low Reynolds numbers for which the pressure gradient and flow rate are linearly related in a single phase flow. Consequently it might be expected that the two distinct control methods, flow rate versus pressure, would lead to the same details of drop formation. Instead, we document distinct differences between these two approaches for the multiphase flows of interest.

Although we have not yet succeeded in rationalizing all of these differences, it is clear that the significant influence of surface tension, which is known to introduce nonlinearities into the theoretical description (due to the coupling of the shape and the fluid stresses, such as pressure, in the boundary conditions) is likely the major contributor to the significant differences we have identified between volume flow rate and pressure control of drop formation in multiphase flows.

In a first part, we describe the experimental setup for the formation of water drops in oil streams.

We then report, the differences between the two methods by varying the ratio of the dispersed to continuous phase flow parameter, either the ratio of flow rates Q_w/Q_o or the ratio of applied pressures P_w/P_o. In order to characterize the drop formation process we report the droplet speed U, frequency of droplet production f, distance between two consecutive drops d, and the drop length ℓ (which is a measure of the drop size). In the last part, we discuss surface tension effects as a possible difference between the two experiments.

A.1.1 Experimental sets-up and image analysis

Flow-focusing geometry

The microfluidic experiments use relief molds that are produced using common soft-lithography techniques as detailed in section 4.2.2. The experiments are performed using a flow-focusing geometry [64, 65, 66] with a single input channel for both fluids. An illustration of the setup is shown in Figure A.1. The channel height is 75 μm, as measured by a profilometer, the inlet channel width is 100 μm, and the outlet channel width is 100 μm with a 50 μm contraction.

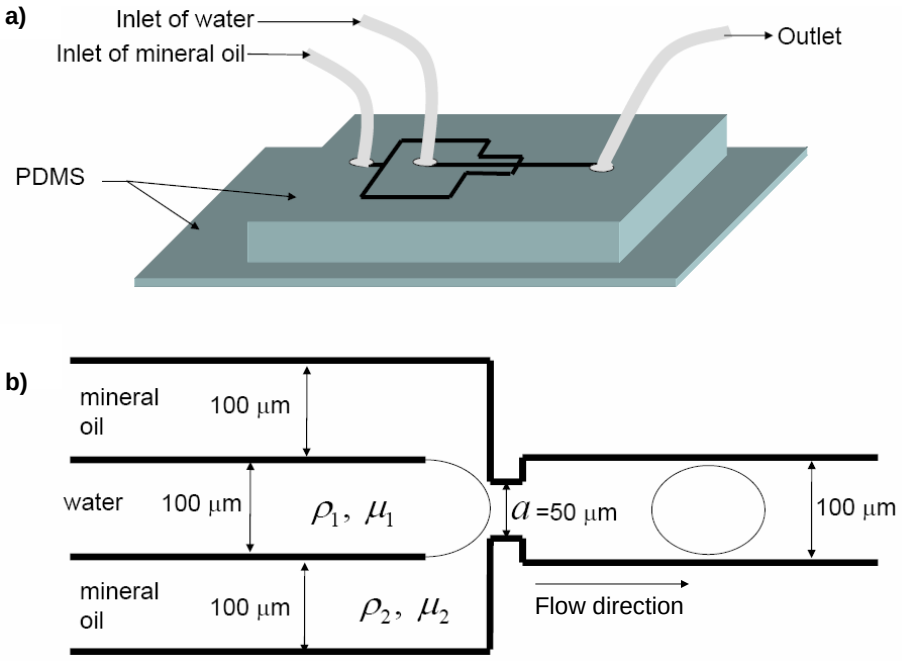

Figure A.1: *Microfluidic setup for the two-phase flow in a flow-focusing geometry. The channel height is 75 μm. (a) Side view. (b) Top view. The principle of the flow-focusing lies in the focusing and then breaking of the water stream by the two streams of oil.*

Propulsion of the fluids

The fluids are driven two ways (described in 4.2.2): by static pressure and by a syringe pump. These methods are distinct since the use of specified pressures sets up corresponding flow rates of the two phases while a syringe pump maintains a specified volume flow rate by appropriate adjustment of the force applied to the syringe, which changes the pressure in the fluid. Although in a single-phase flow these two types of experiment would be equivalent, the same is not true in a multiphase flow since the shape of the fluid-fluid interface, which is determined by the flow

itself, complicates the relationship between the pressure drop and the flow rate.

In the static pressure pumping approach the fluids are placed in syringe tubes and the air pressure above the fluid is regulated. The pressure is controlled by precision regulators (Bellofram Type 10) with a sensitivity of 5 mPsi. The pressure is measured using a test gauge (Wika brand) with a resolution of 150 mPsi. The syringes are connected to their respective inputs of either the dispersed or the continuous phase channel. The syringe approach for fluid delivery requires the choice of a tube diameter and then uses standard motor-driven pumping to achieve a given flow rate.

Solutions

The fluids are mineral oil (viscosity $\eta = 0.123$ Pa.s at room temperature and density $\rho = 880$ kg.m^{-3}) and deionized water for the continuous and dispersed phases respectively. The interfacial tension is estimated to be $\gamma =$O(10) mN.m^{-1} from published data for surfactant free mineral oil and water systems. We assume that all of the fluid properties remain constant at their established values at room temperature.

Image analysis

The images are obtained using high-speed video and drop speeds are determined by tracking the center of mass of individual drops using commercially available software Image J. Distances between droplets, typical size of the objects and frequency of production are also extract from the movies.

A.1.2 Visual differences in flow-rate versus pressure controlled experiments

We first contrast the qualitative features of drop production using flow-rate control (syringe pumping) versus pressure-controlled flow. Typical results are shown side by side in Figure A.2. A direct qualitative comparison is made by visual inspection of the change in the drop size as either the flow rate of the dispersed water phase Q_w is increased for fixed continuous phase flow rate Q_o of the oil phase (Figure A.2a) or as the inlet pressure of the dispersed phase fluid P_w is increased for fixed inlet pressure of the continuous oil phase P_o (Figure A.2b).

The pictures are taken one frame after the liquid thread at the focusing nozzle breaks into a drop. The pictures of drops produced using flow-rate driven pumping show a striking difference to their pressure-driven counterparts. The most notable difference is that as the dispersed phase pressure is increased (by not quite a factor of two) the drop size increases significantly. This response is not true for the flow-rate driven experiments where the drop sizes only change slightly as the water flow rate is increased by a factor of ten.

A.1.3 Quantitative measurements

In a typical experiment, drops of a certain size are formed at a given frequency f and move down the channel at a speed U. The frequency f of drop production is measured by direct counting from high-speed video, and the speed U is measured by tracking the drop center of mass for a short distance down the channel. The photos shown in Figure A.2 gave a qualitative indication of the drop size, and we will return to this topic below. Now we consider contrasting the speeds

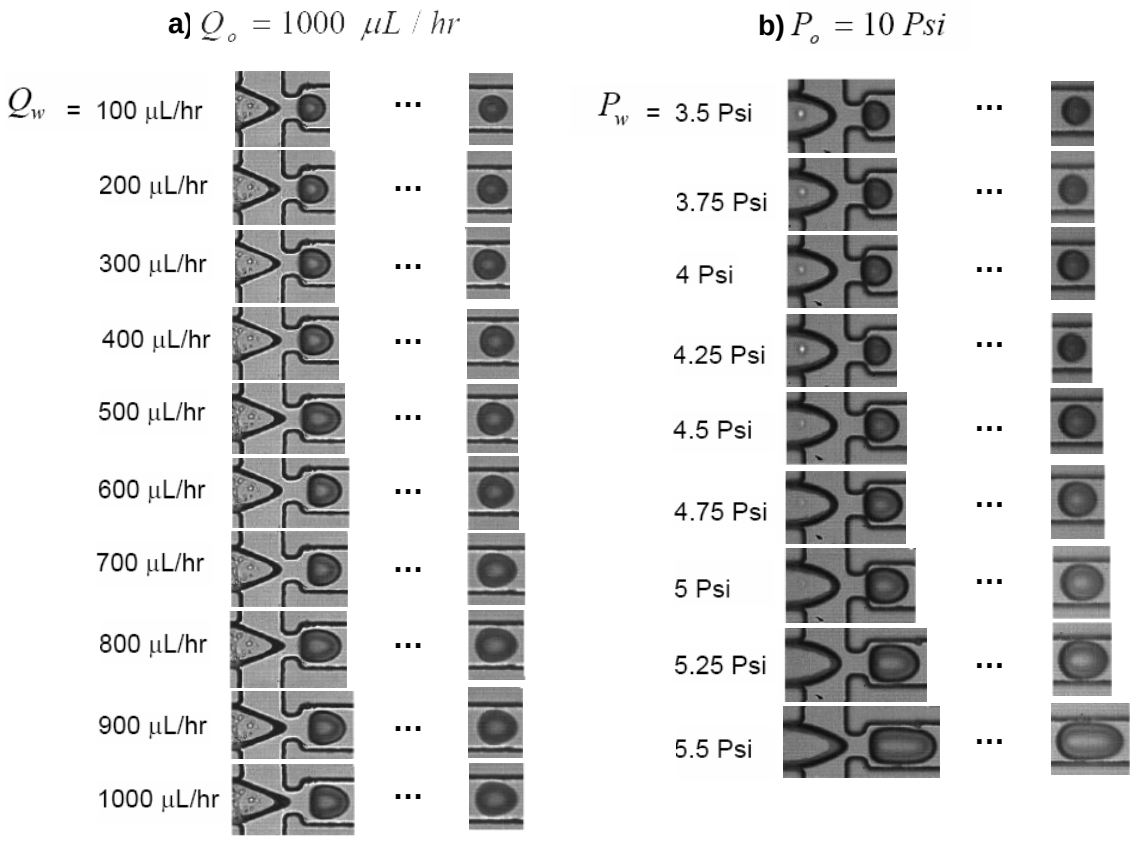

Figure A.2: *Drops produced using (a) flow-rate controlled flow-focusing setup where the oil flow-rate is constant and the dispersed phase flow rate varies as indicated; and (b) pressure controlled setup where the oil inlet pressure is constant and the dispersed phase inlet pressure varies as indicated. A picture is taken one frame after the liquid thread at the focusing nozzle breaks into a drop and a second picture is taken at the exit of the channel to show the equilibrium shape of the drops.*

of the drops in the flow-rate driven versus the pressure-driven approaches.

The drop speeds versus the flow-rate or pressure ratio for different conditions in the continuous phase are shown in Figure A.3. In this figure and all of the other figures below, we use closed symbols to represent the case where the continuous phase flow parameter is held constant, while the dispersed phase flow parameter is increased until a liquid jet is produced and drops no longer form at the orifice. The open symbols are the opposite experiment, where a liquid jet is initially formed at higher values of the operating conditions and then the dispersed phase flow parameter is decreased until the dispersed phase fluid no longer forms drops.

In all these experiments we expect a small difference in velocity between the speed of the drops and the average velocity of the continuous phase due to hydrodynamics of the two-phase flow; we have not however tried to measure this slip velocity systematically. The error bars are typically the symbol size or smaller. In Figure A.3, for flow-rate driven pumping the drop speeds increase approximately linearly with Q_w. In contrast, for pressure-driven pumping there is a minimum pressure ratio, or pressure of the water phase, below which no drops are formed, while above this critical pressure the speeds are approximately independent of the pressure until a higher

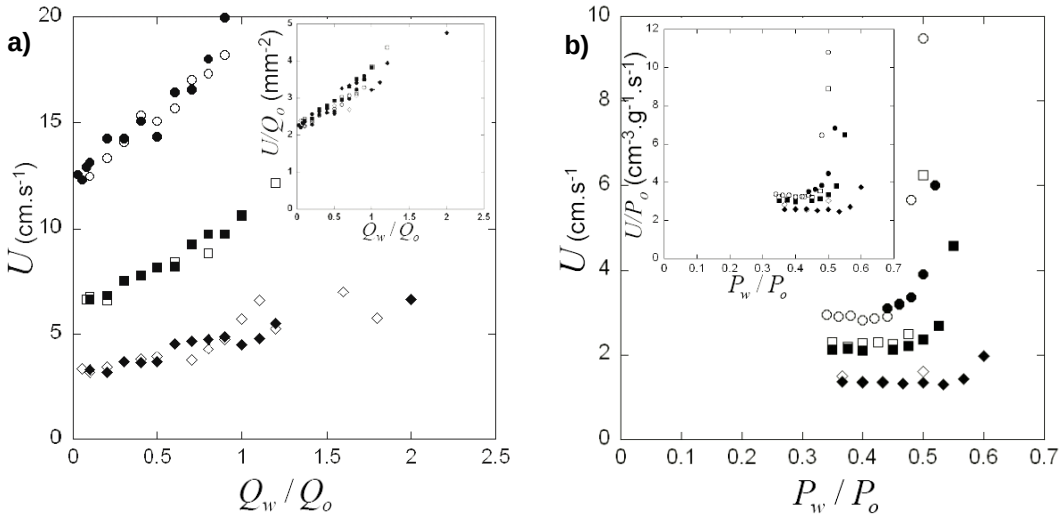

Figure A.3: *Measured velocity U versus (a) flow-rate and (b) inlet pressure ratio for different values of the continuous phase flow conditions.*

critical value at which the speeds increase rather rapidly.

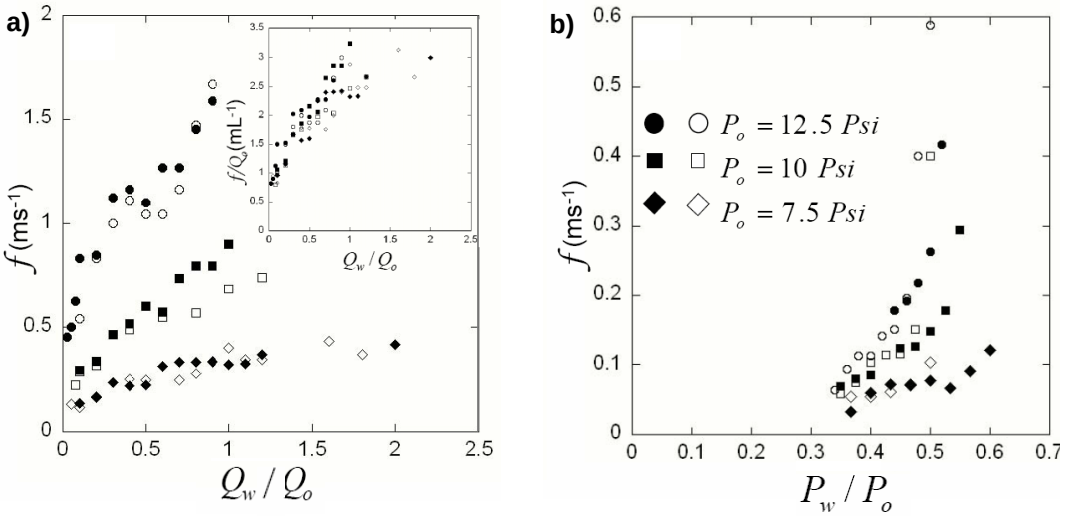

Figure A.4: *Frequency f of drop formation versus (a) flow-rate and (b) inlet pressure ratio for different values of the continuous phase flow conditions.*

The corresponding results for the frequency of drop formation for the two methods of flow control are shown in Figure A.4. The results are reported as the number of drops per millisecond. Again, the error bars are typically the symbol size or smaller. For the conditions used in our experiments there are from zero up to more than 1000 drops formed per second for the flow-rate driven experiments. For the pressure-driven experiments the frequencies are about one-third to one-half as large. In both sets of experiments, the frequencies increase approximately linearly as the independent variable is increased.

Also, for all of the experiments shown in Figures A.3 and A.4 there is essentially no difference

to the results upon either increasing or decreasing the independent variables. For the flow-rate controlled experiments, we have also plotted the frequencies normalized by the external flow rate, and as shown in the inset of Figure A.3 this effectively collapses all of the data.

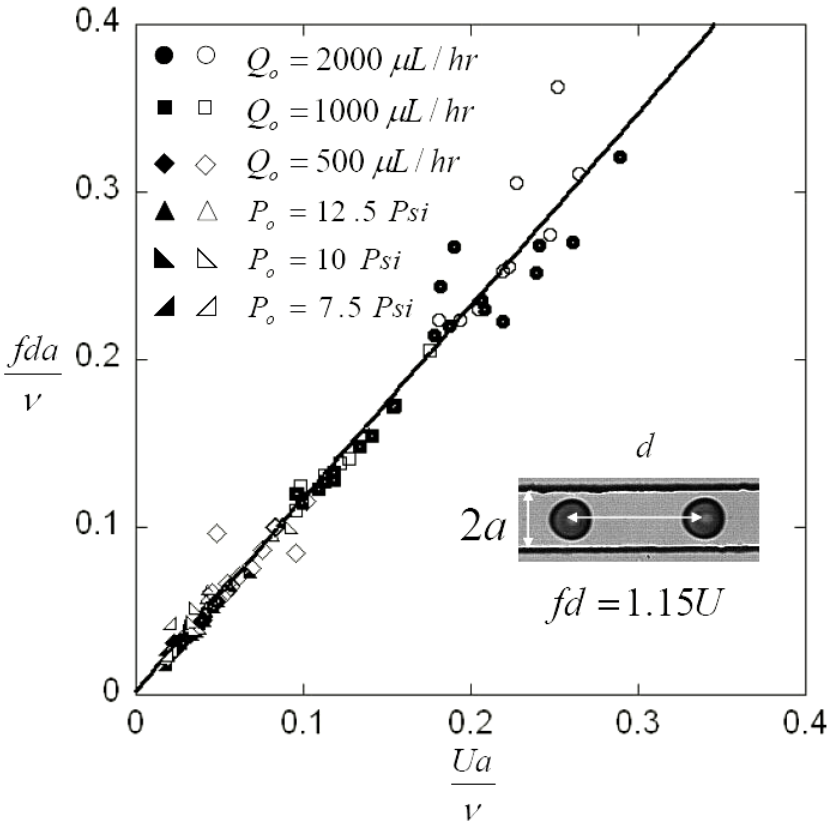

Figure A.5: *Frequency f of drop formation times the distance between drops d versus measured drop velocity U. Both parameters are made dimensionless by scaling with η/a.*

We next provide data on the relative spacing d between the drops as a function of the speed and frequency of drop formation. If the drop spacing is sufficiently large relative to the channel width we expect the train of drops to be stable, though there is evidence for instabilities in the motion of a train of drops when the drops are too closely spaced (S. Quake, private communication). We expect $fd = U$ on geometric grounds and have independently measured all three quantities, d, f, and U.

In Figure A.5 we present a plot of fd versus U in dimensionless terms by essentially converting to an equivalent Reynolds number (e.g. Ua/η, where $2a$ is the width of the channel). As expected the plot is nearly linear, independent of the flow control parameter (inlet pressure or flow-rate); we believe the small difference of the slope from unity reflects experimental errors in the independently measured quantities. It is also now clear that the Reynolds numbers Ua/η are all less than one for all of our experiments so viscous effects should be more important than inertial effects in the dynamical processes.

We next consider in more detail quantitative aspects of the variation of the drop size, ℓ, which,

because of the rectangular shape of the channel, is convenient to report as the end-to-end distance. The results are normalized by the width of the orifice a, which is half the width of the channel for all of the experiments reported here. In Figure A.6 the drops sizes are reported as a function of the flow-rate ratio Q_w/Q_o. The corresponding drop sizes as a function of the pressure ratio P_w/P_o are reported in Figure A.8.

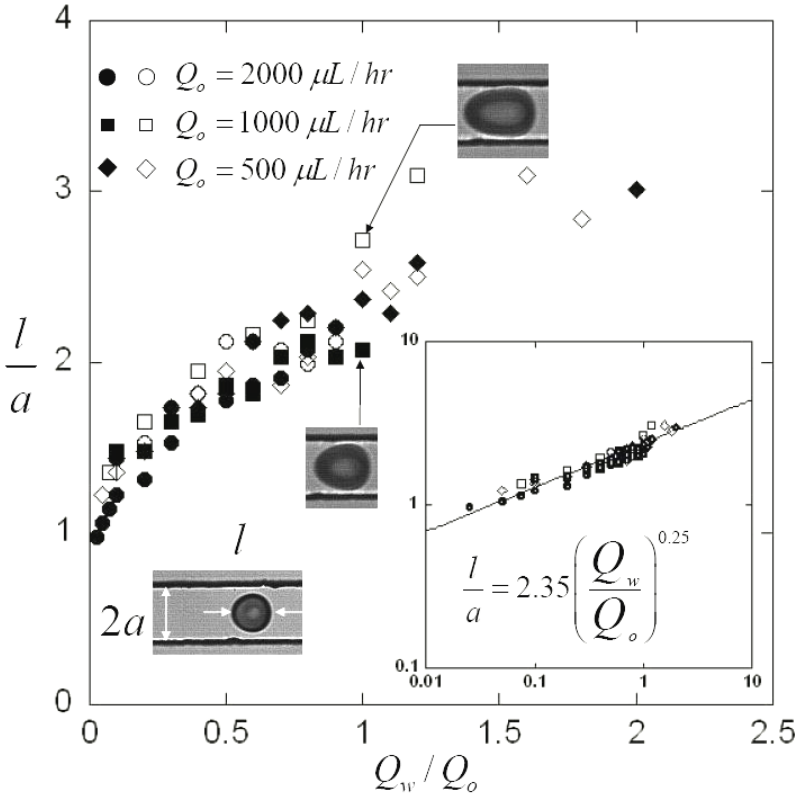

Figure A.6: *Dimensionless drop length ℓ/a versus flow-rate ratio Q_w/Q_o. The inset shows same data using log-log coordinates, where the solid line has slope 0.25.*

In Figure A.6, the drop size as a function of the flow-rate ratio Q_w/Q_o shows very little variation even when the oil flow rate is varied. At the lowest flow-rate ratios the drop sizes are nearly on the order of the flow-focusing orifice size, $\ell/a \approx 1$, which indicates the geometric control of drop size common to many microfluidic experiments. The inset shows the same data on a log-log plot with more than a factor of ten variation in Q_w/Q_o, which indicates an approximate power-law relationship, $\ell/a \propto (Q_w/Q_o)^{0.25}$, obtained by a best fit of the data.

We continue with the data corresponding to the flow-rate driven experiments in Figure A.7a) where we plot the distance, d, between the center of mass of two drops, normalized by the orifice size a, versus the flow rate ratio Q_w/Q_o. At low flow-rate ratios the distance between drops is large and this distances decreases rapidly to a nearly constant value of about three times the width of the orifice; with this spacing the train of drops is stable. We then combine the above results by showing in Figure A.7b) the relationship between the drop size ℓ scaled by the distance between drops d as a function of the flow-rate ratio. When plotted with log-log coordinates, as shown in the inset, the data again appears to be reasonably fit with a power-law

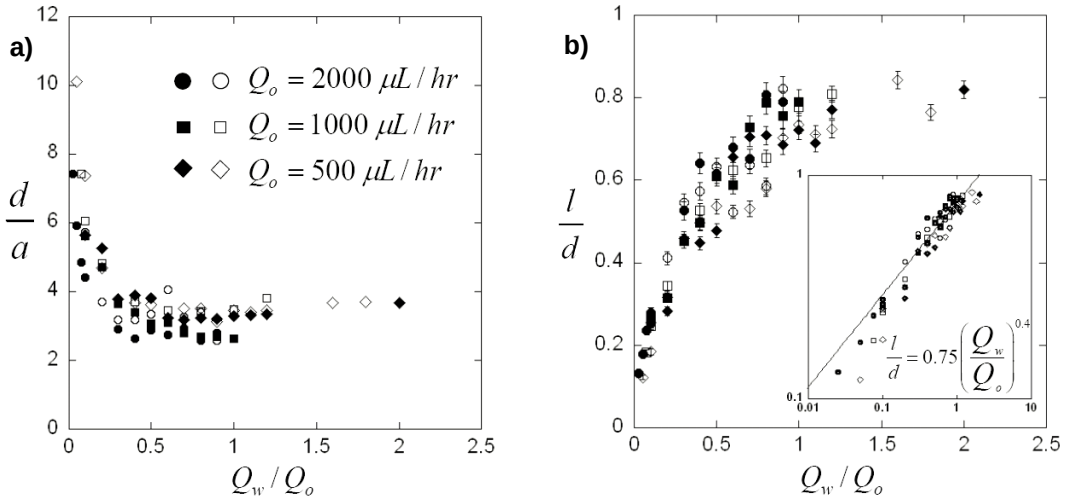

Figure A.7: *a) Distance d between the center of mass of two consecutive drops over versus the flow-rate ratio. b) Dimensionless drop length ℓ/d versus flow-rate ratio. The inset shows the same data plotted in log-log coordinates, where the solid line has slope* 0.4*, which appears the fit the data over two decades of the flow rate ratio Q_w/Q_o.*

relation. Unlike the data scaled by the orifice width the asymptotic value of $\ell/d \approx 1$ is reached at $(Q_w/Q_o)_{max} \approx 1.5$.

The pressure-driven flow rate experiments have some similarities to the flow-rate driven results, though as we shall now see there are both quantitative and qualitative differences. In Figure A.8 we begin with the data for the drop size ℓ/a as a function of the pressure ratio, P_w/P_o. As already indicated above, there is a minimum pressure ratio $(P_w/P_o)_{min} \approx 0.3$ below which the dispersed phase fluid does not penetrate the continuous phase. The minimum drop size for each curve is about the orifice size ($\approx 50\ \mu m$), which indicates the strong geometry dependence in these systems. When plotted in log-log coordinates, as shown in the inset though now there is only a small variation in P_w/P_o, again there appears to be a reasonable fit with a power-law relation, $\ell/a \propto (P_w/P_o)^2$.

In Figure A.9 we show data corresponding to the inlet pressure-controlled experiments. In Figure A.9a) we plot the distance, d, between the center of mass of two drops, normalized by the orifice size a, versus the inlet pressure ratio P_w/P_o. At low inlet pressure ratios $P_w/P_o \to (P_w/P_o)_{min}$ the distance between drops is large and this distances decreases rapidly to a nearly constant value of a little over three times the orifice width, as observed in the flow-rate control experiments. As with the flow-rate driven experiment we combine the results by showing in Figure A.9b) the relationship between the drop size ℓ scaled by the distance between drops d as a function of the inlet pressure ratio. When plotted in log-log coordinates, as shown in the inset with only a slight variation in P_w/P_o, again appears to be reasonable fit with a power-law relation, $\ell/d \propto (P_w/P_o)^3$. Unlike the data scaled by the orifice width the asymptotic value of $\ell/d \approx 1$ is reached at $(P_w/P_o)_{max} \approx 0.55$.

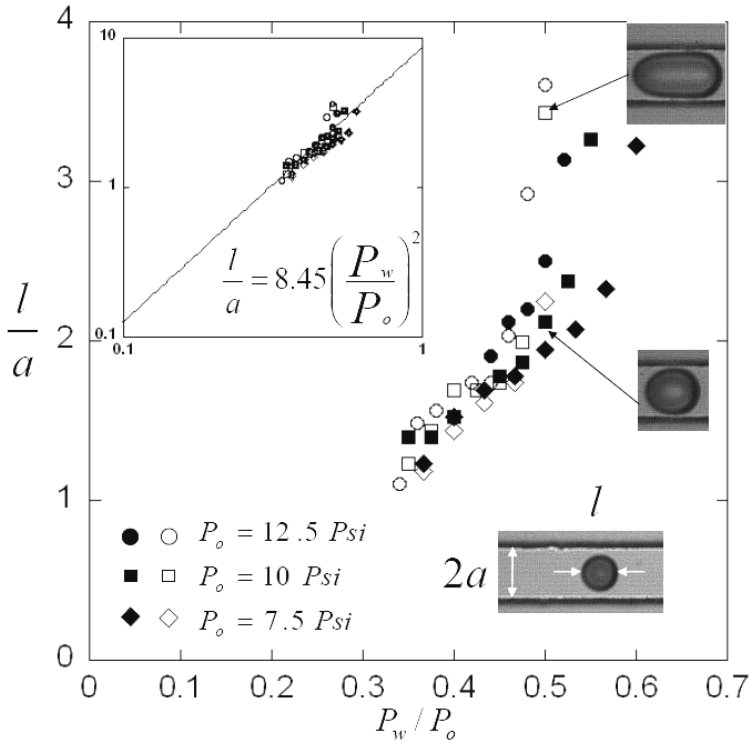

Figure A.8: *Dimensionless drop length ℓ/a versus inlet pressure ratio P_w/P_o. The inset shows the same data using log-log coordinates, where the solid line has slope 2.*

A.1.4 Discussion

In this section we present some ideas for rationalizing the experimental results reported above. To the best of our knowledge there are no general quantitative theories for two-phase flow in a geometry such as the flow-focusing configuration. In the special case that a very narrow thread is formed at and downstream of the orifice, then Ganan-Calvo and coworkers have given quantitative models that are in good agreement with the measurements. All the results presented here are not in this regime. Furthermore, in two-phase flows, the viscosity ratio between the drops is a parameter and our experiments have only considered one viscosity ratio, while varying other parameters and considering two methods of flow control.

There are many quantitative aspects of the flow that can be rationalized using basic fluid dynamical principles. First, the primary difference between fixing the flow rates and fixing the inlet pressures is that in the former case the corresponding pressures are established. The pressure distribution can have a substantial influence on the breakup of the narrow thread formed in the orifice. For example, in gas-liquid flow with a specified flow rate of the external phase, Garstecki et al. (2004) have shown that the rate of drop formation is proportional to the external flow rate, i.e. $f \propto Q_o$. This observation is also at least approximately consistent with the data shown in Figure A.4a) (see the inset). Nevertheless, there is also dependence on the internal flow rate and on dimensional grounds (i.e. dimensional analysis) we thus expect f/Q_o to depend on a capillary number, e.g. $\mathcal{C}_w = Q_w\mu/\gamma a^2$, where μ is the shear viscosity and γ is the interfacial tension. We note that if we assume $f/Q_o \propto \left(Q_w\mu/\gamma a^2\right)^{1/2}$ then we would find $\ell/a \propto (Q_w/Q_o)^{1/4}$, which is consistent with the data in Figure A.6.

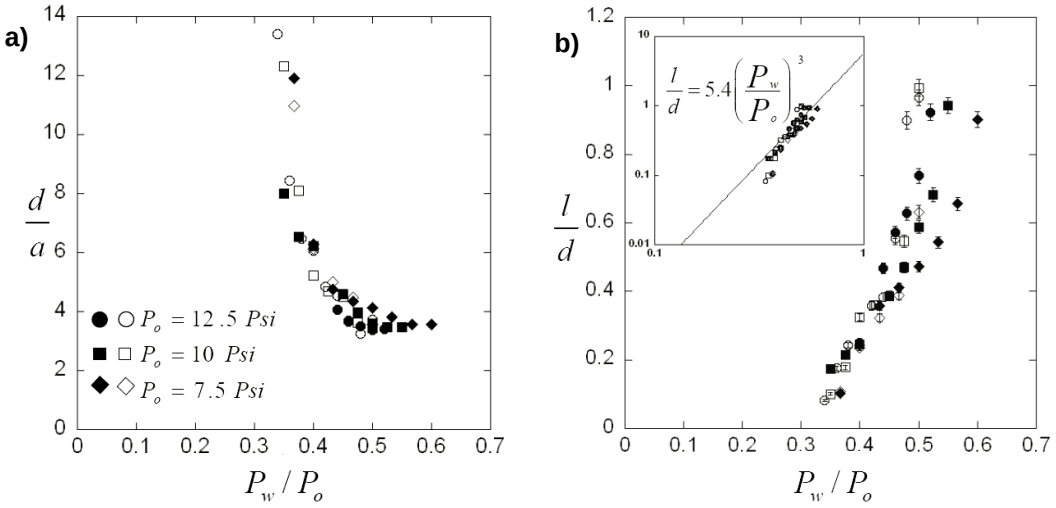

Figure A.9: *a) Distance between the center of mass of two consecutive drops versus inlet pressure ratio. b) Dimensionless drop length ℓ/a versus flow-rate ratio. The inset shows the same data plotted in log-log coordinates, where the solid line has slope* 3.

Most significantly, for the pressure-controlled experiments there is a minimum water pressure below which no drop formation is observed. Just below this pressure the continuous phase fluid pressure is too high for the dispersed phase fluid to penetrate into the main channel after the contraction. But the inlet pressure for the dispersed phase fluid is not zero and there must be another force to create the static or zero velocity dispersed phase flow.

At pressures just below $(P_w/P_o)_{min}$ a static spherical cap of dispersed phase fluid is formed just before the contraction, which suggests the significant role of surface tension. Below this critical pressure the external flow exerts shear and normal stresses on the liquid-liquid interface but these stresses are insufficient to cause the internal fluid to extend into the orifice and break. It is tempting to draw an analogy with the viscous withdrawal flows [35] where there is also a minimum external flow rate (or shear stress or capillary number) below which no drop or jet formation is observed. The geometry is much more complicated here so it is not possible to draw any quantitative analogies.

It is well known in the viscous flow literature that small drops moving in circular or rectangular channels move at nearly the same speed as the external phase fluid. Whether they lag or lead the flow depends on geometry in a very complicated way that has not been completely characterized, but in any event the velocity difference between the two phases is proportional a small power of the external phase capillary number, i.e. to $\mathcal{C}_o^{1/3} = (U_o\mu/\gamma)^{1/3}$, when the capillary number is small. In our case $U_o\mu/\gamma \approx 1 - 10$, so existing theories are not useful for providing any quantitative insight.

A.1.5 The role of flow control: flow-rate versus pressure

Now we discuss a possible mechanism for the difference in flow-rate and inlet pressure driven droplet production. To begin we relate the global transport of momentum with $\Delta P \propto g(a)Q$ where the function $g(a)$ is a resistance that usually depends on geometry and ΔP is the pressure

drop across the microfluidic device. This is analogous to Ohms law $V = IR$ which relates the voltage V to the product of the current I and the resistance. In the fluid dynamical case, if we fix the pressure difference then the flow rate depends on the resistances $\Delta P/g(a) \propto Q$. If these resistances are high $g(a) \gg 1$ then the flow rate is minimal $Q \ll 1$. This is what we see when we control the inlet pressures that the resistances play a dominant role in determining the flow rate.

A.1.6 Conclusion

We have presented results of microfluidic experiments conducted to study micrometer-sized droplet production using a flow-focusing geometry. We study droplet production using either the flow-rate ratio or the inlet pressure ratio as the flow-control parameter. In each experiment the drop size ℓ, velocity U and production frequency f are measured and compared for the different flow-control parameters. Perhaps surprisingly, there are significant differences between these two methods of flow control. The minimum drop size in each experiment is on the order of the flow-focusing contraction width, and illustrates one aspect of the geometric control possible if the results are to be scaled down (or up). The transition in drop size as we vary the flow-control parameter contrasts sharply in the two distinct two-phase flow experiments. It is this distinct difference between the two different manners of flow control used here, which has not been previously noted, that is one of the major conclusions of the present paper.

In each set of experiments the data for the drop size are qualitatively similar when plotted versus the ratio of the flow parameter i.e Q_w/Q_o for the flow-rate driven case and P_w/P_o for the inlet pressure controlled case where w and o denote the dispersed (water) and continuous (mineral oil) phase fluid, respectively. But a power-law fit through the data for the drop size versus the flow control parameter ratio shows quantitative differences, in spite of the viscous (low-Reynolds-number) flow conditions where pressure gradient and average velocity are expected to be proportional. This results suggest a fundamental difference in drop break up between the two types of experiments, and the influence of surface tension on this free-surface flow is likely the origin of the differences.

Appendix B

Explicit calculus for the swinging RBC's model

Nous explicitons dans cette annexe le détail du calcul des équations du mouvement d'un globule rouge sous écoulement de cisaillement, sur lequel notre modèle repose.

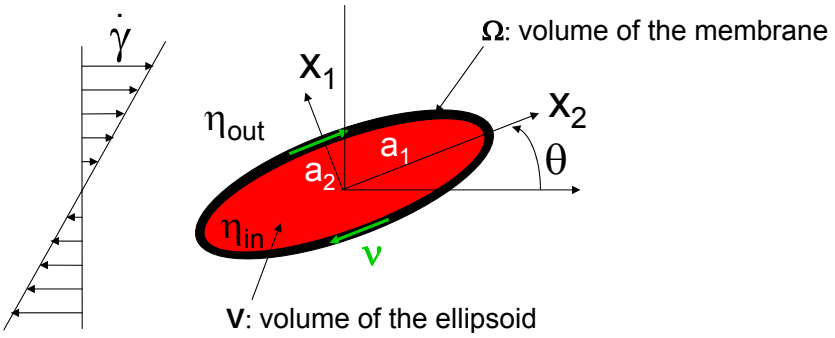

Figure B.1: *Schematic of the system and definition of the parameters.*

The foundation of this phenomenon is the approach of Keller and Skalak [91]. Their model is based on two assumptions allowing to calculate the movement of a fluid ellipsoid under shear flow:

1. Equilibrium of movements: the total moment of the system fluid + ellipsoid is equal to zero,

2. Energy conservation: the rate of work done by the external fluid is equal to the rate at which the energy is dissipated in the internal fluid. The membrane contribution to the dissipation is taken into account by substituting η_{in} by η_{app}=(1+d)η_{in}. In the calculation of Keller and Skalak, the shape memory of the membrane is not taken into consideration. In deed, the rim or the dimple of the RBC are not equivalent during tanktreading. Hence, for each π rotation, the cytoskeleton in rotation, stocks and releases shear strain elastic energy. We propose to take into account this periodic exchange of energy by modifying the assumption 2 of the model of Keller and Skalak. The new assumption we propose is:

3. Energy conservation: the rate of work done by the external fluid is equal to the sum of the internal dissipation rate and the energy stored in the periodic elastic shear strain of the

cytoskeleton.

The elements of the membrane are prescribed to move on ellipsoidal trajectories with a kinematical law given by:

$$\left\{ \begin{array}{lcl} x_1(\vec{x^0},t) & = & x_1^0 cos(\omega) - \frac{a_1}{a_2} sin(\omega) \\ x_2(\vec{x^0},t) & = & x_2^0 cos(\omega) + \frac{a_2}{a_1} sin(\omega) \\ x_3(\vec{x^0},t) & = & x_3^0 \end{array} \right. \tag{B.1}$$

where $\omega = \int_0^t \nu(t')dt'$ and ν is the frequency of tanktreading, and x_i^0 is the position of a material point on the membrane at the time t=0. This imply that if ν is constant, the membrane moves completely around the cell interior with a period T_{tt}:

$$T_{tt} = 2\pi/|\nu| \tag{B.2}$$

Hence the velocity of a material point attached to the membrane relatively to the referential fixed to the ellipsoid, is given by:

$$\left\{ \begin{array}{lcl} v_1 & = & \dot{\omega}(-\frac{a_1}{a_2})x_2 \\ v_2 & = & \dot{\omega}(\frac{a_2}{a_1})x_1 \\ v_3 & = & 0 \end{array} \right. \tag{B.3}$$

The estimation of the shear strain elastic power is simply given by:

$$P_{el} = \int_\Omega Tr(\underline{\underline{\sigma}}.\underline{\underline{D}})d\Omega \tag{B.4}$$

where $\underline{\underline{\sigma}}$ is the shear stress tensor in the membrane and $\underline{\underline{D}}$ the deformation rate tensor. By definition, $\underline{\underline{D}}$ is simply given by:

$$\underline{\underline{D}} = \frac{1}{2}(\underline{\underline{\nabla\ v}} + \underline{\underline{{}^t\nabla v}}) \tag{B.5}$$

Knowing that:

$$\underline{\underline{\nabla\ v}} = \begin{bmatrix} 0 & -\nu\frac{a_1}{a_2} & 0 \\ \nu\frac{a_2}{a_1} & 0 & 0 \\ 0 & 0 & 0 \end{bmatrix} \text{ and } \underline{\underline{{}^t\nabla v}} = \begin{bmatrix} 0 & \nu\frac{a_2}{a_1} & 0 \\ -\nu\frac{a_1}{a_2} & 0 & 0 \\ 0 & 0 & 0 \end{bmatrix}$$

we deduce an expression for $\underline{\underline{D}}$:

$$\underline{\underline{D}} = \frac{1}{2}\nu(\frac{a_2}{a_1} - \frac{a_1}{a_2}) \begin{bmatrix} 0 & 1 & 0 \\ 1 & 0 & 0 \\ 0 & 0 & 0 \end{bmatrix} \tag{B.6}$$

We note that the trace $Tr(\underline{\underline{D}})$=0, the movement of the membrane is then producing a pure shear deformation of its constitutive elements.

In the case of $\underline{\underline{\sigma}}$, we need to give ourselves a constitutive law of the material forming the membrane. We propose as a first approximation (used by many authors) a Kelvin-Voigt model of the

membrane. The shear stress is then the sum of a viscous part and an elastic part. The viscous part comes indeed from the fluid nature of the lipid bilayer while the elastic strain resistance comes from the underlying cytoskeleton capable of bearing shear stresses:

$$\underline{\underline{\sigma}} = \underline{\underline{\sigma_{vis}}} + \underline{\underline{\sigma_{el}}} \tag{B.7}$$

If we consider the membrane as being an isotropic, incompressible, homogeneous, linear and elastic material then we can express its constitutive law simply by the Piola-Kirchhoff stress tensor:

$$\underline{\underline{\sigma_{el}}} = \pi^0 \underline{\underline{I}} + 2\mu_m \underline{\underline{e}} = 2\mu_m \underline{\underline{e}} \tag{B.8}$$

where π^0 is the initial stress of the membrane that we will consider equal to zero, μ_m is the shear modulus of the membrane, $\underline{\underline{I}}$ represents the identity matrix in three dimensions and $\underline{\underline{e}}$ the strain tensor in the lagrangian representation. By definition, $\underline{\underline{e}}$ is given by:

$$\underline{\underline{e}} = \frac{1}{2}(\underline{\underline{\nabla\xi}} + \underline{\underline{{}^t\nabla\xi}} + \underline{\underline{{}^t\nabla\xi}}.\underline{\underline{\nabla\xi}}), \tag{B.9}$$

where $\xi_i = x_i - x_i^0$:

$$\left\{ \begin{array}{lcl} \xi_1 & = & (\cos(\omega)-1)x_1^0 - \frac{a_1}{a_2}sin(\omega)x_2^0 \\ \xi_2 & = & (\cos(\omega)-1)x_2^0 + \frac{a_2}{a_1}sin(\omega)x_1^0 \\ \xi_3 & = & 0 \end{array} \right.$$

Therefore, as:

$$\underline{\underline{\nabla\xi}} \equiv \frac{\delta\xi_i}{\delta x_j^0} = \begin{bmatrix} \cos(\omega)-1 & -\frac{a_1}{a_2}sin(\omega) & 0 \\ \frac{a_2}{a_1}sin(\omega) & \cos(\omega)-1 & 0 \\ 0 & 0 & 0 \end{bmatrix}, \underline{\underline{{}^t\nabla\xi}} = \begin{bmatrix} \cos(\omega)-1 & \frac{a_2}{a_1}sin(\omega) & 0 \\ -\frac{a_1}{a_2}sin(\omega) & \cos(\omega)-1 & 0 \\ 0 & 0 & 0 \end{bmatrix}$$

and

$$\underline{\underline{{}^t\nabla\xi}}.\underline{\underline{\nabla\xi}} = \begin{bmatrix} [\cos(\omega)-1]^2 + (\frac{a_2}{a_1})^2\sin^2(\omega) & (\frac{a_2}{a_1}-\frac{a_1}{a_2})sin(\omega)[\cos(\omega)-1] & 0 \\ (\frac{a_2}{a_1}-\frac{a_1}{a_2})sin(\omega)[\cos(\omega)-1] & [\cos(\omega)-1]^2 + (\frac{a_1}{a_2})^2\sin^2(\omega) & 0 \\ 0 & 0 & 0 \end{bmatrix},$$

the elastic stress tensor is given by:

$$\underline{\underline{e}} = \frac{1}{2}\begin{bmatrix} [(\frac{a_2}{a_1})^2-1]sin^2(\omega) & (\frac{a_2}{a_1}-\frac{a_1}{a_2})sin(\omega)cos(\omega) & 0 \\ (\frac{a_2}{a_1}-\frac{a_1}{a_2})sin(\omega)cos(\omega) & [(\frac{a_1}{a_2})^2-1]sin^2(\omega) & 0 \\ 0 & 0 & 0 \end{bmatrix} \tag{B.10}$$

Because Tr($\underline{\underline{D}}$)=0, the viscous stress tensor is simply given by:

$$\underline{\underline{\sigma_{vis}}} = p\underline{\underline{I}} + 2\eta_m\underline{\underline{D}}, \tag{B.11}$$

where p is the pressure in the membrane. Finally, from B.8 and B.11, the total stress tensor is expressed as:

$$\underline{\underline{\sigma}} = -p\underline{\underline{I}} + 2\eta_m\underline{\underline{D}} + 2\mu_m\underline{\underline{e}} \tag{B.12}$$

We conclude that the viscoelastic power produced in the membrane per unit time and volume is expressed by:

$$\begin{array}{rcl} Tr(\underline{\underline{\sigma}}.\underline{\underline{D}}) & = & Tr((-p\underline{\underline{I}} + 2\eta_m\underline{\underline{D}} + 2\mu_m\underline{\underline{e}}).\underline{\underline{D}}) \\ & = & -p\underbrace{Tr(\underline{\underline{I}}.\underline{\underline{D}})}_{0} + 2\eta_m\underbrace{Tr(\underline{\underline{D}}.\underline{\underline{D}})}_{\frac{1}{2}\dot{\omega}^2(\frac{a_2}{a_1}-\frac{a_1}{a_2})^2} + 2\mu_m\underbrace{Tr(\underline{\underline{e}}.\underline{\underline{D}})}_{\frac{1}{2}\dot{\omega}(\frac{a_2}{a_1}-\frac{a_1}{a_2})^2sin(\omega)cos(\omega)} \end{array}$$

$$Tr(\underline{\underline{\sigma}}.\underline{\underline{D}}) = \frac{1}{2}\dot{\omega}(\frac{a_2}{a_1} - \frac{a_1}{a_2})^2[2\eta_m\dot{\omega} + \mu_m sin(2\omega)] \tag{B.13}$$

The total viscoelastic power exchanged within the whole membrane is:

$$P_{el} = \int_\Omega Tr(\underline{\underline{\sigma}}.\underline{\underline{D}})d\Omega = \frac{1}{2}\dot{\omega}(\frac{a_2}{a_1} - \frac{a_1}{a_2})^2[2\eta_m\dot{\omega} + \mu_m sin(2\omega)]\Omega \tag{B.14}$$

where Ω is the volume of the membrane.

The two assumptions of the model of Keller and Skalak allow to write two ordinary differential equations of the first order on the variable controlling the movement: θ and ω.

1. The equilibrium of the moments gives the equation of θ analogous to the movement of a solid ellipsoid:

$$\dot{\theta} = \widetilde{A} + \widetilde{B}cos(2\theta), \text{ where } \widetilde{A} = -(\frac{1}{2}\dot{\gamma} + \frac{2a_1a_2}{a_1^2+a_2^2}\dot{\omega}) \text{ and } \widetilde{B} = \frac{1}{2}\dot{\gamma}\frac{a_1^2-a_2^2}{a_1^2+a_2^2} \tag{B.15}$$

2. If W_p is the work done by the external fluid on the ellipsoid and D' the internal viscous dissipation due to the movement of the fluid, the modified conservation of energy is expressed as:

$$W_p = D' + P_{el} \tag{B.16}$$

The fluid ellipsoid model developed by Keller and Skalak tells us that:

$$\Rightarrow W_p = V\eta_{out}(f_2\dot{\omega}^2 + f_3\dot{\gamma}\dot{\omega}cos(2\theta)), \tag{B.17}$$

$$\text{where } \left\{ \begin{array}{lcllcl} f_2 & = & 4z_1^2(1-2/z_2), & f_3 & = & -4z_1/z_2 \\ z_1 & = & \frac{1}{2}(r_2^{-1} - r_2), & z_2 & = & g_3'(\alpha_1^2+\alpha_2^2) \end{array} \right.$$

The terms f_2 and f_3 are functions of the axis ratio r_2 and r_3, defined as $r_2 = a_2/a_1$ and $r_3 = a_3/a_1$, and of the parameters α_1, α_2 and g_3' which are also geometrical parameters defined by:

$$\alpha_i = \frac{a_i}{(a_1a_2a_2)^{1/3}} \text{ and } g_3' = \int_0^\infty \frac{ds}{(\alpha_1^2+s)(\alpha_2^2+s)\sqrt{(\alpha_1^2+s)(\alpha_2^2+s)(\alpha_3^2+s)}}$$

$$\Rightarrow D' = V\eta_{in}f_1\dot{\omega}^2, \text{ with } f_1 = (\frac{a_2}{a_1} - \frac{a_1}{a_2})^2 \tag{B.18}$$

The balance of energy can be developed as:

$$V\eta_{out}(f_2\dot{\omega}^2 + f_3\dot{\gamma}\dot{\omega}\cos(2\theta)) = V\eta_{in}f_1\dot{\omega}^2 + \frac{1}{2}\dot{\omega}f_1(2\eta_m\dot{\omega} + \nu_m sin(2\omega))\Omega$$

which gives

$$\dot{\omega} = -\frac{\eta_{out}f_3\dot{\gamma}}{\eta_{out}(f_2 - \eta_{in}f_1(1+\eta_m/\eta_{in}\Omega/V)}\cos(2\theta) + \frac{\frac{1}{2}f_1\mu_m\Omega/V}{\eta_{out}(f_2 - \eta_{in}(1+\eta_m/\eta_{in}\Omega/V)}sin(2\omega) \tag{B.19}$$

Hence, from B.15 and B.19 the differential system that we obtain is:

$$\left\{ \begin{array}{l} \dot{\theta} = -(\frac{1}{2}\dot{\gamma} + \frac{2a_1a_2}{a_1^2+a_2^2}\dot{\omega}) + \frac{1}{2}\dot{\gamma}\frac{a_1^2-a_2^2}{a_1^2+a_2^2}cos(2\theta) \\ \dot{\omega} = -\frac{\eta_{out}f_3\dot{\gamma}}{\eta_{out}(f_2-\eta_{in}f_1(1+\eta_m/\eta_{in}\Omega/V)}\cos(2\theta) + \frac{\frac{1}{2}f_1\mu_m\Omega/V}{\eta_{out}(f_2-\eta_{in}f_1(1+\eta_m/\eta_{in}\Omega/V)}sin(2\omega) \end{array} \right. \tag{B.20}$$

We numerically solve the equations using the following set of parameters: a_1=a_3=4 μm , a_2=1.5 μm, Ω=Σ.e, where Σ is the oblate ellipsoid area and e=50 nm is the membrane thickness [77]. The approximate formula of the surface of such an ellipsoid ($a_1 = a_3$) is given (with 2% error) by:

$$\Sigma = 2\pi a_1^2[1 + (\frac{a_2}{a_1})^2 \frac{\tanh^{-1}(ex)}{ex}]$$

with ex=1/2(1-a_2^2/a_1^2) the excentricity.

Appendix C

Red blood cells loading of Fatty Acid Ethyl Ester

La procédure complète du traitement des globules rouges avec des acides gras ethyl ester.

Unlabeled ethyl oleate (E18:1), and ethyl palmitate (E16:0), were purchased from Nu-Check Prep (Elysian, MN).

The blood was prepared at the Massachusetts General Hospital and brought in the lab for the experiments. Whole blood was from a healthy adult volunteer. Blood samples were collected in vacutainer tubes containing Ethylenediaminetetraacetic acid (EDTA) to prevent blood coagulation. The whole blood was centrifuged immediately at 2000 x g at 5^oC for 10 minutes to separate RBCs from plasma. Following the initial centrifugation step, the RBCs were washed three times. Each RBCs washing entailed the addition of five times the volume of isotonic 0.9% normal saline, gentle dispersion of RBCs by mixing with a plastic pipette, and centrifugation at 650 x g for 10 minutes at 10^OC. The saline wash was aspirated and discarded. The final centrifugation was at 1500 x g for 10 minutes at 10^oC to pack the RBCs sample more tightly and to minimize the volume of saline. The final saline wash was discarded and the cells were re-suspended in phosphate buffered saline (PBS) at pH=7.4. The washed RBCs were re-suspended to approximately 20% hematocrit and represent on average 98.9% as a percent of total cells in the sample.

Figure C.1: *Fatty Acid Ethyl Esters (FAEEs) are the esterification products of ethanol and fatty acids.*

FAEE was obtained by mixing ethyl oleate (E18:1) and ethyl palmitate (E16:0) with a molar ratio of 1:1 according to the reaction shown Figure C.1. Both chemicals were purchased from Nu-Check Prep (Elysian, MN). FAEE at 20 μM was dried on the walls of glass conical tubes under a stream of nitrogen [25] and subsequently re-suspended in human fatty acid free albumin, in a 1:1 albumin to FAEE molar ratio. Washed red cell preparations were added to the conical

tubes and slightly vortexed.

The cells were then submitted to the same preparation than cells extracted from whole blood. RBCs preparations were made within 1 hour of blood collection, and experiments were performed within 5 hours of RBCs preparation.

Appendix D

Table units

Nous avons rassemblé ici les équivalences entre les différentes unités utilisées dans ce manuscrit.

We gather in the Table D, the equivalence between the units of the quantities used in this manuscript.

Quantity	units
Pressure	1.45×10^{-4} Psi $\approx$ 1 Pa $\approx$ 1 N.s.m^{-2} $\approx 10^{-5}$ bar
Dynamic viscosity	1 Pa.s $\approx 10^{3}$ cP $\approx$ 1 kg.m^{-1}.s^{-1}
Energy	1 J $\approx$ 1 N.m $\approx$ 1 dyn.cm
Force	1 N $\approx 10^{5}$ dyn
Shear modulus	1 N.m^{-1} $\approx 10^{8}$ dyn.cm^{-1}
Surface shear viscosity	1 N.s.m^{-1} $\approx 10^{8}$ dyn.s.cm^{-1}

Table D.1: *Equivalence between the units of diverse quantities used in the present manuscript.*

List of Figures

List of Tables

Bibliography

[1] www.es.hokudai.ac.jp/labo/nano_device/Droplet-on-surface.jpg.

[2] http://www.avantilipids.com.

[3] www.leucemie-espoir.org/spip/IMG/jpg/.

[4] www.deas.harvard.edu/projects/weitzlab/research/Microfluidics/Multicomponent.html.

[5] www.microscopyu.com/tutorials/java/phasecontrast/opticaltrain/index.html.

[6] www.olympusmicro.com/primer/techniques/fluorescence/.

[7] http://rsb.info.nih.gov/ij/.

[8] www.gmwgroup.harvard.edu.

[9] http://rsb.info.nih.gov/ij/docs/menus/image.html.

[10] M. Abkarian. *Dynamique et formes d'envelloppes deformables sous champs externes*. PhD thesis, Univerity Joseph Fourier, Grenoble, France, 2002.

[11] M. Abkarian, M. Faivre, and H.A. Stone. High-speed microfluidic differential manometer for cellular-scale hydrodynamics. *Proc. Natl. Acad. Sci. USA*, 103(3):538–542, 2006.

[12] M. Abkarian, M. Faivre, and A. Viallat. Swinging of red blood cells under shear flow. *submitted to Phys. Rev. Lett.*

[13] M. Abkarian, C. Lartigue, and A. Viallat. Tank treading and unbinding of deformable vesicles in shear flow: determination of the lift force. *Phys. Rev. Lett.*, 88(6):068103–1 068103–4, 2002.

[14] M. Abkarian and A. Viallat. Dynamics of vesicles in a wall-bounded shear flow. *Biophys. J.*, 89:1055–1066, 2005.

[15] B. Alberts, D. Bray, and J. Lewis et al. *Biologie moléculaire de la cellule*. Flammarion, Paris, 2003.

[16] M.I. Angelova, S. Soléau, P. Méléard, J. Faucon, and P. Bothorel. Preparation of giant vesicles by external a.c. electric fields. *Progr. Coll. Pol. Sci.*, 89:127–133, 1992.

[17] S.L. Anna, N. Bontoux, and H.A. Stone. Formation of dispersions using "flow focusing" in microchannels. *App. Phys. Lett.*, 82):364–366, 2003.

[18] R. Banerjee, K. Nageshwari, and R. Puniyani. *Clin. Hemorheol. Microcirc.*, 19:21–, 1988.

[19] J.H. Barbee and G.R. Cokelet. The fahreus effect. *Microvasc. Res.*, 34:6–21, 1971.

[20] D. Barthes-Biesel. Role of interfacial properties on the motion and deformation of capsules in shear flow. *J. Fluid Mech.*, 361:117–143, 1991.

[21] D. Barthès-Biesel, A. Diaz, and E. Dhenin. Effect of constitutive laws for two-dimensional membranes on flow-induced capsule deformation. *J. Fluid Mech.*, 460:211–222, 2002.

[22] D. Barthes-Biesel and J.M. Rallison. The time-dependent deformationof a capsule freely suspended in a linear shear-flow. *J. Fluid Mech.*, 113:251–, 1981.

[23] D. Barthes-Biesel and H. Sgaier. Role of membrane viscosity in the orientation and deformation of a spherical capsule suspended in shear flow. *Physica A*, 172:103–124, 1985.

[24] C.A. Best and M. Laposata. Red blood cell fatty acid ethyl esters: a significant component of fatty acid ethyl esters in the blood. *J. Lipid Res.*, 44:612–620, 2003.

[25] C.A. Best, M. Laposata, V.G. Proios, and Z.M. Szczepiorkowski. Method to assess fatty acid ethyl ester binding to albumin. *Alcohol Alcohol.*, 41:240, 2006.

[26] D. Braun and A. Libchaber. Trapping of dna by thermophoretic depletion and convection. *Phys. Rev. Lett.*, 89:188103, 2002.

[27] H. Brenner and P.M. Bungay. Rigid-particle and liquid-droplet models of red cell motion in capillary tubes. *Fed. Proc.*, 30:1565–1576, 1971.

[28] M. Burns, C.H. Mastrangelo, T.S. Sammarco, F.P. Man, and J.R. Webster. Microfabricated structures for integrated dna analysis. *Proc. Natl. Acad. Sci. USA*, 93:5556–5561, 1996.

[29] C. Campillo. PhD thesis, Univerity Joseph Fourier, Grenoble, France, In progress.

[30] C.E. Chaffey, H. Brenner, and S.G. Mason. Particle motions in sheared suspensions viii: Wall migration (theoretical). *Rheol. Acta*, 4:64; Correction 1967, **6**:100, 1965.

[31] K.S. Chang and W.L. Olbricht. Experimental studies of the deformation and breakup of a synthetic capsule in steady and unsteady simple shear-flow. *J. Fluid Mech.*, 250:609–633, 1993.

[32] S. Chien. Red-cell deformability and its relevance to blood-flow. *Ann. Rev. Phisiol.*, 69:177–192, 1987.

[33] S. Chien, S.A. Luse, and C.A. Bryant. Hemolysis during filtration through micropores: a scanning electron microscopic and hemorheologic correlation. *Microvasc. Res.*, 3:183–203, 1971.

[34] S. Chien, K.L. Paulsung, and R. Skalak. Viscoelastic properties of red cell membrane. *Biorheology*, 15(5-6):451–451, 1978.

[35] I. Cohen and S.R. Nagel. Scaling at the selective withdrawal transition through a tube suspended above the fluid surface. *Phys. Rev. Lett.*, 88(7), 2002.

[36] J.H. Collier and P.B. Messersmith. Phospholipid strategies in biomineralization and biomaterials research. *Annu. Rev. Mater. Res.*, page 237, 2001.

[37] R.A. Dean. Tipstreaming of drops in simple shear flows. *Chemical Engeeriring Science*, 48(2):277–284, 1993.

[38] A. Diaz and D. Barthès-Biesel. Entrance of a bioartificial capsule in a pore. *CMES*, 3:321–337, 2002.

[39] R. Dimova, C. Dietrich, A. Hadjiisky, and et al. Falling ball viscosimetry of giant vesicle membranes: Finite-size effects. *EPJB*, 12(4):589–598, 1999.

[40] R. Dimova, B. Pouligny, and C. Dietrich. *Pretransitional effects in dimyristoylphosphatidylcholine vesicle membranes: Optical dynamometry study.* 79, 340-356, 2000.

[41] J. Dobbe, G. Streekstra, M. Hardeman, C. Ince, and C. Grimbergen. Measurement of the distribution of red blood cell deformability using an automated rheoscope. *Cytometry*, 50:313–325, 2002.

[42] H.-G. Döbereiner, E. Evans, M. Kraus, U. Seifert, and M. Wortis. Mapping vesicle shapes into the phase diagram: A comparison of experiment and theory. *Phys. Rev. E*, 55(4):4458–4474, 1997.

[43] H.-G. Döbereiner, E. Evans, U. Seifert, and M. Wortis. Spinodal fluctuations of budding vesicles. *Phys. Rev. Lett.*, 75:3360, 1995.

[44] A. Drochon. Rheology of dilute suspensions of red blood cells: experimental and theoretical approaches. *Eur. Phys. J. AP*, 22:155–162, 2003.

[45] P. Erni, P. Fischer, and E.J. Windhab. Deformation of single emulsion drops covered with a viscoelastic adsorbed protein layer in simple shear flow. *Appl. Phys. Lett.*, 87:24:4104, 2005.

[46] E. Evans. Structure and deformation properties of red blood cells: concepts and quantitative methods. *Methods Enzymol.*, 173:3–33, 1989.

[47] E. Evans and Y.C. Fung. Improved measurements of the erythrocyte geometry. *Microvasc. Res.*, 4:335–347, 1972.

[48] E. Evans and R.M. Hochmuth. New membrane concept applied to the analysis of fluid shear - and micropipette - deformed red blood cell. *Biophys. J.*, 93:941–954, 1973.

[49] E. Evans and R.M. Hochmuth. Membrane viscoelasticity. *Biophys. J.*, 16(1):1–11, 1976.

[50] E. Evans and D. Needham. Physical properties of surfactant bilayer membranes: Thermal transitions, elasticity, rigidity, cohesion, and colloidal interactions. *J. Phys. Chem.*, 91:4219–4228, 1987.

[51] E. Evans and W. Rawicz. Entropie-driven tension and bending elasticity in condensed-fluid membrane. *Phys. Rev. Lett.*, 64(17):2094–2097, 1990.

[52] R. Fähraeus and T. Lindqvist. The viscosity of the blood in narrow capillary tubes. *Am. J. Physiol.*, 96:562–568, 1931.

[53] M. Faivre, M. Abkarian, K. Bickraj, and H.A. Stone. Geometrical focusing of cells in a microfluidic device: An approach to separate blood plasma. *Biorheology*, 43(2):147–159, 2006.

[54] M. Faivre, C. Campillo, B. Pepin-Donat, and A. Viallat. Enhanced resistance and reversible temperature-triggered volume change of giant vesicles enclosing poly(n-isopropylacrylamide) solutions or gels. *Progress in Colloid. Sci.*, 2006.

[55] J. M. Fernandez and G. M. Homsy. Chemical reaction-driven tip-streaming phenomena in a pendant drop. *Physics of Fluids*, 16(7):2548–2555, 2004.

[56] T.C. Fischer, R.B. Wenby, and H.J. Meiselman. Pulse shape analysis of rbc micropore flow via new software for the cell transit analyser (cta). *Biorheology*, 29:185–201, 1992.

[57] T.M. Fischer. Shape memory of human red blood cells. *Biophys. J.*, 86:3304–3313, 2004.

[58] T.M. Fischer and H. Schmid-Schönbein. Tank tread motion of red cell membranes in viscometric flow: behavior of intracellular and extracellular markers (with film). *Blood Cells*, 3:351–365, 1977.

[59] T.M. Fischer, M. Stöhr-Liesen, and H. Schmid-Schönbein. The red blood cell as a fluid droplet: tank tread-like motion of the human erythrocyte membrane in shear flow. *Science*, 202:894–896, 1978.

[60] Y.C. Fung. *Biomechanics - mechanical properties of living tissues.* Springer, New York, 1993.

[61] Y.C. Fung. *Circulation.* Springer, New York, 1996.

[62] P. Gaehtgens, C. Dührssen, and K.H. Albrecht. Motion, deformation, and interaction of blood cells and plasma during flow through narrow capillary tubes. *Blood Cells*, 6:799–812, 1980.

[63] K. Gao and L. Huang. Solid core liposomes with encapsulated colloidal gold particles. *Biochim Biophys Acta*, 897:377, 1987.

[64] P. Garstecki, I. Gitlin, W. DiLuzio, G.M. Whitesides, E. Kumacheva, and H.A. Stone. Formation of monodisperse bubbles in a microfluidic flow-focusing device. *App. Phys. Lett.*, 85:2649–2651, 2004.

[65] A.M. Gañàn-Calvo. Generation of steady liquid microthreads and micron-sized monodisperse sprays in gas streams. *Phys. Rev. Lett.*, 80:285–288, 1998.

[66] A.M. Gañàn-Calvo and J.M. Gordillo. Perfectly monodisperse microbubbling by capillary flow focusing. *Phys. Rev. Lett.*, 87:274501, 2001.

[67] A.J. Goldman, R.G. Cox, and H. Brenner. Slow viscous motion of a sphere parallel to a plane. *CES*, 637, 1967.

[68] H.L. Goldsmith. Microscopic flow properties of red cells. *Fed. Proc.*, 26:1813–1819, 1967.

[69] H.L. Goldsmith. Red cell motions and wall interactions in tube flow. *Fed.Proc.*, 30:1578–1588, 1971.

[70] H.L. Goldsmith, G.R. Cokelet, and P. Gaehtgens. Robin fähraeus: evolution of his concepts in cardiovascular physiology. *Am. J. Physiol.*, 257(Heart Circ. Physiol. 26):H1005–H1015, 1989.

[71] H.L. Goldsmith and J. Marlow. Flow behavior of erythrocytes. i. rotation and deformation in dilute suspensions. *Proc. R. Soc. Lond. B.*, 182:351–384, 1972.

[72] H.L. Goldsmith and S.G. Mason. Flow of suspensions through tubes. 1. single spheres, rods, and discs. *J. Colloid Sci.*, 17:448–476, 1967.

[73] A. Groisman, M. Enzelberger, and S.R. Quake. Microfluidic memory and control devices. *Science*, 300:955–958, 2003.

[74] W. Haeckl, M. Baermann, and E. Sackmann. Shape changes of self-assembled actin bilayer composite membranes. *Phys. Rev. Lett.*, 80:1786, 1998.

[75] M. Hara, H. Yuan, M. Miyake, S. Iijima, Q. Yang, and V. Miyake. Amphiphilic polymer-liposome interaction: a novel immobilization technique for liposome on gel surface. *J Mater Sci Eng C*, 1(3):117, 2000.

[76] M. Hartwig and H. DeSisto. The cytoskeleton of the resting human blood-platelet - structure of the membrane skeleton and its attachment to actin-filaments. *Journal of Cell Biology*, 112(3):407–425, 1991.

[77] V. Heinrich, K. Ritchie, N. Mohandas, and E. Evans. Elastic thickness compressibility of the red cell membrane. *Biophys. J.*, 81:1452–1463, 2001.

[78] E. Helfer, S. Harlepp, L. Bourdieu, J. Robert, F.C. MacKintosh, and D. Chatenay. Viscoelastic properties of actin-coated membranes. *Phys. Rev. E*, 63:021904, 2001.

[79] B.P. Helmke, S.N. Bremner, B.W. Zweifach, R. Skalak, and G.W. Schmid-Schönbein. Mechanisms for increased blood flow resistance due to leukocytes. *Am. J. Physiol.*, 273:H2884–H2890, 1997.

[80] S. Hénon, G. Lenormand, A. Richert, and F. Gallet. A new determination of the shear modulus of the human erythrocyte membrane using optical tweezers. *Biophys. J.*, 78:1145–1151, 1999.

[81] Y. Hirokawa and T. Tanaka. Volume phase transition of a noionic gel. *J. Chem. Phys.*, 81(12):6379–6380, 1984.

[82] S. Hirotsu, Y. Hirokawa, and T. Tanaka. Volume-phase transitions of ionized n-isopropylacrylamide gels. *J. Chem. Phys.*, 87(2):1392–1395, 1987.

[83] R.M. Hochmuth, N. Mohandras, and J.P. Blackshear Jr. Measurement of the elastic modulus for red blood cell membrane using a fluid mechanical technic. *Biophys. J.*, 13:747–762, 1982.

[84] R.M. Hochmuth and R. E. Waught. Erythrocyte membrane elasticity and viscosity. *Ann. Rev. Phisiol.*, 49:209–219, 1987.

[85] G.B. Jeffery. The motion of ellipsoidal particles immersed in a viscous fluid. *Proc. Roy. Soc. Lond. A*, 102:161–179, 1922.

[86] A. Jesorka, M. Amarkström, and O. Orwar. Controlling the internal structure of giant unilamellar vesicles by means of reversible temperature dependent sol-gel transition of internalized poly (n-isopropyl acrylamide). *Langmuir*, 21, 2005.

[87] T. Jin, P. Pennefather, and P.I. Lee. Lipobeads: a hydrogel anchored lipid vesicle system. *FEBS Lett.*, 70:397, 1996.

[88] V. Kantsler and V. Steinberg. Transition to tumbling and two regimes of tumbling motion of a vesicle in shear flow. *Phys. Rev. Lett.*, 96:036001, 2006.

[89] A. Karnis, H.L. Goldsmith, and S.G. Mason. Axial migration of particles in poiseuille flow. *Nature*, 200:159–160, 1963.

[90] S. Kazalov, M. Kaholek, I. Teraoka, and K. Levon. Uv-induced gelation on nanometer scale using liposome reactor. *Macromol*, 35:1911, 2002.

[91] S.R. Keller and R. Skalak. A tank treading ellipsoidal particle in shear flow. *J. Fluid Mech.*, 120:27–47, 1982.

[92] P.F. Kiser, G. Wilson, and D. Needham. A synthetic mimic of the secretory granule for drug delivery. 394:459, 1998.

[93] M. Kraus, W. Wintz, U. Seifert, and et al. Fluid vesicles in shear flow. *Physical review letters*, 77(17):3685–3688, 1996.

[94] N. Kučerka, M. A. Kiselev, and P. Balgavý. Determination of bilayer thickness and lipid surface area in unilamellar dimyristoylphosphatidylcholine vesicles from small-angle neutron scattering curves: a comparison of evaluation methods. *EBJ*, 33:328–334, 2004.

[95] R. Kwok and E. Evans. Thermoelasticity of large lecithin bilayer vesicles. *Biophys. J.*, 35:637, 1981.

[96] E. Lac and D. Barthès-Biesel. Deformation of a capsule in simple shear flow: Effect of membrane prestress. *Physics of Fluids*, 17:072105:1–8, 2005.

[97] K. Laszlo, K. Kosik, C. Rochas, and E. Geissler. Phase transition in poly(n-isopropylacrylamide) hydrogels induced by phenols. *Macromol*, 36:7771–7776, 2003.

[98] G. Lenormand. *Elasticité du squelette du globule rouge humain - une étude par pinces optiques*. PhD thesis, Université Paris 6, Paris, 2001.

[99] G. Lenormand, S. Hénon, A. Richert, J. Siméon, and F. Gallet. Direct expansion of the area expansion and shear moduli of the human red blood cell membrane skeleton. *Biophys. J.*, 81):43–56, 2001.

[100] L. Limozin, A. Roth, and Sackmann. Structure and mechanics of actin cortex contained in vesicles. *Biophys. J.*, page 84, 2003.

[101] R. Lipowsky. Bending of membranes by anchored polymers. *Europhys. Lett.*, 30:197, 1995.

[102] J.C. Lopez-Montilla, P.E. Herrera-Morales, S. Pandey, and D.O. Shah. Spontaneous emulsification : Mechanisms, physicochemical aspects, modeling, and applications. *J. Disp. Sci. Tech.*, 23(1-3):219–263, 2002.

[103] J.C. MacDonald, D.C. Duffy, J.R. Anderson, D.T. Chiu, H. Wu, O.J.A. Schueller, and G.M. Whitesides. Microfluidic sorting in an optical lattice. *Electrophoresis*, 21:27–40, 2000.

[104] M. Mader, V. Viktova, M. Abkarian, and et al. Dynamics of viscous vesicles in shear flow. *Eur. Phys. J.E.*, pages 389–397, 2005.

[105] E. Sato Matsuo and T. Tanaka. Kinetics of discontinuous volume-phase transition of gels. *J. Chem. Phys.*, page 1695, 1988.

[106] F.M. Menger and M.I. Angelova. Giant vesicles: Imitating the cytological processes of cell membranes. *Acc Chem Res*, page 789, 1998.

[107] L. Miao, U. Seifert, M. Wortis, and H. G. Dbereiner. Budding transitions of fluid-bilayer vesicles: The effect of area-difference elasticity. *Phys. Rev. E*, 49(6):5389–5407, 1994.

[108] N. Mohandas and E. Evans. Mechanical properties of the red cell membrane in relation to molecular structure and genetic defects. *Annu. Rev. Biophys. Biomol. Struct.*, 23:787–818, 1994.

[109] F. Mokken, M. Kedaria, C. Henny, M. Hardeman, and A. Gelb. The clinical importance of erythrocyte deformability, a hemorrheologicalparameter. *Ann. Hematol.*, 64:113–122, 1992.

[110] B. L. S. Mui, H. G. Dbereiner, T. D. Madden, and P. R. Cullis. Influence of transbilayer area asymmetry on the morphology of large unilamellar vesicles. *Biophys. J.*, 69:930–941, 1995.

[111] G.B. Nash. Filtrability of blood cells: methods and clinical applications. *Biorheology*, 27:873–882, 1990.

[112] D Needham and E. Evans. Structure and mechanical properties of giant lipid (dmpc) vesicle bilayers from 20^oc below to 10^oc above the liquid crystal-crystalline phase transition at 24^oc. *Biochemistry*, 27:8261–8269, 1988.

[113] D Needham, T.J. McIntosh, and E. Evans. Thermomechanical and transition properties of dimyristoylphosphatidylcholine/cholesterol bilayers. *Biochemistry*, 27:4668–4673, 1988.

[114] T. Nishimi and C.A. Miller. Spontaneous emulsification produced by chemical reactions. *J. Col. Inter. Chem.*, 10(4):542–544, 2001.

[115] H. Noguchi and G. Gompper. Shape transitions of fluid vesicles and red blood cells in capillary flows. *Proc. Natl. Acad. Sci. USA*, 102(40):12159–14164, 2005.

[116] K. Olbrich, W. Rawicz, D. Needham, and et al. Water permeability and mechanical strength of polyunsaturated lipid bilayers. *Biophys. J.*, 79(1):321–327, 2000.

[117] P. Olla. The lift on a tank-treading ellipsoidal cell in a shear flow. *J. Phys. A*, 30:317–329, 1997.

[118] P. Olla. The role of tank-treading motions in the transverse migration of a spheroidal vesicle in a shear flow. *J. Phys. France II*, 7:1533–1540, 1997.

[119] J. Pécréaux. *Mesure du spectre de fluctuations de vésicules géantes par analyse de contours; application aux membranes passives et actives.* PhD thesis, University Paris 6, Paris, 2004.

[120] J.M. Poiseuille. Recherche expérimentales sur le mouvement des liquides dans les tubes de très petits diamètres. *Comptes Rendus Hebdomadaires de l'Académie des Sciences*, 11:961–967 & 1041–1048, 1840.

[121] C. Pozrikidis. Effect of membrane bending stiffness on the deformation of capsules in simple shear flow. *J. Fluid. Mech.*, 440:269–291, 2001.

[122] C. Pozrikidis. Axisymmetric motion of a file of red blood cells through capillaries. *Physics of Fluids*, 17:031503:1–14, 2005.

[123] A.R. Pries, K. Ley, and P. Gaehtgens. Generalization of the fähraeus principle for microvessel networks. *Am. J. Physiol.*, 251(Heart Circ. Physiol. 20):H1324–H1332, 1986.

[124] A.R. Pries and T.W. Secomb. Rheology of the microcirculation. *Cardiovasc. Res.*, 29:143–148, 2003.

[125] A.R. Pries, T.W. Secomb, and P. Gaehtgens. Biophysical aspects of blood flow in the microvasculature. *Cardiovasc. Res.*, 32:654–667, 1996.

[126] C. Quéguiner and D. Barthès-Biesel. Axisymmetric motion of capsules through cylindrical channels. *J. Fluid Mech.*, 348:349–376, 1997.

[127] F. Quemeneur. PhD thesis, Univerity Joseph Fourier & Universität Konstanz, Grenoble, France, In progress.

[128] S. Ramanujan and C. Pozrikidis. Deformation of liquid capsules enclosed by elastic membranes in simple shear flow: large deformations and the effect of fluid viscosities. *J. Fluid Mech.*, 361:117–143, 1998.

[129] W. Rawicz, K.C. Olbrich, T. McIntosh, and et al. Effect of chain length and unsaturation on elasticity of lipid bilayers. *Biophys. J.*, 79, 2000.

[130] F. Risso, F. Collé-Paillot, and M. Zagzoule. Experimental investigation of a bioartificial capsule flowing in a narrow tube. *J. Fluid Mech.*, 547:149–173, 2006.

[131] O. Sandre. *Pores transitoires, adhésion et fusion des vésicules géantes.* PhD thesis, Thèse de doctorat de l'université Paris 6, Paris, 2000.

[132] S. Sasaki and S. Koga. Slow relaxation of the elastic n-isopropylacrylamide gel. *Macromolecules*, page 857, 2002.

[133] H. Schmid-Schönbein, R. Wells, and J. Coldston. Increased viscous resistance of blood due to hypertonicity a possible mechanism for internal distribution of blood flow. *Federation Proceedings*, 28(2):716–, 1969.

[134] T.W. Secomb. *Modeling and Simulation of Capsules and Biological Cells.* Chapman & Hall, London, 2003.

[135] U. Seifert. Configurations of fluid membranes and vesicles. *Adv. Phys.*, 46:13, 1997.

[136] N. Shahidzadeh, D. Bonn, and J. Meunier. A new mechanism of spontaneous emulsification: Relation to surfactant properties. *Europhys. Lett.*, page 459.

[137] T. Shiga, N. Meada, and K. Kon. Erythrocyte rheology. *Critical Reviews in Oncology/Hematology*, 10:9–48, 1990.

[138] A. Sin and P. Odier. Gelation by acrylamide, a quasi-universal medium for the synthesis of fine oxide powders for electroceramic applications. *Advanced Materials*, 12(9):649, 2000.

[139] R. Skalak and P. I. Branemark. Deformation of red blood cells in capillaries. *Science*, 164:717–719, 1969.

[140] J. Skotheim and M. Abkarian. *Private Communication*, 2005.

[141] K. Smistrup and M. Faivre. *Private Communication*, 2006.

[142] O. Stauch, R. Schubert, G. Savin, and W. Burchard. Structure of artificial cytoskeleton containing liposomes in aqueous solution studied by static and dynamic light scattering. *Biomacromolecules*, 3:565, 2002.

[143] O. Stauch, T. Uhlmann, M. Fröhlich, R. Thomann, M. El-Badry, Y.K. Kim, and R. Schubert. Mimicking a cytoskeleton by coupling poly(n-isopropylacrylamide) to the inner leaflet of liposomal membranes: Effects of photopolymerization on vesicle shape and polymer architecture. *Biomacromolecules*, 3:324, 2002.

[144] N. Sutera, P.R. Pierre, and G.I. Zahalak. Deduction of intrinsic mechanical-properties of the erythrocyte-membrane from observations of tank-treading in the rheoscope. *Biorheology*, 26:177–197, 1989.

[145] Y. Suzuki, N. Tateishi, M. Soutani, and N. Maeda. Deformation of erythrocytes in microvessels and glass capillaries: effects of erythrocyte deformability. *Microcirculation*, 3:49–57, 1996.

[146] T. Tanaka. Collapse of gels and the critical endpoint. *PRL*, 40(12):820–823, 1978.

[147] T. Tanaka. *Nature*, 358:482, 1987.

[148] T. Tanaka and D.J. Fillmore. Kinetics of swelling of gels. *J. Chem. Phys.*, 70(03):1214–1218, 1979.

[149] T. Tanaka, D.J. Fillmore, S.T. Sun, I. Nishio, G. Swislow, and A. Shah. Phase transitions in ionic gels. *PRL*, 45:1636–1639, 1980.

[150] R. Tran-Son-Tay, S.P. Sutera, and P.R. Rao. Determination of red blood cell membrane viscosity from rheoscopic observations of tank-treading motion. *Biophys. J.*, 46:65–72, 1984.

[151] R. Tran-Son-Tay, S.P. Sutera, G. Zahalak, and P.R. Rao. Membrane prestress and internal-pressure in a red blood cell freely suspended in a shear flow. *Biophys. J.*, 51:915–924, 1987.

[152] K. Velikov, C. Dietrich, and A. Hadjiisky et al. Motion of a massive microsphere bound to a spherical vesicle. *Europhys. Lett.*, 40(4):405–410, 1997.

[153] A. Viallat, J. Dalous, and M. Abkarian. Giant lipid vesicles filled with a gel: Shape instability induced by osmotic shrinkage. *Biophys. J.*, 86:2179–21887, 2004.

[154] V. Vitkova, M. Mader, and T. Podgorski. Deformation of vesicles flowing through capillaries. *Europhys. Lett.*, 68(3):398–404, 2004.

[155] A. Walter, H. Rehage, and H. Leonhard. Shear induced deformation of microcapsules: shape oscillations and membrane folding. *Colloids and surfaces A:Physicochem. Eng. Aspects*, 123:183–185, 2001.

[156] T. Ward, M. Faivre, M. Abkarian, and A.H. Stone. Microfluidic flow focusing: Drop size and scaling in pressure versus flow-rate-driven pumping. *Electrophoresis*, 26(19):3716–3724, 2005.

[157] R. E. Waught and P. Agre. Reductions of erythrocyte membrane viscoelastic coeffients reflect sprectrin deficiencies in hereditary spherocytosis. *J. Clim. Invest.*, 81:133–141, 1988.

[158] S.H. White and M.C. Wiener. *Permeability and stability of lipid bilayers.* Elsevier, 1995.

[159] W. Wintz, H.-G. Döbereiner, and U. Seifert. Starfish vesicles. *Europhys. Lett.*, 33:403, 1996.

[160] Y. Xia, X. Yin, N.A.D. Burke, and H.D.H Stöver. Thermal response of narrow-dispersed poly(n-isopropylacrylamide) prepared by atom transfer radical polymerization. *Macromolecules*, 38:5937–5943, 2005.

[161] Q. Yang, X. Liu, S. Ajiki, M. Hara, P. Lundahl, and V. Miyake. Avidin-biotin immobilization of unilamellar liposomes in gel beads for chromatographic analysis of drug-membrane partitioning. *J. Chromatog. B.*, 707:131, 1998.

Résumé

Les gouttes, les vésicules et les globules rouges sont des objets mous et déformables, structurés et de taille micrométrique (de 1 à 100 microns de diamètre). L'objectif de ce travail est de déterminer la participation de chaque paramètre mécanique (tension de surface, élasticite, viscosité) des objets étudiés à partir de leur comportement sous écoulement. Nous avons choisi de nous intéresser tout particulièrement à la réponse de ces objets sous écoulement confiné (ou semi-confiné) en utilisant une approche de type "microfluidique".
Nous avons étudié l'effet de la production de tensioactif *in situ* à l'interface d'une goutte sur sa forme et sa dynamique.
Nous avons également rapporté la fabrication et l'étude sous contraintes externes de vésicules, aux propriétés visco-élastiques - dites "complexes" - modulables par une modification de la température ; les deux systèmes étudiés sont des vésicules géantes remplies d'une solution de polymère ou d'un gel covalent de PolyNIPAm et des vésicules DMPC, en phase fluide et gel.
Dans le cas des globules rouges soumis à un cisaillement, deux types de mouvements sont connus : un mouvement de bascule et un mouvement de chenille de char. Nous avons mis en évidence l'existence d'un nouveau régime d'oscillations superposé au mouvement de chenille de char. Notre étude a également porté sur le comportement de globules rouges s'écoulant dans des canaux de dimension comparable à leur taille. Un diagramme de forme a été établi en fonction de la vitesse de l'objet, de la viscosité externe et de la section du capillaire. Nous avons développé un système mesurant la chute de pression associée au passage d'une cellule unique dans un canal de même dimension. Cette mesure permet notament de corréler le signal obtenu avec les propriétés physiques et mécaniques des objets étudiés. Nous nous sommes enfin intéressé au cas d'une suspension concentrée de cellules sanguines dans un écoulement pathologique: la thrombose.

Abstract

Drops, vesicles and red blood cells are soft and deformable, structured (or organized), micron-size particles (from 1 to 100 microns in diameter). The objective of this work is the determination of the participation of each mechanical parameter (surface tension, elasticity, viscosity...) of the objects studied from their behavior under flow. We chose to focus particularly on the response of these particles under confined flow by using the "microfluidic" approach.
We detailed the consequences of surfactant production - due to chemical reaction - at the surface of a droplet flowing in a close fitting channel.
We reported the fabrication the characterization of giant vesicles enclosing a polymer solution or a covalent gel of PolyNIPAm. We studied the effect of temperature on the behavior of DMPC vesicles, in the fluid or the gel phase, under shear flow near a plane.
In the case of red blood cells under shear flow, two types of motion are known : the tumbling and the tank-treading. We highlight the existence of a new swinging regime superimposed to the tanktreading. We also studied the behavior of red blood cells flowing in a close fitting channel. We established a shape diagram as a function of the object velocity, the external viscosity and the capillary diameter. We developed a system able to measure the drop of pressure associated with the flow of a single cell in a close fitting channel. This measurement allows the correlation the signal obtain and the physical and mechanical properties of the objects. We finally studied the flow of a concentrated suspension of blood cells in a pathologic case : the thrombosis.